WWU
MÜNSTER

Measurement of the energy loss of 18.6 keV electrons on deuterium gas and determination of the tritium Q-value at the KATRIN experiment

Rudolf Sack, Dissertation 2020

wissen.leben

Institut für Kernphysik

Westfälische Wilhelms-
Universität Münster

Experimentelle Physik

Dissertationsthema

Measurement of the energy loss of 18.6 keV electrons on deuterium gas and determination of the tritium Q-value at the KATRIN experiment

Messung der Energieverlustfunktion von 18.6 keV Elektronen an Deuterium Gas und Bestimmung des Q-Werts von Tritium am KATRIN Experiment

Inaugural-Dissertation
zur Erlangung des Doktorgrades der Naturwissenschaften
im Fachbereich Physik
der Mathematisch-Naturwissenschaftlichen Fakultät
der Westfälischen Wilhelms-Universität Münster

vorgelegt von

Rudolf Sack

aus Ludwigshafen am Rhein

— 2020 —

überarbeitete Version

Ergänzung

Änderungen im Vergleich zur Abgabeversion:
Die Abgrenzung dieser Arbeit zu anderen Arbeiten wurde deutlicher hervorgehoben.
Es wurden zusätzliche Literaturhinweise hinzugefügt und Vorzeichenfehler korrigiert. Diese Änderungen haben keine Auswirkungen auf die präsentierten Ergebnisse.

Dekan:	Prof. Dr. Gerhard Wilde
Erster Gutachter:	Prof. Dr. Christian Weinheimer
Zweiter Gutachter:	Prof. Dr. Kathrin Valerius
Tag der mündlichen Prüfung:	07.09.2020
Tag der Promotion:	07.09.2020

Ich versichere, dass ich die Arbeit selbständig verfasst und keine anderen als die angegebenen Quellen und Hilfsmittel benutzt, sowie Zitate kenntlich gemacht habe.

Ort, Datum Unterschrift

Ich freue mich, wenn es regnet. Denn wenn ich mich nicht freue, regnet es auch.

— Karl Valentin

Contents

Abstract **v**

Abstract (deutsch) **vii**

Summary **ix**

Zusammenfassung **xiii**

1 Neutrino physics **1**
1.1 Postulation and discovery 1
1.2 Neutrinos in the Standard Model 2
1.3 Neutrino oscillation 3
1.3.1 Search for δ_{CP}: 4
1.3.2 Hint at mass ordering: 5
1.4 Neutrino mass theory 6
1.4.1 Seesaw mechanism 6
1.5 Neutrino mass determination 7
1.5.1 Observational cosmology 7
1.5.2 Neutrinoless double beta decay $0\nu\beta\beta$ 9
1.5.3 Direct neutrino mass measurements from the kinematics of weak decays 11

2 KATRIN experiment **15**
2.1 Measurement principle 16
2.2 Tritium beta spectrum 16
2.3 MAC-E-Filter 17
2.3.1 Electric filtering 17
2.3.2 Magnetic adiabatic collimation 19
2.3.3 Energy resolution 19

2.3.4 Magnetic mirror . . . 20
2.3.5 Magnetic flux tube . . . 21
2.3.6 Transmission of the main spectrometer . . . 21
2.3.7 Background of the main spectrometer . . . 21
2.4 Source and transport section (STS) . . . 22
2.5 Stability of the source . . . 23
2.5.1 Temperature stability . . . 23
2.5.2 Tritium circulation . . . 23
2.6 Transport section . . . 26
2.6.1 Differential pumping section . . . 26
2.6.2 Cryogenic pumping section . . . 27
2.7 Spectrometer and detector section (SDS) . . . 29
2.7.1 Pre spectrometer (PS) . . . 30
2.7.2 Main spectrometer (MS) . . . 30
2.7.3 Focal plane detector - FPD . . . 31
2.7.4 Monitor spectrometer - MoS . . . 31
2.7.5 High voltage at KATRIN . . . 32
2.8 Calibration and monitoring tools . . . 33
2.8.1 Rear wall and instrumentation . . . 33
2.8.2 Activity monitoring . . . 34
2.8.3 Composition monitoring . . . 36
2.8.4 Precision electron sources . . . 39

3 Precision photoelectron source 43
3.1 Working principle and concept . . . 44
3.2 Description of the e-gun flange . . . 47
3.3 Optical components . . . 49
3.3.1 Optics box and light sources . . . 50
3.3.2 Laser driven light source . . . 51
3.3.3 Pulsed UV-laser . . . 51
3.4 HV concept of the electron gun . . . 54
3.5 Measurements with the electron gun at a test stand . . . 58
3.6 Photoelectron gun in KATRIN: . . . 65
3.6.1 Vacuum system . . . 65
3.6.2 Electromagnetic design of the rear section . . . 67
3.6.3 Rate and rate stability . . . 72
3.6.4 Voltage stability . . . 73

3.6.5 Beam diameter . . . 75
3.6.6 Transmission function . . . 77
3.6.7 Zero angle . . . 81
3.6.8 Transmission function measurements with higher B-field and non-zero angles . . . 83

4 Energy loss due to scattering with D_2 molecules 87
4.1 General idea of electron scattering in KATRIN . . . 87
4.1.1 Response function . . . 88
4.1.2 Details on scattering in KATRIN . . . 89
4.2 Energy loss measurement on deuterium in STS3a . . . 90
4.2.1 Integral measurement . . . 91
4.2.2 Time of flight method . . . 92
4.2.3 Measurement and data handling . . . 92
4.2.4 Novel parametrization for energy loss model with BED ionization tail 102
4.2.5 Fit of the Eloss data . . . 105
4.2.6 Mean energy loss comparison with stopping power . . . 111
4.2.7 Comparison with other energy loss models . . . 113
4.2.8 Discussion and outlook . . . 115

5 Q-value of tritium 117
5.1 Motivation to measure the Q-value . . . 117
5.2 Q-value from other experiments . . . 117
5.3 Endpoint and recoil . . . 118
5.4 Determination of $Q(T_2)$ in KATRIN . . . 120
5.4.1 Overview over the potentials in KATRIN . . . 120
5.4.2 Fowler method . . . 120
5.4.3 Numerical artifacts in fitting the Fowler function . . . 124
5.4.4 Corrections to the measured data . . . 125
5.4.5 Fowler model including corrections . . . 129
5.4.6 Work function of the e-gun . . . 132
5.4.7 Determination of the spectrometer work function . . . 135
5.4.8 Stability of the work functions . . . 137
5.5 Work function of the rear wall . . . 142
5.5.1 Work function investigations in STS3a . . . 142
5.5.2 Work function investigations before KNM1: . . . 146
5.5.3 Summary of RW work function investigations . . . 149

5.6 Starting potential in the WGTS 149
5.7 Q-value of tritium in the first tritium campaign 150
5.8 Q-value of tritium in the first science run of KATRIN 151

6 Possible plasma instabilities in KATRIN **155**
6.1 General introduction to plasma instabilities 155
6.2 General Introduction 157
6.3 Electron spectrum 158
6.4 Current driven instability in partially ionised media 161
6.5 Plasma instability in the Whistler mode caused by a gyrating electron stream 162
6.6 Two stream instability 163

A Appendix **165**
A.1 Eloss results 165
A.2 Transmission functions 168
A.3 E-gun diode efficiency 171
A.4 Appendix: Edge positions 171
A.5 Light intensity distribution on rear wall 174
A.6 Contact potential difference with Kelvin probe on rear wall 175
A.7 KNM2 e-gun work function measurement 176
A.8 Plasma 178

Abstract

Neutrinos are fundamental particles with interesting, yet not fully revealed properties. They are the only fermions without electric charge and by far the lightest massive particles in the standard model of elementary particle physics. Their nature is studied in particle physics, astroparticle physics and cosmology. A direct way to determine the rest mass of the neutrino is high-precision spectroscopy of electrons from β-decay or electron capture close to the kinematic endpoint.

The Karlsruhe tritium neutrino experiment KATRIN aims to measure the mass of the electron antineutrino with a sensitivity of $0.2\,\mathrm{eV/c^2}$ with a model-independent approach. In the β-decay of tritium an electron and an electron antineutrino are created. The rest mass of the latter distorts the shape of the energy spectrum of the electron close to the kinematic endpoint. KATRIN measures this spectrum with a high-resolution MAC-E-Filter to determine the neutrino mass with an unprecedented precision that is one order of magnitude better than previous laboratory experiments. A difficulty in this type of experiment is that any unaccounted broadening of the measured tritium spectrum results in a negative shift of the observed neutrino mass squared. One way to cross-check that no unconsidered effects appear is by comparing the Q-value with the ^{3}He,T mass difference. The Q-value is the amount of energy released in the β-decay and can be determined with KATRIN. The ^{3}He,T mass difference can be measured with high precision in Penning trap measurements.

One of the main goals of this thesis is to investigate the absolute energy scale of the KATRIN experiment and to determine the Q-value of tritium β-decay. To achieve this ambitious goal the starting potential of the electrons in the windowless gaseous tritium source as well as the potential in the analyzing plane of the main spectrometer needs to be determined. To investigate the potential in the analyzing plane an angular selective, monoenergetic photoelectron source, referred to as 'e-gun', is assembled, commissioned, and characterized during this work. The Fowler method is introduced and used to determine the work function of the e-gun. With this information the work function of the main spectrometer is determined in another measurement. The Fowler method is also used to

determine the work function of the rear wall. The rear wall is a gold plated disk at the upstream end of KATRINs windowless gaseous tritium source (WGTS) and influences the starting potential of the β-electrons in the WGTS. The reason for this is the fact that a conductive plasma forms in the WGTS if a sufficient amount of tritium is inside. A theory chapter in this thesis investigates the possibility of instabilities in the plasma. With the knowledge of the potentials in the source and the analyzing plane, it is possible to determine the Q-value of tritium beta day. This is done for the first tritium commissioning campaign of KATRIN and for the first science run.

The aforementioned e-gun is a multipurpose tool in KATRIN. Its most important task is the measurement of the energy loss function, which describes the energy loss of signal electrons passing the gaseous source and possibly scattering with the molecules of the source gas. In this work, this measurement is performed on deuterium gas with a normal integrating measurement and also with a quasi-differential method using the time of flight information of the electrons. Based on these measurements a new model parametrization is created and fitted to the data. The mean energy loss is calculated from this model and cross-checked with literature data.

The assembly and commissioning of the e-gun, the measurement of the energy loss function with deuterium gas and the determination of the Q-value in the first science run are crucial contributions to understand and improve the KATRIN experiment.

Abstract (deutsch)

Neutrinos sind Elementarteilchen mit interessanten Eigenschaften. Sie sind die einzigen Teilchen aus der Familie der Fermionen ohne elektrische Ladung und sie sind von allen massebehafteten Teilchen im Standard Modell der Teilchenphysik mit Abstand die leichtesten. Ihre Eigenschaften werden in der Teilchenphysik, der Astroteilchenphysik und in der Kosmologie erforscht. Eine direkte Möglichkeit ihre Ruhemasse zu bestimmen ist die hochpräzise Spektroskopie von Elektronen aus dem β-Zerfall oder dem Elektroneneinfang nahe an der maximal in dem Zerfall möglichen Energie, dem kinematischen Endpunkt des Spektrums. Das Karlsruher Tritium Neutrino Experiment KATRIN hat das Ziel, die Masse des Elektron-Antineutrinos mit einer Sensitivität von $0.2\,\mathrm{eV/c^2}$ durch eine modellunabhängige Herangehensweise zu bestimmen. Bei dem β-Zerfall von Tritium werden neben dem Tochterkern noch ein Elektron und ein Elektron-Antineutrino erzeugt. Die Ruhemasse des Antineutrinos verändert die Form des Energiespektrums des Elektrons in der Nähe des kinematischen Endpunkts auf eine charakteristische Art und Weise. Das KATRIN Experiment misst dieses Spektrum mit einem hochauflösenden MAC-E-Filters, um die (Anti-)Neutrinomasse mit einer Präzision zu Messen, die um eine Größenordnung sensitiver ist als vorhergehende Laborexperimente. Eine der Schwierigkeiten in diesem Experiment ist, dass jede unbeachtete Verschmierung des Spektrums zu einer Verschiebung des gemessenen Neutrino Massenquadrates zu negativen Werten führt. Eine Möglichkeit die Messung auf Konsistenz mit anderen Experimenten zu überprüfen und auf diese Art einen Hinweis auf potenziell übersehene Effekte zu bekommen, ist der Vergleich des Q-Werts. Der Q-Wert gibt die Menge an Energie an, die beim β-Zerfall frei wird, und kann mit der Massendifferenz von Tritium zu Helium-3 verglichen werden. Diese Massendifferenz wurde bereits mehrfach in hochpräzisen Penning-Fallen gemessen, und steht als Referenz zur verfügung.
Ein Hauptziel dieser Arbeit ist die Untersuchung der absoluten Energieskala von KATRIN um den Q-Wert des β-Zerfalls von Tritium mit dem KATRIN Experiment zu bestimmen. Um dieses ambitionierte Ziel erreichen zu können, muss das Startpotenzial der Elektronen in der fensterlosen gasförmigen Tritiumquelle, so wie auch das Potenzial in

der Analysierebene des Hauptspektrometers, bestimmt werden. Um das Potenzial in der Analysierebene untersuchen zu können, wurde eine winkelselektive und monoenergetische Photoelektronenquelle, die als 'e-gun' bezeichnet wird, in dieser Arbeit zusammengebaut, kommissioniert und charakterisiert. Die Fowler Methode wird erklärt und verwendet um die Austrittsarbeit der e-gun zu bestimmen. Mit dem Wissen über diese Austrittsarbeit, kann mit Hilfe einer Transmissionsmessung die Austrittsarbeit des Hauptspektrometers bestimmt werden. Die Fowler Methode wird zudem auch dazu verwendet die Austrittsarbeit der KATRIN 'rear wall' zu bestimmen. Die rear wall ist eine vergoldete Edelstahlscheibe, die das geschlossene Ende des Quellrohrs darstellt (das offene Ende zeigt zum Detektor). Die rear wall beeinflusst das Startpotenzial der β-Elektronen, da sich in der Quelle ein leitfähiges, selbstionisierendes Plasma ausbildet, wenn sich eine ausreichende Menge an Tritium in der Quelle befindet. Ein Theoriekapitel in dieser Arbeit untersucht zudem mögliche Instabiltitäten in diesem Plasma. Mit dem gesammelten Wissen über die Potenziale in der Quelle und der Analysierebene ist es möglich den Q-Wert des β-Zerfalls von Tritium zu bestimmen. In dieser Arbeit wird der Tritium-Q-Wert mit den Daten der ersten Tritium Kommissionierungsphase (FT) von KATRIN und für die erste Neutrino-Messkampagne (KNM1) bestimmt. Die e-gun kann für viele Untersuchungen im KATRIN Experiment verwendet werden. Ihre wichtigste Aufgabe ist die Bestimmung der Energieverlustfunktion, welche den Energieverlust von Elektronen beschreibt, die beim Durchqueren der Quelle mit den Molekülen des Quellgases stoßen und dabei Energie verlieren können. In dieser Arbeit wird diese Messung mit Deuterium als Quellgas durchgeführt. Dabei werden zwei verschiedene Messmodi verwendet, eine integrale Messung, und auch eine quasi-differenzielle Methode, in der die Flugzeit der Elektronen als zusätzliche Information verwendet wird. Basierend auf diesen Messungen wird eine neue Parametrisierung für die Energieverlustfunktion vorgeschlagen und an die Daten gefittet. Mit diesem Energieverlustmodell kann der mittlere Energieverlust berechnet werden und mit dem Literaturwert verglichen werden, um das Modell zu testen.
Der Zusammenbau und die Kommissionierung der e-gun, die Bestimmung der Energieverlustfunktion in Deuterium Gas, und die Bestimmung des Q-Werts im ersten Wissenschaftslauf von KATRIN sind wichtige Beiträge zum Gelingen des gesamten KATRIN Experimentes.

Summary

The Karlsruhe tritium neutrino experiment KATRIN aims to measure the neutrino mass by scanning the energy spectrum of electrons from tritium β-decay close to the kinematic endpoint. It has recently set the best upper limit on the antineutrino mass measured with a laboratory experiment of $m_{\bar{\nu}} \leq 1.1\,\mathrm{eV/c^2}$ (90 % C.L.). The final assembly of the beamline, the commissioning phase and the first science run were performed within the time frame of this thesis. The work and analysis performed in this thesis contributed to its success.
In the first part of this work a monoenergetic and angular selective electron source, the so-called rear section e-gun, was assembled and first used on a test stand. These measurements are described at the beginning of chapter 3 and show that the e-gun can sustain the required high voltage and produces photoelectrons with the required rate and rate stability with the laser driven light source (LDLS). The optical power of the light source is monitored with a diode. The required optical system, which includes the light source, a fiber splitter and the diode itself, is characterized with respect to its wavelength dependence. With this knowledge, the work function of the e-gun can be determined. This is described in chapter 5.4.2. The work function of the e-gun changed from $\Phi = 4.02(3)\,\mathrm{eV}$ in the test stand to $\Phi = 4.43(3)\,\mathrm{eV}$ in the KATRIN beamline in the STS3a measurement phase. This change can most likely be explained with the improved vacuum conditions in KATRIN compared to the test stand. Also, the rate of the e-gun decreased a lot, roughly from 80 kcps at the test stand to only 2 kcps in KATRIN STS3a with the LDLS. The reason for this strong drop is not known. Possibly a hardware modification before mounting the e-gun to the beamline has caused a problem. The modification increased the distance from the optical fibers to the entrance window of the e-gun. The e-gun can be operated with an alternative light source, a pulsed 266 nm laser with adjustable power. This laser has enough power to achieve at least 100 kcps, which surpasses the specification by a factor of five. In the commissioning measurements the zero angle of the electron source is determined. It is further shown that the beam can be steered across the focal plane detector with the superconducting dipole coils of the WGTS. It is also demonstrated that the angular selectivity via the tilting of the e-gun plates works. When the e-gun is set to the zero angle it

has a width of only 80 meV at the 266 nm of the laser and 130 meV at the optimal LDLS wavelength of 250 nm, which clearly surpasses the requirement of $\sigma \leq 200$ meV. The LDLS is a continuous wave source, whereas the UV-laser is a pulsed source with a repetition rate of 20-100 kHz, which is used for measurements with additional time of flight information.
One of the main topics of this work is the determination of the tritium Q-value with the KATRIN experiment. This value can be compared to $\Delta M(^3\mathrm{He,T})$ measurements with Penning traps, which differ only by the molecular binding energies, which are well known. The current best value measured with a Penning trap has an absolute uncertainty of only 70 meV. The value determined at KATRIN can be compared to this value as an important validation of the energy scale and endpoint fits. This is an important check because the fitted endpoint is correlated with the fitted squared neutrino mass. In this work, the e-gun is used to determine the work function of the main spectrometer. For the KNM 1 campaign a value of $\Phi_{\mathrm{MS,\,KNM\,1}} = 4.1(2)$ eV is measured. The work function of the rear wall is measured at the beginning of the KNM1 measurement phase to be $\Phi_{\mathrm{RW}} = 4.3$ eV. This measurement is performed with a spatial resolution of 100 pixels and covers about 70 % of the RW area. A measurement before and after exposure of the rear wall to deuterium gas during the STS3a campaign shows that the work function of the RW is lowered by roughly 100 meV. The method used in this work does not work under tritium conditions due to the high residual tritium activity. For this reason, the measured decrease of the work function after exposure to deuterium is used. It is further assumed that the plasma inside the WGTS is conductive and therefore the RW potential determines the starting potential of the electrons in the source. For the KNM1 campaign this potential is $\Phi_{\mathrm{WGTS,\,KNM\,1}} = 4.35(40)$ eV. This input can be used to calculate the Q-value from the fitted endpoint of the tritium spectrum. In [33] the KATRIN collaboration reports a value of $Q_{\mathrm{KNM\,1}}(\mathrm{T_2}) = 18575.2(5)$ eV. The derivation of this Q-value from the fitted endpoint is performed in chapter 5 of this work. The result is in good agreement with the Q-values derived from the Penning trap measurements.
The second major topic of this work is the measurement of the energy loss function. Electrons passing through the windowless gaseous tritium source of the KATRIN experiment have a certain chance for an inelastic scattering process with the tritium molecules in the source. In this process, the tritium molecule goes into an electronically excited state or even gets ionized. In this process, the initial electron can lose between 11 eV and half of its kinetic energy. The probability to lose a particular amount of energy is described by the energy loss function.
The e-gun is used to measure the response function at different column densities and in two different measurement modes. The first one is a standard integral measurement with the main spectrometer acting as a high pass filter. The second one uses additional time of flight

information of the UV-laser. In chapter 4 the energy loss measurements on deuterium are described and a new parametrization for the energy loss function is introduced and fitted to the measured data to deconvolve the energy loss function from the measurement. It is shown that the measurement technique and the analysis are well justified, and they yield a robust result with reasonably small uncertainties. This model is a significant improvement to previously available models and removes the energy loss model from the list of the large systematic uncertainties of the KATRIN experiment. The analysis of the energy loss measurements with tritium gas, which have been performed in the KNM1 measurement phase, is outside the scope of this thesis, but it has been performed with the same method and the same parametrization as the deuterium based data which is analysed in this work. In the first publication of a neutrino mass result from the KATRIN collaboration, the systematic uncertainties on the neutrino mass due to the uncertainties of the energy loss model are described as 'negligible' [33]. This is an important contribution to the experiment and it opens up the possibility to scan further below the endpoint where the exact knowledge of the energy loss function becomes even more important.
The final chapter of this thesis deals with potential plasma instabilities in the windowless gaseous tritium source of KATRIN. In a simplified approach, the electrons are described as two populations. One of them are the fast β-electrons, the others are thermal electrons. The electron velocities and densities, as well as other parameters of the source such as the magnetic field are used to estimate the growth rate of potential plasma instabilities based on analytical formulas. These results can give an analytical insight and input for simulation-based studies, such as the particle in cell simulations which are currently being used to investigate the plasma conditions in the WGTS. These simulations, in combination with other measurements such as the measurement of the electric current at the rear wall and the coupling measurements at different rear wall potentials, can give a more conclusive picture of the behavior of the plasma and the true starting potential of the electrons in the source. In this work, the source potential is the dominant uncertainty for the Q-value determination and the possibility of a longitudinal gradient, which would result in an additional broadening of the spectrum and an effective shift of the energy loss function, is not yet excluded and has to be investigated in further measurements. One of the promising ways to do that is a measurement with ^{83m}Kr admixed to the tritium gas inside the source. Those measurements have been performed in the past and will be extended in the next measurement phase of KATRIN. This will improve the accuracy of the Q-value determination as well as the neutrino mass measurement.

Zusammenfassung

Das Karlsruher Tritium Neutrino Experiment KATRIN hat das Ziel die Neutrinomasse, durch Spektroskopie des integralen Energiespektrums des Elektrons aus dem β-Zerfall von Tritium nahe dem kinematischen Endpunkt, zu bestimmen. Die KATRIN Kollaboration hat im Jahr 2019 eine neue Obergrenze von $m_{\bar{\nu}} \leq 1.1\,\mathrm{eV/c^2}$ (90 % C.L.) bestimmt. Die Fertigstellung des Strahlrohrs, die Kommissionierungsphase und die erste Messphase zur Bestimmung der Neutrinomasse fanden im Zeitraum dieser Doktorarbeit statt. Die Arbeit und die Analyse die in dieser Arbeit durchgeführt wurden, haben zu dem Erfolg des Experimentes beigetragen.

Im ersten Teil dieser Arbeit wurde eine monoenergetische, winkelselektive Photoelektronenquelle, die sogenannte e-gun, zusammengebaut und zunächst in einem Teststand auf ihre funktionsfähigkeit überprüft. Die dazugehörigen Messungen werden am Anfang von Kapitel 3 beschrieben. Sie zeigen, dass die e-gun die erforderliche Hochspannung aushält und Elektronen mit ausreichender Rate und Ratenstabilität produzieren kann. Als Lichtquelle zur Erzeugung der Photoelektronen wird hierbei die sogenannte LDLS (laser driven light source) verwendet, deren optische Leistung stets mit einer Photodiode gemessen wird. Die hierzu benötigte Ausrüstung, wie die LDLS, ein Fasersplitter und die Diode, werden, wie in Kapitel 5 beschrieben wird, auf ihre Wellenlängenabhängigkeit untersucht. Mit Hilfe dieser Informationen ist es möglich die Astrittsarbeit der e-gun zu bestimmen, was in Kapitel 5.4.6 beschrieben wird. Die Austrittsarbeit hat sich von $\Phi = 4.02(3)\,\mathrm{eV}$ auf dem Teststand zu $\Phi = 4.43(3)\,\mathrm{eV}$ im KATRIN Strahlrohr in der Kommissionierungsphase des KATRIN Experiments, die als STS3a Messkampagne bezeichnet wird, geändert. Die Änderung der Austrittsarbeit kann plausibel mit der Verbesserung der Vakuumbedingungen erklärt werden. Zudem hat sich die mit der LDLS als Lichtquelle erreichte Elektronenrate der e-gun stark verringert. Von etwa 80 kcps auf dem Teststand zu gerade mal 2 kcps in der STS3a Messphase. Der Grund für diesen Rateneinbruch ist nicht genau bekannt. Möglicherweise hat eine Modifikation der Hardware, der Einbau eines Abstandshalters zur Vermeidung eines virtuellen Lecks in an der Faserhalterung, die kurz vor dem Einbau der e-gun am Katrin Strahlrohr durchgeführt wurde, dieses Problem verursacht. Durch diesen Umbau

wird der Abstand der Glasfaser, die das Licht auf der Vakuumseite bis zur Emissionskathode transportieren, und dem Fenster durch welches das Licht hineingelangt, vergrößert. Die e-gun kann auch mit einer anderen Lichtquelle, einem gepulsten Nd:YVO_4 Laser mit 266 nm Wellenlänge und einstellbarer Leistung, betrieben werden. Mit diesem Laser erreicht die e-gun eine Elektronenrate von mindestens 100 kcps und übertrifft damit deutlich die Anforderung von 20 kcps. In der STS3a Messphase wird zudem der Nullwinkel der e-gun bestimmt, also der Plattenwinkel bei dem die erzeugten Elektronen möglichst wenig Transversalenergie haben. Es wird des Weiteren gezeigt, dass die Position des Elektronenstrahls mit Hilfe der supraleitenden magnetischen Dipolspulen der WGTS gesteuert werden und dadurch jeder Pixel auf dem Detektor erreicht werden kann. Schließlich wird noch gezeigt, dass die Winkelselektivität der e-gun durch das Kippen der Platten der e-gun funktionert. Wenn die e-gun auf den Nullwinkel eingestellt und mit dem 266 nm Laser betrieben wird, hat sie eine Breite von nur 80 meV. Mit der LDLS bei 250 nm wird eine Breite von knapp 130 meV gemessen. Damit wird die Anforderung von $\sigma \leq 200$ meV deutlich erfüllt. Die LDLS ist eine Dauerstrich-Quelle, wohingegen der Laser eine gepulste Lichtquelle mit einer einstellbaren Wiederholungsrate von 20 - 100 kHz ist. Dies ermöglicht es bei Messungen mit dem laser die Flugzeit der Elektronen als zusätzliche Information zu verwenden.

Eines der Hauptthemen in dieser Arbeit ist die Bestimmung des Q-Werts von Tritium mit dem KATRIN Experiment. Dieser Wert kann mit Messungen des Massenunterschiedes $\Delta M(^3\mathrm{He,T})$ verglichen werden, der in Experimenten mit Penningfallen bestimmt werden kann. Der Q-Wert und $\Delta M(^3\mathrm{He,T})$ unterscheiden sich lediglich dich molekulare und atomare Bindungsenergieen, welche gut bekannt sind. Die genaueste Messung mit einer Penningfalle hat eine Unsicherheit von nur 70 meV. Der bei KATRIN bestimmte Wert kann damit verglichen werden. Dadurch kann die absolute Energieskala von KATRIN und der Fit des Endpunktes überprüft werden. Dies ist ein wichtiger Test, da der ermittelte Endpunkt mit dem Neutrino-massenquadrat korreliert ist. In dieser Arbeit wird die e-gun verwendet, und mit ihrer Hilfe die Austrittsarbeit des Hauptspektrometers bestimmt. Für die erste Neutrinomassen-Messphase (KNM1) wird ein Wert von $\Phi_{\mathrm{MS,\,KNM1}} = 4.1(2)\,\mathrm{eV}$ bestimmt. Die Austrittsarbeit der Rear Wall (RW) wird zu Beginn dieser Messphase zu $\Phi_{\mathrm{RW}} = 4.3\,\mathrm{eV}$ bestimmt. Diese Messung wird mit einer räumlichen Auflösung von 100 Pixeln durchgeführt und deckt etwa 70 % der Fläche der RW ab. Eine Messung der Austrittsarbeit der RW vor und nach der Exposition von Deuteriumgas während der STS3a Messkampagne zeigt, dass die Austrittsarbeit dadurch um etwa 100 meV gesenkt wird. Die in dieser Arbeit verwendete Methode funktioniert allerdings nicht unter Tritiumbedingungen, da die Restaktivität diese Art von Messung mit der vorhandenen Ausrüstung unmöglich macht. Aus diesem Grund wird der in STS3a mit Deuterium ermittelte Wert

angenommen. Des Weiteren wird angenommen, dass sich in der WGTS unter Tritiumbedingungen ein leitfähiges Plasma ausbildet und daher die RW, welche in Kontakt mit dem Plasma steht, das Startpotenzial der Elektronen in der Quelle bestimmt. Für die KNM1 Messphase wird dieses Potenzial zu $\Phi_{\mathrm{WGTS,\,KNM1}} = 4.35(40)\,\mathrm{eV}$ bestimmt. Mit diesen Werten kann der Q-Wert aus dem bestimmten Endpunkt des Spektrums ermittelt werden. Die KATRIN Kollaboration berichtet in ihrer Veröffentlichung zur KNM1 Messphase [33] einen Wert von $Q_{\mathrm{KNM1}}(\mathrm{T}_2) = 18575.2(5)\,\mathrm{eV}$. Die Bestimmung des Q-Werts aus dem Endpunkt wird in Kapitel 5 dieser Arbeit beschrieben. Der hier bestimmte Wert stimmt mit den aus den Penning-Fallen-Experimenten abgeleiteten Werten gut überein.
Das zweite große Thema dieser Arbeit ist die Messung der Energieverlustfunktion. Elektronen lönnen beim Durchqueren der Fensterlosen Tritumquelle des KATRIN Experimentes inelastisch mit den dort vorhandenen Gasmolekülen stoßen. Dabei kann das Elektron zwischen 11 eV und der Hälfte seiner kinetischen Energie, im Fall der für Katrin interessanten Elektronen sind das knapp 9.3 keV, verlieren. Die Wahrscheinlichkeit eine bestimmte Menge Energie zu verlieren wird durch die Energieverlustfunktion, kurz Eloss-Funktion, beschrieben, und kann mit der e-gun gemessen werden.
Die e-gun wird verwendet um die Antwortfunktion bei verschiedenen Säulendichten und in zwei verschiedenen Betriebsmodi zu messen. Der erste Modus ist eine normale integrierende Messung bei der das Hauptspektrometer als Hochpassfilter agiert. Der Zweite Modus nutzt zusätzlich die Flugzeitinformation, um ein quasi-differenzielles Spektrum zu erhalten. In Kapitel 4 dieser Arbeit werden die Messungen zur Energieverlustfunktion von Elektronen mit Deuterium beschrieben. Des Weiteren wird eine neue Parametrisierung motiviert und an die Daten angepasst, um aus den Messdaten die Energieverlustfunktion zu entfalten. Es wird gezeigt, dass die Messmethoden und Analysen geeignet sind und ein robustes Resultat mit geringen Unsicherheiten liefern. Das hierdurch erhaltene Modell ist eine signifikante Verbesserung im Vergleich zu den zuvor vorhandenen Beschreibungen und streicht die Energieverlustfunktion von der Liste der großen systematischen Unsicherheiten des KATRIN Experimentes. Die Analyse der Energieverlustmessungen mit Tritium, die in der KNM1 Messphase durchgeführt wurden, sind außerhalb des Themengebietes dieser Arbeit, werden aber mit den gleichen Methoden gemessen und mit der gleichen Parametrisierung beschrieben wie die Daten in dieser Arbeit. In der ersten Publikation einer Obergrenze für die Neutrinomasse durch die KATRIN Kollaboration, wird die systematische Unsicherheit durch das Energieverlustmodell als 'vernachlässigbar' beschrieben [33]. Das ist ein wichtiger Beitrag zum Erfolg des Experiments und eröffnet die Möglichkeit tiefer in das Spektrum hinein zu messen, wo die exakte Kenntnis der Energieverlustfunktion noch wichtiger wird.
Das letzte Kapitel dieser Arbeit handelt von potenziellen Plasmainstabilitäten in der fensterlosen gasförmigen Quelle von KATRIN. In einem stark vereinfachendem Ansatz werden

die Elektronen in der Quelle als zwei Populationen mit einer Gaussförmigen Geschwindigkeitsverteilung beschrieben. Die eine Population bilden die schnellen β-Elektronen, die Andere thermalisierte Elektronen. Die Geschwindigkeiten, Dichten und weitere Parameter der Elektronen, sowie das magnetische Feld der Quelle, werden verwendet um, die Wachstumsrate von potenziellen Plasmainstabilitäten mit Hilfe analytischer Formeln abzuschätzen. Diese Ergebnisse können analytische Einsichten geben und Hinweise für simulationsbasierte Studien geben. Zum Beispiel für die 'particle in cell' Simulationen, die verwendet werden um, die Plasmabedingungen in der Quelle genauer zu untersuchen. Zusammen mit weiteren Messungen wie etwa der Änderung des elektrischen Stroms an der RW und der Kopplungsmessungen des Quellpotenzials bei verschiedenen Bias-Spannungen der RW, können diese Simulationen zu einem konsistenteren Bild des Quellplasmas, und damit des Startpotenzials der Elektronen, führen. In dieser Arbeit ist das Quellpotenzial die dominante Unsicherheit bei der Bestimmung des Q-Werts. Weitere Untersuchungen des Quellpotenzials, zum Beispiel durch Messungen mit zugesetztem ^{83m}Kr in der Tritiumquelle können weitere Einsichten in das Quellpotenzial geben. Dadurch kann sowohl die Genauigkeit des Q-Werts, als auch die Messung der Neutrinomasse verbessert werden.

Chapter 1

Neutrino physics

Neutrino physics is an active field in modern particle physics with links also to other fields such as cosmology. The following chapter will give a brief overview of neutrino physics, neutrino oscillation, neutrino mass states and about experiments trying to measure the neutrino mass.

1.1 Postulation and discovery

In 1930 Wolfgang Pauli postulated an electrically neutral particle with a mass smaller than the electron mass [100]. This particle serves to explain the observed continuous energy spectrum of β-decay. If β-decay was a two-body decay, as was thought at that time, the energy of the electron would be mono-energetic because of energy and momentum conservation, just as it is observed in α- and γ- decay events. The continuous energy spectrum, however, requires a third particle which is created in the decay. Enrico Fermi used the name neutrino for this particle and described β-decay as [36]

$$ {}^{A}_{Z}X \rightarrow {}^{A}_{Z+1}Y + e^{-} + \bar{\nu}_e \tag{1.1} $$

where Y is the daughter nucleus of X after the decay, A the number of nucleons in the core, Z the number of protons in the core, e^{-} the β electron and $\bar{\nu}_e$ the electron antineutrino. In 1956 Cowan and Reines discovered the (electron anti-) neutrino in the reaction

$$ \bar{\nu}_e + p \rightarrow n + e^{+} \tag{1.2} $$

in a water tank [106]. The e^{+} was detected through pair annihilation and the neutron via neutron capture of ^{113}Cd. Both reactions emit characteristic photons which could be

detected.
Neutrinos exist in three different flavors ν_e, ν_μ and ν_τ. Since the lepton flavor is conserved in the weak interaction, the ν_μ and the ν_τ can be detected by the appearance of a μ or a τ in an experiment. The ν_μ was directly discovered in 1962 by Lederman, Schwartz and Steinberger at Brookhaven National Laboratory [19], where they could show that neutrinos produced in the decay of muons can again create muons when they interact with matter, but not electrons. The ν_τ was discovered in 2000 in the DONUT experiment [79], where a neutrino beam went through a system of scintillators and drift chambers, where the creation of the τ particle was identified as a suddenly starting track with a king after a few millimeters, which indicates the decay of short-lived τ lepton.
The ν_e, ν_μ and ν_τ are the three known neutrinos. In theory, it would be possible to have more than three different neutrino types. One way to get information on this is to study the decay of the Z^0. The decay width of the Z^0 boson depends on the number of weakly interacting (so-called 'active') neutrino generations with a mass $m_\nu < Z^0/2$. The result reported from LEP [132] is

$$N_\nu = 2.9840 \pm 0.0082. \tag{1.3}$$

This is in agreement with the known three active Neutrinos. To this date no additional neutrino flavors have been found.

1.2 Neutrinos in the Standard Model

The Standard Model (SM) of particle physics describes all known elementary particles and their interactions. The particles are separated into two groups: The fermions, which have a spin of $S = 1/2$ (more generally $S = n/2$, where n is an odd number. Only elementary particles with $n = 1$ are known.) and the bosons, which have an integer spin. All known elementary bosons have a spin of $S = 0$ or $S = 1$. The bosons with a spin of $S = 1$ are the carrier particles of the three forces which are described by the Standard Model. The photon mediates the electromagnetic force, the $W^\pm$ and the Z^0 mediate the weak force, and the Gluon mediates the strong force. The fermions are split into two subgroups. The Quarks on the one hand, which participate in all three interactions of the Standard Model, and the leptons, which do not take part in the strong interaction. The leptons are again split into two groups, those with an electric charge, the e, μ and τ, and the respective Neutrinos ν_e, ν_μ and ν_τ, which have no electric charge. The Masses of all the above-mentioned particles are known, except for the Neutrinos. Neutrinos are much lighter than any other fermion and within the framework of the Standard Model their mass is even neglected completely.

However, neutrino oscillation, which is described in chapter 1.3, is a strong hint that at least two of the three neutrino mass states have a finite rest mass.

1.3 Neutrino oscillation

The fact that the flavor of a neutrino oscillates during the propagation of the neutrino is one of the most striking properties of these particles. Not only does this show that lepton family number is not a conserved quantity, but it also indicates that at least two of the three neutrino mass eigenstates have a finite rest mass. 'For the discovery of neutrino oscillations, which shows that neutrinos have mass' T. Kajita for Super-Kamiokande [44], and A. McDonald for SNO [129], have been awarded the 2015 Nobel Prize in physics [97]. To describe neutrino oscillation one needs a unitary $n \times n$ matrix which connects the n neutrino flavor eigenstates $|\nu_a\rangle$ and the n neutrino mass eigenstates $|\nu_k\rangle$.

$$|\nu_a\rangle = \sum_k U_{ak} |\nu_k\rangle \tag{1.4}$$

The matrix U can be parameterized by $n(n-1)/2$ mixing angles, $(n-2)(n-1)/2$ Dirac phases and (n-1) Majorana phases. The time evolution of a neutrino is given by

$$|\nu(x,t)\rangle = e^{-i(E_k t - p_k x)} |\nu_k\rangle \tag{1.5}$$

where p is the momentum and x the spatial coordinate. The probability for a neutrino to change its flavor is given by [147]

$$P(\nu_\alpha \to \nu_\beta)(L,E) = \sum_k |U_{ak} U^*_{\beta k}|^2 + 2\, Re \sum_{k<l} U_{ak} U^*_{al} U^*_{\beta k} U_{\beta l}\, exp(-i \frac{L}{E} \frac{\Delta m^2_{kl}}{2}). \tag{1.6}$$

In this equation the notation $\Delta m^2_{ab} = m^2_a - m^2_b$ is used for the difference of the squared masses between two states a and b. The length L in equation 1.6 is the so-called baseline-length, which is in practical terms the distance between the source where the neutrino is born and the detector where the interaction of the neutrino is measured.
In the simplest case with only two neutrino flavors, we need only one angle θ to parameterize U. The equation then simplifies to[147]

$$P(\nu_\alpha \to \nu_\beta)(L,E) = sin^2(2\theta) sin^2 \left(\frac{L}{E} \frac{\Delta m^2_{12}}{4} \right). \tag{1.7}$$

From this equation, one can directly see that the angle and Δm^2 can be measured with oscillation experiments, but not the absolute values of m_k.
In the case of three flavors, which seems to be realized in nature, a total of three mixing angles θ_{ij}, two independent Δm^2_{ij} and one CP-phase δ exist.

In this case, the neutrino mixing matrix U can be written as

$$U = \begin{pmatrix} c_{12}c_{13} & s_{12}c_{13} & s_{13}e^{-i\delta_{cp}} \\ -s_{12}c_{23} - c_{12}s_{13}s_{23}e^{i\delta_{cp}} & c_{12}c_{23} - s_{12}s_{13}s_{23}e^{i\delta_{cp}} & c_{13}s_{23} \\ s_{12}s_{23} - c_{12}s_{13}c_{23}e^{i\delta_{cp}} & -c_{12}s_{23} - s_{12}s_{13}c_{23}e^{i\delta_{cp}} & c_{13}c_{23} \end{pmatrix}. \tag{1.8}$$

Where the abbreviations $s_{ij} = sin(\theta_{ij})$ and $c_{ij} = cos(\theta_{ij})$ are used. In case neutrinos are their own antiparticles, two additional phases α_a exist. These phases can lead to a smaller effective mass of the neutrino, if the neutrino appears only as a virtual particle in the reaction, for example in neutrinoless double beta decay. In this case, U needs to be multiplied with an additional Matrix

$$\begin{pmatrix} e^{i\alpha_1} & 0 & 0 \\ 0 & e^{i\alpha_2} & 0 \\ 0 & 0 & 1 \end{pmatrix}, \tag{1.9}$$

which describes the interference of the individual mass states. For Dirac neutrinos, which are not their own antiparticles, this notation can be used with $\alpha_{1,2} = 0$. Experimental results from solar experiments or KamLAND show that the mass difference $\Delta m^2_{21} \approx 7.5 \cdot 10^{-5}\,\mathrm{eV}^2$ is much smaller than the mass difference of any of the two to the third state $\Delta m^2_{3x} \approx 2.5 \cdot 10^{-3}\,\mathrm{eV}^2$. The case in which the two mass states m_1 and m_2 are lighter than m_3 is called normal ordering. The case where m_3 is the lightest mass eigenstate is called inverted ordering. To the present date, it is not clear which ordering is realized in nature and the interpretation of some experiments depends on this ordering. Figure 1.1 shows the results of current neutrino oscillation experiments depending on the mass ordering.

1.3.1 Search for δ_{CP}:

The CP phase of the neutrino mixing matrix is of major interest for the field of physics, because it gives rise to an asymmetry between matter and antimatter. In the quark sector this phase has already been observed and an overview of the findings can be found in [89]. In the neutrino sector present and future long-baseline neutrino oscillation experiments like T2K and Dune try to observe this value. Other oscillation experiments, like reactor experiments and atmospheric neutrino oscillation experiments do also contribute to the

		Normal Ordering (best fit)		Inverted Ordering ($\Delta\chi^2 = 4.7$)	
		bfp $\pm 1\sigma$	3σ range	bfp $\pm 1\sigma$	3σ range
without SK-atm	$\sin^2\theta_{12}$	$0.310^{+0.013}_{-0.012}$	$0.275 \to 0.350$	$0.310^{+0.013}_{-0.012}$	$0.275 \to 0.350$
	$\theta_{12}/^\circ$	$33.82^{+0.78}_{-0.76}$	$31.61 \to 36.27$	$33.82^{+0.78}_{-0.76}$	$31.61 \to 36.27$
	$\sin^2\theta_{23}$	$0.580^{+0.017}_{-0.021}$	$0.418 \to 0.627$	$0.584^{+0.016}_{-0.020}$	$0.423 \to 0.629$
	$\theta_{23}/^\circ$	$49.6^{+1.0}_{-1.2}$	$40.3 \to 52.4$	$49.8^{+1.0}_{-1.1}$	$40.6 \to 52.5$
	$\sin^2\theta_{13}$	$0.02241^{+0.00065}_{-0.00065}$	$0.02045 \to 0.02439$	$0.02264^{+0.00066}_{-0.00066}$	$0.02068 \to 0.02463$
	$\theta_{13}/^\circ$	$8.61^{+0.13}_{-0.13}$	$8.22 \to 8.99$	$8.65^{+0.13}_{-0.13}$	$8.27 \to 9.03$
	$\delta_{\rm CP}/^\circ$	215^{+40}_{-29}	$125 \to 392$	284^{+27}_{-29}	$196 \to 360$
	$\frac{\Delta m^2_{21}}{10^{-5}\ \mathrm{eV}^2}$	$7.39^{+0.21}_{-0.20}$	$6.79 \to 8.01$	$7.39^{+0.21}_{-0.20}$	$6.79 \to 8.01$
	$\frac{\Delta m^2_{3\ell}}{10^{-3}\ \mathrm{eV}^2}$	$+2.525^{+0.033}_{-0.032}$	$+2.427 \to +2.625$	$-2.512^{+0.034}_{-0.032}$	$-2.611 \to -2.412$

Figure 1.1: List of parameters of the neutrino mixing matrix as published in 2019. The abbreviation 'bfp' stands for best fit parameter. The values for Δm^2_{31} and Δm^2_{32} are averaged and given as Δm^2_{3l}. Table taken from [31].

current limits. A recent overview paper by Salas et al. [20] states a best fit value of

$$\delta_{CP}/^\circ = 238^{+38}_{-27} \tag{1.10}$$

with $1\,\sigma$ errors. This is in agreement with the value in Figure 1.1.

1.3.2 Hint at mass ordering:

The paper by de Salas et al. also claims a hint for normal mass ordering based on their comparison of the preferred value for Δm^2_{13} by Daya Bay and T2K, which is in better agreement for normal ordering. Also, the value for θ_{13} found by long-baseline experiments is in better agreement with the value found by reactor experiments in case of the normal ordering, according to de Salas et alii. The preference for normal ordering is also present in the analysis of Esteban et al. as can be seen in the increased χ^2 of $\Delta\chi^2 = 4.7$ in the fit for inverted ordering.

1.4 Neutrino mass theory

In the Standard Model (SM) of particle physics, Dirac particles have a mass term in the Lagrangian which can be written as

$$\mathcal{L} = m_D(\overline{\psi}_L\psi_R + \overline{\psi}_R\psi_L) \tag{1.11}$$

after the spontaneous symmetry breaking. Here m_D is the Dirac mass, L and R indicate right- and left-handed particles. Since there are only left-handed neutrinos and right-handed antineutrinos in the Standard Model, the mass term vanishes, and neutrinos do not get a mass according to this theory. As discussed in the chapter about neutrino oscillation, the fact that neutrinos oscillate shows that at least two of the three known neutrino mass states have non-zero masses. This implies that the SM needs to be modified to generate a neutrino mass term.

1.4.1 Seesaw mechanism

One popular way to extend the standard model, which also gives an explanation why the neutrino mass is so small compared to the other fermions in the SM, is by creating a so-called seesaw mechanism. The most simple extension which does that is the type 1 seesaw, where not only the three known light neutrinos exist, but also a hypothetical heavy Majorana fermion is added. In this case, the Lagrangian has the form

$$\mathcal{L} = \begin{pmatrix}\overline{\psi}_L & \overline{\psi}_L^C\end{pmatrix}\begin{pmatrix}m_L & m_D\\ m_D & m_R\end{pmatrix}\begin{pmatrix}\psi_R^C\\ \psi_R\end{pmatrix} + h.c. \tag{1.12}$$

with $m_L \approx 0$ and $m_R >> m_D$. The eigenvalues of the Matrix give two mass states

$$m_\pm = \frac{m_R \pm \sqrt{m_R^2 + 4m_D^2}}{2}. \tag{1.13}$$

In this model $m_+ \approx m_R$ is the mass of a hypothetical heavy right-handed neutrino and $m_- \approx -m_D^2/m_R$ is the small mass of the known left-handed neutrino.
This is, however, only one way to generate a neutrino mass with a seesaw type mechanism. More information can be found e.g. in [16][92].

1.5 Neutrino mass determination

The absolute mass scale of neutrinos, which is not known yet, can be probed with different methods and experiments. In the following three promising approaches will be covered: Observational cosmology, neutrinoless double beta decay ($0\nu\beta\beta$) and the kinematic approach with standard beta decay (β^-) and electron capture (EC).

1.5.1 Observational cosmology

The evolution of the universe depends on its composition. One of the most simple and commonly used models is the so-called ΛCDM model. It describes the universe based on the equations of general relativity and assuming a cold dark matter (CDM) component and a dark energy constant (Λ) in addition to the matter components described in the standard model. From measurements of the structure of the universe, measurements of the CMB, e.g. by the Planck satellite and models of structure formation based on the early universe, one can estimate the number of light neutrino flavours, the number density of relic neutrinos and the sum of the mass of all light neutrino flavours. In this case 'light' means that they are relativistic particles at the time of recombination. The number density of neutrinos from the early universe can be calculated as

$$n_\nu = N_{eff} \left(\frac{3}{4}\right) \left(\frac{4}{11}\right) n_\gamma. \tag{1.14}$$

N_{eff} is the effective number of neutrino flavors, which can be determined e.g. from the width of the Z-boson decay. In the Standard Model $N_\nu = 3$ and measurements from both collider experiments and observations from cosmology are in agreement with this value. The value determined from Planck data is $N_{eff} = 2.99 \pm 0.17$ [17]. The photon density at present time $n_{\gamma,0}$ can be determined from the measurements of the CMB to be [114]

$$n_{\gamma,0} \approx 410\,\mathrm{cm}^{-3}. \tag{1.15}$$

Using the ΛCDM model in combination with Baryon acoustic oscillation (BAO) they set a limit on the sum of the neutrino masses [17] of

$$\sum m_\nu < 0.12\,\mathrm{eV/c^2}. \tag{1.16}$$

In this paper, the Planck collaboration also gives a value for the Hubble constant, which describes the expansion rate of the universe:

$$H_0 = 67.4 \pm 0.5 \, \frac{\mathrm{km}}{\mathrm{s} \cdot \mathrm{Mpc}} \tag{1.17}$$

This value is interesting because it has a tension with other measurements, e.g. Riess et al. who find a value of

$$H_0 = 74.03 \pm 1.42 \, \frac{\mathrm{km}}{\mathrm{s} \cdot \mathrm{Mpc}} \tag{1.18}$$

using a distance ladder approach [110]. This is a $4.4\,\sigma$ discrepancy with the result from Planck. Unless a mistake was made by one of the groups, this asks whether the used models describe the evolution of the universe correctly. The results are again summarized in Table 1.1.

Observable	value
number density of relic neutrinos per flavour $n_{\nu_i,0}$	$112\,\mathrm{cm}^{-3}$
number of neutrino flavours $N_{\nu,eff}$	3 ± 0.1
Sum of neutrino masses $\sum_i m_i$	$< 0.12\,\mathrm{eV/c}^2$

Table 1.1: Results from observational cosmology [17].

1.5.2 Neutrinoless double beta decay $0\nu\beta\beta$

The normal double beta decay ($2\nu\beta\beta$) can occur in certain nuclei with an even number of protons and neutrons in which normal β^--decay is energetically not allowed. In $2\nu\beta\beta$ decay the reaction

$$X(Z,A) \rightarrow Y(Z+2,A) + 2\,e^- + 2\,\bar{\nu}_e \tag{1.19}$$

changes the number of protons in the nuclei by two and creates two e^- and two $\bar{\nu}_e$. If the hypothesis of Ettore Majorana that neutrinos are their own anti particles, so-called Majorana particles, is correct, then the double beta decay is also possible without the emission of neutrinos. This is called the so-called neutrinoless double beta decay ($0\nu\beta\beta$):

$$X(Z,A) \rightarrow Y(Z+2,A) + 2\,e^- + 0\,\bar{\nu}_e \tag{1.20}$$

This requires the emitted antineutrino to be converted to a neutrino, for example by Lorentz transformation. Then it can be adsorbed in the vertex of the second beta decay instead of the emission of a second antineutrino, as displayed in figure 1.2. This leads to an energy spectrum, where the sum of the electron energies is a constant instead of a continuous spectrum as in the $2\nu\beta\beta$ case. Since the probability to undergo this transition via Lorentz transformation depends on the velocity of the neutrino and thereby by its mass, the probability of this process is a probe for the mass of this neutrino. The mass relevant in this process is the coherent sum of the neutrino mass states

$$m_{\beta\beta} = \left| \sum_i U_{ei}^2 m_i \right|. \tag{1.21}$$

The mass is measured via the half-life $T_{1/2}^{0\nu}$ of the element

$$\frac{1}{T_{1/2}^{0\nu}} = G^{0\nu} \left| M^{0\nu} \right|^2 \left(\frac{m_{\beta\beta}}{m_e} \right)^2. \tag{1.22}$$

Here $G^{0\nu}$ is the phase space integral, $M^{0\nu}$ is the transition matrix element and m_e the mass of the electron. The elements used for this type of neutrino mass search are among others ^{76}Ge, ^{130}Te and ^{136}Xe. The detectors used are either cryogenic bolometers e.g. CUORE and others, or scintillator experiments like KamLAND-Zen which claims the current best limit from $0\nu\beta\beta$ decay based on their measurements with enriched ^{136}Xe. In a paper from 2016 [47] they state a limit of the half-life time of ^{136}Xe

$$T_{1/2}^{0\nu} > 1.07 \times 10^{26}\,\mathrm{yr} \quad (90\%\,C.L.) \tag{1.23}$$

which leads to a limit on the Majorana neutrino mass of

$$m_{0\nu\beta\beta} < 0.061 - 0.165\,\mathrm{eV/c^2}. \tag{1.24}$$

An overview of the status and prospects of neutrinoless double-beta decay can be found in [22].
However, the existence of $0\nu\beta\beta$ decay is not proven. In case it does not exist these type of experiments could set very strong limits on $m_{\beta\beta}$ independent of the real mass of the neutrino.

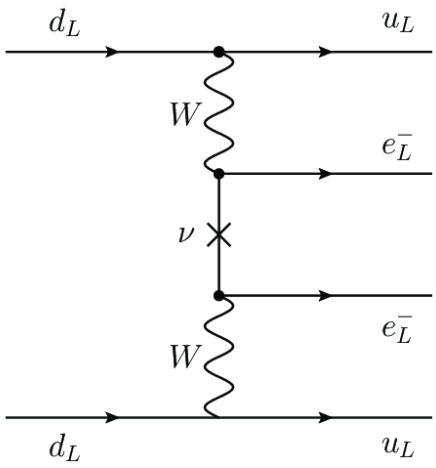

Figure 1.2: Diagram showing the neutrinoless double beta decay process with a ν_L to ν_R transition. This transition of the neutrino can only take place if the neutrino is a Majorana particle and if it has a finite invariant mass. The image is taken from [54].

1.5.3 Direct neutrino mass measurements from the kinematics of weak decays

In normal β^- decay

$$X(Z, A) \rightarrow Y(Z + 1, A) + e^- + \bar{\nu}_e \tag{1.25}$$

a nucleus X with a proton number Z decays into a daughter nucleus Y with a proton number Z+1. By emitting an electron and an anti-electron neutrino it is made sure that the baryon number, the lepton number and the electric charge are conserved in the interaction. The conservation of energy and momentum in a three-particle system leads to a continuous energy spectrum of the electron and the neutrino, which influence each other, as can be seen in figure 1.3. This gives rise to the idea that the neutrino mass can be determined without measuring the neutrino itself, only with spectroscopy of the emitted electron. Close to the endpoint of the electron spectrum, where the electron takes all the kinetic energy and the neutrino is almost at rest, the shape of the electron spectrum is distorted by a finite neutrino mass. The idea of weak decay experiments is to measure this distortion of the electron energy spectrum near the endpoint to deduce the neutrino mass from this. To get good statistics in the region of interest a low Q-value is favorable. Elements with a low Q-value β decay isotope are for example hydrogen and rhenium. Another candidate with a low Q-value is a holmium isotope, which performs an electron capture (EC). In this case, the spectrum close to the endpoint behaves similar to that of a β decay experiment. The mentioned elements are listed again in Table 1.2. ^{187}Re is a β^- emitter with a very low Q-value. However, there are presently no experiments running using this isotope. Previous attempts, for example in MANU [18] and MIBETA [128], have shown only a very limited energy resolution of the cryo bolometers of about 20 eV and gave an upper limit on the neutrino mass of about 15 eV (90% C.L.) [37].

Nucleus	Q-value (keV)	$T_{1/2}$ (y)	type	Experiments
^{3}H	18.6	12.3	β^-	KATRIN, Project 8
^{163}Ho	2.8	4570	EC	ECHo, HOLMES, NuMECS
^{187}Re	2.6	$4 \cdot 10^{10}$	β^-	-

Table 1.2: Possible candidates for neutrino mass search in kinematic experiments.

Close to the endpoint the spectrum of the electron capture of ^{163}Ho has a similar shape to the β spectrum with the same shape distortion caused by a finite neutrino mass. The rate near the endpoint depends strongly on the Q-value of ^{163}Ho. In 2015 a direct measurement of the ECHo experiment increased the Q-value from the assumed 2555(16) eV to a new

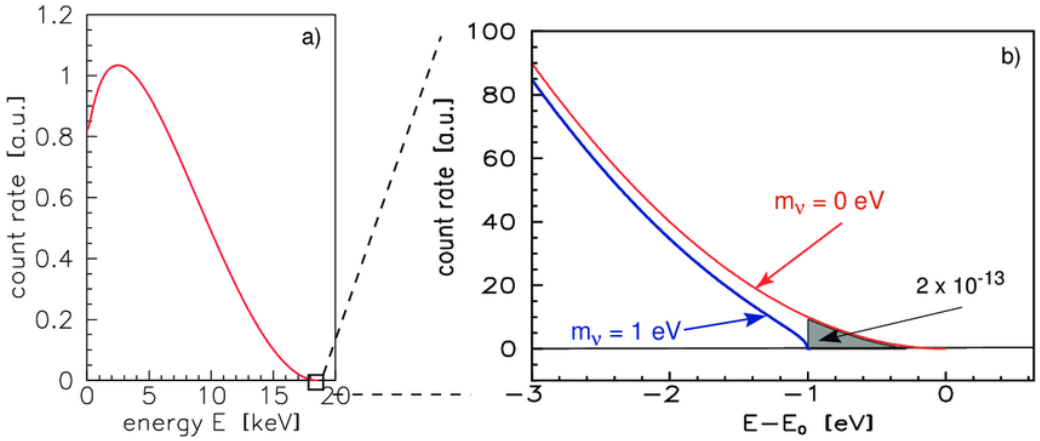

Figure 1.3: Electron energy spectrum from the beta decay of tritium. A finite neutrino mass changes the shape of the spectrum close to the endpoint.

value of [25]

$$Q = 2833(30_{stat})(15_{sys})\,\mathrm{eV}. \tag{1.26}$$

Figure 1.4 shows the spectrum of ECHo and a zoom into the endpoint region calculated for the updated Q-value of 2833 eV. In its first phase, ECHo plans to reach a sensitivity below 10 eV [26]. The Echo experiment uses low temperature metallic magnetic calorimeters to measure the energy released in the electron capture process. The ^{163}Ho is embedded in the absorber. The Q-value was independently measured with Penning trap measurements.

The current best limit on $m_{\bar{\nu}}$ by a direct kinematic measurement was presented in 2019 by the KATRIN collaboration [33]:

$$m_{\bar{\nu}} < 1.1\,\mathrm{eV/c^2}\ (90\%\,\mathrm{C.L.}). \tag{1.27}$$

KATRIN, which stands for **Kar**lsruhe **Tri**tium **N**eutrino Experiment, is a next generation β decay experiment which aims to measure the neutrino mass with a sensitivity of 0.2 eV (90 % C.L). KATRIN uses a windowless gaseous tritium source and an integrating spectrometer of the MAC-E filter type, which will be explained in great detail in the next chapter. The β decay spectrum of tritium and the shape distortion resulting from a finite neutrino mass is shown in figure 1.3. Despite its slightly higher Q-value compared to Re and Ho, the use of tritium has many advantages. Tritium has a half-life of $t_{1/2} = 12.3$ a which allows a high rate and the decay is super allowed, which simplifies the theoretical calculation of the spectrum. Furthermore, it can be used in a gaseous form where no com-

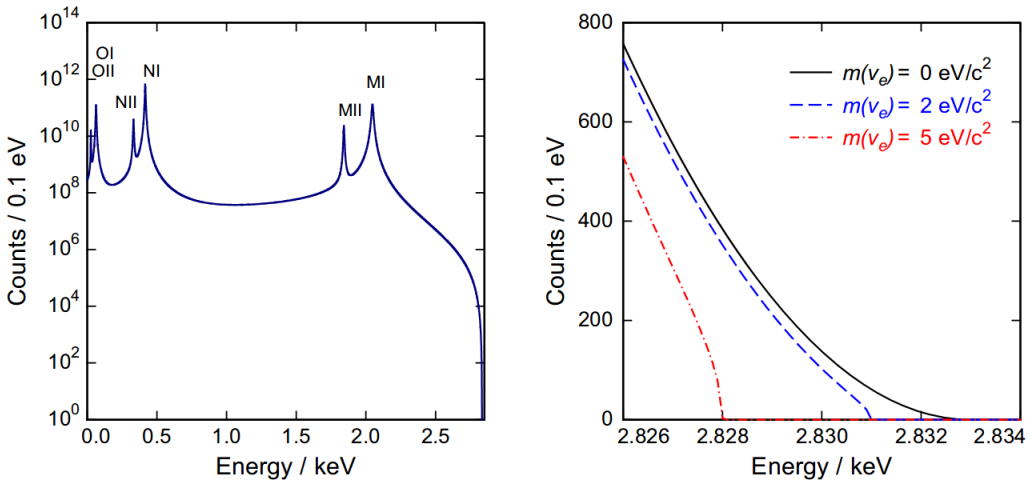

Figure 1.4: Electron capture spectrum of ^{163}Ho for a Q-value of 2833 eV. The right graphics shows a zoom into the endpoint region and the shape distortion of the spectrum created by a hypothetical neutrino mass of 2 and 5 eV. The image is taken from [49].

plicated solid state effects are present. Due to the low number of electrons in tritium (one for atomic T, two for molecular T_2), the calculation of the final states is not as complicated as for systems with more electrons in the shell. One of the limiting factors of experiments using T_2 is the width of the spectrum which results from the manifold of final states of the remaining $(^3\text{T-}^3\text{He})^+$ ion. To avoid this systematic effect and to push the limit on the neutrino mass even further the future experiment PROJECT 8 plans the use of an atomic tritium source. The atomic tritium will be stored in a magnetic bottle at a low temperature. The β spectrum will be recorded with an antenna array, which measures the emitted cyclotron radiation of the β electron after the decay. The technique is called CRES, which stands for **c**yclotron **r**adiation **e**mission **s**pectroscopy. The frequency of the cyclotron motion is given by

$$f_\gamma = \frac{1}{2\pi}\frac{eB}{m_e + K_e/c^2}, \tag{1.28}$$

where B is the magnetic field of about 1 T and K_e is the kinetic energy of the electron. Project 8 aims at a final sensitivity on the neutrino mass of 40 meV/c^2 [3].

Chapter 2

KATRIN experiment

The Karlsruhe tritium neutrino experiment (KATRIN) is a next-generation β-decay experiment. It aims at a sensitivity on the neutrino mass of $0.2\,\mathrm{eV/c^2}$ with 90 % C.L., which is an order of magnitude more sensitive than the previous best experiments at Mainz [82] and Troitzk [6]. The sensitivity for a $5\,\sigma$ discovery is $0.35\,\mathrm{eV/c^2}$. To achieve this, a windowless gaseous tritium source and a spectrometer of the MAC-E filter type is used. Figure 2.1 shows a side view of the KATRIN experiment. In the following sections, the individual components and the physics of the KATRIN experiment are described in more detail.

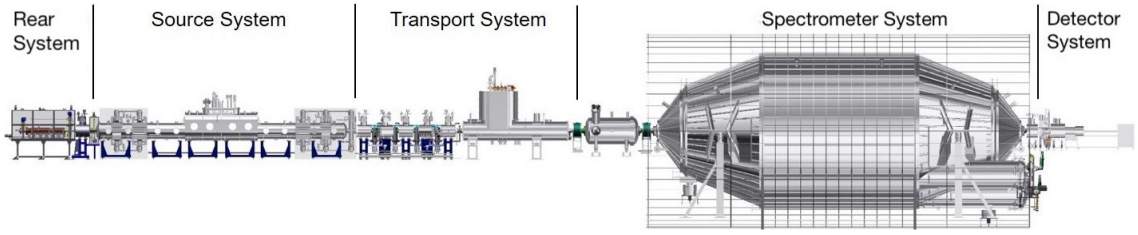

Figure 2.1: Overview of the KATRIN experiment. The tritium is inserted in the center of the WGTS. The energy filtering is done at the main spectrometer and the counting of the signal electrons at the focal plane detector. Sections from left to right: Rear section (RS), windowless gaseous tritium source (WGTS), transport section (differential and cryogenic pumping section), spectrometer section (pre and main spectrometer), focal plane detector (FPD).

2.1 Measurement principle

In the β-decay of a tritium nucleus a ^{3}He daughter nucleus, an electron e^- and an electron antineutrino $\bar{\nu_e}$ are created. The energy spectrum of the electron contains information about the effective mass of the neutrino $m_{\bar{\nu}}$. The observable in this kind of measurement is the squared neutrino mass $m_{\bar{\nu}}^2$. Its effect on the differential spectrum can be seen in figure 1.3. In the KATRIN experiment, the measurement is done by scanning this region with a high-resolution MAC-E-Filter, which acts as a high pass filter and leads to an integrated measurement of the tritium spectrum.

2.2 Tritium beta spectrum

The KATRIN experiment measures the neutrino mass by measuring the electrons from the weak beta decay of tritium. In its most simple form, the beta decay can be written as

$$(A, Z) \rightarrow (A, Z+1)^+ + e^- + \bar{\nu}_e + Q, \tag{2.1}$$

where Q is the energy released in the decay. In the case of tritium it is

$$\mathrm{T} \rightarrow {}^3\mathrm{He}^+ + e^- + \bar{\nu}_e + Q(\mathrm{T}). \tag{2.2}$$

The electron energy spectrum of this decay can be described by Fermi's golden rule [36]

$$T_{i\rightarrow f} = \frac{2\pi}{\hbar}|M_{fi}|^2\rho(E_f). \tag{2.3}$$

Here $T_{i\rightarrow f}$ is the transition rate from an initial state i to a final state f, M_{fi} is the transition matrix element between those two states and $\rho(E_f)$ is the final state density at energy E_f. To get the energy spectrum this partial transition rate needs to be integrated over all states. After some calculation, which can be seen for example in [99], one obtains the differential energy spectrum

$$\frac{d\Gamma}{dE} = A \cdot |M|^2 \cdot F \cdot p \cdot (E + m_e c^2) \cdot (E_0 - E) \cdot \sqrt{(E_0 - E)^2 - m_\nu^2 c^4}\Theta \tag{2.4}$$

with $A = G_F^2 \cdot cos^2\theta_c/(2\pi^3 c^5 \hbar^7)$ and $\Theta = \theta(E_0 - E - m_\nu c^2)$. E_0 is the maximum energy of the electron from the beta decay assuming zero neutrino mass. For more details on E_0 see chapter 5. G_F^2 is the Fermi coupling constant, θ_C the Cabibbo angle and Θ a Heaviside function which restricts the Formula to the allowed energy values. F is the Fermi function

$$F = F(Z+1, E) = \frac{2\pi\eta}{1 - exp(-2\pi\eta)} \tag{2.5}$$

with $\eta = \alpha(Z+1)\beta$, where α is the fine structure constant and $\beta = v/c$. Formula 2.4 contains a few simplifications: As mentioned in chapter 1.3 the eigenstate of the weak interaction is a mixing of the mass eigenstates. This means, that the mass m_ν, which can be observed in the KATRIN experiment, is a sum of these mass eigenstates m_i

$$m_\nu^2 = \sum_i |U_{ei}|^2 m_i^2 \tag{2.6}$$

Furthermore, the KATRIN experiment uses molecular tritium T_2, which has a final state distribution [120], which modifies the maximum available energy of the electron. In the KATRIN experiment the β-spectrum is measured with an integrating Mac-E-Filter (see chapter 2.3). Also energy losses (see chapter 4) due to scattering of electrons with molecules need to be taken into account.

2.3 MAC-E-Filter

The main spectrometer (MS) of the KATRIN experiment is an integrating spectrometer with high angular acceptance and high energy resolution. These features are obtained using magnetic adiabatic collimation (MAC) and electric filtering (E) [10][87][102]. The principle of this technique is illustrated in figure 2.2. The details are explained in the following paragraphs.

2.3.1 Electric filtering

The electrons are guided through the spectrometer by magnetic field lines. To filter them an electric retardation field is applied parallel to the magnetic field. In the case of KATRIN this is done by applying a voltage of roughly $-18.4\,\mathrm{kV}$ to the MS-vessel, and an additional $-200\,\mathrm{V}$ to a segmented inner wire electrode system. The electric field filters the electrons according to their longitudinal energy $E_\parallel$. In the standard configuration of the main spectrometer, the voltages to the inner electrode system are applied in such a way that the maximal absolute value of the electric potential is at $z = 0$. More generally speaking, the maximal absolute electric potential should be at the same z position as the minimum magnetic field.

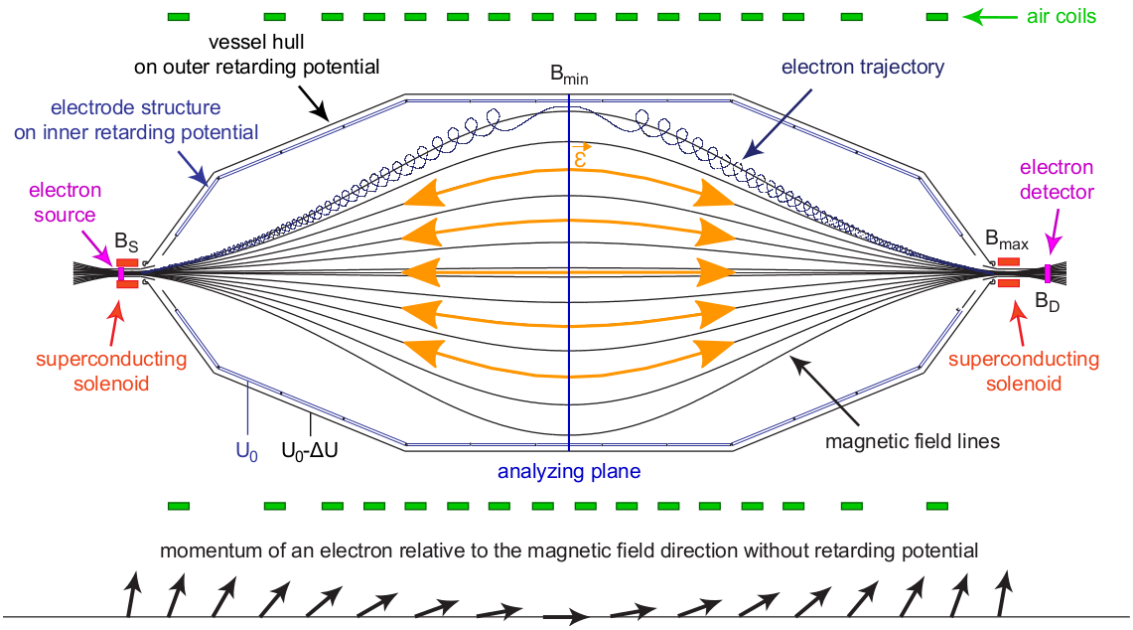

Figure 2.2: Scheme of the KATRIN main spectrometer, which is a MAC-E-filter type spectrometer. Magnetic adiabatic collimation converts transversal energy in a high magnetic field into longitudinal energy in a low magnetic field, as indicated with the arrows in the bottom of the picture. In the analyzing plane the electric potential is maximal and the magnetic field minimal. This leads to an optimal energy resolution. The magnetic field lines are shown in the standard configuration: B_{min} and $|U|_{max}$ are in the center of the MS and form a homogeneous analyzing plane with high energy resolution. The magnetic field is shaped by the two superconducting solenoids (red) and the LFCS (green). The maximum magnetic field is present at the pinch magnet on the detector side of the spectrometer. The electric field is shaped by the inner electrodes, which are on an offset potential with respect to the main vessel of $\Delta U \approx -200\,\mathrm{V}$. The picture is taken from [126].

2.3.2 Magnetic adiabatic collimation

The concept of magnetic adiabatic collimation is the most important feature of this spectrometer and allows to achieve a high energy resolution. Since the electric field only acts on the longitudinal energy $E_{\parallel}$, the magnetic field is needed to convert the perpendicular energy $E_{\perp}$ as effectively as possible to $E_{\parallel}$.
If the electric and magnetic fields change slowly compared to the distance covered by the electron in one cyclotron motion, the term

$$\gamma\mu = \frac{\gamma + 1}{2} \cdot \frac{E_{\perp}}{B} \tag{2.7}$$

is a constant. In this case, γ is the relativistic factor and μ the orbital magnetic moment. In KATRIN the highest kinetic energy for an electron from tritium beta decay is $E_0 \approx 18.6\,\mathrm{keV}$, which leads to a γ-factor of 1.04. With the approximation $\gamma \approx 1$ we get

$$\mu = \frac{E_{\perp}}{B} = \text{constant}. \tag{2.8}$$

From this equation, it is immediately clear, that the energy resolution of the spectrometer, which is dominated by the remaining part of $E_{\perp}$ in the analyzing plane, is directly proportional to the reduction factor of the magnetic field. However, the electric potential must not rise too fast. Otherwise, the electron might be reflected before its perpendicular energy is fully converted. This effect is called early retardation and needs to be avoided to ensure a good energy resolution of the MAC-E-Filter.

2.3.3 Energy resolution

The energy resolution of the MAC-E-Filter is limited by the amount of perpendicular energy $E_{\perp}$ which is not transformed to $E_{\parallel}$. This depends on the ratio of the maximum magnetic field in the experiment B_{max}, the magnetic field in the analyzing plane B_{min} and the angular distribution of the electrons. If all electrons have the same angle relative to the magnetic field, all electrons are retarded at the same potential. In case of an isotropic source the energy resolution is given by

$$\Delta E = E \cdot \frac{B_{min}}{B_{max}} \tag{2.9}$$

In the case of KATRIN B_{max} is the magnetic field of the Pinch magnet, which is located at the exit of the MS and has a magnetic field of $B = 6\,\mathrm{T}$. The minimum magnetic field is the field in the analyzing plane in the main spectrometer, which is in the order of

$B_A = B_{min} = 0.3\,\mathrm{mT}$. The maximum energy of the electrons is $E_{e,max} = 18.58\,\mathrm{keV}$. This results in an energy resolution of

$$\Delta E = 18.58\,\mathrm{keV} \cdot \frac{3 \cdot 10^{-4}\,\mathrm{T}}{6\,\mathrm{T}} \approx 0.93\,\mathrm{eV} \qquad \text{(design value)} \tag{2.10}$$

However, it was found out that the background of the KATRIN experiment has a volume dependence. As a result of this one can achieve a lower background at the cost of energy resolution. The first science run of KATRIN was performed with a reduced magnetic field in the pinch magnet of $B_{max} = 4.2\,\mathrm{T}$ and an increased magnetic field in the analyzing plane of $B_{min} \approx 0.63\,\mathrm{mT}$, which results in an energy resolution of

$$\Delta E = 18.58\,\mathrm{keV} \cdot \frac{6.3 \cdot 10^{-4}\,\mathrm{T}}{4.2\,\mathrm{T}} \approx 2.8\,\mathrm{eV} \qquad \text{(first science run)} \tag{2.11}$$

To include relativistic effects one can introduce the relativistic Lorentz factor γ as

$$\gamma = 1 + \frac{E}{mc^2} \tag{2.12}$$

and modify the energy resolution to

$$\Delta E = E \cdot \frac{B_{min}}{B_{max}} \cdot \frac{\gamma_s + 1}{\gamma_a + 1} \approx E \cdot \frac{B_{min}}{B_{max}} \cdot 1.018 \quad | \, at\, E \approx 18.58\,\mathrm{keV}, \tag{2.13}$$

where $\gamma_s = 1.018$ is the relativistic factor in the source at an energy of $E = 18575\,\mathrm{eV}$ and $\gamma_a = 1$ in the analyzing plane. This leads to a broadening of about 1.8 %.

2.3.4 Magnetic mirror

In analogy to the above mentioned magnetic adiabatic collimation effect, the angle of an electron with respect to the magnetic field gets larger if the magnetic field increases. If the angle reaches 90° the particle gets reflected. This is called the magnetic mirror effect. For the KATRIN experiment, this results in a cutoff angle θ_{max} for electrons starting in the magnetic field of the source B_{source} of

$$\theta_{max} = arcsin\left(\sqrt{\frac{B_{source}}{B_{max}}}\right) = arcsin\left(\sqrt{\frac{3.6\,\mathrm{T}}{6\,\mathrm{T}}}\right) \approx 50.8^\circ \tag{2.14}$$

2.3.5 Magnetic flux tube

In the case of adiabatic motion, which we assume to be the case in the KATRIN experiment, the magnetic flux, defined as

$$\Phi = \int_A \vec{B} d\vec{A} \tag{2.15}$$

is conserved. In the design report, this value is $\Phi = 191\,\mathrm{Tcm}^2$. However, for magnet safety reasons the whole global magnetic field of KATRIN was reduced to 70 %, lowering this value to $\Phi = 134\,\mathrm{Tcm}^2$. The conservation of the magnetic flux is the reason why the diameter of the main spectrometer has to be a factor of 100 larger than the diameter of the source tube to have a sharp energy resolution and a large angular acceptance as described above.

2.3.6 Transmission of the main spectrometer

The transmission function of the main spectrometer for an isotropic source is given by

$$T(E,qU) = \begin{cases} 0 & E - qU < 0 \\ \frac{1-\sqrt{1-\frac{E-qU}{E}\cdot\frac{B_S}{B_a}\cdot\frac{\gamma_a+1}{\gamma_s+1}}}{1-\sqrt{1-\frac{B_s}{B_{max}}}} & 0 \leq E - qU \leq \Delta E \\ 1 & E - qU > \Delta E \end{cases} \tag{2.16}$$

where E is the starting energy, ΔE is the energy resolution given in eq. 2.13, and U is the retardation voltage. From an experimentalist's point of view, E and γ are given by the energy scale of the tritium beta decay. Thus, only the magnetic fields can be changed to influence the energy resolution. For the first science run of KATRIN the magnetic field in the analyzing plane B_A has been significantly increased compared to the design report in order to lower the background. This leads to a broadening of the transmission function by a factor of three from 0.93 eV to 2.79 eV. At the same time the volume of the flux tube in the spectrometer is shrunk by roughly the same factor. For details and investigations see [12][30].

2.3.7 Background of the main spectrometer

To achieve the high sensitivity demand of the KATRIN experiment, a low background rate of O(10 mcps) is desired. Investigations of the background in 2013 showed a significantly higher rate than expected and countermeasures have to be taken. The background consists presumably of two compounds: One is radon emanated from the non-evaporable getter (NEG) pumps and the other compound is created by Rydberg atoms which are

ionized in the volume of the flux tube [60][134].
The amount of radon going into the spectrometer is reduced with cold baffles [55]. These baffles provide a large, cold copper surface on which the radon atoms can attach to. The geometry of the copper rods is such that the direct line of sight from the getter pumps to the spectrometer is completely blocked.
The measured rate of background electrons from the main spectrometer has in first approximation a linear dependence on the flux tube volume between the analyzing plane and the exit of the spectrometer towards the focal plane detector (FPD). From equation 2.15 we see that the radius of the flux tube scales with the magnetic field as $r(z) \propto \sqrt{B_{ref}/B(z)}$, where B_{ref} is a global reference indicating, that only a relative change of $B(z)$ changes the radius, whereas a global change of the magnetic field does not. For the first science run of KATRIN the magnetic field in the analyzing plane was increased by a factor of three compared to the global magnetic field. This reduced the background rate approximately by a factor of three, but at the same time worsens the energy resolution ΔE of the main spectrometer by a factor of three as mentioned above. To further reduce the volume downstream of analyzing plane without affecting the energy resolution one can shift the analyzing plane in z-direction towards the FPD [23]. This concept, known as shifted analyzing plane (SAP), can reduce the background by another factor of two. A potential drawback of this setting is, that the gradients of the electric and magnetic fields are steeper than in the standard setting with the analyzing plane in the center of the spectrometer. This requires more detailed knowledge of the fields in the spectrometer.

2.4 Source and transport section (STS)

Measuring the neutrino mass with high accuracy is a challenging task and has high demands on the source section of the experiment [83]. The source should have a high luminosity, high stability, and small systematic effects. To achieve this the KATRIN experiment uses a windowless gaseous tritium source (WGTS). The source tube is a 10 m long stainless steel tube with 9 cm inner diameter. The tube is temperature stabilized at $T = 30\,\mathrm{K}$ with a neon cooling system. The gaseous tritium is stored at room temperature in a pressure controlled buffer vessel before it is fed into the center of the source tube via a capillary which is gradually cooled down to the source temperature. Three superconducting magnets provide a homogeneous magnetic field along the center axis of the tube with a nominal strength of $B_{source} = 3.6\,\mathrm{T}$.

2.5 Stability of the source

For the experiment to succeed it is important to have a source which delivers a stable rate of beta decays, which in case of a radioactive source like tritium translates to a constant amount of tritium atoms in the source. From the ideal gas law

$$N = \epsilon_T \frac{pV}{k_B T} \propto \epsilon_T \frac{p}{T} \tag{2.17}$$

we see, that the amount of tritium N depends linearly on the tritium purity ϵ_T, the pressure p and the temperature T. The effect of an unstable rate on the measured m_ν^2 has been studied in the design report (see p. 204 fig. 126 in [74]). The effect strongly depends on the scanning range below the endpoint. For the default scanning range of 30 eV below the endpoint, a stability on the 10^{-3} level is required. This requirement directly propagates to each factor on the right-hand side of eq. 2.17. If the scanning range would be increased further into the spectrum, the demands on the source stability would increase.

2.5.1 Temperature stability

The temperature stability at the operating temperature of $T \approx 30\,\mathrm{K}$ is ensured with a dual-phase neon cooling system. Two pipes filled with neon in a partly liquid, partly gaseous phase are mounted alongside the beam tube and control the temperature. The temperature can be controlled via the pressure of the system of roughly two bar. Fig.2.3 shows the vapor pressure curve of neon based on the formula

$$log_{10}(P) = A - (B/(T + C)) \tag{2.18}$$

where P is the pressure in bar, T the temperature in K and the coefficients are A = 3.7564, B = 95.599 and C = -1.503 [130].
The temperature of $T \approx 30\,\mathrm{K}$ is a compromise between on the one hand minimizing the broadening of the spectrum due to the Doppler effect by thermal motion and on the other hand avoiding the formation of tritium clusters.

2.5.2 Tritium circulation

To achieve the high luminosity, high stability, and purity necessary for the KATRIN experiment, a dedicated tritium loop is needed. Before it is injected the tritium is stored at a temperature of $T = 40\,C^\circ$ in the pressure controlled buffer vessel, which is pressure stabilized to $\Delta P/P < 10^{-3}$. This ensures a stable injection rate which leads to a stable column density. The performance of this system was demonstrated during the First Tritium (FT)

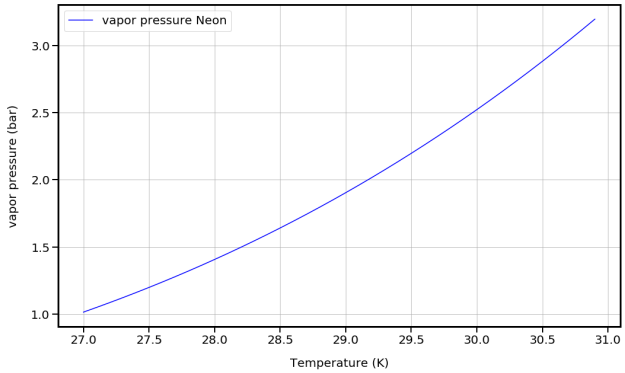

Figure 2.3: Vapor pressure of neon based on [130]. The regulation of the pressure allows to control the temperature of the dual-phase neon.

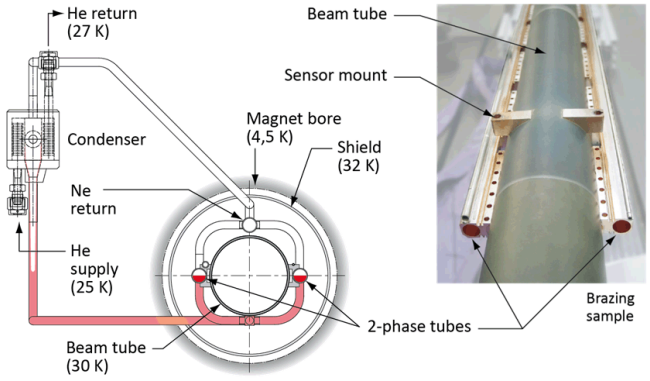

Figure 2.4: Cooling concept of the WGTS beam tube. Two pipes with a two-phase neon mixture are mounted along the beam tube to keep it at a stable and homogeneous temperature of $T \approx 30\,\mathrm{K}$. Picture adapted from [64].

campaign [2]. As can be seen in fig. 2.6 the required stability was surpassed by a factor of 10. The gas then streams through a 2.1 mm diameter capillary where it is cooled down to $T = 30\,\mathrm{K}$ and injected in the center of the 10 m long beam tube via 415 small orifices [131]. It then flows to both sides. To either side of the beam tube multiple TMPs are mounted which pump the gas to the inner loop. About 0.1 % of the gas does not get pumped and continues towards the rear section (RS) or the differential pumping section (DPS), where more TMPs are mounted. The tritium pumped from there goes to the outer loop system, where it is cleaned before injection into the inner loop. A permeator in the loop system removes non-hydrogen-like gas components, such as methane. In the outer loop, an isotope separation system ensures a high tritium purity ϵ_T of new tritium batches from the feed loop. Before the tritium enters the pressure controlled buffer vessel again, a laser Raman spectroscopy is performed with the so-called LARA system [124] [123]. This system is capable of measuring the amount of each hydrogen isotopologue due to their individual Raman shifts. For more details on LARA see chapter 2.8.3. In KATRIN a tritium purity of $\epsilon_T = 95\,\%$ and a stability of $\Delta\epsilon_T/\epsilon_T < 0.1\,\%$ is required.

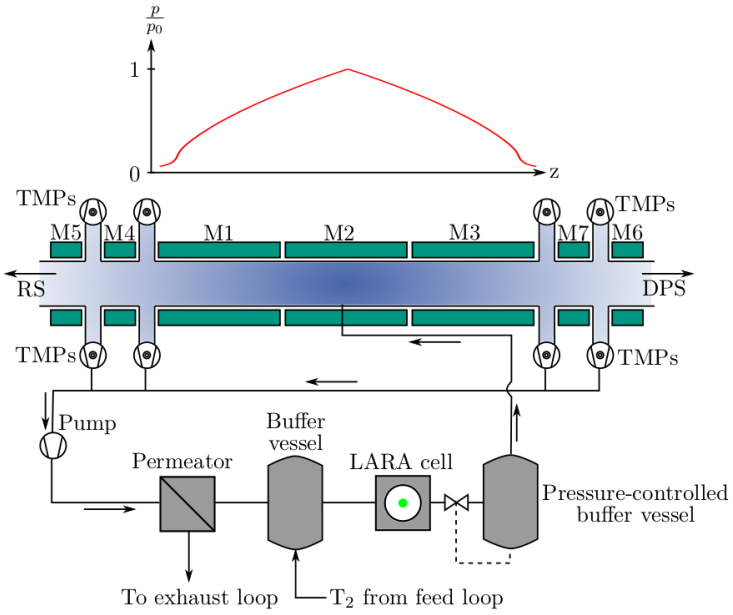

Figure 2.5: Tritium injection system and gas profile in the WGTS.

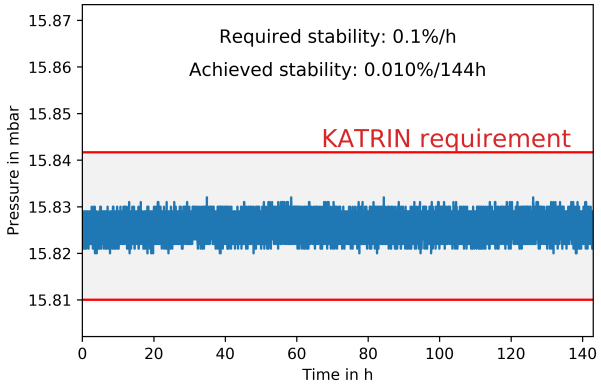

Figure 2.6: Pressure in the pressure controlled buffer vessel during the First Tritium campaign [2]. The required stability of $\Delta P/P < 10^{-3}$ is easily achieved in this 6-day window.

2.6 Transport section

The tritium which is injected into the WGTS must not enter the spectrometer section because it would increase the background of KATRIN. To ensure the tritium retention the transport section, consisting of the differential pumping section (DPS) and the cryogenic pumping section (CPS), is located between the source and the spectrometer section. The transport section has to reduce the gas flow by 12 orders of magnitude and also has to block ions while the signal electrons must be guided towards the spectrometer and their energy must not be changed.

2.6.1 Differential pumping section

The differential pumping section (DPS) is located downstream of the source. Its main tasks are the reduction of the tritium gas flow by five orders of magnitude [40] and the blocking of ions without effecting the energy spectrum of the signal electrons which are guided towards the spectrometer. In contrast to the WGTS and the CPS, the DPS beam tube is operated at ambient temperature of about $T \approx 300\,\mathrm{K}$. The effect on the beta spectrum, however, is minimal, because only a fraction of 10^{-6} of all beta decays happen in the DPS [51]. This estimation of the tritium amount in the DPS, which is based on measurements in 2019, is two orders of magnitude lower compared to the simulation result in [84].
The gas flow reduction in the DPS is done via cascaded turbo molecular pumps. The scheme of the vacuum system can be seen in figure 2.7. The cascaded pumping prevents back diffusion. The exhaust of the last TMP is connected to the outer Loop system, where

the gas will be cleaned and prepared for new injection to the WGTS. The gas flow towards the CPS is reduced by a factor of 10^5 according to simulation [40] and also to measurement [32]. As mentioned above, no tritium must get to the spectrometer. This requires the blocking and removal of ions (i.e. T^-, T^+, T_3^+, ...). To do this the DPS is equipped with four electric dipole electrodes and two ring electrodes, as can be seen in figure 2.8. The electric dipole electrodes are placed in BT1 - BT4 and can move ions perpendicular to the magnetic guiding field with the so-called E-cross-B drift. In the approximation of uniform fields, the drift velocity is given by

$$\vec{v} = \frac{\vec{E} \times \vec{B}}{B^2}. \tag{2.19}$$

This drift velocity is the same for electrons and ions. The voltage applied to the electrodes, which creates the electric field $\vec{E}$, has to be chosen in such a way, that the effect on the fast-moving signal electrons of the β-decay is negligible. The ions are about 1000 times slower and are therefore drifted 1000 times further than the electrons in one pass. The ring electrodes are placed in and behind BT5 and are used to reflect the ions. The voltage applied to them is about +100 V. The ions can be reflected on both sides of the DPS, on one side by the ring electrode, on the other side by the gas flow. During every pass, they are drifted by the E-cross-B drift until they hit a metal surface and get neutralized. The geometry of the dipole electrodes has been modified with lobes to make sure that particles cannot be stored in one of the electrodes. Stored particles could create a space charge, which could have unwanted effects, such as altering the plasma potential of the source or neutralizing the blocking potential of the ring electrodes.

2.6.2 Cryogenic pumping section

The cryogenic pumping section (CPS) reduces the tritium flow rate towards the spectrometer by a factor of 10^7 by freezing it to a cold surface [70]. The CPS is a cryostat with seven superconducting magnets, which guide the signal electrons through the seven beam tube elements. The beam tube elements at the entrance and the exit of the CPS are cooled to liquid nitrogen temperature. The beam tubes 2-5 can be cooled down to $T = 3\,\mathrm{K}$, a temperature which is reached by active pumping of liquid helium. This low temperature is needed because the time a molecule stays adsorbed to a wall goes down exponentially with temperature. To increase the surface area a layer of argon snow can be frozen onto the cold beam tubes.
The gas flow reduction of the CPS has been tested with deuterium gas. At the design Ar frost temperature of 3 K the reduction could not be measured because the method is not

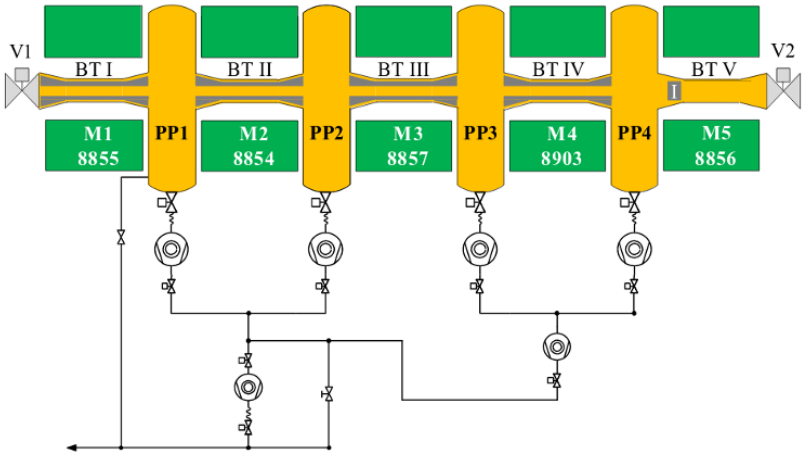

Figure 2.7: DPS beam tube with superconducting magnets (green) and the scheme of the vacuum components for the cascaded pumping with TMPs. The exhaust of the last TMP (bottom left) is connected to the outer Loop system. Picture adapted from [56].

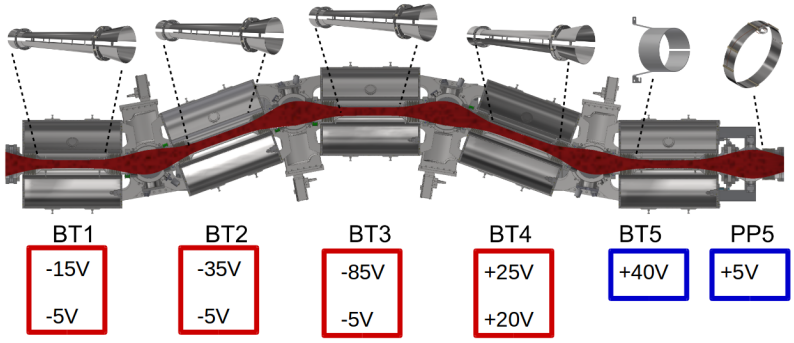

Figure 2.8: DPS beam tube with the dipole and ring electrodes and their respective voltage setting during neutrino mass measurements in the KNM2 measurement campaign. Picture adapted from [35].

sensitive enough. Extrapolation from higher beam tube temperature predicts a reduction factor $R > 10^{10}$ [118][40]. This is in good agreement with the simulations and surpasses the requirement by 10^3.
The CPS must not accumulate a tritium activity of more than 1Ci. If this limit is reached the Ar frost layer needs to be regenerated.
Downstream of the cold trap behind the cold gate valve the forward beam monitor (FBM) and the condensed krypton source (CKrS) can be entered into the beam tube.

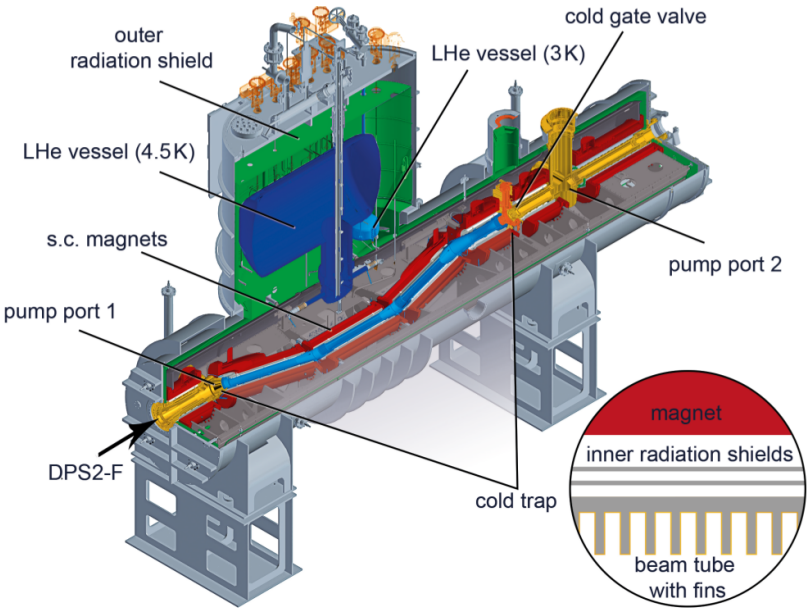

Figure 2.9: CAD drawing of the CPS. The gold-plated beam tube (yellow/light blue) is surrounded by seven superconducting magnets (red), which guide the signal electrons. The cold trap is cooled down to $T = 3\,\mathrm{K}$. A cold gate valve is mounted at the end of the cold trap. The cold trap can be covered with argon frost to increase the surface area. Picture taken from [118].

2.7 Spectrometer and detector section (SDS)

The spectrometer and detector section (SDS) does the energy filtering and counting of the signal electrons.

2.7.1 Pre spectrometer (PS)

The PS [103][43][53] is a spectrometer of the MAC-E filter type. It has an energy resolution of $\Delta E = E/300$ and is used to block all signal electrons which have energies far below the scanning range of the KATRIN experiment. This is done because these electrons could ionize gas atoms or molecules in the main spectrometer, which would induce background. During the first neutrino mass measurement run of KATRIN, the pre spectrometer was used with a blocking voltage of $U = -10\,\mathrm{kV}$.
If the pre- and the main spectrometer are operated at the same time, which is the case in standard KATRIN mode, the spectrometers form a Penning trap. To prevent the trap from filling and igniting, which could cause an additional background or even damage to the detector, three penning wipers are installed between the spectrometers. For more information about the penning trap and the penning wipers see [34]. The inner electrode system of the pre spectrometer is further used to continuously monitor the ion rate. During the ramp-up of the column density dedicated measurements have been carried out to set an upper limit on the ion flux towards the main spectrometer. The pre spectrometer is the most sensitive device in KATRIN to detect an ion flux towards the main spectrometer [78].

2.7.2 Main spectrometer (MS)

The main spectrometer (MS), which is schematically displayed in figure 2.2 is a high pass filter with a narrow energy resolution of $\Delta E = E/2000$ in its design configuration. For more details of the transmission properties, see chapter 2.3. The main spectrometer has a length of $l = 24\,\mathrm{m}$ and a diameter of $d = 10\,\mathrm{m}$.
The magnetic field is shaped by the superconducting magnets at each end of the spectrometer and additionally by a low field correction system (LFCS) and an earth magnetic field compensation system (EMCS)[29]. The LFCS consists of 14 normal conducting coils which can create a magnetic field in z-direction of more than $B = 10\,\mathrm{G}$. In 2019 it has been upgraded to the extended LFCS (eLFCS). This upgrade allows magnetic fields of more than $B = 15\,\mathrm{G}$ at any position and even higher fields in a region downstream of the center, where additional coils have been added to allow a stronger and more detailed shaping of the magnetic field. This can be used to shrink the volume of the flux tube and to shift the minimum of the magnetic field along the beam axis (z-direction).
The electric field in the MS is shaped by a dedicated inner electrode system. In its usual configuration, a voltage of $U_{\mathrm{IE}} = -200\,\mathrm{V}$ with respect to the vessel is applied in the center region and slightly less negative voltage near the entrance and exit region to prevent retardation of electrons with high pitch angles before their transversal energy is converted

to parallel energy. The negative offset of the inner electrode with respect to the vessel acts as an electric barrier for electrons emitted from the vessel wall. With the LFCS and inner electrode system, the MS has both electric and magnetic shielding from charged particles emitted from the vessel walls. The inner electrode system is highly segmented in z-direction. This can be used to shape the electric field in the MS. The maximum of the electric field which, together with the minimum of the magnetic field, defines the analyzing plane, can be shifted towards the detector to reduce the volume of the flux tube between the analyzing plane and the detector. This has proven to be a way to reduce the background of the KATRIN experiment.

2.7.3 Focal plane detector - FPD

The focal plane detector (FPD) [4] is the main detector of KATRIN and responsible for counting the electrons which get transmitted through the main spectrometer. It is important to note that the energy resolution of the KATRIN experiment of $\approx 1\,\mathrm{eV}$ is provided by the MS and not by the FPD.
The FPD is a Si-PIN diode with 148 pixels. The pixels are arranged in 12 rings with 12 pixels each and 4 pixels in the center. The radius of the rings is chosen such that every pixel has the same area. The FPD has an energy resolution of $\Delta E_{\mathrm{FPD}} = 1.8\,\mathrm{keV}$ and a detection efficiency of about 95 %. The sensitive area of the FPD has a diameter of 9 cm and is located in a magnetic field of $B_{\mathrm{FPD}} = 0.55\,B_{max}$.
To achieve KATRINs challenging background requirements the FPD has a low intrinsic background. A major source of detector background are events induced by cosmic muons. These signals can be excluded by a coincidence analysis with muon panels, which are mounted around the detector and give a signal if a muon traverses.
To improve the signal-to-noise ratio, the electrons are boosted with a post acceleration electrode (PAE), which is operated at $U = +10\,\mathrm{kV}$. The FPD is also cooled down to $T = -50\,°C$ (during KNM2) to reduce thermal noise.

2.7.4 Monitor spectrometer - MoS

The monitor spectrometer is a MAC-E filter type spectrometer which has been used as the energy filter of the Mainz neutrino mass experiment [82]. Now it is being used to monitor the stability of the KATRIN high voltage system. The monitor spectrometer measures the K-32 line of ^{83m}Kr. The high voltage of the monitor spectrometer is directly connected to the high voltage of the KATRIN main spectrometer. The source can be set to an offset potential to match the K-32 line position with the scanning region of the KATRIN m_ν scans. The calibration of the monitor spectrometer can be done by comparing the line

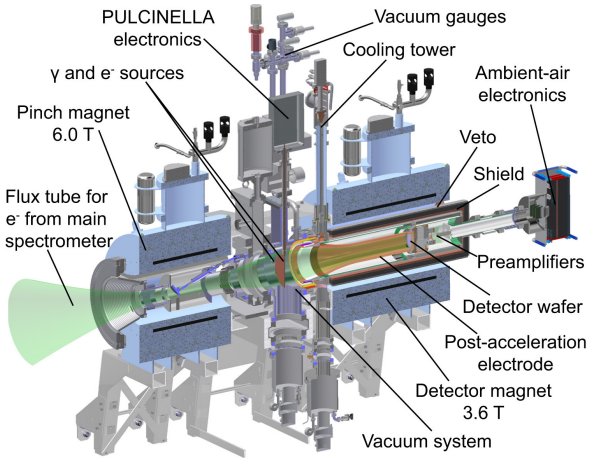

Figure 2.10: Setup of the detector section. The picture is taken from [4].

position of the L3-32 and the K-32 line [88].

2.7.5 High voltage at KATRIN

The KATRIN experiment uses a MAC-E-Filter type spectrometer to achieve its great energy resolution (see chapter 2.3). The stability of the high voltage needed to generate the electric retarding potential is crucial for the success of the experiment, as any unaccounted drift or a fluctuation of magnitude σ leads to a shift of the neutrino mass:

$$\Delta m^2 = -2\sigma^2 \tag{2.20}$$

For the determination of the Q-value of tritium, also the absolute value of the applied voltage is necessary. The KATRIN experiment aims to set the voltage with an uncertainty of only $\delta U = 20\,\mathrm{mV}$ at $U = 18.6\,\mathrm{kV}$. This ambitious goal can be achieved due to a novel absolute calibration method [107]. To avoid a long term drift, calibrations of the voltmeter are performed twice a week. The long term stability could be confirmed by a measurement of the line distance of K-32 and L_3-32 of ^{83m}Kr [88]. Short term fluctuations, such as the 50 Hz ripple from the power grid, are reduced by a post-regulation system. The remaining ripple has spikes of only $20\,\mathrm{mV_{pp}}$. A detailed description of the KATRIN high voltage system can be found in [108]. The description above focuses completely on the HV system which supplies the main spectrometer. Figure 2.11 shows where HV is also used in KATRIN.

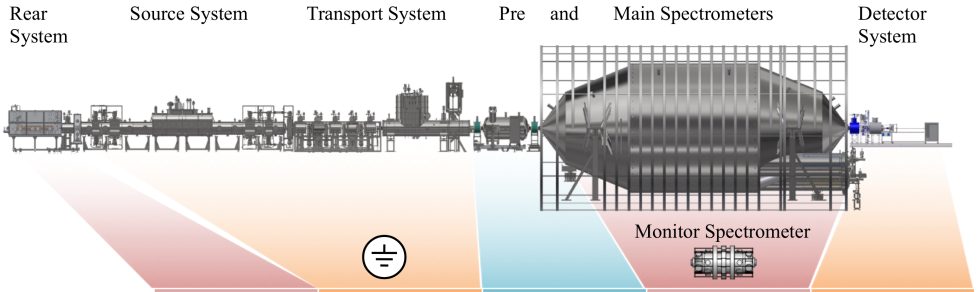

	angular selective electron gun	beam tube and condensed ^{83m}Kr source	Pre Spectrometer	Main and Monitor Spectrometers	Post acceleration system
Voltage	-35 kV	0	-35 kV	-35 kV	+25 kV
Stability	± 20 mV	uncritical	uncritical	± 20 mV	uncritical
Ripple and HF noise	shielded or compensated	grounded	uncritical	compensated	shielded
Relevance to m_υ	high	low	low, bg reduction	very high	low, bg reduction
Interfaces	coupled to main spectrometer potential, closed high voltage cage	no high voltage, but beam tube is overall reference ground	high voltage on surface, interlock system	high voltage on surface, interlock system, distributed high voltage	grounded housing, standalone system

Figure 2.11: Overview of the high voltage in the KATRIN experiment. The voltage values are the maximal values according to the design. At present time the voltage of the e-gun is limited to −20 kV and the post acceleration to +10 kV. Picture from [75].

2.8 Calibration and monitoring tools

2.8.1 Rear wall and instrumentation

The rear wall (RW) is the upstream end for β-electrons. It is located between the source system and the rear system (RS). The rear wall is a stainless steel disk coated with gold and a thin layer of titanium in between. The rear wall is located near the edge of the rear section superconducting magnet (RSCM). The magnetic fields in KATRIN are such that the magnetic field value in the 10 m long source tube is never exceeded at any point between the source tube and the rear wall. This ensures, that all electrons can reach the rear wall and do not get reflected by the magnetic mirror effect. Gold is a good electrical conductor and does not form an oxide layer on the surface, which means that the electrical conductance of the rear wall is good at the surface. Furthermore, the high number of protons in the nucleus of gold (Z=79) leads to a lot of X-rays induced by the β-electrons. These X-rays can be used to monitor the activity as is described in the next chapter. The rear wall can be set to a voltage of up to ±500 V. During neutrino mass scans a more precise power supply is used, which can provide a voltage of ±5 V. According

to simulations of the WGTS plasma (i.e.[84]) the rear wall voltage influences the radial and longitudinal homogeneity of the source potential. For the KATRIN experiment it is important to minimize the longitudinal inhomogeneity because it is difficult to measure and has a non-trivial influence on the neutrino mass analysis because it leads to an effective shift of the Eloss function [90]. The source potential can be investigated with the GKrS, which is described in chapter 2.8.4.2.

2.8.2 Activity monitoring

As mentioned in chapter 2.5 the KATRIN experiment needs a source stability on the 0.1 % level to achieve the required sensitivity on the neutrino mass. To ensure that this is fulfilled, the KATRIN experiment has multiple ways to monitor the source stability. The activity of the tritium source is constantly measured with the BIXS (**B**eta **I**nduced **X**-ray **S**pectroscopy) system and the Forward Beam Monitor and regularly with a special column density measurement with the rear section electron gun. Furthermore also the gas composition of the source is measured in real-time with the Laser Raman (LARA) system. These systems will be explained in more detail in the following sections.

2.8.2.1 BIXS

The BIXS system is designed to measure the KATRIN WGTS activity by **b**eta-**i**nduced **X**-ray **s**pectroscopy [117]. In normal KATRIN neutrino mass measurements about 10^{11} beta decays of tritium occur per second in the source volume. The electric and magnetic fields in KATRIN are such that only a tiny fraction of less than $100\,e^-$ per second make it to the FPD, while all other end up at the gold-coated RW, where they produce X-rays. The rear wall chamber has two CF-40 ports with BIXS systems looking at the RW under a 33-degree angle, as can be seen in figure 2.12. Since the intensity of the X-rays is proportional to the beta decay rate in the source, the BIXS system can directly monitor the source activity.
The energy loss of electrons (in the energy regime of KATRIN) in matter consists mainly of losses due to ionisation and bremsstrahlung [104][113]:

$$\left(\frac{dE}{dx}\right)_e = \left(\frac{dE}{dx}\right)_{ionis.} + \left(\frac{dE}{dx}\right)_{brems.} \tag{2.21}$$

These can be estimated as [21]

$$\left(\frac{dE}{dx}\right)_{ionis.} \approx \frac{Z^2 e^4 n_e}{4\pi\epsilon_0^2 m_e v^2}\, ln\left(\frac{m_e v^2}{2\langle E_b\rangle}\right) \tag{2.22}$$

and

$$\left(\frac{dE}{dx}\right)_{brems.} = \frac{4n_a Z^2 \alpha^3 \hbar^2 c^2 E_e}{m_e^2 c^4} \, ln\left(\frac{a(E)}{Z^{1/3}}\right) \tag{2.23}$$

The resulting radiation consists mainly of bremsstrahlung and characteristic X-rays. The characteristic X-rays depend on the quantum numbers and create a line spectrum. The bremsstrahlung is a continuous spectrum, which can be described by Kramers' law [81]:

$$dI(\lambda) = K\left(\frac{\lambda}{\lambda_{min}}\right)\frac{1}{\lambda^2}d\lambda \tag{2.24}$$

In this formula I is the intensity (i.e. the number of photons), λ the wavelength and K a constant which is proportional to the atomic number Z. λ_{min} is given by the kinetic energy of the electron. An important aspect in detecting the radiation is the transmittance through matter, i.e. the entrance window in front of the detector. The fraction of the transmitted light can be written as [21]

$$I = I_0 \, exp\left(-\int n\sigma \, dx\right) \tag{2.25}$$

with the starting intensity I_0, the density n, a material-dependent cross section σ and the distance traveled through the medium x. Finally, also the energy-dependent detector efficiency plays an important role. For a more detailed discussion and test measurements see [113], [104]. The BIXS system in KATRIN aims at a signal rate of $R > 10^4$ cps which allows a rate determination on the 0.1 % level in 100 seconds [104][77].

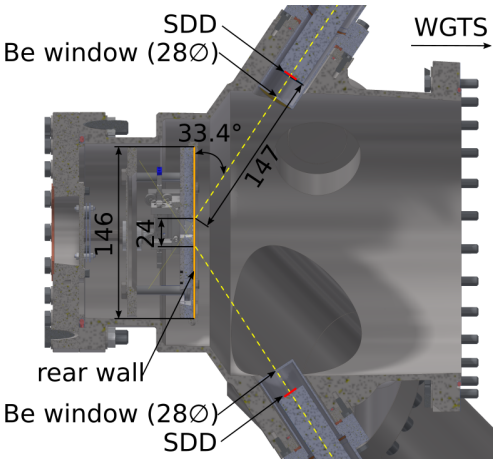

Figure 2.12: Drawing of the rear wall chamber showing the BIXS system and the rear wall. The silicon drift detector (SDD) of the BIXS system is placed behind a gold-coated Be window. Picture adapted from M. Röllig.

2.8.2.2 Forward beam monitor

The **f**orward **b**eam **m**onitor (FBM) is an electron detector which can be inserted into the KATRIN flux tube behind the cold section of the CPS. While the FBM is movable and can scan across the whole flux tube, it is usually positioned close to the edge of the flux tube, such that there is no shadow on the focal plane detector of KATRIN, as can be seen in figure 2.13. The task of the FBM is to monitor the source activity with 0.1 % precision [61]. Additionally, it is equipped with a Hall-sensor to measure the magnetic field in the flux tube.

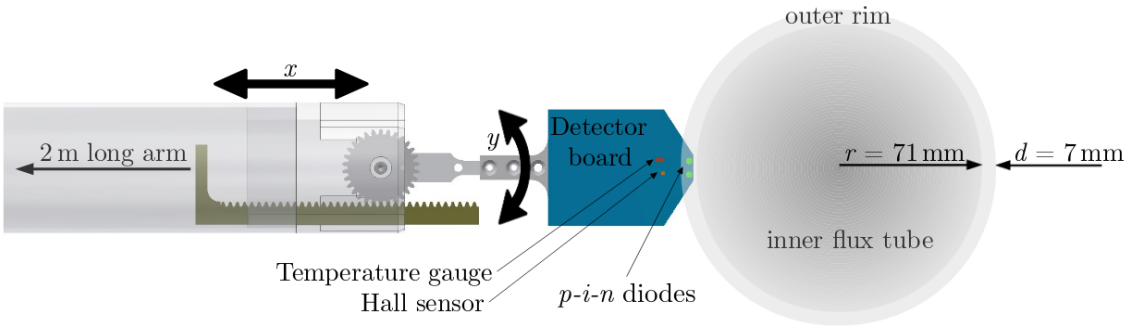

Figure 2.13: Scheme of the Forward Beam Monitor (FBM) in KATRIN. The FBM is equipped with two p-i-n diodes to measure the source activity. In normal measuring mode, it is placed at the outer rim of the flux tube. Image from [61].

2.8.3 Composition monitoring

For the analysis of the tritium beta decay spectrum, it is important to know the isotopologue composition of the source gas and to monitor it over time. The reasons for this are mainly the different final state distributions of HT, DT and T_2, and also the fact that the scattering probability of an electron in the source depends on the gas density, which is only proportional to the activity if the gas composition is constant over time. In the KATRIN experiment, the gas composition is measured by the LARA system. In KATRIN a tritium purity of $\epsilon_T = 95\,\%$ and a stability of $\Delta\epsilon_T/\epsilon_T < 0.1\,\%$ is required.

2.8.3.1 LARA

The **La**ser **Ra**man system in the KATRIN inner loop system (see figure 2.5) is designed to measure the isotopologue composition of the source gas in almost real-time. The idea of this spectroscopy is that light traveling through the low-pressure gas can excite molecules

in the gas. The light emitted in the deexcitation process can be shifted in wavelength depending on the initial and final states involved in the process. Figure 2.14 explains the basic idea in a model with three energy levels. Figure 2.15 shows a schematic view of the expected spectra for a specific molecule and figure 2.16 shows real measurement data. This explanation is mainly taken from [122]. For more information see also [38].

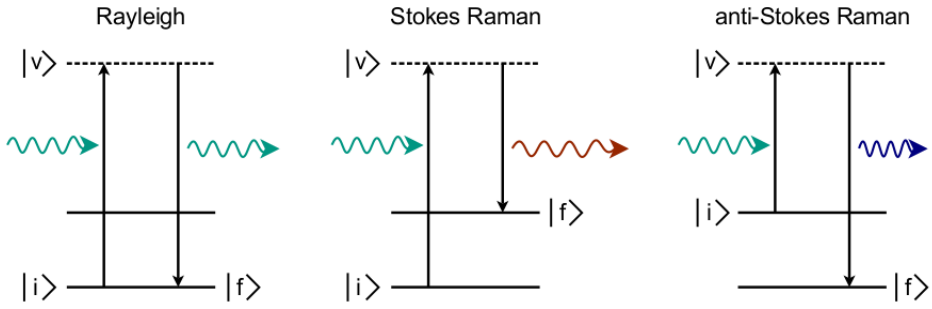

Figure 2.14: Photon scattering in a three-level diagram. The incoming photon excites the molecule from an initial state $|i\rangle$ into a virtual state $|v\rangle$. The molecule then goes into the final state $|f\rangle$ and emits a photon in the process. If $|i\rangle = |f\rangle$ the wavelength of the incoming and the outgoing photon is the same and the process is called Rayleigh scattering. If $E|i\rangle < E|f\rangle$ the photon is shifted towards a larger wavelength. This is called Stokes Raman. If $E|i\rangle > E|f\rangle$ the wavelength of the outgoing photon is shorter and the process is called anti-Stokes Raman. Adapted from [122].

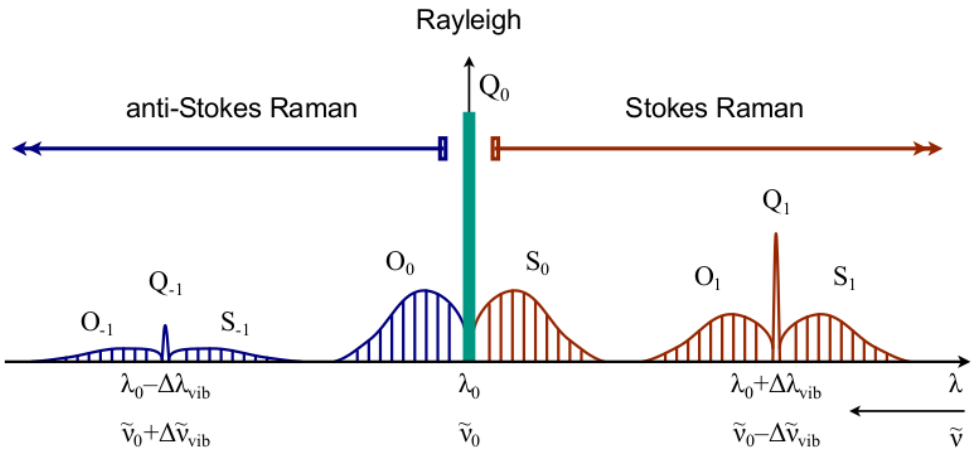

Figure 2.15: Schematic view of a Raman spectrum of a diatomic molecule. Rayleigh scattering does not shift the wavelength. Because of this, there is usually a large peak at the incident wavelength λ_0. S_0 and O_0 emerge from rotational states. The index denotes a vibrational excitation. Adapted from [122].

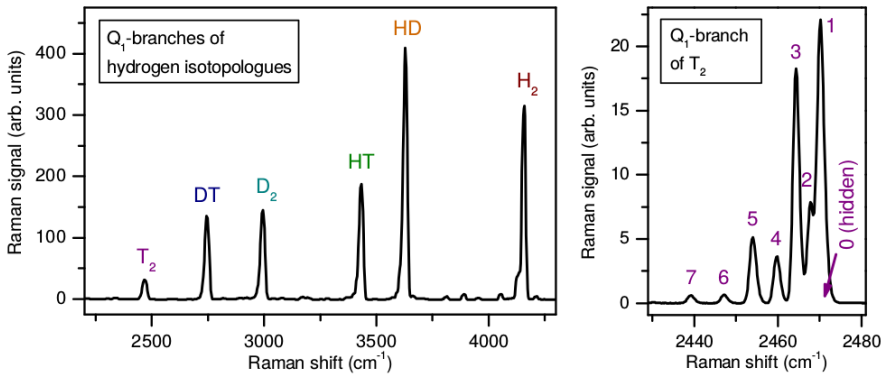

Figure 2.16: Raman spectra of hydrogen isotopologues. The left plot shows the Q_1 branches of the six hydrogen isotopologues. The right plot shows the Q_1 branch of T_2 with higher resolution. Picture taken and text adapted from [122].

2.8.4 Precision electron sources

The KATRIN experiment needs to be well understood to minimize systematic effects in the neutrino mass measurement. Individual components and certain properties of the experiment can be tested and calibrated with precision electron sources. Within the KATRIN experiment, there is a condensed ^{83m}Kr source (CKrS) which can be inserted into the flux tube between the CPS and the pre spectrometer. There is also the possibility to inject ^{83m}Kr into the WGTS and use it as a gaseous krypton source (GKrS). These sources are isotropic emitters and therefore underlie the energy resolution of the spectrometer given in equation 2.13. Therefore, also a different type of source, an angular selective and monoenergetic electron gun ('e-gun'), is mounted at the KATRIN rear section. The setup and commissioning of this e-gun is a major topic of this work and is required for the energy loss measurements described in chapter 4.

2.8.4.1 Condensed krypton source

The condensed krypton source (CKrS) [23][9] is a calibration source which can be inserted into the KATRIN beamline between the cold section of the CPS and the pre spectrometer. The basic idea is to have ^{83m}Kr Atoms sitting on a cold HOPG substrate.
^{83}Rb can decay to the metastable ^{83m}Kr, which then decays to stable ^{83}Kr. In the process, it emits two virtual or real photons, which are highly likely to interact with an electron from a shell of the Kr atom and to emit a conversion electron. The decay scheme with the branching ratios and half-life times can be seen in figure 2.17. The process of internal conversion was described by von Baeyer, Hahn and Meitner [57][91]. The kinetic energy of the emitted electron is in first approximation given by

$$E_{kin,e} = E_\gamma - E_b \qquad \text{(recoil of nucleus and gamma neglected)} \tag{2.26}$$

where E_γ is the energy of the gamma emitted by the nucleus and E_b is the binding energy of the electron in its shell. Since this is a two-body final state the energy spectrum is quasi monoenergetic. In the process electrons of higher shells can be excited (shake-up) or emitted (shake-off process) which leads to a reduction of the energy of the outgoing electron. The fraction of electron emission versus gamma emission is described with the conversion coefficient

$$\alpha_{IC} = \frac{T_e}{T_\gamma}. \tag{2.27}$$

The line width of the emitted electron is determined by the uncertainty relation $\Gamma \cdot \tau = \hbar$ and has contributions from the lifetime of the nuclear transition and the lifetime of the

electron hole:

$$\Gamma = \frac{\hbar}{\tau_e} + \frac{\hbar}{\tau_\gamma}, \tag{2.28}$$

where Γ is the full width at half maximum (FWHM) of the line. The shape of the line is given by a Lorentzian curve

$$L = A \cdot \frac{\Gamma/2}{(E - E_0)^2 + (\Gamma/2)^2}. \tag{2.29}$$

Here E_0 is the peak position and E the energy [146]. A detailed list of electron lines from ^{83m}Kr can be found in [141].

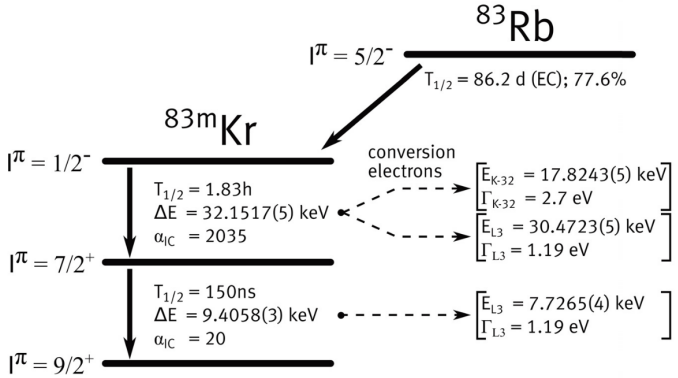

Figure 2.17: Decay scheme of ^{83}Rb. In the process of the decay photons of $E_{\gamma,32} = 32.15\,\text{keV}$ and $E_{\gamma,9.4} = 9.41\,\text{keV}$ are emitted and converted to conversion electrons. Image taken from [23].

The ^{83m}Kr can be admixed with stable ^{83}Kr to reduce the activity of a film of a given thickness. This mixing can be done in the gas system, which is described for example in [23]. An often used technique, which is described in [45], is the so-called pre-plating where first a film of stable krypton is frozen onto the substrate before the radioactive krypton is used. The HOPG substrate (Optigraph, model AGraphZ) has an area of $2\,\text{cm} \times 2\,\text{cm}$. However, there is a cylindrical aperture in front of it which has a diameter of 2 cm. The substrate is cooled to 26 K for normal operation but can be heated up to 140 K for cleaning purposes. The substrate can also be cleaned by a pulsed ablation laser with $\lambda = 532\,\text{nm}$. The film thickness of the condensed Krypton can be measured with an ellipsometry system [8].

The CKrS is placed right in front of the spectrometers and can be used to study the properties in the spectrometer section. Compared to the gaseous Krypton source, which is described in the next chapter, one of the main differences is, that the atoms are sitting on

a conducting surface, which means that a positively charged state after the emission of an electron is very short-lived. This allows also spectroscopy of the electrons resulting from the second gamma transition with an energy of $E_{\gamma,9.4} = 9.41\,\mathrm{keV}$, which happens about $150\,ns$ after the first transition.
The CKrS was designed with a high voltage system which allows the substrate to be at a voltage of up to 10 kV with respect to the KATRIN beamline. This would allow to match the energies of the K_{32} line, which has an energy of 17.8 keV with the KATRIN endpoint of about 18.6 keV. However, this HV setup has not been used yet.

2.8.4.2 Gaseous krypton source

The WGTS beam tube can be heated up to 100 K instead of the normal 30 K. In this setting, not only tritium, but also gaseous ^{83m}Kr can be inserted into the WGTS. Information about the system can be found in [142]. For technical reasons the krypton is inserted constantly at the front of the WGTS and is circulated in the inner loop. In this mode, the permeator, which is normally used to remove non-hydrogen-like gases, is not used. The ^{83m}Kr gas can be used alone, or together with tritium or deuterium.
The general aspects of conversion lines from ^{83m}Kr have been discussed in the previous paragraph. Since the krypton is inside the WGTS, it can not only be used to investigate the spectrometer, but also to study the source properties. One of the most important tasks of the GKrS is the investigation of the source potential along the beam axis. A longitudinal inhomogeneity of the potential would not only lead to a broadening of the spectrum, but it could also give rise to an effective shift of the energy loss function [90]. This can be seen in a measurement with ^{83m}Kr and tritium in the source, where the electrons from the L_3-32 line are being measured and a fraction of them is scattered by the tritium molecules. The energy difference between the scattered and unscattered L_3 electrons can be compared with the expectation from the eloss model (see chapter 4).

2.8.4.3 Photoelectron source (e-gun)

The photoelectron source ("e-gun") is a monoenergetic, angular selective electron source, which is located at the upstream end of the KATRIN experiment and is the largest part of the so-called control and monitoring section (CMS), which is usually called rear section (RS). A description of the main parts can be found in [7][125].
The main component of the e-gun is the e-gun flange, where the electrons are created via photo effect and accelerated with high voltage. The plates of the e-gun can be tilted relative to the magnetic field to give the electrons a starting angle with respect to the magnetic field lines. The electromagnetic transport system consists of solenoid coils, magnetic dipole

coils and a pair of electrodes. This part of the e-gun transports the electrons from the e-gun towards the WGTS and at the same time protects the photo cathode of the e-gun from neutral tritium gas and ions.
The e-gun has an energy resolution of $\sigma < 0.15\,\text{eV}$ and can produce rates of more than 10 kcps. The beam of the e-gun can be steered with the superconducting dipole coils of the WGTS. A more detailed description of the e-gun can be found in the next chapter.

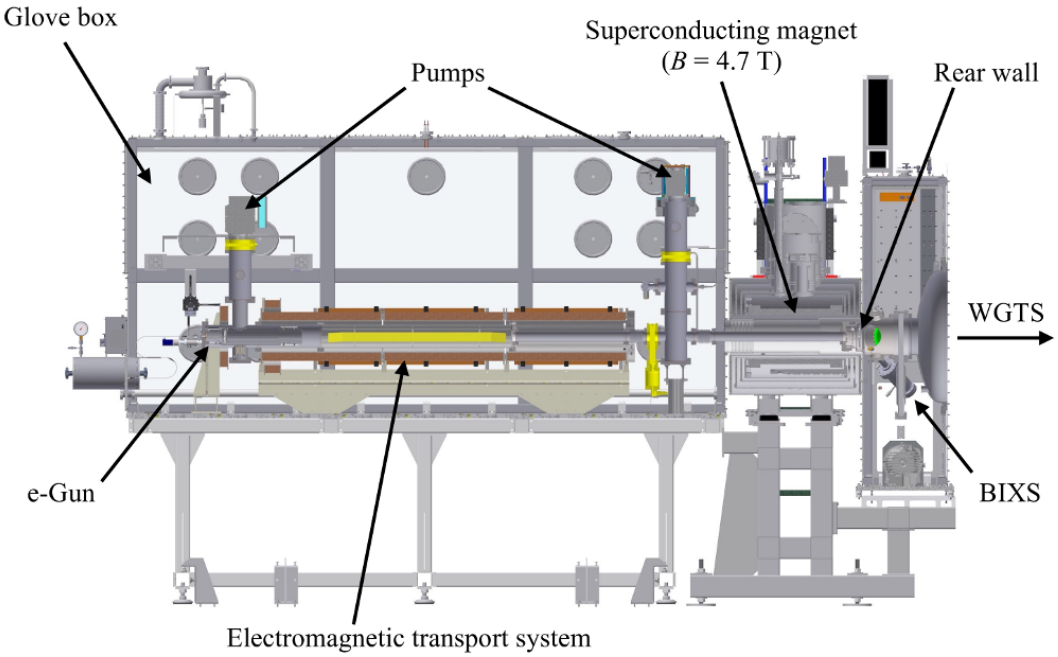

Figure 2.18: Control and monitoring section, also called 'rear section', of the KATRIN experiment. A vacuum system with two TMPs ensures sufficiently good vacuum. The normal conducting coils guide the electrons up to the superconducting magnet. The system is described in more detail in the next chapter.

Chapter 3

Precision photoelectron source

The KATRIN experiment requires precise knowledge of the spectrometer and the source properties. To investigate them, a precision photoelectron source ("e-gun") was developed and installed at the rear section (RS). This electron source provides a narrow, monoenergetic electron beam with adjustable energy and angle relative to the magnetic field. The idea of the angular selective photoelectron source was developed and tested in many previous works [137][66][138][145][11][12]. The design of the photoelectron source used in this thesis is described in detail in [7].
The main tasks of the e-gun are the work function determination of the main spectrometer, the measurement of the transmission function of the main spectrometer, regular monitoring of the column density and the determination of the energy loss function. The design requirements are listed in table 3.1.
The assembly and commissioning of the e-gun as well as the work function and energy loss measurements on deuterium are a major part of this thesis. The optical system was partly developed in [7] and [125]. The final hardware assembly and commissioning was done in this work together with Lutz Schimpf [121].

Parameter	Design requirement of the e-gun
electron energy	0 to 18.6 keV
electron rate	$O(10^4)$ cps
rate stability	0.1 % over hours
energy resolution	0.2 eV
angular spread	$< 4°$

Table 3.1: Design requirements of the rear section e-gun. Adopted from [7].

3.1 Working principle and concept

The working principle of the e-gun is based on the photoelectric effect [63][24], which describes the emission of low energy electrons from a metal surface under the illumination of UV-light. In a simplified model, one can assume a work function Φ, which is the energy needed to move an electron from inside the metal to the vacuum. When a photon with a given wavelength λ is absorbed it transfers its energy $E = hc/\lambda$ to the electron, which can be ejected if the photon energy is larger than the work function. The emitted electron has the kinetic energy

$$E_{\mathrm{e,\,kin}} = E_\gamma - \Phi = \frac{hc}{\lambda} - \Phi \tag{3.1}$$

where h is the Planck constant, c the speed of light and λ the wavelength of the photon. Even though this model is too simple, it shows that one can produce electrons with low kinetic energy if one has a photon energy slightly above the work function of a material. At the e-gun of KATRIN this is realized by guiding UV-light through an optical fiber which is coated with a thin metallic layer. Here 'thin' means, that a few percent of the light should be transmitted through the metal. The KATRIN e-gun uses gold as a coating material and titanium as an intermediate layer. Fibers which have been coated in 2019 and will be used in future measurement campaigns, use 3 nm of titanium and 20 nm of gold. The coating used for all e-gun measurements in this thesis is 3 nm of titanium and $>$ 20 nm of gold. Titanium is used as an adhesive layer. In previous electron sources also coatings with gold or silver without an adhesive layer have been used [11][12][145]. The thickness of the metal coating is a compromise between absorbing as much light as possible to generate more electrons, but also not blocking the electrons at the same time. According to [73] the mean free path for electrons of 5.5 - 7.5 eV for scattering with phonons in gold is about 25 nm. The mean free path for electron - electron scattering in gold is only 1.5-4.5 nm. The refractive indices of titanium [72] and gold [71] are

$$n_{Ti}(266\,\mathrm{nm}) = 1.27 + i2.04 \tag{3.2}$$

and

$$n_{Au}(266\,\mathrm{nm}) = 1.37 + i1.78. \tag{3.3}$$

This means, that the intensity of 266 nm light going through 3 nm of Ti and 20 nm of Au once is decreased by about 85 %. This does not account for reflections, which further reduce the amount of transmitted light. From these basic estimates, one can already see that the chosen thickness is reasonable. One should also consider that a thicker layer is likely to be more robust and that the coating process might not be completely homogeneous across

the area of the fiber. The e-gun has seven fibers and the thickness might also differ slightly from one fiber to another. The seven fibers are in place for redundancy because they can not easily be changed if a fiber brakes. The measurements described in this thesis are all performed with the same fiber. A scheme of how the fiber is glued into the plate and where the coating is can be seen in figure 3.1.

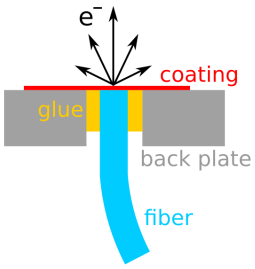

Figure 3.1: Schematic drawing of the fiber, its connection to the back plate and the coating. The e-gun at the rear section has 7 fibers. The coating is about 3 nm of Ti and 20 nm of Au. The picture is taken from [145].

After the electrons have been ejected by the photoelectric effect, they have small kinetic energy of less than 1 eV and are emitted in all possible directions. The electrons are then immediately accelerated by a strong electric field of about $E_{\mathrm{acc}} = 500\,\mathrm{V/mm}$. The electric field is needed to create a mono-angular electron beam.

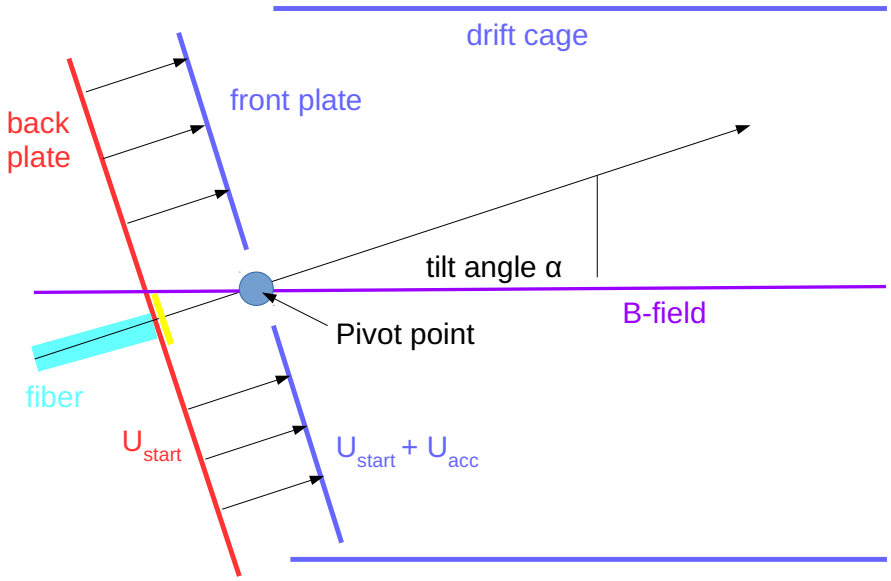

Figure 3.2: Schematic drawing of the e-gun plates. The electric field is at an adjustable angle relative to the magnetic field and accelerates the electrons, giving them an angle relative to the magnetic field. The drift cage is on the same voltage as the front plate. The electrons are emitted from the gold patch on the fiber, which is on the back plate potential. The plate system can be rotated around the pivot point, which changes the starting position of the electrons and their angle to the magnetic field. The maximum tilt angle is $\alpha \approx 14°$.

3.2 Description of the e-gun flange

The e-gun is mounted on a CF-150 vacuum flange made out of non-magnetic stainless steel. It has two CF-40 and three CF-16 mounts. A UV-transparent window is mounted to the CF-16 port at the center of the flange. Right after the window is fiber holding structure is mounted. The UV-light from the light source enters through the window and is coupled into one of the seven fibers, which transport it to the back plate. The holding structures for the plates are mounted onto the flange with screws. Insulating ceramic rods ensure that there is no electric contact between the flange, the back plate and the front plate. A mechanical linear feedthrough is mounted to one of the CF-16 holes outside the center. It is connected via a ceramic rod to the front plate. A motor placed on the outside can move the rod up and down, which tilts both plates. The plates are connected to each other via ceramic insulators. The front plate is mounted to the holding structures with rotating ceramic bearings. Rotating springs ensure that the plates have no backlash. The electrical connection of the plate is done via the two CF-40 feedthroughs. A copper wire connects the feedthrough with the metal holding structure. A metallic spring connects one of the holding structures with the back plate. The optical fibers are glued into a peek holding structure, which is clamped to the back plate. The front plate has a circular hole, such that the electrons can be emitted. The plates can rotate about 14° in each direction. The rotation is such that the position of the hole in the front plate does not change. This construction has the disadvantage, that the emission point of the electrons changes in east-west direction (in the KATRIN beamline) when the plates are tilted. As a direct consequence of this, the magnetic dipole coils in the rear section need to be adjusted if the electron angle is changed significantly as otherwise the beam can be cut off at the aperture in the rear section. A schematic drawing of the e-gun plates with and the pivot point can be seen in figure 3.2. A photograph of the e-gun flange with a description of the parts is shown in figure 3.3.

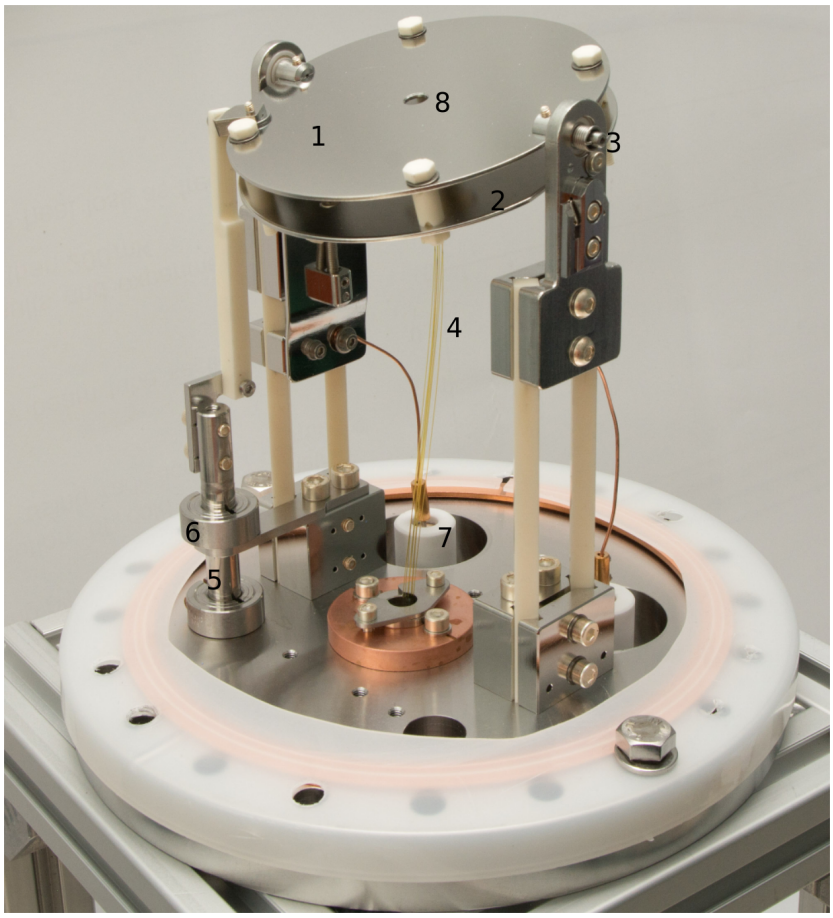

Figure 3.3: Picture of the e-gun flange. This e-gun is used in the STS3a, KNM1, and KNM2 measurement campaign of KATRIN.
1) Front plate **2)** Back plate **3)** Rotating springs to ensure that there is no backlash in the plate position **4)** Seven optical glass fibers **5)** Mechanical feedthrough connected to the motor to control the plate angle **6)** Mechanical stop to limit the movement of the rod to protect the e-gun **7)** High voltage feedthrough to provide high voltage to the plates **8)** Aperture in the front plate - electrons leave here.

3.3 Optical components

The light from a light source has to be coupled into the glass fibers of the e-gun. To be able to choose one of the seven fibers of the e-gun, this is realized with a pair of lenses, which are mounted to a movable stage. The focusing lens system was designed in [125] and can be seen in figure 3.4 and figure 3.5. In an early testing phase of the gun, the lens

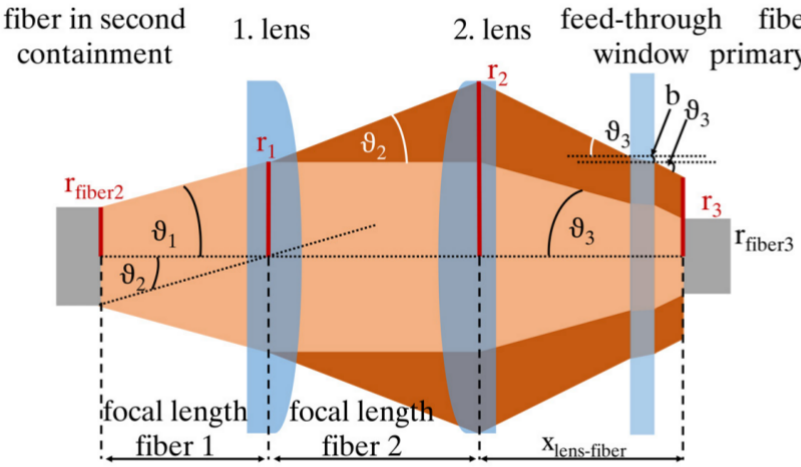

Figure 3.4: Lens system of the e-gun. The light from a UV-light source comes from the left through an optical fiber. At the end of the fiber, the light exits with an opening angle depending on the numerical aperture of the fiber. The lenses have to collimate the light to focus it to the entrance of the fiber on the right. In the KATRIN experiment, the distance from the left fiber to the lenses is fixed, but the distance between the second lens and the entrance window can be changed with a stepper motor. Picture from [125].

system was adjusted using a green ($\lambda = 532\,\mathrm{nm}$) laser and then checked with a UV laser and fluorescence paper. The distance between the incoming fiber from the UV-light source to the first lens, and also the distance between the first and second lens are fixed. It was chosen in such a way that the light is focused on a spot a few centimeters behind the second lens. This whole setup with the fiber and the two lenses is mounted to a movable three-axis stage, such that the beam can be focused on a fiber. A rough adjustment was usually done with a green laser. An optimization was done later by optimizing the electron rate on the detector. In the final setup at the KATRIN beamline the lens system is covered with a black laser curtain. During testing the setup was not covered as can be seen in figure 3.5. To monitor the light intensity which is going to the e-gun, a beam splitter and a UV-diode is used. In the KATRIN experiment, a temperature-stabilized diode of type Hamamatsu S2592-04 is used. For test measurements also other diodes have been used.

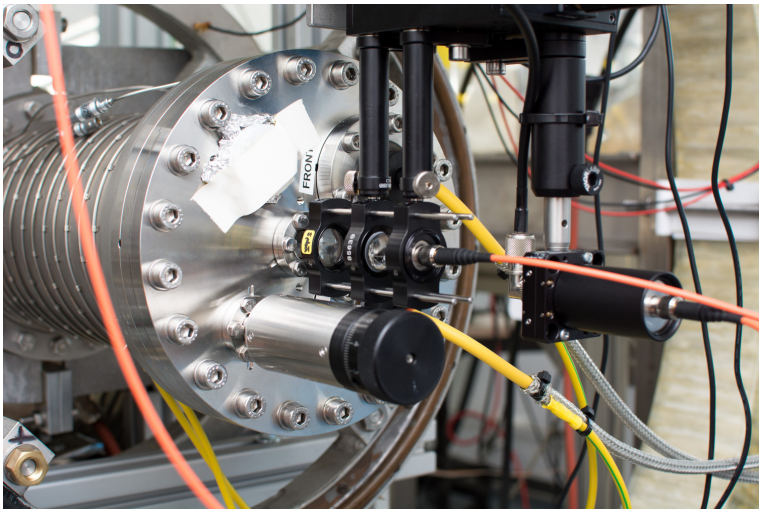

Figure 3.5: Picture of the e-gun flange at a test setup showing the lens system. The lenses are mounted in an optical cage system, which is mounted to a three-axis-stage with stepper motors. The orange fiber guides the UV-light, the yellow cables provide the high voltage and the turning wheel on the bottom left changes the plate angle. At the KATRIN experiment, the lens system is covered by a black curtain. The UV-Diode on the right is used to measure the light intensity.

3.3.1 Optics box and light sources

To operate the e-gun with high stability and high energy resolution, a high quality UV-light source is required. To be able to operate such light sources in the Karlsruhe tritium laboratory environment, an optical box was built. The box is based on a 2000 mm × 700 mm × 59 mm breadboard [1]. The dimensions, especially the width of only 700 mm, are limited by the space available in the laboratory. To avoid laser-induced contamination, as little plastic as possible is used. If plastic is used it is covered to avoid a direct line of sight to a laser source. The Box is built with black anodized aluminium rails [2]. The walls are made from black anodized aluminium. To get wires and fibers from one section of the box to another a rectangular hole is placed in the center of the intermediate walls. This hole is covered with brushes to block light. Since these brushes are made of plastic, a metallic shield is placed in front of them to block the direct line of sight to the light source. At each end of the optic box, two small boxes are added to form an entrance. Light from the

[1] Newport, Honeycomb Optical Breadboard, M6 Holes, Industrial Grade, 25 mm grid
`https://www.newport.com/f/ig-3.4-mm-skin-honeycomb-core-breadboards`

[2] Thorlabs, 25 mm Optical Construction Rails, M6
`https://www.thorlabs.de/newgrouppage9.cfm?objectgroup_id=194`

outside is blocked by brushes, a 90° corner, and by more brushes to get into the box.

3.3.2 Laser driven light source

One of the light sources which is used for the e-gun is the so-called LDLS (laser driven light source). The LDLS is a continuous wave (CW) light source with a broadband light spectrum. Technically it is a xenon plasma cell that is pumped with a near-infrared laser ($\lambda = 974\,\text{nm}$, CW). The xenon plasma has a broadband light spectrum from UV to infrared light, as can be seen in figure 3.7. To select the desired wavelength, a monochromator is used. The whole system of the laser, the xenon cell, and the monochromator is completely fiber coupled. The fiber from the exit of the monochromator goes out of the optic box. In the test setup, the fiber splitter is directly connected to the fiber. In the KATRIN setup, an optical feedthrough to the second containment is needed with the fiber mounted on the outside and the splitter mounted at the inside of the containment. One end of the splitter is connected to a diode, the other one to the lens system in front of the e-gun flange.

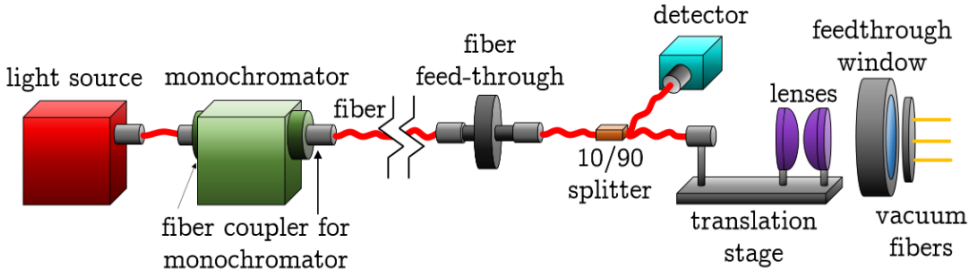

Figure 3.6: Schematic view of the optical system with LDLS: The light source is the xenon plasma cell of the LDLS. A fiber transports the light to the monochromator. From the exit of the monochromator, a fiber guides the light outside of the optic box. Via a fiber feedthrough, the light enters the second containment. A fiber splitter directs a few % of the light to a photodiode (for details see chapter 5.4.4). Most of the light goes through a pair of lenses and a window into the vacuum part of the e-gun. The picture is taken from [125].

3.3.3 Pulsed UV-laser

A pulsed UV-laser of type 'InnoLas mosquito-266-0.1-V' can also be used as a light source of the e-gun. It is a frequency quadrupled Nd:YVO_4 laser which produces short laser pulses with 266 nm wavelength (width $\approx 1\,\text{nm}$ FWHM) with a repetition rate of 20 kHz to 100 kHz. The duration of a pulse is < 20 ns [12]. This laser can use a function generator as

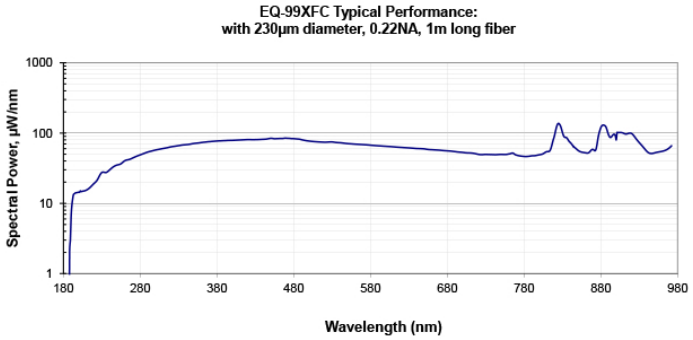

Figure 3.7: Light spectrum of the LDLS according to the manufacturer's website [28]. The relevant range for the e-gun at KATRIN is between 240 nm and 310 nm.

an external trigger. The intensity of the laser can be controlled via the laser diode current of 6 - 8 A and also via a half-wave plate and a birefringent crystal placed directly behind. A calibration curve for this is shown in figure 3.8. The half-wave plate was not used to adjust the laser intensity in STS3a, but in the KNM1 campaign and afterward. At the exit of the laser, a dark purple colored window filters out the remaining 532 nm green light and only the 266 nm UV-light is emitted. At this point, the beam path is open and optical components can be placed into the beam path. At a distance of about 10 cm from the laser, the light is coupled into a fiber. The fiber coupling is placed onto an optical stage with millimeter screws. Because of the open beam path between the laser and the fiber coupling the interlock of the laser is always triggered if the optic box is opened. While the interlock is triggered, the laser cools down and it takes a few minutes before all inner parts have reached their nominal temperature again and the laser can be restarted. The laser is mounted on an aluminium block with a cooling pipe inside. This cooling pipe guarantees a stable temperature of the laser housing. The connected cooling compressor causes strong mechanical vibrations. For this reason, the bottom plate, with the cooler on it, can be mechanically decoupled from the rest of the optic box.
Figure 3.9 shows the optic box from above. In the left segment, one can see the laser, in the center segment the LDLS with the monochromator, and on the right side a few diodes which were used for testing purposes before the optic box was connected to the e-gun. After the STS3a campaign, a so-called noise eater [121] was added in the right segment. The purpose of the noise eater is to stabilize the light output of the light source. The signal from a photodiode is read by software, which can control an iris diaphragm to counteract changes in the measured light intensity.

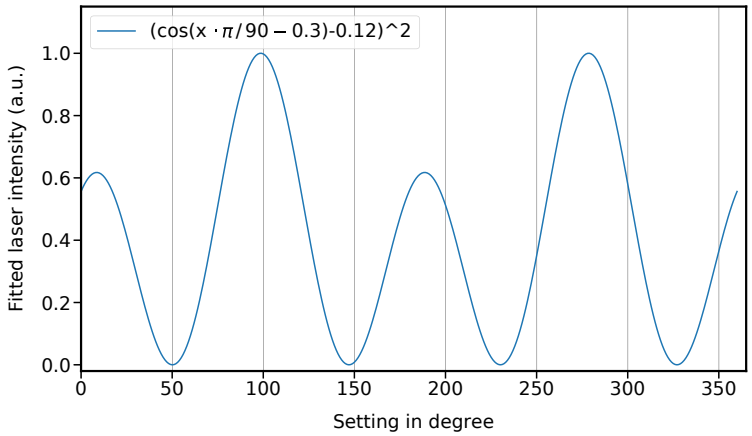

Figure 3.8: Light intensity of the laser over the setting of the half-wave plate. The angle of the plate can only be changed on site by opening the laser and adjusting it by hand. For important measurements, the laser intensity should be adjusted this way because it is reproducible and does not affect the stability of the laser. For quick changes and less important measurements the intensity can be regulated via the diode current of 6 - 8 A. During STS3-a the $\lambda/2$ plate was set to about 10°. The function is provided by V. Hannen.

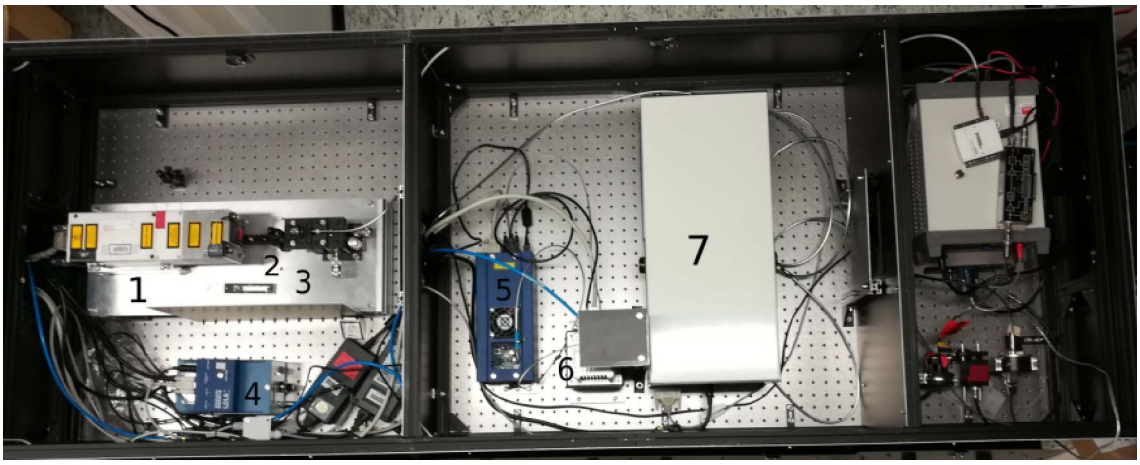

Figure 3.9: Optic box before the first measurement phase of the e-gun. **1)** UV-laser mounted on a temperature stabilized metal plate. **2)** Optical components like an optional neutral density filter and a lense. **3)** Three-axis stage for fiber coupling. **4)** LDLS controller. **5)** IR-laser of LDLS **6)** LDLS plasma cell **7)** Monochromator. **Segment at the right)** Diodes and measurement equipment for testing purposes. After the STS3a campaign the so-called 'noise eater' was installed here.

3.4 HV concept of the electron gun

A precise and stable high voltage at the back plate of the e-gun with respect to the inner electrode system of the main spectrometer is essential for precision measurements with the e-gun. The voltage of the back plate (BP) determines the starting energy of an e-gun electron (in addition to the sub eV energy remaining from the photoelectric effect). In standard operation conditions, the BP voltage is given by the voltage of the main spectrometer vessel (MSV) and an additional offset ($U_{\mathrm{BP\ offset}}$) of up to $\pm 500\,\mathrm{V}$:

$$U_{\mathrm{BP}} = U_{\mathrm{MSV}} + U_{\mathrm{BP\ offset}}. \tag{3.4}$$

The retardation voltage in the analyzing plane (AP) is given by the vessel voltage and the inner electrode offset voltage ($\mathrm{U}_{IE\,common}$)

$$U_{\mathrm{AP}} = U_{\mathrm{MSV}} + U_{\mathrm{IE\ common}} + \delta U. \tag{3.5}$$

To account for the detailed geometry of the KATRIN MS a correction $\delta U = 1.93\,V$ (assuming normal spectrometer settings) has to be added. To investigate the system in the typical energy regime of KATRIN, the voltage in the analyzing plane has to be around $U_{\mathrm{AP}} \approx -18.6\,\mathrm{kV}$. It can be seen, that the surplus energy of the electrons and the respective energy stability depends only on the offset power supplies of the IE and the BP. The front plate (FP) accelerates the electrons. The voltage of the front plate is given by

$$U_{\mathrm{FP}} = U_{\mathrm{MSV}} + U_{\mathrm{FP\ offset}}. \tag{3.6}$$

To achieve the necessary non-adiabatic motion in the acceleration process, a field strength of about $E_{\mathrm{acc}} = 500\,\mathrm{V/mm}$ is needed [12]. This field strength is given by the voltage difference between the front and the back plate, and by the distance of the plates, which is given by the design:

$$E_{\mathrm{acc}} = (U_{\mathrm{FP}} - U_{\mathrm{BP}})/8\,\mathrm{mm}. \tag{3.7}$$

The aperture in the front plate should be as small as reasonably possible to have a homogeneous electric field. After the electrons have passed the hole in the front plate they move through the so-called drift cage, a cylinder at the same potential as the front plate of the e-gun. This ensures that the electric field at the front side of the e-gun is well-behaved with no spikes in the field strength. After that two post-acceleration electrodes smooth the transition to ground potential. These two cylindrical electrodes are at 2/3 and 1/3 of the front plate voltage with respect to the beam tube. This setup is displayed in figure 3.10. Detailed field calculations of this setup have been done and are described in [7].

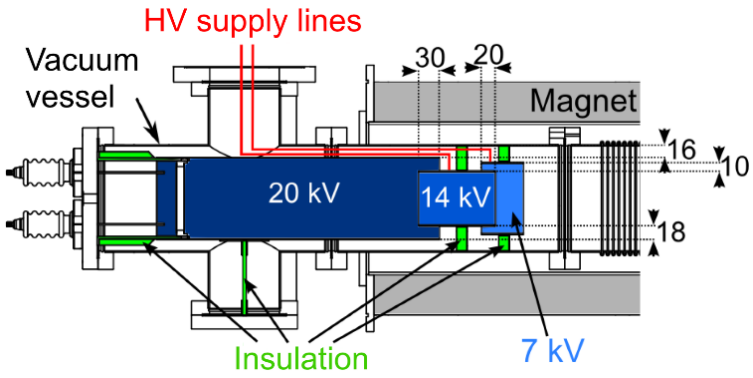

Figure 3.10: Schematic drawing of the high voltage electrode configuration of the rear section e-gun assuming a front plate voltage of 20 kV. The picture is taken from [7]. The alignment of the drift cage (dark blue) and the supply lines (red) is not precise and might be a cause for the observed HV problems at high voltages.

The position of the e-gun plates should be quite accurate. However, the position of the cylindrical electrodes is not known with the same precision, and the HV supply lines are by far the most uncertain components with respect to their actual position. In case HV problems occur, these supply lines should be checked.

To supply these voltages to the e-gun, a high voltage cage, almost identical to the one used at the main spectrometer HV system, was built. While the outer cage is on ground potential, the inner cage can be operated at up to 35 kV [108]. An insulating transformer placed below the inner cage provides power for electrical devices inside the inner cage. The communication of these devices to the outside is done with optical cables. In standard operation of the e-gun, the inner cage is on the same potential as the vessel of the main spectrometer. For special measurements, it is also possible to provide an independent voltage.

Inside the inner cage a power supply of type 'Iseg MMC 500' provides a ± 500 V offset voltage (with respect to the inner cage), which is used for the back plate. This voltage is measured with a digital voltmeter of type 'Fluke 8846A'. Ideally, the back plate is electrically isolated from the beam tube. However, in case of a flashover, the back plate can be connected to ground potential for a short time. To protect the voltmeter and the power supply, a $R = 100\,\mathrm{k}\Omega$ resistor is built in in series. The power supply for the front plate can provide an offset voltage of ± 6 kV. This voltage is connected to the beam tube ground with a chain of three 100 MΩ resistors, which serve as a voltage divider and provide the 2/3 and 1/3 voltages for the cylindrical electrodes. A technical drawing of this setup is shown in figure 3.11. The protective diode parallel to the three times 100 MΩ resistors

was added after KNM1.

High voltage resistance: The high voltage stability of the e-gun flange itself (figure 3.3) has been tested in a separate test stand before mounting it to the KATRIN beamline. During the commissioning of the HV it was found out that the HV-cables (yellow cables in figure 3.5) charge up on the outside and need a grounded screen (grey part). It was possible to ramp up the e-gun to high voltage. After some initial voltage flashovers it was possible to ramp the plates of the e-gun up to a voltage of $-35\,\mathrm{kV}$, which is the limit of the power supply. However, a strong increase of the background was observed with increasing voltage (compare figure 3.15 and figure 3.16). The energy of the electrons coincides with the voltage of the front plate. This means, that electrons have been ejected from the front plate if the voltage was above roughly $25\,\mathrm{kV}$. This could also be observed if the light source of the e-gun was turned off, which is expected if the electrons are emitted from the front plate. In this configuration, which was able to go to $-35\,\mathrm{kV}$, the e-gun flange was mounted to a grounded CF-150 tube without any of the cylindrical electrodes mentioned above. When the e-gun was mounted at TLK with the complete setup of all electrodes displayed in figure 3.11, the high voltage of $-35\,\mathrm{kV}$ could not be reached. At voltages of about $-27\,\mathrm{kV}$ high voltage flashovers occurred. One can clearly hear them (they sound like firecracker) and see sparks at the $100\,\mathrm{k}\Omega$ resistor in the HV-cage, which is part of the connection to the front plate. The pressure gauge, which is mounted above the chamber of the e-gun, can be used as an indicator for electric discharges inside the vacuum chamber: Discharges are expected to cause short spikes in the pressure reading. These spikes can be seen, and they get more frequent at higher voltages of the e-gun. However, there is not always a clear signal in the pressure reading when a discharge was noticed in the HV-cage. This might be caused by the slow readout speed of the pressure gauge. The pressure value is written to the database only every five seconds.

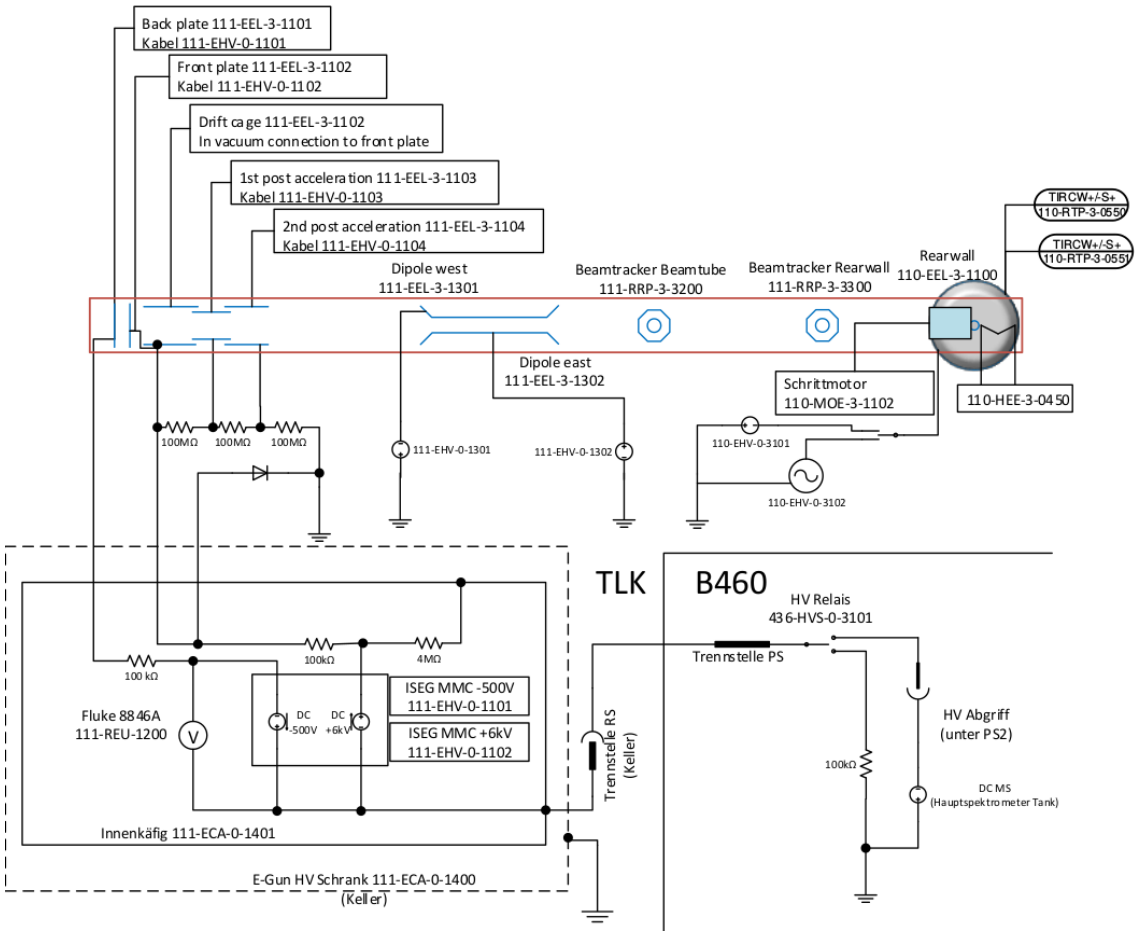

Figure 3.11: Technical drawing of the high voltage electrode configuration of the rear section e-gun. The dashed line shows the outer HV cage, which is on ground potential. The inner cage inside is usually connected to the vessel of the main spectrometer. This connection can be opened at two points, which are labeled with the German word 'Trennstelle'. The 100 kΩ resistors in the cables going to the back and the front plate have been added to protect the electronic devices in case of a flashover. Picture provided by K. Schlösser, KIT.

3.5 Measurements with the electron gun at a test stand

Before the e-gun was mounted to the KATRIN beamline, a first commissioning was done at a test stand. This test stand consisted of a vacuum chamber, a Si-diode to detect electrons, and a pair of Helmholtz coils to provide a magnetic field. The e-gun flange was mounted to the test stand, but none of the cylindrical electrodes which are present in the KATRIN beamline. This does of course change the electric fields at the e-gun, especially at the front plate, which is normally inside the drift cage. The diode is operated at room temperature and has no shielding or veto against background sources such as cosmic muons. Therefore, the energies below 15 keV are cut away and a small background rate is expected. The vacuum system is built around a copy of the former rear wall chamber. This chamber has a CF-250 port on one side and CF-150 on the other. Additionally, it has four CF-40 ports on the sides. One of those ports is used for pumping. While this chamber is placed in the center of the Helmholtz coils, the pumping is done via a long tube, because the turbomolecular pump has to be placed outside the magnetic field. The pressure gauges, which are also placed far away from the chamber and outside of the magnetic field, show a pressure of a few times 10^{-7} mbar. The vacuum in the chamber, which means at the e-gun, can be expected to be roughly the same, if not a bit worse. The magnetic field provided by the Helmholtz coils is homogeneous at the position of the e-gun and the detector and can reach up to 50 mT. This is about twice the nominal field of the e-gun at the KATRIN beamline. For most measurements, a rather low magnetic field of about 3 mT was used. In this configuration, the rate was optimal with the magnetic field and the mechanical alignment of the test stand. A higher magnetic field was only used to test and confirm the high voltage resistance of the e-gun, which did not show a significant dependence on the magnetic field.

Rate: The specification of the e-gun is to achieve a rate of about 20 kcps with a stability of 0.1 % over hours as mentioned in table 3.1. A measurement of rate over wavelength, which can be seen in figure 3.12, shows that the required rate of 20 kcps is achieved in a large wavelength range. At a wavelength of 270 nm a rate of more than 100 kcps was achieved. The highest rates were usually found at wavelengths from 260 nm to 270 nm. Measurements at a constant wavelength over many hours show that the rate is also quite stable and the requirement of a 0.1 % rate stability over time is fulfilled. An example measurement at a fixed wavelength can be seen in figure 3.13.

Background at high voltages: As mentioned in the previous chapter, a high voltage of $U < -25$ kV leads to the emission of electrons. These electrons have a non-poissonian rate with higher multiplicity. This can be seen in figure 3.16. At the nominal voltage of -18.6 keV the background rate in a measurement without the light source was measured to

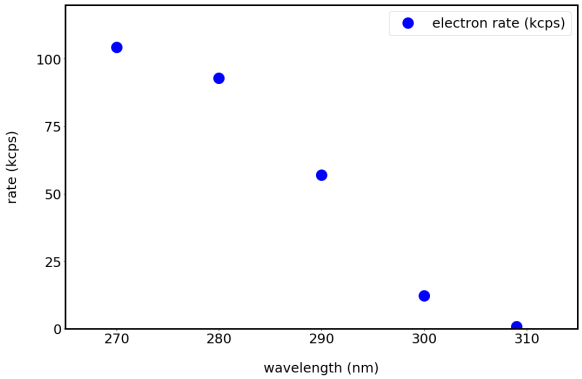

Figure 3.12: Measurement of rate over wavelength at the e-gun test stand. The width of the monochromator was set to 3 mm. The measurement was performed with a new LDLS. This measurement demonstrates, that the e-gun with the LDLS can provide the required rate of 20 kcps. Note: This measurement was done without the fiber splitter. Using the fiber splitter reduces the rate by 20 to 30 %. Such a measurement (including a diode to measure the light intensity) can be used to determine the work function with the Fowler method (see chapter 5.4.2 ff.). The result of the Fowler fit of a similar measurement gives $\Phi_{\text{egun}} = 4.02(3)\,\text{eV}$. Note that this value is obtained in a test stand with poor vacuum conditions compared to the KATRIN rear section.

be 8 cps, as can be seen in figure 3.15. These events might be caused by natural background sources such as cosmic rays or radioactive materials. At $-30\,\text{kV}$ however, the background is increased to 1520 cps and shows high multiplicity events. The peak positions are defined by the front plate voltage, and not by the back plate voltage as one would expect for the normal operation of the e-gun. This indicates that electrons are emitted from the front plate at these high voltages. The voltage dependence is the only indication of the origin of the electrons since no spatial resolution or other diagnostic tools were available in this test setup.

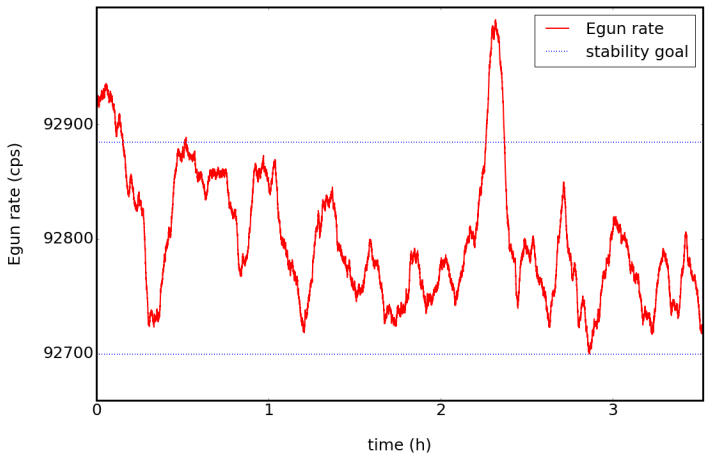

Figure 3.13: Measurement of rate over time at the e-gun test stand. The red curve shows the e-gun rate over time. The blue dashed lines indicate the $\pm 0.1\,\%$ stability goal. The width of the monochromator was set to 3 mm. The measurement was performed with a new LDLS. This measurement shows, that the e-gun with the LDLS can provide the required rate of more than 20 kcps with a stability of better than $0.1\,\%$ over hours. The standard deviation in this measurement is $0.061\,\%$.

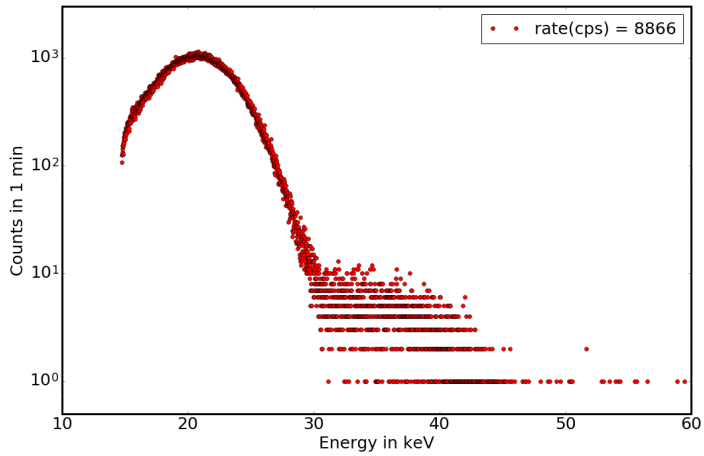

Figure 3.14: Histogram of counts in one minute over energy measured with $U = -18.6\,\mathrm{kV}$ at the back plate. The distribution looks as expected and there is no hint for high multiplicity events. Those would form additional peaks at multiples of the normal peak position. The measurement was performed with a wavelength of 300 nm and a rate of 8.9 kcps to avoid large pile-up effects. Note: The energy calibration of the detector is very rough and should not be taken to seriously.

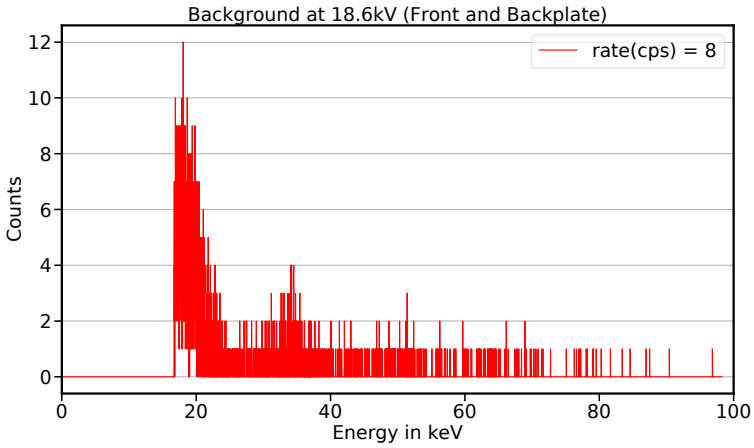

Figure 3.15: Background rate over energy measured with $U = -18.6\,\mathrm{kV}$ at the front and back plate. In this measurement, the light source of the e-gun was turned off and only the background was measured. The background has a rate of 7.88 cps which is negligible for the simple test measurements. The diode was operated at room temperature, might cause a part of this background.

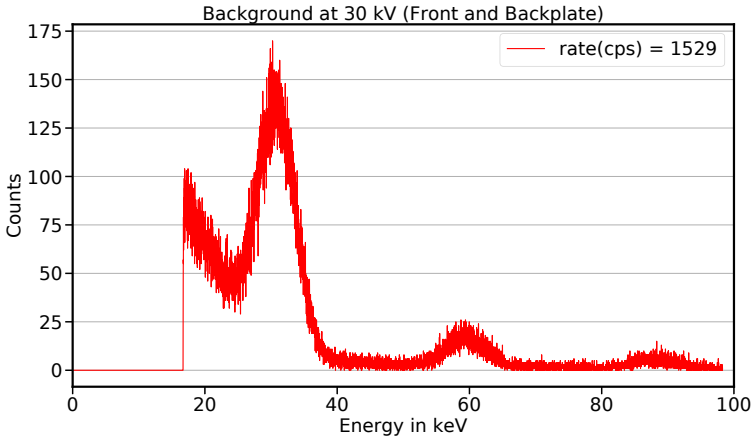

Figure 3.16: Background rate over energy measured with $U = -30\,\mathrm{kV}$ at the front and back plate. In this measurement, the light source of the e-gun was turned off and only the background was measured. The background has a rate of 1.5 kcps and clearly shows high multiplicity events. The peak positions shift if the voltage at the front plate is changed. This indicates, that the electrons are emitted from the front plate of the e-gun.

Correlation of diode signal and rate: Changing the slit width of the monochromator is, in some approximation, a well-controlled and reproducible way to vary the intensity of the light without changing other properties such as the wavelength. The correlation between the slit width and the measured light intensity is almost linear. A downside of the used setup is, that the fiber couplings to the monochromator need to be adjusted every time the slit width is changed. Figure 3.17 shows a measurement of the rate over the measured signal from the photodiode. In this measurement, the monochromator was set to 265 nm and the slit width was changed to control the light intensity. The measured light intensity and the electron rate are almost proportional to each other. The change of the slit width and the fiber coupling can change the spectrum of the light and might cause a slight nonlinearity in this measurement.
The test measurements, such as the one in figure 3.17, indicate that the rate of the e-gun is proportional to the measured light intensity. In the stability measurements (i.e. figure 3.13) the diode current was also monitored, but apparently the noise of the diode reading was much larger than the fluctuations of the e-gun rate. From this, we conclude that in the used setup it is not possible to correct fluctuations on the 0.1% level with the diode signal. Only long term drifts over at least some minutes could be corrected. The photodiode used in this measurement was not temperature stabilized. In the final setup, a diode with a Peltier element is used to improve the stability of the light measurement.
Stability of the light signal: The rate of the e-gun needs to be stable on short and long time scales. This can only be achieved, if the UV-light, which creates the photoelectrons, is stable. Test measurements show, that the LDLS needs a warm-up time of at least 15 minutes. During that time the rate constantly increases. To make this warm-up process as short as possible and to stabilize the rate, the LDLS plasma cell is mounted to a Peltier element which stabilizes the temperature. In the measurements described in this thesis, a temperature of 25°C was set. The LDLS was previously tested with 40°C, which did not lead to any obvious changes. For the correct measurement of the light intensity the light-guiding fibers as well as the cable which connects the diode with the amplifier (type FEMTO DLPCA 200) needs to be free of shock and vibrations. It turned out, that we get the best performance if there is just a rigid BNC connector between the diode and the amplifier without a cable. In this test measurements, however, there was always a short cable between the diode and the amplifier.
A search for patterns in the light spectrum, for example by an auto-correlation method or a Fourier transformation revealed patterns in the Hz and sub-Hz regime. A Fourier transformation of the light intensity of a used and a new LDLS can be seen in figure 3.18. The older lamp, which has run for several months, has a 30% lower light output and shows distinct frequencies in the Fourier spectrum. The dominant frequency of about $f = 0.5\,\mathrm{Hz}$

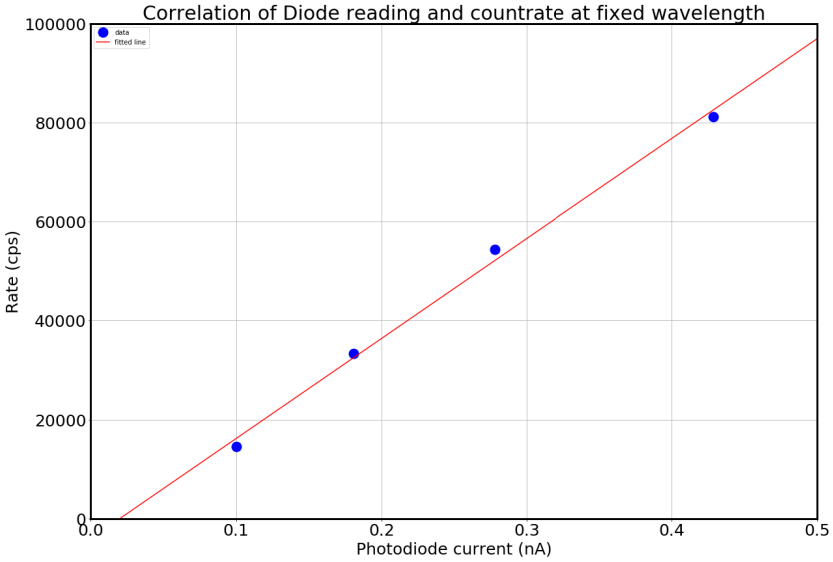

Figure 3.17: Electron rate of the e-gun over measured diode current. The slit width of the monochromator was changed to alter the amount of light going to the photocathode of the e-gun, while keeping the center wavelength of the UV-light constant at 265 nm. The measured rate of the e-gun is nearly proportional to the measured UV-intensity.

directly translates to the electron rate of the e-gun, which shows the same frequency in a Fourier analysis. When the same measurement was performed with a new LDLS, no distinct frequencies could be seen. From this, it is concluded that not only the absolute amount of electrons produced decreases over time, but also distinct features may occur. Since these are visible in the signal of the UV-diode and also in the e-gun rate they should be easy to identify if they reoccur in future measurements.

Work function: The work function of the e-gun can be determined with the so-called Fowler method, which is presented in chapter 5.4.2. For the measurement, the LDLS was used and the light intensity was measured with a photodiode[3] at the 10 % end of the 90:10 fiber splitter. The measured rate was normalized with the measured light intensity, taking into account the information of the diode efficiency from the manufacturer's website. The Fowler fit gives a work function of $\Phi = 4.02(3)\,\mathrm{eV}$. This value is very small compared to literature values of gold of 5.3 eV or higher [119], but it is within the expected range from previous investigations on e-gun work functions [139][12][11][145]. As mentioned earlier in this chapter, the vacuum conditions at the e-gun in this test setup are not ideal. The

[3]Thorlabs SM1PD2A,
https://www.thorlabs.com/thorproduct.cfm?partnumber=SM1PD2A

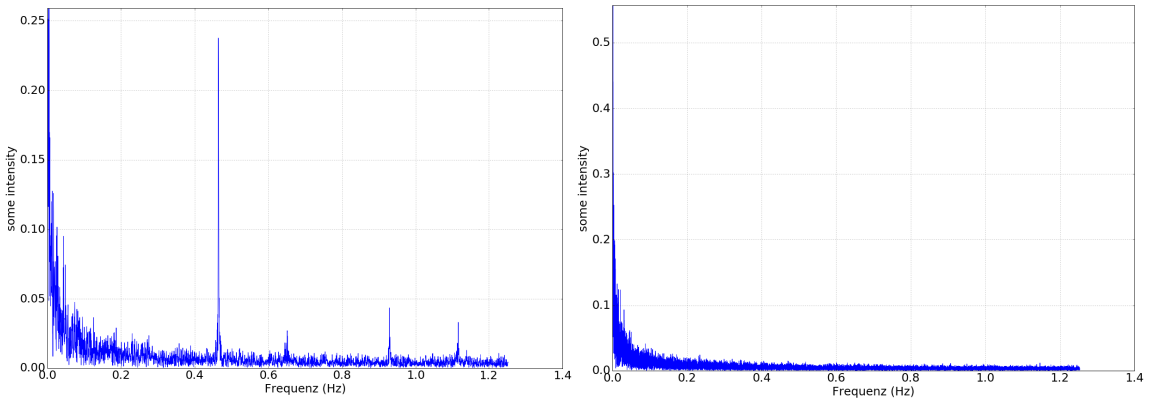

Figure 3.18: Fourier transform of the UV-light measured at the photodiode. **Left:** Measurement with an old LDLS, which has run for thousands of hours. **Right:** Same measurement with a new LDLS. The old LDLS shows distinct frequencies in the sub-Hz regime. These frequencies also show up in an e-gun measurement if this LDLS is used. In the measurement with the new LDLS no distinct frequencies can be seen.

system was pumped down for only a few days and there was no baking of the vacuum system or any other measure to clean the system. It can be expected, that a variety of molecules such as hydrogen, water, and carbohydrates are present on the surfaces. It is known, that surface contamination with gases like hydrogen, oxygen, or carbohydrates can change the work function of metallic surfaces [62][127].

3.6 Photoelectron gun in KATRIN:

The photoelectron gun (e-gun) is mounted at the upstream end of the KATRIN experiment and is part of the control and monitoring section (CMS), which is often called 'rear section' (RS). The rear section provides the vacuum system as well as the electric and magnetic field, which is needed to operate the e-gun.

3.6.1 Vacuum system

The major components of the vacuum system are the beam tube and two pump ports consisting of CF-150 Chambers and turbomolecular pumps (TMPs). In between the pump ports and also between the front pump port and the rear wall there are two apertures to reduce the gas flow. The rear wall itself also acts as an aperture for gas flow. The

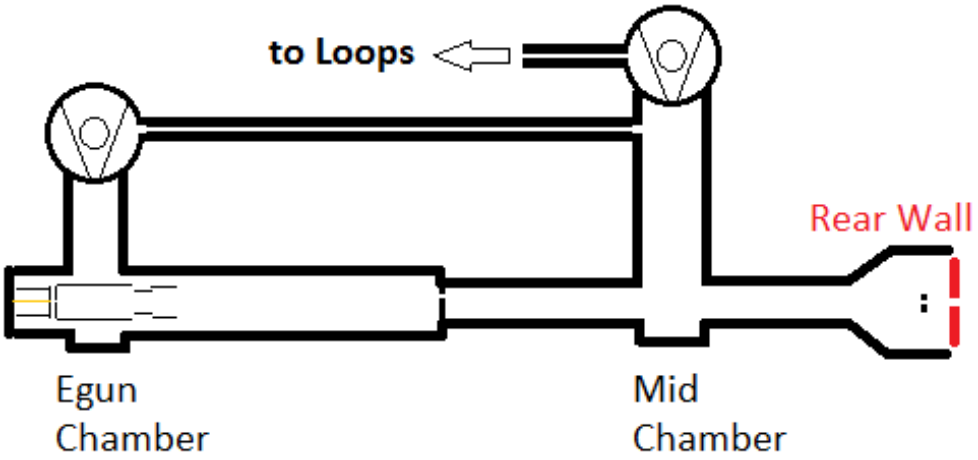

Figure 3.19: Schematic view of the vacuum system at the rear section. Only pipes with significant conductance are shown. The cylindrical electrode in the e-gun chamber has a grid of small holes at the top to ensure good pumping of gas at the e-gun.

exhaust side of the TMP above the e-gun chamber is connected to the mid chamber. The exhaust of the TMP above the mid chamber is connected to the outer loop system. In [7] a calculation shows, that in the mid chamber of vacuum pressure of 10^{-7} mbar can be reached assuming that both TMPs are of type 'Leybold Mag-W 600'. It was assumed that the pressure in the loops system would be 1 to 7 mbar [105]. Since the circulated gas is tritium, it has to be assumed that the partial pressure of tritium is a significant fraction of those 1 to 7 mbar. Since the compression factor of the TMP for hydrogen is only $3 \cdot 10^4$ [85], it is not realistic to reach a pressure of 10^{-7} mbar. Because of this, it was decided

to use a different TMP of type 'Pfeiffer HiPace 300' [101], which has a better compression ratio for hydrogen of $9 \cdot 10^5$. The replacement of the pump also required a redesign of the magnetic shielding of the pump.
The vacuum conditions at the e-gun should be as good as possible to improve the high voltage resistance and to minimize the creation of ions near the e-gun, which can cause a background effect or damage the thin gold cathode. In the measurement campaign in September 2018 the pressure near the e-gun was about

$$P_{\text{egun}} \approx 4 \cdot 10^{-7}\,\text{mbar} \qquad \text{(STS3a, Sept 2018)}. \tag{3.8}$$

Due to constant pumping the vacuum conditions improved by one order of magnitude in one year to

$$P_{\text{egun}} \approx 5 \cdot 10^{-8}\,\text{mbar} \qquad \text{(KNM2, Sept 2019)}. \tag{3.9}$$

The pressure gauge is mounted to a 1/4" tube above the e-gun chamber. The pressure at the e-gun might be lower than the value at the pressure gauge because of the better conductance to the TMP. The pressure gauge is not mounted near the e-gun because it creates ions that should not reach the e-gun.

3.6.2 Electromagnetic design of the rear section

The electromagnetic design of the rear section has two main tasks. First, it has to ensure that the electrons that are leaving the e-gun are adiabatically transported to the WGTS. This means, that the orbital momentum μ of the electron has to be conserved (see also chapter 2.3.2, equation 2.7). The second task is to remove ions and to make sure, that as few charged particles as possible hit the gold cathode of the e-gun, as this can create an unwanted background and also damage the e-gun.
To achieve this a magnetic design consisting of multiple solenoid coils and dipole coils has been developed and tested in the group of B. Monreal at UCSB and is described in [7]. The main idea is to protect the e-gun from neutral gas particles by blocking the direct line of sight from the e-gun to the source with an off-axis aperture and to remove charged particles with the $\vec{E} \times \vec{B}$ motion.
A schematic drawing of the coil positions in the rear section can be seen in figure 3.20. The magnetic field at the e-gun is mainly created by the booster coils. The magnetic field

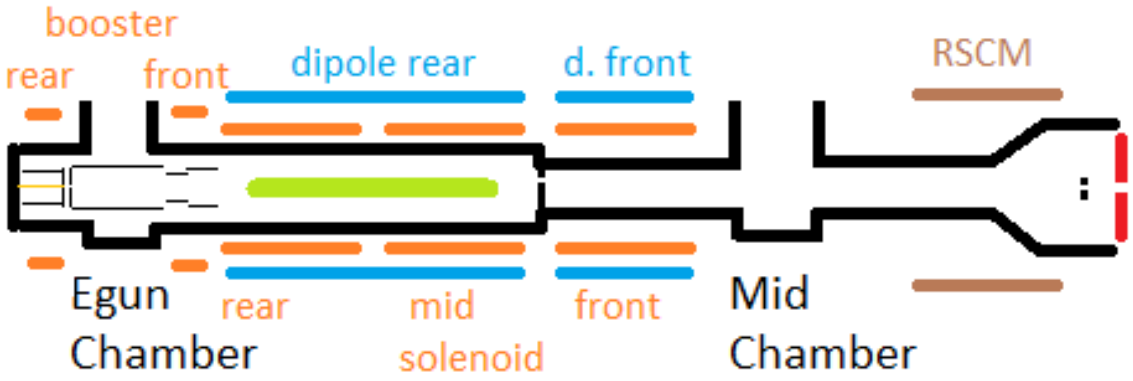

Figure 3.20: Electromagnetic design of the rear section (schematic drawing). **Orange:** Normal conducting solenoids provide the magnetic guiding field for the e-gun electrons. **Blue:** Normal conducting magnetic dipole coils move the beam. The rear dipole is needed to get the electrons through the off-axis aperture and the front dipole to get them back on the beam axis. **Green:** Electric dipoles for $\vec{E} \times \vec{B}$ drift. **Brown:** Rear section superconducting magnet (RSCM, identical to the magnets used in the DPS).

at the e-gun is about

$$B_{\text{egun, nominal}} = 25\,\text{mT} \tag{3.10}$$

with nominal settings. However, during the STS3a measurement phase, a reduced setting of only 75 % was used. This reduction of the magnetic field was needed for technical reasons (mainly due to the heat load in an electrical cabinet due to a malfunctioning fan).

For the future, it is recommended to increase the magnetic field to the nominal value to ensure adiabatic transport at all angles and energies used at the e-gun. The three normal conducting solenoid coils guide the electrons from the e-gun towards the mid chamber. The magnetic field is about 50 mT. From the mid chamber towards the rear wall, the magnetic field is dominated by the rear section superconducting magnet (RSCM), which produces a field of up to 4.7 T. Between the e-gun chamber and the mid chamber two sets of dipole coils, each with an x and a y component, can steer the beam. This is needed because there is an off-axis aperture in between. This aperture ensures, that there is no direct line of sight from the WGTS to the e-gun, and no tritium molecule can come towards the e-gun without multiple hits of the wall. The aperture has a diameter of 3 mm and is placed 10 mm above the normal beam axis. From the point of view of an electron going from the e-gun towards the rear wall, the rear dipole moves the electron upwards to pass through the aperture and the front dipole moves it back down again such that it can pass through the second aperture directly in front of the rear wall, which is centered on the beam axis. To remove charged particles, a set of dipole electrodes are mounted. The electrodes are mounted in such a way that the electric field points in y-direction. To minimize the current needed at the rear dipole coil, the polarization was chosen in such a way that the $\vec{E} \times \vec{B}$ motion is upwards. The speed of a particle due to this drift is given by

$$\vec{v}_{drift} = \frac{\vec{E} \times \vec{B}}{B^2}. \tag{3.11}$$

The electric field strength during STS3a measurements was

$$E = \frac{\Delta U}{d} = \frac{400\,V}{0.04\,m} = 10^4\,\mathrm{V/m}. \tag{3.12}$$

The design magnetic field is about $B = 50\,mT$, but in the STS3a measurement phase it was reduced to 75 % of this value. The distance d a particle is drifted in one pass through the dipoles depends on the kinetic energy of the particle. Neglecting relativistic effects it is given by

$$d_{drift} = v_{drift} \cdot t = v_{drift} \cdot \frac{l_{\mathrm{dipole}}}{cos\,\theta} \cdot \sqrt{\frac{m}{2}} \cdot \frac{1}{\sqrt{E_{kin}}} \propto \frac{1}{\sqrt{E_{kin}}}. \tag{3.13}$$

Here d_{drift} is the distance the particle is drifted, $l_{\mathrm{dipole}} = 700$ mm is the length of the dipole electrode, m is the mass of the particle, and E_{kin} the kinetic energy of the particle. Due to the small magnetic field at the rear section compared to the pinch magnet, the pitch angle θ of the electrons is $< 8°$ and causes an increase of the drift for electrons at high pitch angles of only 1 % compared to electrons with zero pitch angle, which is a negligible effect. For energies around 18.6 keV the energy dependent drift of the beam does not affect the

operation. A change of the electron energy of a few keV does not cause the beam to miss the aperture. For measurements with low electron energy, however, this effect becomes significant and the beam can easily get lost when the starting energy of the electrons is changed.

Typical settings for the rear section magnets: The rear section magnets guide the electrons from the e-gun towards the WGTS. The electrons have to pass through an off-axis aperture located between the dipole rear and the dipole front, and also through an on-axis aperture in front of the rear wall and the rear wall hole itself. The latter two are well aligned and can be treated as one aperture. The setting needed to guide electrons to the WGTS depends not only on the rear section geometry and the electron energy but also on the rear section superconducting magnet (RSCM) and the superconducting dipole coils on the rear side of the WGTS. For most measurements with the e-gun − for example the work function measurement (see chapter 5.4.6), the Eloss measurement (see chapter 4) and the column density measurement − the electrons do not need an angle relative to the magnetic field and the beam can be on axis in the beamline. For these measurements, a typical setting is given in table 3.2. During STS3a and KNM1 the normal conducting solenoids have been operated at 75 % of their nominal setting. This was only due to technical reasons and should be changed for future measurements. The currents of the dipole coils should be roughly proportional to the current of the solenoids to keep the ratio of the magnetic field components in x, y, and z direction constant. The magnetic field of the RSCM has been changed multiple times. The influence of the settings in the rear section is small but not negligible. The beam needs to be readjusted every time the RSCM setting is changed. The superconducting dipole coils of the WGTS can be used to steer the beam across the flux tube. These dipole coils exist at the rear and the front section of the WGTS, however, for technical reasons the rear ones are normally used. These dipole coils have a significant influence on the magnetic field in the rear section. The normal conducting dipole coils need to be adjusted if the beam is steered far away from the center. It is not possible to find a setting of the rear section which can be used for all pixels of the FPD. Using different fibers or changing the plate angle also changes the position of the electron beam. In STS3a only one fiber was used to avoid this issue. Changing the plate angle is needed to investigate the transmission properties for different electron angles. Since the e-gun plates rotate around the axis of the front plate, the back plate, and the position where the electrons are emitted from the fiber changes with the angle. This change is significant, but it is possible to find a setting such that all possible angles can be measured on a pixel without a change of the dipole coils in between these measurements. These settings depend on the setting of the superconducting dipole coils of the WGTS.

parameter	design value	value (STS3a, 20.09.2018)
back plate voltage		18.6 kV
front plate voltage offset		+4 kV
electron angle		$\approx 0°$
electric dipoles	$\pm$ 200 V	$\pm$ 200 V
RS solenoid rear	40 A	30 A
RS solenoid mid	35 A	26.25 A
RS solenoid front	35 A	26.25 A
rear booster coil	55 A	41.25 A
front booster coil	58 A	43.5 A
RS dipole rear x		-0.68 A
RS dipole rear y		0.28 A
RS dipole front x		-1.5 A
RS dipole front y		3.7 A
WGTS dipole rear		off
WGTS dipole front		off
KATRIN beamline		70 % B field

Table 3.2: Settings of the rear section. These settings transport the electron beam from the e-gun to the first pixel of the FPD. They work for almost all electron angles and in a back plate voltage range of several kV. For lower back plate voltages the current in the dipole rear y has to be lowered or even reversed. To reach outer pixels on the detector, the currents in the dipole coils need to be adjusted. It is not possible to find a setting that works for all pixels on the FPD.

Front plate offset voltage: The offset voltage of the front plate is set relative to the potential of the high voltage cage, which normally is equivalent to the potential of the MS vessel. The electric field that accelerates the electrons when they are emitted at the cathode is determined by the difference of the front plate offset and the back plate offset. In the first commissioning measurements, a voltage difference of only 2 kV was used. However, it turned out, that the transmission properties of the e-gun depend on this voltage. For this reason, the difference voltage was increased to 4200 V. With this setting the energy spread (which could result from an angular spread) was slightly narrower and also did not depend on the value of the front plate offset anymore in measurements with the zero angle setting. This gives a hint that a difference voltage between the front and the back plate of 4200 V is sufficient to achieve a good angular selectivity, whereas a value of only 2000 V is not. All dedicated measurements like the Eloss measurements are performed with a difference voltage of $U_{\text{front plate}} - U_{\text{back plate}} = 4200\,\text{V}$. However, it has to be said that this parameter

was not thoroughly tested due to time reasons and also because the broadening at higher angles which is described in 3.6.8 was not known at this point. It should be tested whether this broadening can be reduced by using a higher offset voltage between the front and the back plate.

3.6.3 Rate and rate stability

The e-gun is designed to perform precision measurements with high accuracy. For this, a high rate and good rate stability are required. The design goal of the e-gun was a rate of 20 kcps and a rate stability on the order of 0.1 %. As shown in figure 3.13, this was well achieved in the measurements at the test stand. The same measurement was performed in the STS3a measurement campaign, showing a much smaller rate than expected. This measurement, which is shown in figure 3.21, was performed with the LDLS as the light source of the e-gun and the FBM as the detector. In this hardware configuration, the e-gun is used with a standalone power supply. The electrons have an energy of about 18.6 keV and $\approx 0°$ angle. Since the FBM is located in front of the spectrometers, all electrons are transmitted to the detector. The rate was decreased a lot compared to the measurements at the test stand, where a monochromator slit width of only 3 nm was used. For the measurements in STS3a the slit width was increased to the maximum of 6 nm to increase the rate. Even with this measure, which increases the electron rate by a factor of 2, a rate of only 2.1 kcps was achieved. This is a factor 10 less than the design goal. The rate stability over the 10 hours of measurement time shows a small feature around the 2h mark, where the rate was increased by about 0.5 %. The strong decrease in rate can have many reasons. For example, a different fiber coupling had to be used to get into the second containment, and also a small modification to the e-gun was made when a distance plate was inserted to prevent a potential vacuum problem. This increases the distance of the fibers in the vacuum side from the CF-16 window by about one mm. However, these effects should be small and the main effect might be the significant increase of the work function, which is discussed in chapter 5.4.6.
One way to solve the rate problem is to use the UV-laser as a light source of the e-gun. As mentioned in chapter 3.3, the intensity of the laser can be changed by changing the diode current or by changing the angle of a $\lambda/2$ plate, as shown in figure 3.8. When the laser is used as a light source, the rate is not an issue anymore, because the power of the laser can be increased as much as needed. However, since the laser is a pulsed light source, systematic effects due to detector pile-up become an issue already at rates of about 7 kcps per pixel on the FPD. The rate was eventually set to about 8-9 kcps as a compromise between statistics and pile-up effects. Unfortunately, the option to use the $\lambda/2$ plate was not known to the operators at that time. For this reason, the diode current was used to control the intensity, which might lead to worse stability of the laser. A measurement of the rate stability with the UV-laser similar to the one with the LDLS can be seen in figure 3.22. The long term drift with the UV-laser is significantly larger compared to the long term drift with the LDLS. From this comparison, it is clear that the drift seen in the measurement with the

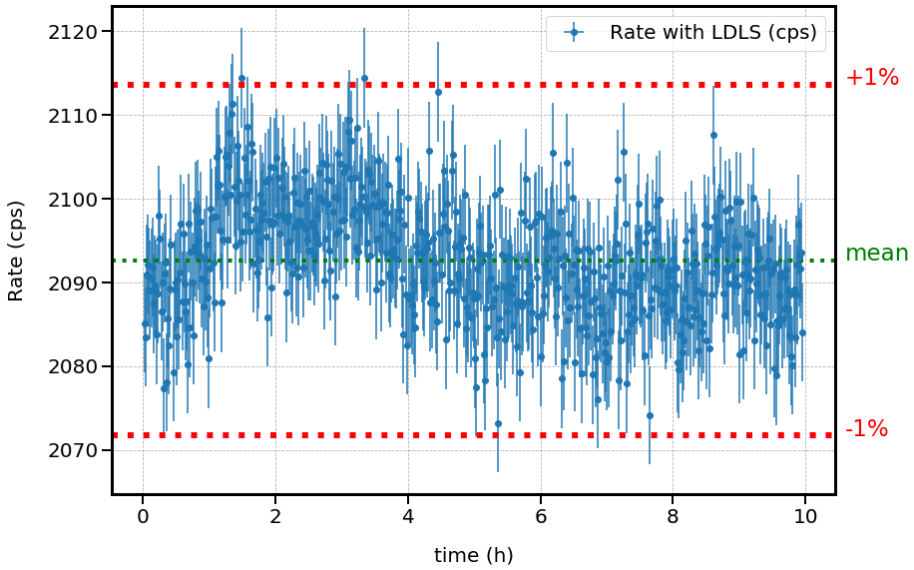

Figure 3.21: Rate stability measurement of the e-gun with the LDLS as the light source and the FBM as the detector. The plotted rate is the rate measured at the detector without any corrections (except for an energy cut at the detector). The rate is significantly lower compared to the measurements at the test stand. This increases the statistical noise. The data points have a 60s time binning. Around the 2h mark, a rate increase of 0.5 % occurs and diminishes two hours later. A long term trend is not visible.

laser is caused by the laser and not by other devices. The achieved rate stability in this setup is not sufficient for all the measurements. There are two possible ways to correct the rate fluctuations: The first way is to monitor the light intensity and to use this data in the analysis to correct the rate. The second possibility is to monitor the light intensity and to use this as a real-time feedback to a regulating device. This second approach is realized with the so-called noise eater. Due to technical problems, the noise eater was not used for important measurements in STS3a, but it is used in later measurement campaigns. The noise eater will be described in more detail in [121].

3.6.4 Voltage stability

The e-gun is a high precision tool to investigate the transmission properties of the main spectrometer and the energy losses in the source. For these measurements, it is crucial to have electrons with an adjustable and stable energy with respect to the retarding voltage of the main spectrometer. The starting energy of the electrons is determined by the wave-

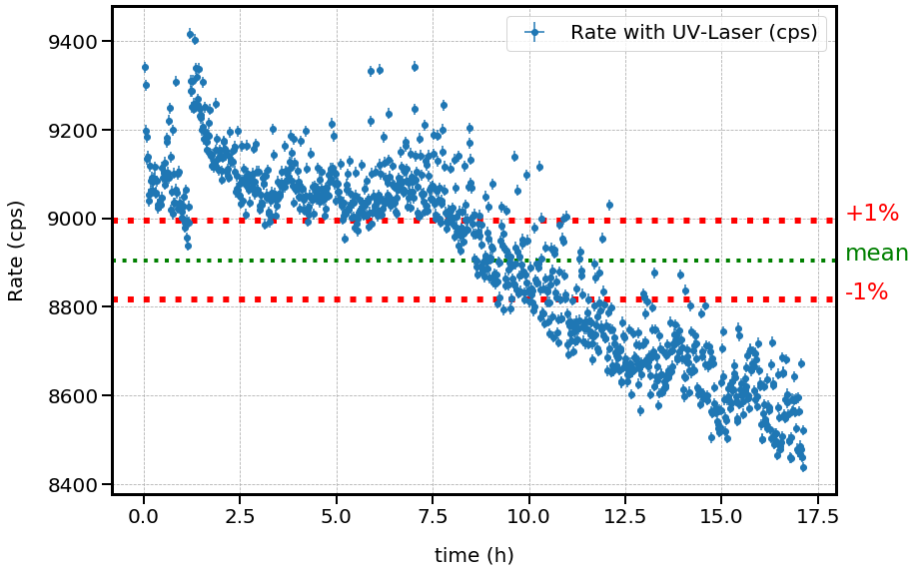

Figure 3.22: Rate stability measurement of the e-gun with the UV-laser as the light source and FBM as the detector. The plotted rate is the rate measured at the detector without any corrections, except for the standard ROI cut. A drift of the rate of several % can be seen as well as point to point fluctuations which are larger than expected if they were of statistical nature only.

length of the photons, the work function and the voltage applied to the back plate. The first two can be assumed to be stable over the time scale of a measurement, which can range from several seconds to several hours. The voltage, however, is not stable enough and needs to be monitored. For the e-gun measurements in KATRIN the absolute starting voltage of the e-gun electrons does not need to be known with sub-volt precision. The important voltage is the potential difference between the inner electrode system of the main spectrometer and the e-gun back plate. The voltage of the inner electrode system is the sum of the vessel voltage (typically around $-18400\,\mathrm{V}$) and an additional offset voltage of about $-200\,\mathrm{V}$. As mentioned in chapter 3.4, the e-gun is operated similarly to the inner electrode system. The inner high voltage cage of the e-gun is connected to the main spectrometer vessel. Additionally, a voltage of up to $\pm 500\,\mathrm{V}$ can be applied to the back plate. This means, that a voltage change in either the power supply of the e-gun back plate or the power supply of the inner electrode system causes a change in the surplus energy of the electrons. The offset voltage of the back plate was measured also with a dedicated voltmeter, however, the offset voltage of the inner electrode system was not. For the inner electrode only the read back value of the device is available.

To test the voltage stability the vessel was set to $U_{\text{vessel}} = -18.4\,\text{keV}$ and the inner electrode voltage to $U_{\text{IE}} = -200\,\text{V}$, which is the standard offset for the inner electrode. The back plate of the e-gun was set to a voltage such that about 50 % of the electrons are transmitted. In this setting a small fluctuation of the back plate voltage or the inner electrode voltage causes a large change of the measured rate. In figure 3.23 it can be seen, that drifts and jumps were observed. The change of the rate is in good agreement with the voltage changes measured by the inner electrode power supply. An investigation of the power supply after the measurement phase showed, that the power supply could measure voltages with 10 mV precision, but set voltages only with 40 mV steps. When the measured voltage is too far away from the setpoint, the device makes a 40 mV jump. As a consequence of these investigations a voltmeter to measure the voltage offset of the inner electrode system with better precision was installed for later measurement phases and also the power supply was changed after the KNM1 campaign.

Treatment of the energy instability: The energy stability is especially important if the measured function has a strong voltage dependence. This is, for example, the case for the transmission function of the e-gun, which is described in detail in the next section. One way to treat the energy instability, which acts as an error on the x-position of the data point, in a least χ^2 fit, is to convert the x-error into a y-error. To do this one can calculate the local derivative and multiply it with the x-uncertainty. As mentioned above, the voltage of the inner electrode system varies within a 40 mV window. The variance of a rectangular distribution is given by

$$V = \frac{1}{12}(a-b)^2. \tag{3.14}$$

With $a - b = 40\,\text{mV}$ a variance of $V = 133\,\text{mV}^2$ is obtained. Since the drift of the voltage is slow, this is only true for measurements of several hours. For shorter measurements, this overestimates the variance.

3.6.5 Beam diameter

The rear section e-gun is designed to provide an electron beam with a negligible width with respect to the dimensions of the KATRIN experiment. The spatial resolution of the measurements is limited by the size of the FPD detector pixels. The size and pixel distribution of the FPD can be seen in figure 5.19. The width of the outermost pixels is about 1.9 mm. From this one can easily conclude, that the e-gun beam can be targeted to any single pixel if the beam has a diameter of $d < 1.9\,\text{mm}$ in a magnetic field of $B_{\text{FPD}} \approx 2.49\,\text{T}$.

A measurement of the e-gun beam size has been performed with the help of the FBM

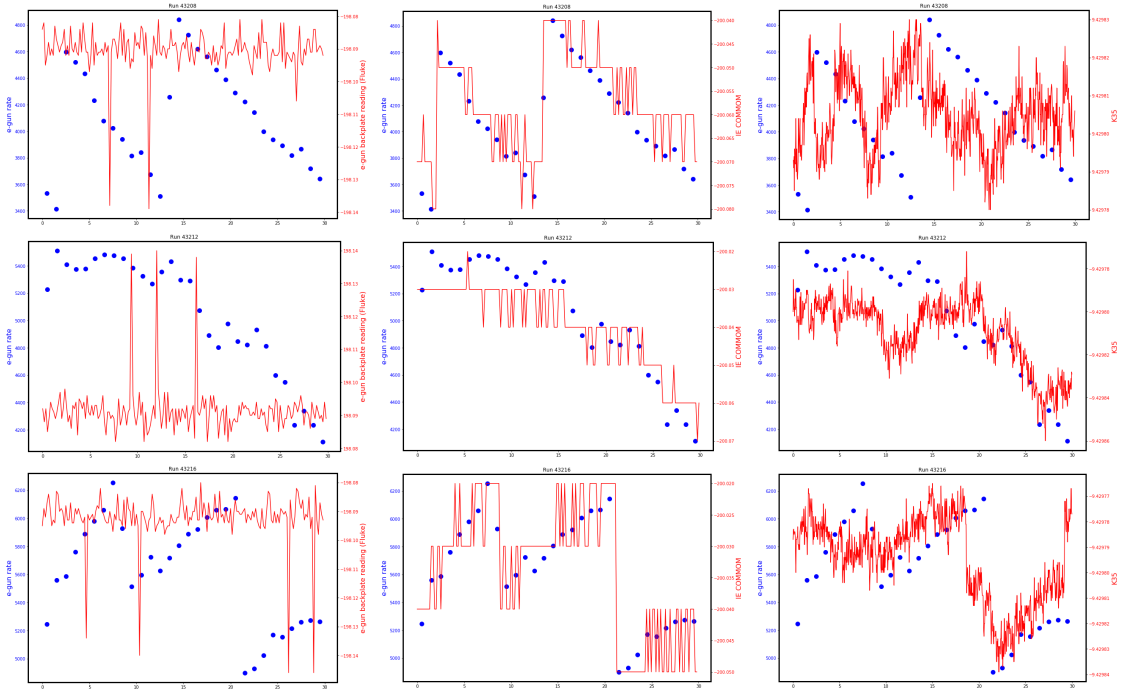

Figure 3.23: E-gun rate stability measurement. **Red line:** from left to right: E-gun offset supply, inner electrode power supply, K35 readout. **Blue points:** Rate measured at FPD. Rows: run 43208, run 43212, run 43216. The voltage measurement in the middle row has limited resolution, but it shows a clear correlation between the measured voltage and the rate. There is also some correlation with the K35 readout, which is expected because the K35 sees the combined voltage of the MS-vessel and the inner electrode system.

detector. The FBM is located in a magnetic field of $B_{\mathrm{FBM}} = 0.87\,\mathrm{T}$ and its diode has a diameter of $r_{\mathrm{diode}} = 0.6\,\mathrm{mm}$. While the e-gun beam was at a constant position, the FBM detector was moved in 0.1 mm steps and the rate was measured to see if the beam hits the diode completely or only in parts or not at all. This measurement was performed by E. Ellinger [27] and an upper limit on the e-gun beam size of $r \leq 0.1\,\mathrm{mm}$ in the magnetic field of the FBM was concluded. Since the magnetic field at the FPD is higher than at the FBM the beam can be narrower at the FPD, but not wider if the adiabatic motion is fulfilled. One can estimate the beam size at the FPD from the ratio of the magnetic field strength to

$$r_{\text{egun beam at FPD}} \leq 0.1\,\mathrm{mm} \cdot \sqrt{0.87\,\mathrm{T}/2.49\,\mathrm{T}} = 0.059\,\mathrm{mm}. \tag{3.15}$$

From this conservative estimation, one can see that the e-gun beam is narrower at the FPD than the width of any FPD pixel. This means that the requirement to have a narrow

beam is fulfilled and the size of the beam does not limit the spacial resolution.
For the beam size at the e-gun, with an assumed magnetic field of $B_{\text{egun}} = 0.75 \cdot 25\,\text{mT}$ $= 18.75\,\text{mT}$, an upper limit of

$$r_{\text{egun beam at egun}} \leq 0.681\,\text{mm} \tag{3.16}$$

can be estimated. However, here one has to consider the cyclotron motion of the electrons, which depends not only on the magnetic field but also on the e-gun plate angle and the energy of the electrons. An electron with an angle of 90° at the pinch magnet ($B_{\text{PCH}} =$ 4.2 T) has an angle of 3.83° at the e-gun ($B_{\text{egun}} = 18.75\,\text{mT}$). Assuming $v_\perp = v \cdot sin(3.83°)$ one can get a maximum cyclotron radius for 18.6 keV electrons near the e-gun of

$$r_{\text{gyro}} = \frac{m \cdot v_\perp}{|q| \cdot B_{\text{egun}}} = 1.52\,\text{mm} \tag{3.17}$$

with a conservative, non-relativistic calculation. The beam diameter and the maximum cyclotron radius combined result in a conservative estimate of the maximum effective beam size at the e-gun.

3.6.6 Transmission function

The transmission function $T(E, \theta)$ describes the transmission probability of electrons with a given surplus energy and angle. The width of the transmission function is determined by the angular spread of the e-gun in combination with the finite energy resolution of the spectrometer for electrons of different angles and energies, and by the broadening from the photoelectric effect. This effect depends on the work function of the gold cathode and the wavelength of the light but is independent of the electron energy and the energy resolution of the spectrometer. The position of the transmission function yields information about the potential in the spectrometer. The shape of the transmission function is important for the energy loss measurement because it needs to be deconvoluted from the measured data. The transmission function of the MAC-E filter for an isotropic source is described in chapter 2.3. The e-gun however, is not an isotropic, but an angular selective source with a small, but finite, angular spread. An analytical description of the such a transmission function is given in [11][12] and shown here for completeness in equations 3.18 to 3.22:

$$T(E, U_{\text{ana}}) = R_0 \cdot \int_E^\infty \eta(\epsilon) \int_0^{\theta_{max}} \zeta(\theta) d\theta d\epsilon + R_b \tag{3.18}$$

Here R_0 is the rate of the e-gun and R_b a general constant for the experimental background. E is the starting energy of the electrons and U_{ana} is the retarding voltage in the analyzing

plane of the main spectrometer. The electrons can only be transmitted if $E > U_{\text{ana}}$. The maximum angle is given by

$$\theta_{max}(E, U_{\text{ana}}) = \begin{cases} min\left(arcsin\left(\sqrt{\frac{E}{U_{\text{ana}}} \cdot \frac{2}{\gamma+1} \cdot \frac{B_{\text{start}}}{B_{\text{min}}}}\right), arcsin\left(\sqrt{\frac{B_0}{B_{max}}}\right)\right) & E > U_{\text{ana}} \\ 0 & E < U_{\text{ana}} \end{cases} \tag{3.19}$$

This general approach allows to describe the underlying distributions independently. In [11] the asymmetric energy distribution is described by a generalized normal distribution

$$\eta(E) = \frac{1}{\sqrt{2\pi}} \cdot \begin{cases} \frac{1}{\alpha_E} \cdot exp\left(-\frac{1}{2}\frac{(E-\hat{E})^2}{\alpha_E^2}\right) & (\kappa = 0) \\ \frac{1}{\alpha_E - \kappa(E-\hat{E})} \cdot exp\left(-\frac{1}{2\kappa^2} ln\left[1 - \kappa\frac{E-\hat{E}}{\alpha_E}\right]^2\right) & (\kappa \neq 0) \end{cases} \tag{3.20}$$

Here $\hat{E}$ is the mean energy and σ_α is the energy width. For $\kappa = 0$ this is a normal distribution. For $\kappa > 0$ the function is limited to $[0, \hat{E} + \frac{\alpha_E}{\kappa})$. The width α_E can be converted to an energy spread σ_E

$$\sigma_E = \frac{\alpha_E}{\kappa} \cdot \sqrt{e^{\kappa^2}(e^{\kappa^2} - 1)}. \tag{3.21}$$

The angular distribution is modeled by two normal distributions:

$$\zeta(\theta) = \frac{1}{\sqrt{2\pi}\sigma} \cdot \left[exp\left(-\frac{(\theta - \hat{\theta})^2}{2\sigma_\theta^2}\right) + exp\left(-\frac{(\theta + \hat{\theta})^2}{2\sigma_\theta^2}\right)\right]. \tag{3.22}$$

Fit function used in this work: To achieve the goals of the measurement phase, the determination of the MS work function and the energy loss measurement, it is not necessary to disentangle different contributions of the broadening. In addition to that the angle of e-gun plates are not well known and could not be set reproducible due to hardware problems with the motor. For these reasons, it is possible to assume that the electron angle is close to zero and to use a more empirical function for the description of the transmission function. The simplest possibility is to assume a normal distribution. Since the MAC-E filter is an integrating device, one has to integrate the distribution. The fit function then has the shape

$$F(x) = \frac{1}{2}\left(1 + erf\left(-\infty, \frac{x - x_0}{\sigma\sqrt{2}}\right)\right) + c, \tag{3.23}$$

where erf is the error function

$$erf(a,b) = \frac{2}{\sqrt{\pi}} \int_a^b e^{-x^2} dx. \tag{3.24}$$

and x_0 the position of the transmission function. For practical reasons, the lower integration bound in eq. 3.23 can be replaced with a finite number below the fitting interval. The resulting offset is absorbed in the constant c in the fitting process. This function, however, can not describe a possible asymmetry of the distribution and can also not cover a potentially steeper drop at the edges of the real transmission function. For this reason, a more general form of the underlying distribution is proposed in this thesis:

$$F(x) = bg + bg_{slope} \cdot x + \int_{-\infty}^{x} 2 \cdot A \cdot G(x', x_0, \sigma, l) \cdot \Phi(x', x_0, \sigma, k)\, dx \tag{3.25}$$

with

$$G(x, x_0, \sigma, l) = exp\left(\frac{-|x - x_0|^{2l}}{2\sigma^2}\right) \tag{3.26}$$

and

$$\Phi(x, x_0, \sigma, k) = \frac{1}{2} \cdot \left(1 + erf\left(-\infty, k \cdot \frac{x - x_0}{\sigma\sqrt{2}}\right)\right). \tag{3.27}$$

Here $G(x)$ is a modified version of a Gauss curve with a parameter l which describes the steepness of the function. For $l = 1$ we get the normal Gauss curve. Φ is a slightly modified version of eq. 3.25 with a skewness parameter k. The idea for this function was introduced in [98] in a different context. More recent measurements, after the first science run of KATRIN with tritium, have shown a small background rate, and also a slight increase of the rate already many σ below the transmission edge. For this reason, a background parameter bg and also a linear slope $bg_{slope} \cdot x$ were introduced. In this parametrization, the parameter σ is no longer a proper estimate of the width. Because of this, a new width W is defined as half the difference between the points x_1 and x_2 where a normalized version of the function with no background has a value of 15.865 % and 84.134 %:

$$F(x_1)/F(\infty) = 15.865\,\% \qquad F(x_2)/F(\infty) = 84.134\,\% \tag{3.28}$$

$$W = \frac{x_2 - x_1}{2} \tag{3.29}$$

This definition is chosen such, that if F(x) is the distribution function of a normal distribution as given in eq. 3.23, W is equivalent to the Gaussian width σ. The center of the function is defined as 50 % of the full height. Due to the asymmetry of the function

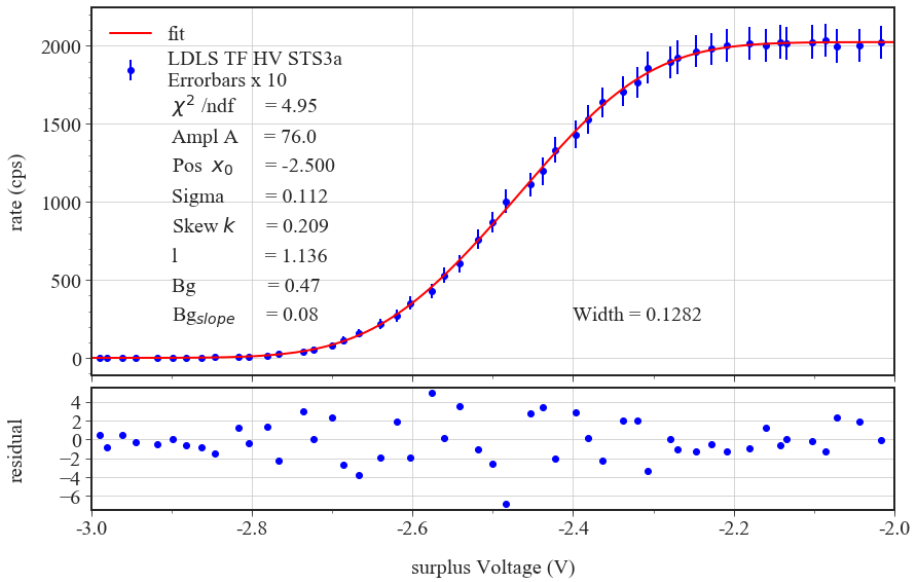

Figure 3.24: Measurement of the transmission function of the e-gun during STS3a. The error bars are enlarged by a factor of 10 for visibility. The used UV light source is the LDLS with a center wavelength of $\lambda = 250\,\mathrm{nm}$. The fitted width is $W = 0.128\,\mathrm{V}$. The large residuals on the transmission edge and the large reduced χ^2 can be explained by voltage instabilities. In this fit only the statistical error was taken into account. The magnetic field in the analyzing plane is $B \approx 1\,\mathrm{G}$.

introduced by the skew parameter k, this can slightly deviate from the fitted x_0 parameter.

The measurement of the transmission function is done by increasing the voltage at the back plate of the e-gun, which determines the electron energy. The surplus energy is defined as the difference between the voltage of the inner electrode system and the back plate of the e-gun.

$$\text{surplus voltage} = U_{\mathrm{IE}} - U_{\mathrm{Backplate}} \tag{3.30}$$

As mentioned before, there was no sufficient voltage readout of the inner electrode voltage in the STS3a measurement phase. For this reason the set value has been used, which is not optimal since a drift of the voltage supply during the measurement would lead to a broadening of the measured transmission function. A measurement of the transmission function with the LDLS is displayed in figure 3.24. The monochromator was set to a center wavelength of $\lambda = 250\,\mathrm{nm}$. The width $W = 128\,\mathrm{mV}$ at an electron energy of $18.6\,\mathrm{keV}$ shows that the e-gun can produce almost monoenergetic electrons and the design goal of $\sigma = 200\,\mathrm{mV}$ is fulfilled. If a normal distribution, as given in eq. 3.23, is fitted, instead of

eq. 3.25, the same width of $\sigma = 128\,\mathrm{mV}$ is obtained. The effect of the additional fitting parameters is small in this case since k and $l - 1$ are close to zero. As one can see, full transmission is already reached two volts below zero. This shift is caused by three different effects: The voltage drop in the analyzing plane, the work function difference between e-gun and main spectrometer, and an offset between the real value of the inner electrode power supply and the set value. For more details on this see chapter 5. The transmission function was also measured with the other available light source, the UV-laser. While the LDLS is a continuous light source with a wavelength centered around 250 nm and a width of $\pm\,3\,\mathrm{nm}$, the UV-laser is a pulsed light source, and has a wavelength of $\lambda = 266\,\mathrm{nm}$ with a negligible spread. The larger wavelength of the laser leads to a narrower energy distribution of the e-gun electrons. An exemplary measurement is shown in figure 3.25.

This measurement was repeated multiple times and gives a width of $W = 76 - 81\,\mathrm{mV}$. This spread in the fitting results, as well as the large residuals in the plateau region above the transmission edge, could result from the instability of the laser. Unfortunately, the monitoring diode did not work correctly in these measurements. The measured width is significantly smaller compared to the measurements with the LDLS, which consistently have a larger width of $W = 124 - 132\,\mathrm{mV}$.
These measurements show that the design goal of $W = 200\,\mathrm{mV}$ is fulfilled with either light source.

3.6.7 Zero angle

The e-gun is an angular selective, mono-energetic electron source. For practical operation it is important to find a setting where the produced electrons have a minimal angle relative to the magnetic field line. These electrons pass the source and the transport section of the KATRIN experiment traveling a minimal distance d, which is given by

$$d = \frac{l}{cos\,\theta} \tag{3.31}$$

with

$$\theta \propto arcsin\left(\sqrt{B/B_{ref}}\right) \tag{3.32}$$

in non-relativistic approximation. Here θ is the angle between the magnetic field $\vec{B}$ and the momentum of the electron $\vec{p}$. These electrons with $\theta = 0°$ have a minimal probability to scatter with gas, have the least losses due to synchrotron radiation and need the least kinetic energy to still pass a MAC-E filter with a given electric field, because they have no transversal energy.
To find the right setting with the e-gun the surplus energy of the electrons was chosen such

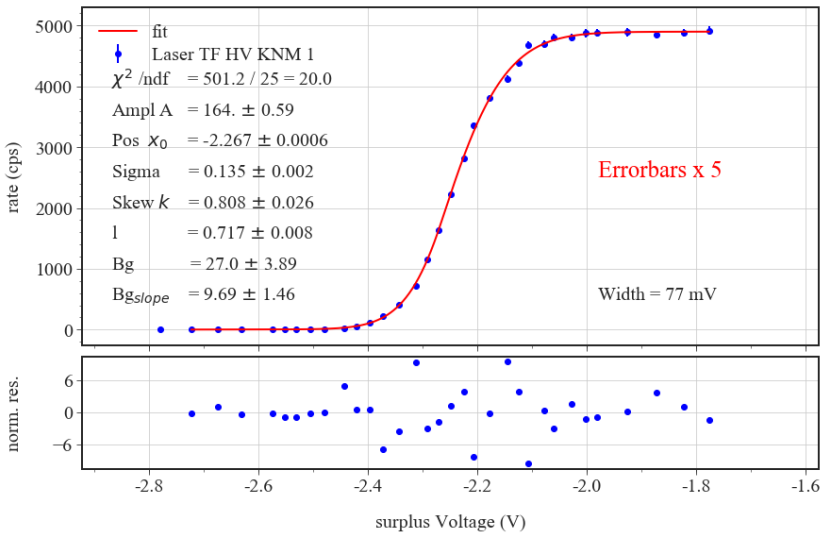

(a) Statistical errors only

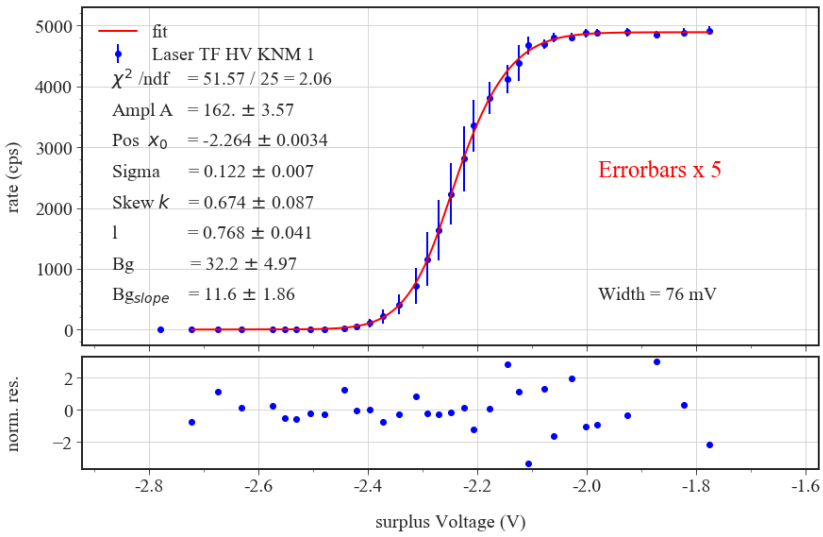

(b) Errors incl. voltage instability

Figure 3.25: Transmission function measurement at U=−18.6 kV with the laser as the light source. The measurement was performed at the beginning of KNM1. Both plots show the same measurement, but using different error estimations. Left: Statistical errors only. Right: Statistical errors and an assumed voltage uncertainty of $\sigma = 4\,\mathrm{mV}$. The voltage uncertainty increases the error bars at the steep part of the transmission function. The error bars in both plots are enlarged by factor 5 for better visibility. The width is calculated according to eq. 3.29.

that the electron rate was about half of the rate in full transmission. At this point the transmission function is very steep and sensitive to small changes of the voltage or the plate angle. If the plate angle of the e-gun is changed, the angle θ of the electron changes. If theta gets closer to zero, the rate gets larger. The maximum of the rate indicates the zero angle. In principle this has to be done only once. In practice, however, the stepper motor often loses steps, and also the mechanical setup probably has a small backlash. For these two reasons, the search of the zero angle has to be redone before important measurements if the angle has been changed in between. For this reason, the angle of the e-gun was not changed during the time of the Eloss campaign. With this simple but effective manual approach, the zero angle can be determined with about ± 500 motor steps, which equals, in a very rough linear interpolation, $\pm 0.5°$ electron angle in the pinch magnet.

3.6.8 Transmission function measurements with higher B-field and non-zero angles

The width of the transmission function consists of the width implied by the energy distribution of the electrons and the angular distribution of the electrons. The broadening inflicted by the angular distribution scales linearly with the magnetic field in the analyzing plane. Because of this, usually a magnetic field of about $B = 1\,\mathrm{G}$ in the analyzing plane is used for measurements with the e-gun. In this section, however, also measurements at a higher magnetic field of $B \approx 6.3\,\mathrm{G}$ are shown. Furthermore, also measurements far away from the zero angle are shown. Since the angular distribution is not centered around zero anymore, the range of angles gets increased by a factor of two, which leads to a broadening of the transmission function. Additional broadening can occur if the transport conditions in the beamline are not optimal. As mentioned earlier, the setup was run at a reduced magnetic field of only 75 % of the nominal B-field value in the rear section due to hardware problems.
The electric and magnetic field in the KATRIN main spectrometer should by design be symmetric around the beam axis. This means, that a measurement of the transmission function at different detector pixels, which are on the same ring of the detector, should give similar results for the position and the width of the measured transmission function. The results of such a measurement for three different pixels, which are all at the same ring of the detector, is shown in table 3.3. This measurement can also be used to estimate the broadening effect from the angular spread when these values, taken at $B = 6.3\,\mathrm{G}$ are compared to the one shown in figure 3.24, which is taken at $B = 1\,\mathrm{G}$. A detailed analysis of the magnetic field in the analyzing plane will be performed by F. Block [14] and is outside

the scope of this thesis.

Pixel on FPD	Center (V)	Width (mV)
89 (top-right)	-2.808 ± 0.004	146 ± 2
92 (top-left)	-2.779 ± 0.003	148 ± 1
95 (bottom-left)	-2.798 ± 0.007	147 ± 2

Table 3.3: Transmission function measurement with LDLS at different pixels which are all on ring 8 and in 90° angular distance on the detector. The pixel in the bottom right could not be measured for technical reasons. To estimate the uncertainty the error bars were scaled such that $\chi^2/ndf = 1$ for each fit. The width is identical within the errors, whereas the center position of pixel 92 is a bit low, which could be a hint for a slight misalignment. The increased width compared to figure 3.24 can be explained by the increased magnetic field of $B \approx 6.3\,\mathrm{G}$. This measurement was performed during KNM1 and using the spectrometer settings of the KNM1 neutrino mass measurements.

Angular selectivity: The rear section e-gun is angular selective. The pitch angle of the electrons with respect to the magnetic field lines can be changed by mechanically tilting the plates of the e-gun with a stepper motor. Five transmission functions, each measured at a different plate angle, are displayed in figure 3.26. The measurements were performed using the LDLS light source and the same magnetic field setting which was used in the KNM1 measurement phase. The magnetic field in the analyzing plane is $B \approx 6.3\,\mathrm{G}$, which corresponds to an energy resolution of 2.79 eV for an isotropic source. As can be seen in the plot, the position of the transmission functions changes with the motor position, which proves that the angular selectivity of the e-gun works. The top right edge of the cyan-colored transmission function at the largest angle and the bottom left edge of the red transmission function at zero angle match well with an overlaid isotropic transmission function, which indicates that in this e-gun measurement the whole angular range of electrons is covered. The width of the e-gun due to other effects of $\sigma \leq 130\,\mathrm{meV}$ is small compared to the width of the isotropic transmission function.
The measured transmission functions do also show that the width increases with the pitch angle. This is an unwanted feature that should be investigated. One reason could be that the magnets at the e-gun are operated with a lower magnetic field (see table 3.2). This was necessary for technical reasons but can be changed in the future. The individual fits to the five transmission functions are shown in figures A.1 to A.5. These measurements are a subset of measurements that were performed to investigate the magnetic field and a more detailed analysis of this measurement will be performed in [14].
According to the motor position, and assuming that the zero angle is set correctly, the center angle in the measurements should be approximately 0°, 30°, 45°, 60°, and 75°.

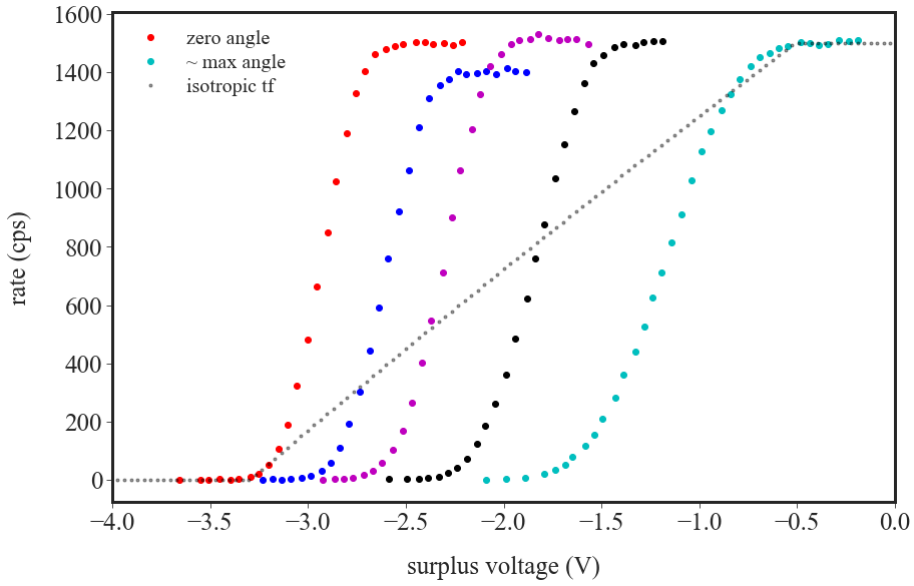

Figure 3.26: Measurement of the transmission function of the e-gun at different angles. The magnetic field settings are the same as in KNM1, which means about 6.3 G in the center of the analyzing plane. The red curve corresponds to zero plate angle, the cyan curve to almost the maximum plate angle. The black dotted curve is the transmission function for a monoenergetic, isotropic source. The width covered by the e-gun corresponds nicely to the expected width of the transmission function. This indicates, that the e-gun can cover the whole range of transmittable angles. According to the motor position the center electron angles in the pinch magnet should be roughly 0°, 30°, 45°, 60° and 75° from left to right.

Taking the first measurement as a reference, the other measurements show an additional broadening of 58 meV, 78 meV, 137 meV, and 239 meV, assuming that the broadening is added in quadrature.

Chapter 4

Energy loss due to scattering with D_2 molecules

4.1 General idea of electron scattering in KATRIN

KATRIN uses a windowless gaseous tritium source (WGTS) and performs high-precision spectroscopy of the β-spectrum generated by the decaying tritium nuclei. The tritium in the WGTS exists almost entirely in the form of T_2 molecules. If an electron passes through this tritium gas, it has a probability to scatter with the T_2 molecules, which can change the kinetic energy of the electron in a significant way. The possible excitations of a molecule can be grouped into two parts. One part are the rotational and vibrational excitations starting in the μeV and meV range, the other part are the electronic excitations with an energy of more than 10 eV. This energy is taken away from the electron, which leads to a deformation of the electron energy spectrum depending on the cross section for the interaction and the number of tritium molecules along the flight path of the electron. If no electronic excitation happens, it is called an elastic scattering in this work, whereas a scattering process with an electronic excitation of the molecule is called an inelastic scattering.
This part of this thesis is dedicated to the measurement of the energy loss (Eloss) of electrons due to scattering in the KATRIN WGTS using the electron gun described in the previous chapter. The measurements described in this chapter were performed in the STS3a measurement phase when the stable deuterium (D_2) isotope was used instead of the radioactive tritium. Measurements with tritium gas have been performed in later measurements and will be described in [121] and [112].

4.1.1 Response function

As mentioned in section 2.3.6 the transmission function of the MAC-E filter for an isotropic source is given by

$$T(E,qU) = \begin{cases} 0 & E-qU<0 \\ \frac{1-\sqrt{1-\frac{E-qU}{E}\cdot\frac{B_S}{B_a}\cdot\frac{\gamma_a+1}{\gamma_s+1}}}{1-\sqrt{1-\frac{B_s}{B_{max}}}} & 0\leq E-qU\leq\Delta E\ , \\ 1 & E-qU>\Delta E \end{cases} \tag{4.1}$$

where the index a denotes the analyzing plane and s the source.
The probability of an electron to lose a specific amount of energy ΔE in a single scattering event can be described by an energy loss function :

$$f(\Delta E) = \frac{1}{\sigma_{tot}}\frac{d\sigma}{d\Delta E}, \tag{4.2}$$

where σ denotes the cross section. We normalize this function such that

$$\int_0^{E/2} f(\Delta E)d\Delta E = 1. \tag{4.3}$$

The probability for n-times scattering is given by

$$P_n(\mu) = \frac{\mu^n}{n!}e^{-\mu}. \tag{4.4}$$

Neglecting angular changes in the scattering process, the response function is then given by [134]

$$R(E,qU) = \int_0^{E-qU} T(E-\epsilon,qU)\cdot(P_0\delta(\epsilon)+P_1 f(\epsilon)+P2(f\otimes f)(\epsilon)+...)d\epsilon \tag{4.5}$$

with the transmission function T, die scattering probabilities P_i and the energy loss function $f(\epsilon)$. The convolution integral is given by

$$(f\otimes f)(\epsilon) = \int_0^{E/2} f(\epsilon-\epsilon')\cdot f(\epsilon')d\epsilon'. \tag{4.6}$$

4.1.2 Details on scattering in KATRIN

The parameter μ in equation 4.4 is a product of the cross section σ_{tot}, the gas density ρ and the traveling distance of the electron through the source $d/cos(\theta)$. The angle θ depends on the magnetic field and transforms as [59]

$$\theta(B) = arcsin\left(sin(\theta_i)\sqrt{\frac{B}{B_i}}\right), \tag{4.7}$$

where the index i denotes an initial condition. The density has to be integrated along the flight distance [134]

$$\lambda(z,\theta) = \frac{1}{cos(\theta)}\int_z^{z_2}\rho(z')dz', \tag{4.8}$$

where ρ is the gas density at a position z and the integration goes from the start position of the electron z to the end of the gas column z_2, which, in the case of KATRIN, is in good approximation the end of the WGTS. The parameter μ can now be written as

$$\mu = \sigma \cdot \lambda(z,\theta). \tag{4.9}$$

The inelastic cross section $\sigma_{inel}(E)$ has an energy dependence as can be seen from the electron inelastic total cross section in the Born-approximation for high energy [86] for hydrogen:

$$\sigma_{inel}(E) = \frac{4\pi a_0^2 R}{T}\left[M_{tot}^2 \cdot ln\left(4\,c_{tot}\frac{T}{R}\right) + \delta_E\right] \tag{4.10}$$

Here R is the Rydberg energy

$$R = R_\infty \frac{1}{1+\frac{m_e}{m_H}} = 13.598\,\mathrm{eV}, \tag{4.11}$$

with the Rydberg constant

$$R_\infty = \frac{m_e e^4}{8\epsilon_0^2 h^3 c}. \tag{4.12}$$

The Bohr radius a_0 is given by

$$a_0 = \frac{4\pi\epsilon_0\hbar^2}{m_e e^2} = 5.29177... \cdot 10^{-11}\,\mathrm{m} \tag{4.13}$$

and the non-relativistic energy T by

$$T = \frac{1}{2} m_e \beta^2, \tag{4.14}$$

which gives a value of T ≈ 17608 eV at the tritium endpoint. From [86] we get

$$c_{tot} = 1.18, \tag{4.15}$$

and a relativistic correction near the tritium endpoint of

$$\delta_E = -0.0097. \tag{4.16}$$

For the sum of the dipole transitions from the initial to all other states the paper gives a value of

$$M^2_{tot}[\mathrm{H_2}] = 1.5487. \tag{4.17}$$

From [80] we deduce that $M^2_{tot}[\mathrm{D_2}] \approx 0.994 \cdot M^2_{tot}[\mathrm{H_2}]$ and $M^2_{tot}[\mathrm{T_2}] \approx 0.991 \cdot M^2_{tot}[\mathrm{H_2}]$. Neglecting the isotopic dependence on c_{tot} we get an estimate on the inelastic cross section near the tritium endpoint of [50]

$$\sigma_{inel}[\mathrm{D_2}] = 3.647(22) \cdot 10^{-18}\,\mathrm{cm}^2 \tag{4.18}$$

and

$$\sigma_{inel}[\mathrm{T_2}] = 3.637(22) \cdot 10^{-18}\,\mathrm{cm}^2. \tag{4.19}$$

4.2 Energy loss measurement on deuterium in STS3a

The basic idea of this measurement is to shoot electrons generated by the e-gun through the WGTS and to measure those electrons with the main spectrometer and the FPD. In case of an empty source, this is the same as a transmission function scan with the e-gun as described in the previous chapter. The e-gun is used with zero plate angle and with the UV-laser as the light source. The electrons travel along the center axis of the beam tube and hit the detector on one of the bullseye pixels. For an optimal energy resolution of the spectrometer, an air-coil setting with a small magnetic field of only $B = 1\,\mathrm{G}$ in the analyzing plane is used.
In our measurement, we change the energy of the electrons within a 60 eV range near the tritium endpoint, and neglect the slight energy dependence of the inelastic cross section

given in equation 4.10. It is assumed that all electrons from the e-gun travel through the whole source with a negligible angle θ. Equation 4.9 can then be simplified to

$$\mu = \rho \cdot d \cdot \sigma, \tag{4.20}$$

because the measurement is only sensitive to the number of molecules along the whole distance d, but not to the z-dependence of the gas profile. The density ρ is in this case the mean density in the 10 m long WGTS, assuming no radial dependence of the gas profile. The amount of deuterium gas in the WGTS is set with a pressure control buffer vessel in the loop system. Also, a flow meter measures the amount of gas streaming through the capillary towards the inlet at the center of the source tube. The column density was estimated based on these settings and gas flow simulations. These numbers have large uncertainties, especially at low column densities. The parameter μ, which can only be determined in the analysis after the measurement, gives a good indication of what the column density actually was.

4.2.1 Integral measurement

In the integral measurement, the voltage of the main spectrometer is constant, and the energy of the electrons from the e-gun is linearly increased from about 5 eV below the transmission edge up to 55 eV above the transmission edge and back down again with the same voltage ramp of 33 mV/s as can be seen in figure 4.1. The transmitted electrons are counted by the FPD. If this measurement is performed with 0 % of the nominal column density (CD), the measurement is equivalent to a transmission function measurement of the e-gun. This measurement can be used as a reference for the width of the transmission function and also for any potentially energy dependent effects like the counting efficiency of the detector. To minimize pile-up effects on the detector, the UV-laser was used with the highest possible repetition rate of 100 kHz and a low diode intensity to limit the rate to below 10 kcps. With only 0.1 electrons per pulse on average, the probability of higher multiplicities is small and problems due to pile-up are not expected. In STS3a the Eloss measurements with these settings were performed with about 0 %, 15 %, 50 % and 100 % of the nominal column density, based on estimations from the pressure and flow measurements. The analysis presented later in this chapter gives a strong hint, that the real column density in the "15 % CD" measurement was actually only about 6 % of the "100 % CD" measurement. So, these numbers need to be taken with care. The 15 % CD setting will, therefore, be referred to as 6 % measurement.
Similar measurements have been performed in the past at the Troitsk neutrino mass experiment [5][1].

4.2.2 Time of flight method

The idea of the time of flight (ToF) method is to generate a quasi differential spectrum by using additional information about the time of flight of the electrons [15]. The usage of this method was proposed by C. Weinheimer [144] and demonstrated by C. Rodenbeck [111]. The main spectrometer acts as a high pass filter and rejects all electrons which cannot pass the analyzing plane. With a time of flight cut, which only accepts electrons with a long time of flight, meaning little surplus energy in the analyzing plane, one ends up with a signal of only those electrons which barely make it past the analyzing plane. In other words, the time of flight cut acts as a low pass filter which effectively differentiates the integral spectrum. To implement this method, the repetition rate of the laser is decreased to $f = 20\,\mathrm{kHz}$ and a timing signal is sent from the laser to the FPD via an optical cable. The delay from the signal going to the laser and the one going to the detector DAQ is estimated to be 930 ns. The flight time of an electron from the e-gun to the spectrometer is of order 1 ns and can be neglected. The counted events from the FPD are filled into a histogram with the time since the start of the measurement (or the voltage of the e-gun) on the x-axis and the arrival time modulo $T = 1/f = 50\,\mu\mathrm{s}$ on the y-axis. The time of flight cut applied to this data rejects all electrons with a flight time below a certain threshold, for example $30\,\mu\mathrm{s}$, and it also rejects electrons with flight times above $50\,\mu\mathrm{s}$. The latter is an unwanted effect that decreases the statistics a bit.

4.2.3 Measurement and data handling

The Eloss measurements of STS3a have been performed after the e-gun commissioning, which is described in chapter 3.6.3 ff. The plate angle of the e-gun was set in such a way that the electrons are emitted under 0° and the air coils of the main spectrometer were set such that the magnetic field in the analyzing plane is as low as 1 Gauss to have an optimal energy resolution. Important parameters for operation are listed in table 4.1.
The voltage ramping was done in a continuous way with a constant ramp up and then again a ramp down with the same ramping speed. One ramp takes 30 minutes. The measurement was performed for 12 hours resulting in 12 up and 12 down scans. In the end, all runs are stacked to increase the statistics. The alternating ramp cancels out linear drifts during the measurement. The voltage ramp was fitted to determine the slope. This slope was then used to convert the time of the measurement to a voltage. This procedure has the advantage that it is robust against missing data points due to network problems, which sometimes occurred during the measurement. An example plot is shown in figure 4.1. Such a fit is performed for every measurement. Comparisons of different runs, for example of up and down scans, show no significant differences. For the analysis the mean

parameter	value	comment
back plate voltage	-18570 to -18630 V	IE at -18575 V
front plate offset	+4200 V	
rear section dipoles	± 200 V	
electron angle	0	
light source	UV-laser	
solenoid rear	30 A	all e-gun magnets
solenoid mid	26.26 A	at 75% nominal field
solenoid front	26.26 A	
booster coil rear	41.27 A	
booster coil front	43.52 A	
WGTS dipole x	0 A	
WGTS dipole y	0 A	
DPS electrodes	-15 V / -5 V	same for all four
ring electrodes	+50 V	same for all four
beamline magnets	70 %	same as KNM1
air coils	1 G	optimal energy resolution
IE common	-200 V	
steep cone offset	+40 V	
post regulation	active	
post acceleration	+10 kV	

Table 4.1: Settings used for Eloss measurements.

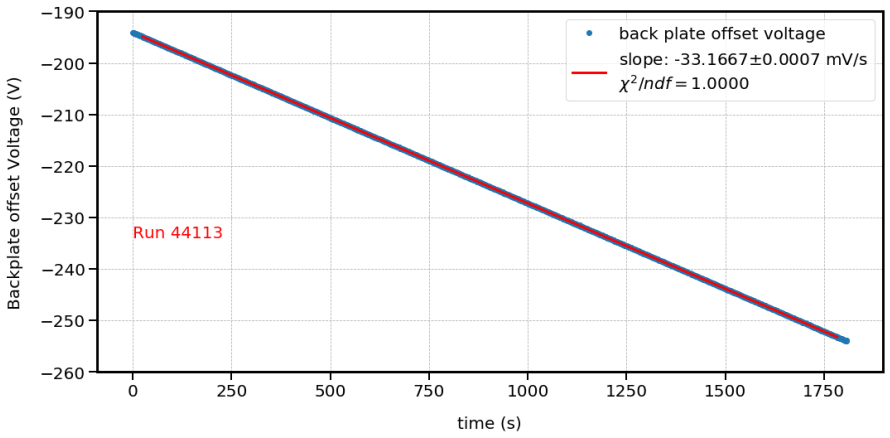

Figure 4.1: Voltage ramp of one run during the Eloss measurements. To estimate the error on the fitted slope, the error on the data points was chosen such that $\chi^2/\text{ndf} = 1$. For the analysis of the Eloss measurements, we assume that the voltage ramp is linear.

value of all 24 slopes in this data set is used.

ToF cut: A time of flight cut removes all events that are outside the chosen time of flight window of 30 μs to 50 μs. The 50 μs correspond to the repetition rate of the laser. The 30 μs are a compromise between resolution and statistics. A longer cut, for example 35 μs, results in a better resolution, but also in a loss of statistics. If the window is larger, for example in a 25 μs cut, the 0-peak, which is basically the differential version of the e-gun transmission function discussed in the previous chapter, has a flat top and can not be properly described with a Gauss function. A comparison of the effect of these three different ToF cuts is shown in figure 4.3 and in table 4.2.

Data handling: To create the ToF data set the data is filled into a histogram with one-second bins. The peak position of the zero loss peak is fitted for every scan and then all scans are stacked together in such a way that the zero loss peak position is matched. Since the shifting is done only with integer numbers of bins, this introduces a small broadening of the final data set, which is taken into account in the analysis, because the zero loss peak is deconvoluted from the Eloss data. The x-axis is shifted to have the zero loss peak at zero volt.

The obtained data is displayed in figure 4.2 for a 30 μs cut. This data was used for the analysis. Figure 4.3 shows how the 0-peak, which is much narrower than the energy loss function, is affected by different time of flight cuts. Figure 4.4 shows a fit of the transmission function to the 0-peak with the 30 μs cut. As can be seen, the peak is asymmetric and the skew factor k takes a large value of 1.4. The reduced χ^2 is a factor of 10 better compared

ToF cut (μs)	FWHM 0-peak (mV)	Amp. 0-peak	Bg rate (mcps)
25	497	12997	137.0
30	273	10810	91.1
35	225	6380	60.5

Table 4.2: Comparison of different ToF cuts. Bg is the mean rate in the region between the 0-peak and the 1a-peak. FWHM is the full width at half maximum of the 0-peak. For the 0-peak with 25 μs cut a Gauss fit is not suitable and the FWHM is read from the data points. For the other cuts, the FWHM is calculated from a Gauss fit. Amp. is the maximum event rate in a one-second bin, similar to the amplitude of a Gauss curve. The error on the width is a few % because a Gauss fit is not a very good description. The 0-peak is asymmetric and not as tail heavy as a Gauss curve. Nevertheless, these numbers give a good impression on the effect of the ToF cut. For the final analysis the 30 μs cut is used.

to a normal Gauss curve. For the analysis of the Eloss data, the data points are used and not this fit.

Background: The region between the 0-peak and the 1a-peak can be used to estimate the background rate, because there are no molecular excitations in this region. The background can be caused by the standard Rydberg and radon background in the KATRIN main spectrometer, by additional ionization by the electron beam, by the intrinsic background from the FPD, by cosmic muons hitting the FPD or by background directly from the e-gun, for example by field emission or from ion impact on the photocathode. The data displayed in figure 4.5 shows a mean background rate of $Bg = 0.091\,\mathrm{s}^{-1}$. This background rate is no threat to the measurement and is treated as a constant in the analysis. If the measurement is performed with tritium instead of deuterium, the background increases significantly and needs a more detailed description. A more detailed investigation of the background in Eloss measurements with tritium see [112].

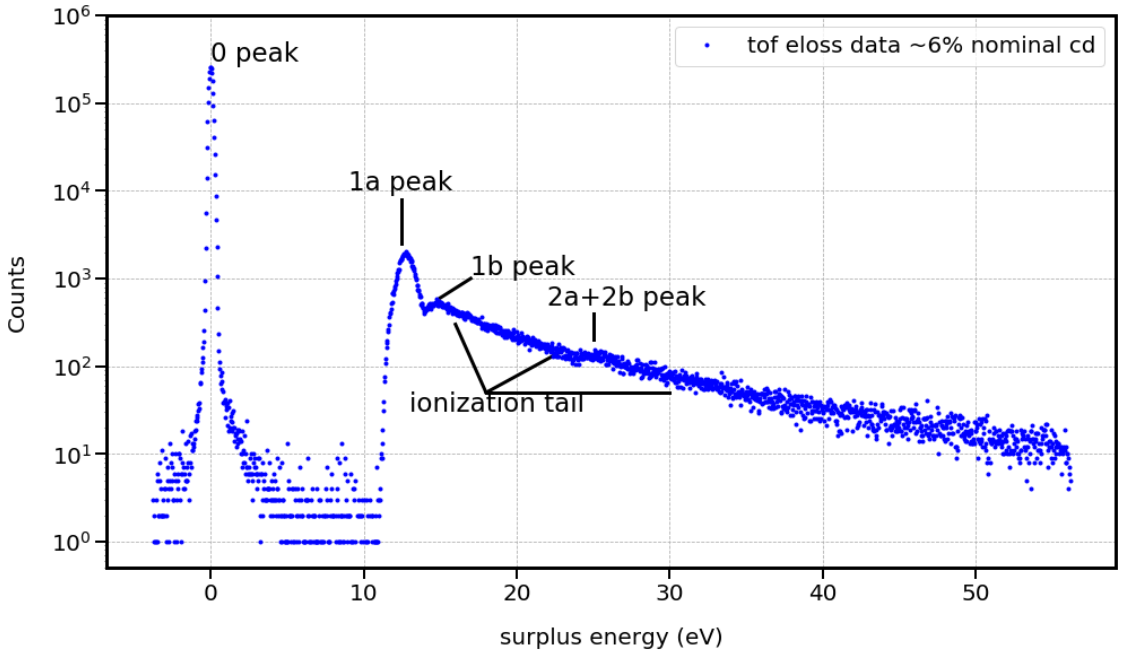

Figure 4.2: Data of ToF Eloss measurement after stacking and 30 μs to 50 μs ToF cut. The measurement was performed on D_2 gas with about 6 % of the nominal column density. The data set consists of 24 individual scans, 12 upwards and 12 downwards. The 0-peak corresponds to the transmission function of the e-gun. In this data set additional broadening is caused by the stacking procedure and possibly also by elastic scattering, which could not be resolved but might increase the width of the peak a bit. The $1a$ and $1b$ peak are caused by electronic excitation of the D_2 molecule. The width is caused by the different electronic levels and also the rovibrational states which can also be excited. The $2a + 2b$ peak is caused by electrons that have scattered twice. Its position is at double the energy of the 1-peak. Above the ionization energy of $E_{ion} = 15.467\,\text{eV}$ [65] a continuum of states exists which forms the ionization tail.

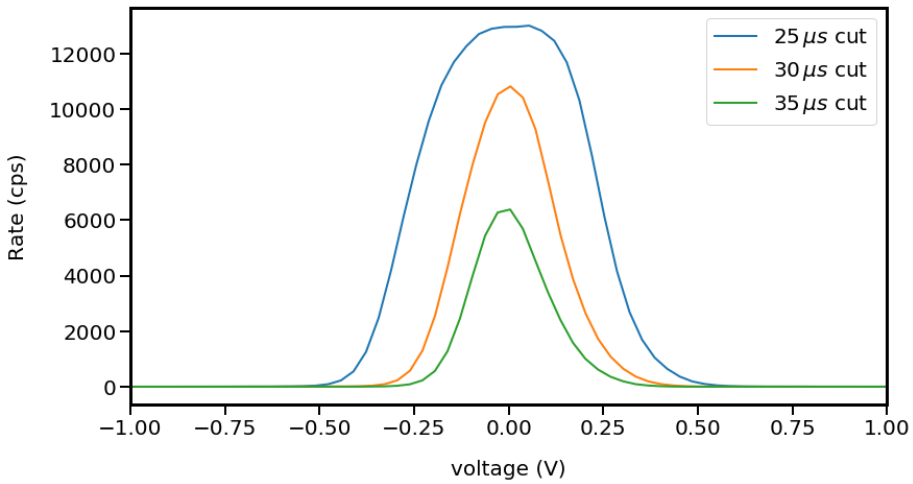

Figure 4.3: 0-peak plotted for different ToF cuts. If the minimum flight time is below 30 μs the 0-peak becomes wider and has a flat top. If the minimum flight time becomes larger than 30 μs the peak becomes a bit more narrow, but also a lot of statistics is lost. The analysis in this work is performed with the 30 μs cut.

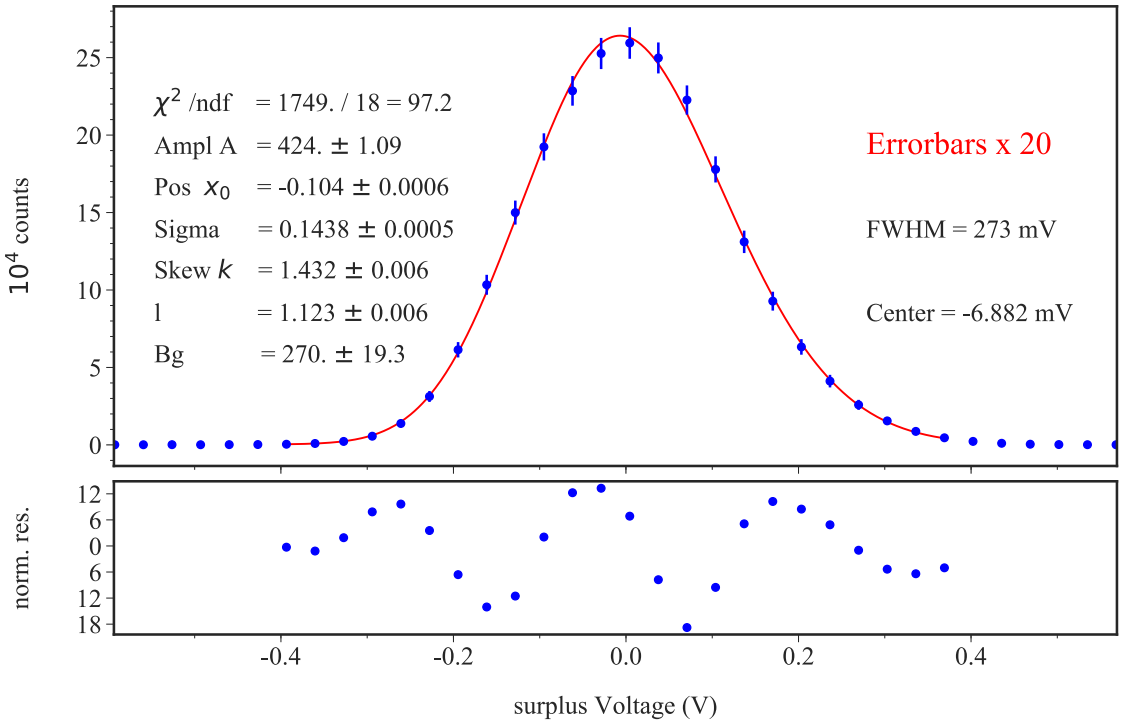

Figure 4.4: 0-peak with 30 μs ToF cut and the integrand of eq. 3.25 fitted to it. Errorbars are statistics only and are enlarged by a factor of 20 in the plot for better visibility. This fit is only for illustrational purpose and is not used for the Eloss analysis. The χ^2 / ndf of this fit function is a factor of 10 better compared to a Gauss curve. The right side shoulder of the curve does not drop as fast as the left side. In the fit this leads to a large skew factor of $k = 1.43$. For this reason also the value of x_0 deviates by 100 mV from the center, which is defined as the maximum of the curve.

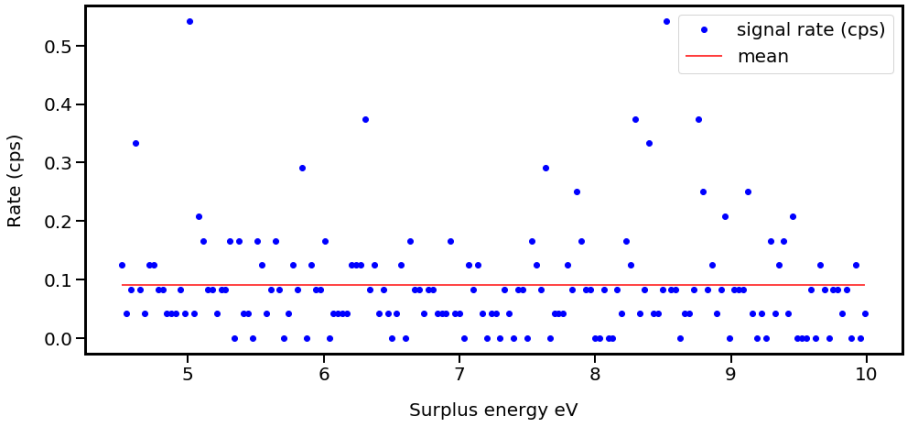

Figure 4.5: Zoom into the region between the 0-peak and the 1a-peak. In this region no signal from scattering is expected. This data is a good indicator of the background rate of the measurement. The mean background rate with a $30\,\mu s$ ToF cut is $Bg = 0.091\,\text{cps}$. The background is not considered an issue for this analysis and is treated as a constant, even though later investigations, see [112], show that the background rate might be about 15 % higher at high surplus energies at this column density.

Handling of integral data: The data handling for the integral measurements is performed by L. Schimpf [121]. Similar to the ToF data, in the integral mode, the data is stacked in such a way, that the transmission edges (the steep rise on the left side) are stacked on top of each other. For the error bars of the data points, a voltage smearing is taken into account, very similar to the description in chapter 3.6.4. This affects mainly the error bars on the transmission edge at $E_{surplus} \approx 0\,\mathrm{eV}$, where the function is the most steep. Without this correction, the χ^2 is dominated by the fluctuations in this part. The bin width is 3 seconds ($\approx 100\,\mathrm{mV}$), which is three times larger compared to the ToF data. The integral measurements have been performed with four different gas densities: Empty source, 6 %, 50 %, and 100 % of the nominal column density. The data is normalized such that the transmission probability is 100 % for large surplus energy. The data sets are displayed in figure 4.6. Due to the lower rate of the e-gun of only $R \approx 8\,\mathrm{kcps}$ and the high laser repetition rate of $f = 100\,\mathrm{kHz}$ pile-up-like effects should not be an issue. However, one can see a slight overshoot at $0\,\mathrm{eV}$ in the data. This indicates, that the pile-up correction has a small systematic effect at the transmission edge, where a lot of electrons with little surplus energy and long flight times occur.

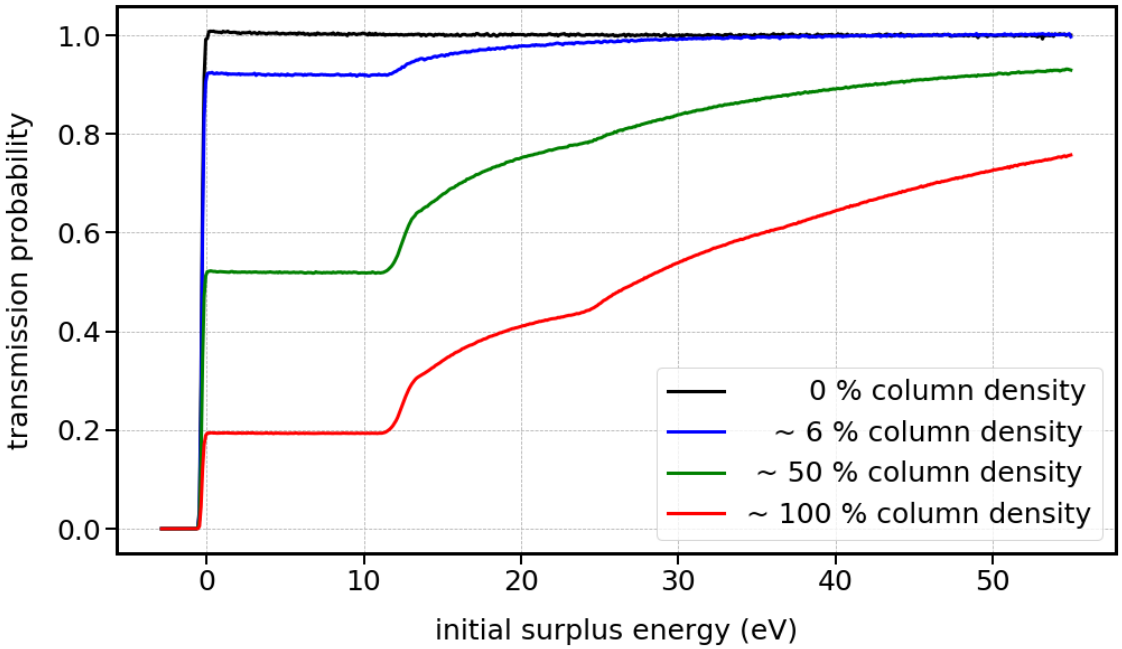

Figure 4.6: Data sets of the integral Eloss measurements. The black curve is used as a reference with an empty source. The steep rise at $\approx 0\,\mathrm{V}$ is the transmission function described in the previous section. It is equivalent to the 0-peak in the ToF data and shows the good energy resolution of the setup.

4.2.4 Novel parametrization for energy loss model with BED ionization tail

The energy loss function of deuterium and tritium has been measured before [5][1]. Those groups used a combination of a Gaussian and a Lorentz curve to fit their data:

$$L(\epsilon) = Norm \begin{cases} A \cdot exp\left(-\frac{2(\epsilon - P_1)^2}{W_1^2}\right) & , \epsilon \leq \epsilon_c \\ \frac{W_2^2}{W_2^2 + 4(\epsilon - P_2)^2} & , \epsilon > \epsilon_c \end{cases} \tag{4.21}$$

This parametrization is not suitable for KATRIN purposes, because we can resolve a double peak structure, labeled 1a and 1b in figure 4.2, which can not be described by this parametrization. Also, the left side of the 1a-peak has almost no tail towards lower energies and thus can not be described with a single Gaussian.
The solution of the energy loss working group is to use a superposition of two Gauss curves to describe the 1a-peak, and a third Gauss curve for the 1b peak. This parametrization can be used up to the ionization energy of the molecule, which in the case of deuterium is $E_{ion} = 15.467\,\text{eV}$ [65].
The fit of the ionization tail is challenging because the incident electron can lose up to $E/2 \approx 9287\,\text{eV}$. Our measured data only covers a range of 55 eV and the fitted function needs to be extrapolated for proper normalization before it can be convoluted with itself to obtain the function describing the n > 1 fold scatterings. Because of this, a function is needed which fits the data and also has a correct tail behavior, as otherwise an error would be introduced by the extrapolation. To find a suitable function an extensive literature search on the ionization of atoms and molecules was performed by F. Glueck at KIT. Five advanced models are displayed in figure 4.7. Those are
Model 1: H-Atom, analytical ionization function of Bethe taken from [68]
Model 2: A semi-empirical model of M. Rudd, eq. 3+4 in [115]
Model 3: A binary-encounter (BE) approximation of M. Rudd, eq. 3 in [116]
Model 4: Binary encounter Bethe (BEB) model, eq. 52-54 in [76]
Model 5: Binary encounter dipole (BED) model, eq. 44 in [76].
As can be seen in figure 4.7, the different tail models vary by up to a factor of two in the ratio between the predicted differential cross section at 15.5 eV and 50 eV. A comparison with our measured data shows, that only the models with a steep decrease of the cross section with energy, like the H-Atom model or the BED model, can be used for an Eloss model.
Binary encounter dipole (BED) model: The binary encounter dipole model is described in equation 44 of a paper by Kim and Rudd [76]. In the paper first Mott scattering

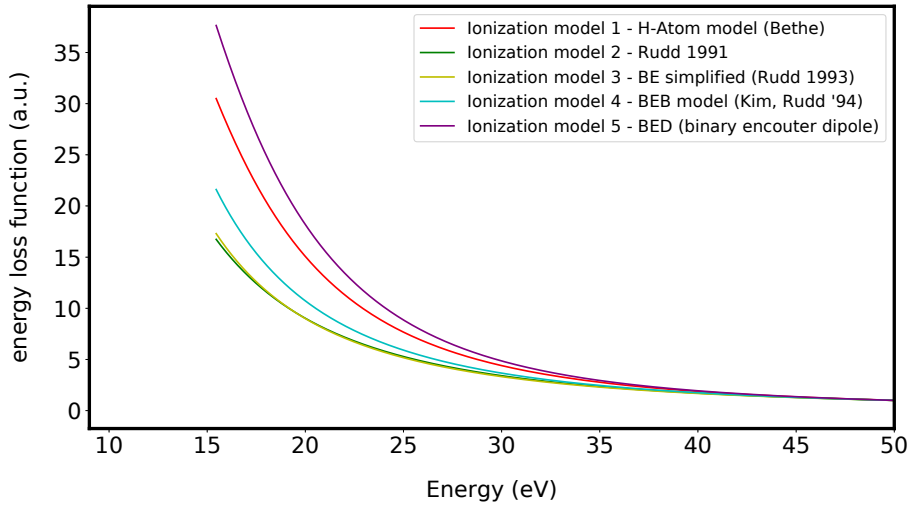

Figure 4.7: Models to describe the ionization tail of the energy loss measurement. All models are normalized to one at 50 eV.

is introduced (eq. 3). Then the binary encounter theory is introduced as a modification with an additional operator for the mean kinetic energy of electrons in a subshell of an atom (eq. 7, 8, 15). Finally, the theory is modified in such a way that the total ionization cross section shows the same high energy dependence as predicted by the Bethe theory (eq. 43). The model in eq. 44 still needs the differential oscillator strength. In table 1 of the paper the coefficients of a power series fit to the oscillator strength of a hydrogen molecule in the ground state ($1\sigma_g$) is given. These numbers (except for the ionization energy) are used for the model, even though it is used to describe scattering on deuterium instead of hydrogen.

New parametrization: The new parametrization is given by

$$f(E) = \begin{cases} G(E, A_1, \mu_1, \sigma_1) + G(E, A_2, \mu_2, \sigma_2) + G(E, A_3, \mu_3, \sigma_3) & E < E_{ion} \\ A_{BED} \cdot \text{BED model}\,(E) & E > E_{ion} \end{cases} \tag{4.22}$$

Here G is a Gauss curve

$$G(E, A, \mu, \sigma) = A \cdot e^{-\frac{1}{2}\left(\frac{E-\mu}{\sigma}\right)^2}, \tag{4.23}$$

and the BED model is taken from the paper as described above. For the ionization energy we use a value of

$$E_{ion,D_2} = 15.46\,\text{eV}. \tag{4.24}$$

The amplitude of the BED model A_{BED} is chosen in such a way that the function is continuous. The amplitudes are scaled to normalize the function

$$\int_0^{9287\,eV} f(E)\,dE = 1. \tag{4.25}$$

The description of the energy loss function with 9 parameters is reasonably simple and uses a sophisticated physics model for the description of the ionization tail without any fit parameters which affect the shape of the tail.

BED Model: For completeness, the BED model as given in [76], is written down here (note that in the equations 4.26 to 4.31 the variables from the paper are used, i.e. T for the kinetic energy of the incident electron):

$$\frac{d\sigma(W,T)}{dW} = A_1 \cdot (A_2 + A_3 + A_4) \tag{4.26}$$

with

$$A_1 = \frac{S}{B(t+u+1)}, \tag{4.27}$$

$$A_2 = \frac{(N_i/N)-2}{t+1} \cdot \left(\frac{1}{\omega+1} + \frac{1}{t-\omega}\right), \tag{4.28}$$

$$A_3 = [2-(N_i/N)] \cdot \left(\frac{1}{(\omega+1)^2} + \frac{1}{(t-\omega)^2}\right), \tag{4.29}$$

$$A_4 = \frac{ln(t)}{N(\omega+1)} \cdot \frac{df(\omega)}{d\omega} \tag{4.30}$$

The differential oscillator strength is approximated with a power series fit:

$$\frac{df}{d(E/B)} = ay + by^2 + cy^3 + dy^4 + ey^5 + fy^6, \tag{4.31}$$

with y= B/E. E = photon energy, B = binding energy in eV. For H_2 ($1\sigma_g$ state) these values are given: B(H_2)=15.43, N_i = 1.173, a = 0, b = 0, c = 1.1262, d = 6.3982, e = -7.8055 and f = 2.1440. U = 25.68 eV is the average kinetic energy of an electron in a H_2 molecule in the $1\sigma_g$ state. T is the kinetic energy of the incident electron, W the kinetic energy of the secondary electron. The 'reduced variables' $t = T/B$, $\omega = W/B$, $u = U/B$ and $S = 4\pi a_0^2 N(R/B)^2$ are used in the equations above.

This thesis aims to find the energy loss function for mono-energetic incident electrons close to the tritium endpoint. In this case A_1 is a constant and can be absorbed in the amplitude A_{BED} in equation 4.22.

4.2.5 Fit of the Eloss data

To perform the fit of the data two programs have been developed. Both use a least χ^2 approach with a minuit minimizer [69].
The first program is a C based program which was developed by C. Weinheimer. The integration of the Eloss model described in the previous section was done in this work. The program performs all integrations and convolutions numerically in a robust but computationally expensive way. The normalization of the Eloss function is strictly enforced every time before the function is convoluted with itself. A relative shift of the x-axis between the data sets is used to account for a potential drift of the inner electrode voltage system, which did not have a precise readout during these measurements.
The second program is a Jupyter python notebook using the *iminuit* package [67]. The transcription from C to Python was done by V. Hannen. In this program, the convolution is done in a discrete way, which is much faster than the method used in the first program. For this method to work, however, the ToF data needs to be rebinned to the same bin size as the integral data. The normalization of the function is enforced with a penalty term in the χ^2, which grows quadratically with the deviation from unity.
In addition to the fit parameters of the model, the scattering probability μ (see eq. 4.4) for each data set and a relative normalization between the data sets are free fit parameters.
A third program to fit the data was created by L. Schimpf [121], but was not used in this work.

Fits with the first program
With the first program a combined fit of the ToF data, the 50 % integral data and the 100 % integral data was performed. A 'tail factor' is used in the fit, which scales the amount of scattered to unscattered electrons. This factor is the same for all data sets and corresponds to the area of the Eloss function in the fitting range of about 94.4 %. The remaining area up to unity is in the tail region from 55 eV to 9287 eV, where the function can only be extrapolated. The fit and the corresponding normalized residuals are shown in figure 4.8 and figure 4.9. The value of the minimizing function is $\chi^2/\text{ndf} = 2741.79/2534 = 1.082$. As can be seen in the plots of the residuals, the largest deviations of the fit are at the transmission function, where small fluctuations of the energy scale, or effects of the binning and stacking procedure, have the largest effect.
The full set of parameters for this fit is shown in the appendix in table A.1.

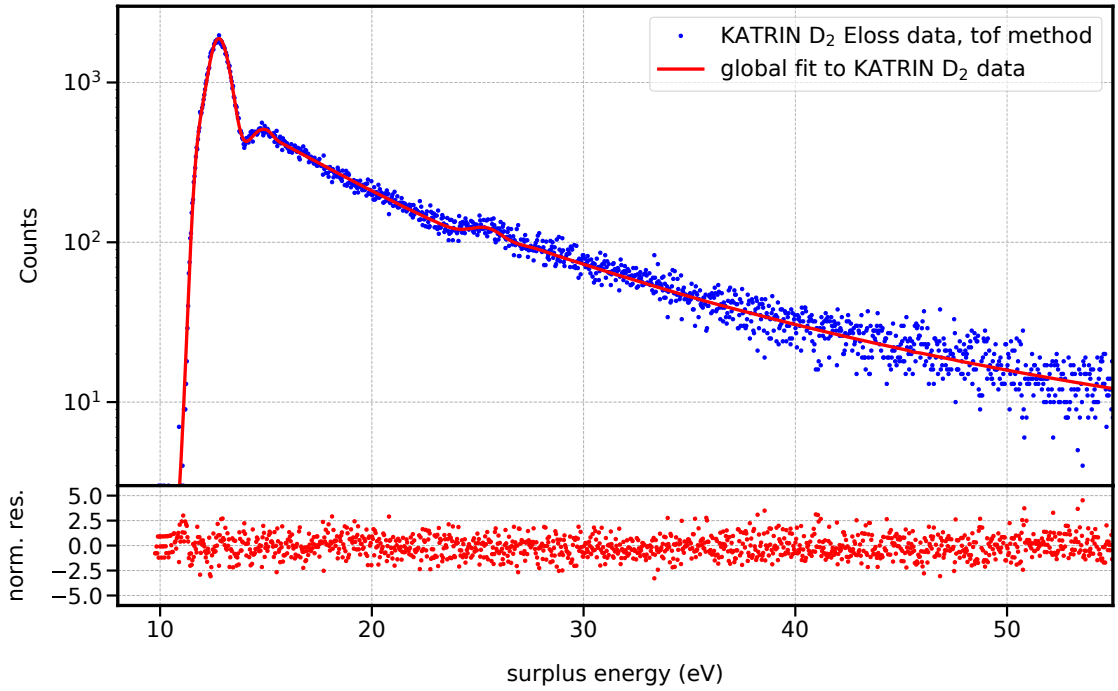

Figure 4.8: Result of the combined fit of the D_2 Eloss data plotted together with the ToF Eloss data. The fit was performed with the C program. The residuals show no significant structures. The assumed errors on the data points are only from Poisson statistics.

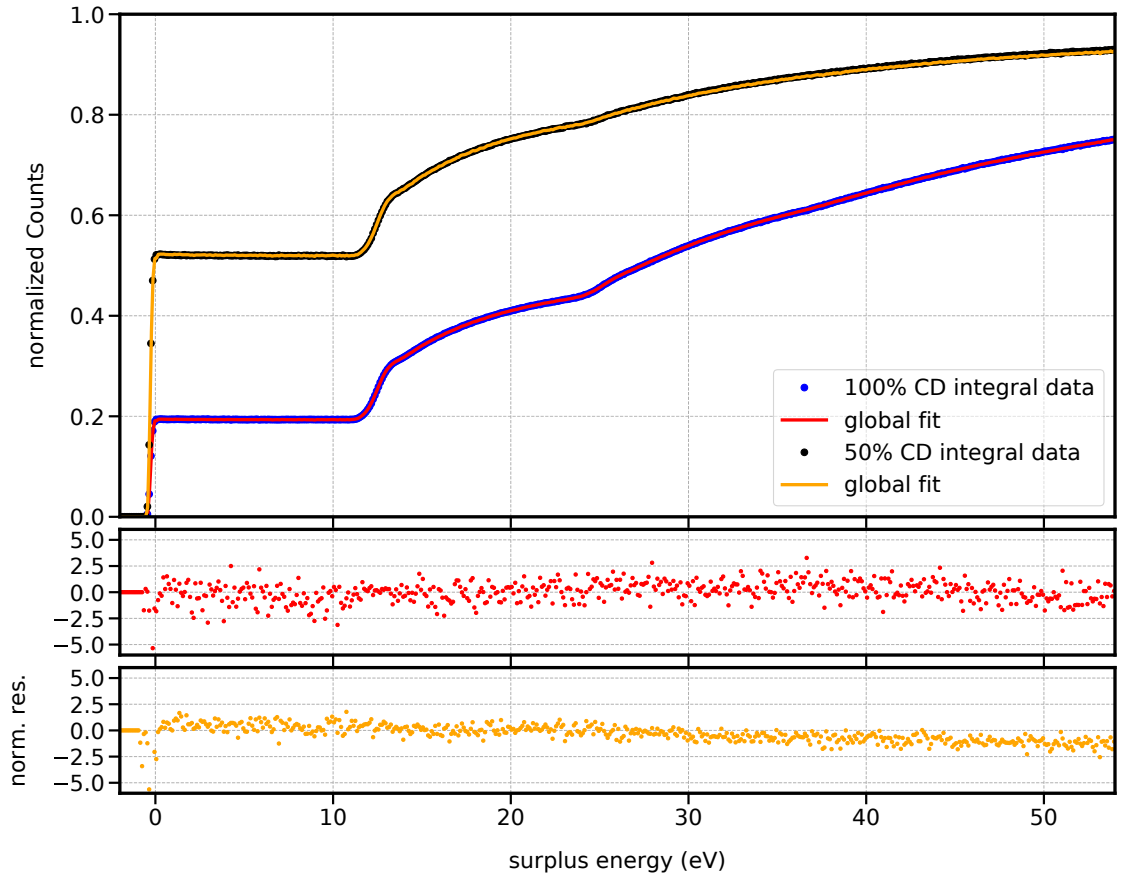

Figure 4.9: Result of the combined fit of the D_2 Eloss data plotted together with the integral Eloss data. The fit was performed with the C program. The residuals show a structure at the transmission edge (0 eV). This region is most sensitive to voltage fluctuations. In the 50 % data also a slope of the residuals is visible which is not present in residuals of the 100 % data.

Fit with the second program

The second program is a python program and because of the discrete convolution method a fit only takes about 1 minute, which is much more convenient to work with compared to the C program. This program does not need the 'tail factor' to scale the scattering probability μ, because the fit function and all the convolutions are always performed up to $E/2$.

If the normalization of the Eloss function is a free parameter, it takes a value of about 0.97. Since the area should be unity, a penalty term in the χ^2 enforces this. This does however lead to a structure in the residuals of the fit, especially for the data set at 100 % CD, which does not only have a large μ, but also the most statistics of all data sets. The reason for this structure in the residuals is not clear. It could be a problem of the detection efficiency in the region of the first scattering peak, where a lot of electrons with long flight times are present. The fit presented here is a combined fit of the ToF data, the 6 % integral data and the 50 % integral data. The fit gives a reduced chi squared of $\chi^2/\,\mathrm{ndf} = 1769/1568 = 1.1285$ and the normalization is $N = 0.9997$, which is reasonably close to unity. The fit of the ToF data is shown in figure 4.10 and the fit to the integral data sets in figure 4.11.

The full set of parameters for this fit is shown in the appendix in table A.2.

Deriving the column density from the fit

The determination of the column density is not a goal of this thesis. Nevertheless, a rough estimation can be made. The value for the scattering probability

$$\mu = \rho \cdot d \cdot \sigma / cos\theta \tag{4.32}$$

is a parameter of the fit. The value for cross section σ is given in equation 4.18. A rough estimation for $\cos\theta$ can be made from the measurements described in the previous chapter: For a transmission measurement with the LDLS in the $B_{\mathrm{ana}} = 1\,\mathrm{G}$ setting a width of about 130 mV is reported and in the $B_{\mathrm{ana}} = 6.3\,\mathrm{G}$ setting a width of about 150 mV. Assuming that this increase of the width is solely caused by an isotropic angular distribution of the e-gun electrons from zero angle up to a maximum angle, a maximum angle of 17.2° at the pinch magnet can be estimated. This corresponds to a maximum angle in the WGTS of 9.7° (using eq. 3.32 and $B_{\mathrm{WGTS}} = 0.6 \cdot B_{\mathrm{PCH}}$). Isotropic electrons follow a uniform distribution in $cos(\theta)$. Using this distribution an effective value of $cos(\theta)_{\mathrm{eff}} = 0.995$ is found. This estimation shows that the error inflicted by the angular spread of the e-gun can be estimated to be of order 0.5 %. The angular spread is estimated from two measurements from different measurement campaigns and might therefore contain unknown errors caused by changes in the system. It should only be taken as a rough estimation.

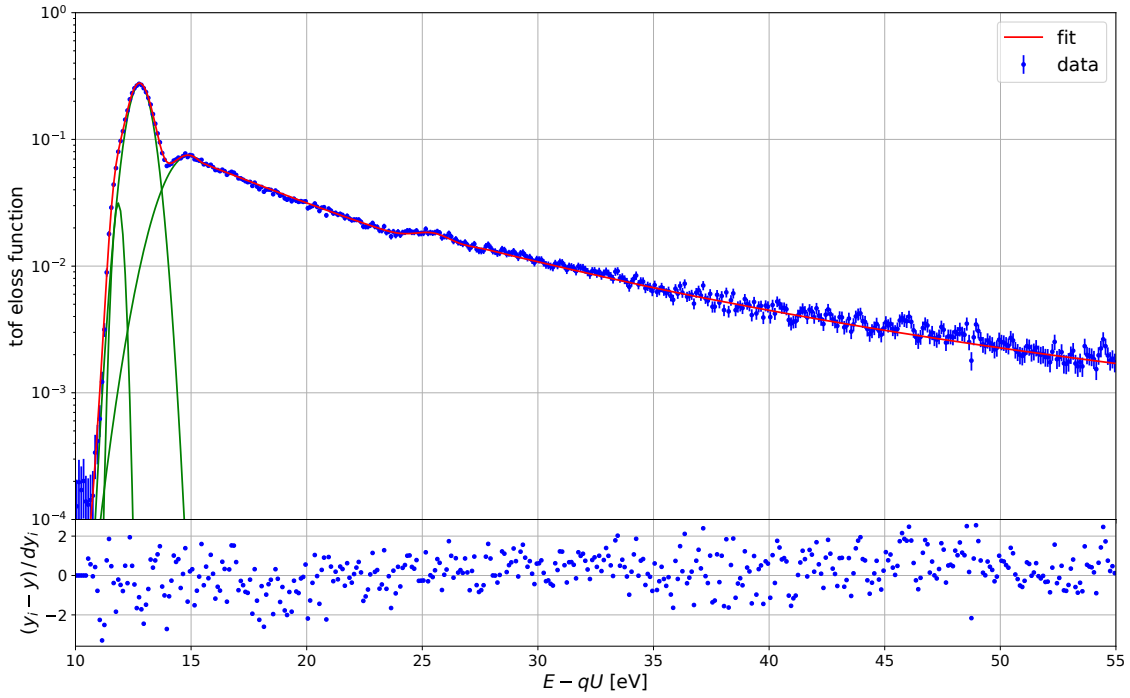

Figure 4.10: Result of the combined fit of the D_2 Eloss data (ToF data, 6 % CD integral data, 50 % CD integral data) plotted together with the ToF Eloss data. The fit was performed with the python program. The residuals show no significant structures. The assumed errors on the data points are only from Poisson statistics.

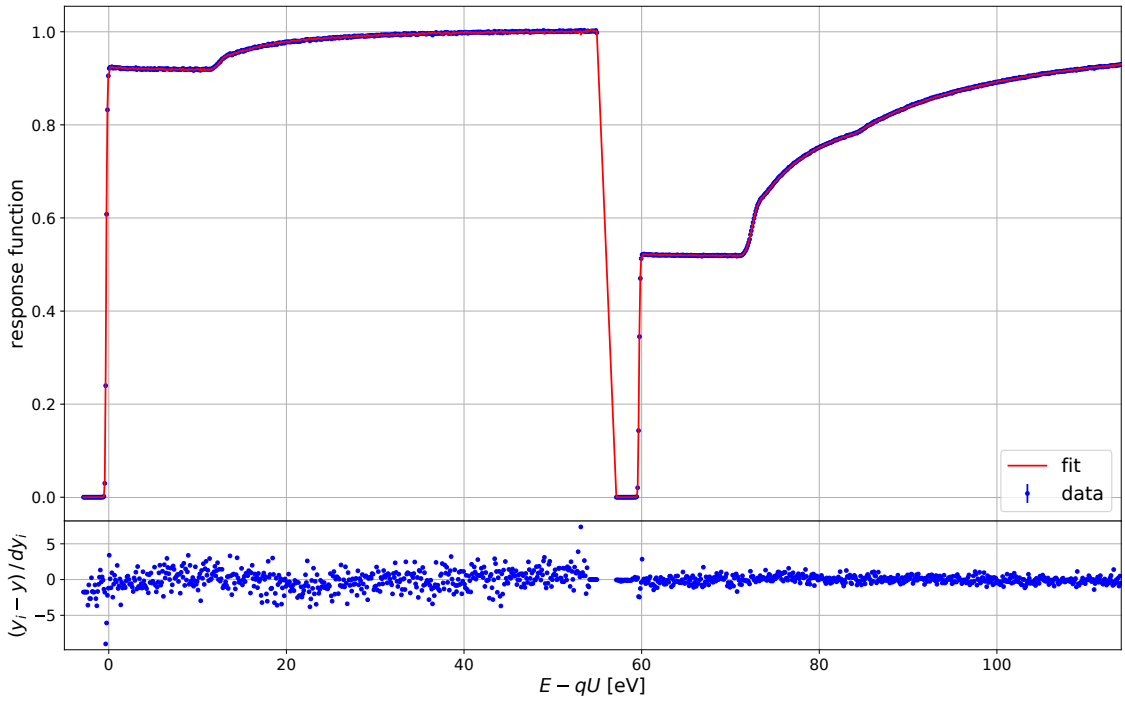

Figure 4.11: Result of the combined fit of the D_2 Eloss data (ToF data, 6 % CD integral data, 50 % CD integral data) plotted together with the integral Eloss data. The fit was performed with the python program. The residuals on the left data set are larger, which might be due to a problem with the e-gun intensity during this measurement. The residuals on the right plot are a bit too small, which hints at an overestimation of the error bars on the data points.

4.2.6 Mean energy loss comparison with stopping power

In the scattering process of an electron on an electron in the shell of an atom or molecule at rest, up to half of the kinetic energy of the incident electron can be transferred. In the case of electrons from tritium beta-decay scattering on tritium molecules in the KATRIN WGTS, this maximum energy is $E_0/2 = 9287\,\mathrm{eV}$. However, our measurement only covers the first $\approx 55\,\mathrm{eV}$. Thus we need to fit our model to our data and extrapolate up to the maximum energy. Our condition is that the function is normalized so

$$\int_0^{E_0/2} f(E)dE \stackrel{!}{=} 1. \tag{4.33}$$

The tail model does not have a large influence on the normalization since about 94.4 % of the area is covered within our fitting range. This number is consistent in both results from the two fitting programs presented in the previous section. The tail model does, however, have a large impact on the calculated mean energy loss

$$\langle E \rangle \;=\; \int_0^{E_0/2} f(E) \cdot E\, dE \;=\; 30.76\,\mathrm{eV}. \tag{4.34}$$

This value, which is calculated using the fit parameters given in table A.2, can be compared to an independent value of the mean energy loss, which can be calculated from the stopping power.
The stopping power of hydrogen for 18.55 keV electrons is [96]

$$\frac{dE}{\rho \cdot dx} = 30.99\,\frac{\mathrm{MeV}\cdot\mathrm{cm}^2}{\mathrm{g}}. \tag{4.35}$$

With the molar mass of hydrogen $\mathrm{M}(\mathrm{H}_2) = 2$ and Avogadros number $\mathrm{N}_A = 6.022 \cdot 10^{23}$ 1/mol we get the stopping power per molecule of $1.029 \cdot 10^{-16}$ eVcm^2. We also need the total inelastic cross section σ_{tot}. From the values presented at the beginning of this chapter (see eq. 4.18), a value of

$$\sigma_{inel}[\mathrm{H}_2] = 3.669(22) \cdot 10^{-18}\,\mathrm{cm}^2 \tag{4.36}$$

can be calculated. In contrast to this Aseev et al. [5] report a value of $\sigma_{tot}[\mathrm{T}_2] = 3.40(7) \cdot 10^{-18}\,\mathrm{cm}^2$. Using the same argumentation as in chapter 4.1.2, this corresponds to a cross section for hydrogen of

$$\sigma_{inel}[\mathrm{H}_2] = 3.43(7) \cdot 10^{-18}\,\mathrm{cm}^2. \tag{4.37}$$

From those two values we get an estimated mean energy loss of hydrogen of

$$\Delta\bar{E} = \frac{\text{stopping power}}{\sigma_{inel}} = \begin{cases} 28.05\,\text{eV} & \text{(Liu, Kolos et al.)} \\ 30.00\,\text{eV} & \text{(Aseev et al.)} \end{cases} \tag{4.38}$$

These values are in reasonable agreement with the value of 30.76 eV (for D_2) obtained from the Eloss model (s. eq. 4.34). This indicates that the BED model gives a good description of the high energy behavior of the ionization tail.

4.2.7 Comparison with other energy loss models

Previous measurements, e.g. [5] and [1] have used a rather simple parametrization with three parameters for the excited states of the molecule, another three for the ionization tale, and one parameter for the transition from one region to the other, see equation 4.21. Our data, especially the ToF data set, gives us a clear picture of the shape of the energy loss function with a good energy resolution on the order of 100 meV. In the data presented in this work, a double peak structure is resolved, labeled 1a+1b in figure 4.2. Further, one can see that the onset on the left side of the 1a-peak is very steep, which can not be described by a single Gauss function. For this reason, a new parametrization is introduced, see equation 4.22. By using the literature value of the ionization energy as the transition point from one part of the model to the other and by using the BED model without any free fit parameters, the number of parameters needed for the model is reduced down to nine.

The analysis in this work was performed with two different fitting programs on slightly different data sets.

Figure 4.12 shows the Eloss models of Aseev et al., Abdurashitov et al. and the two models presented in this work. Analysis 1 is the one performed with the C program and Analysis 2 with the python program. Both curves are in good agreement with each other and show a distinctly different shape compared to the other two models.

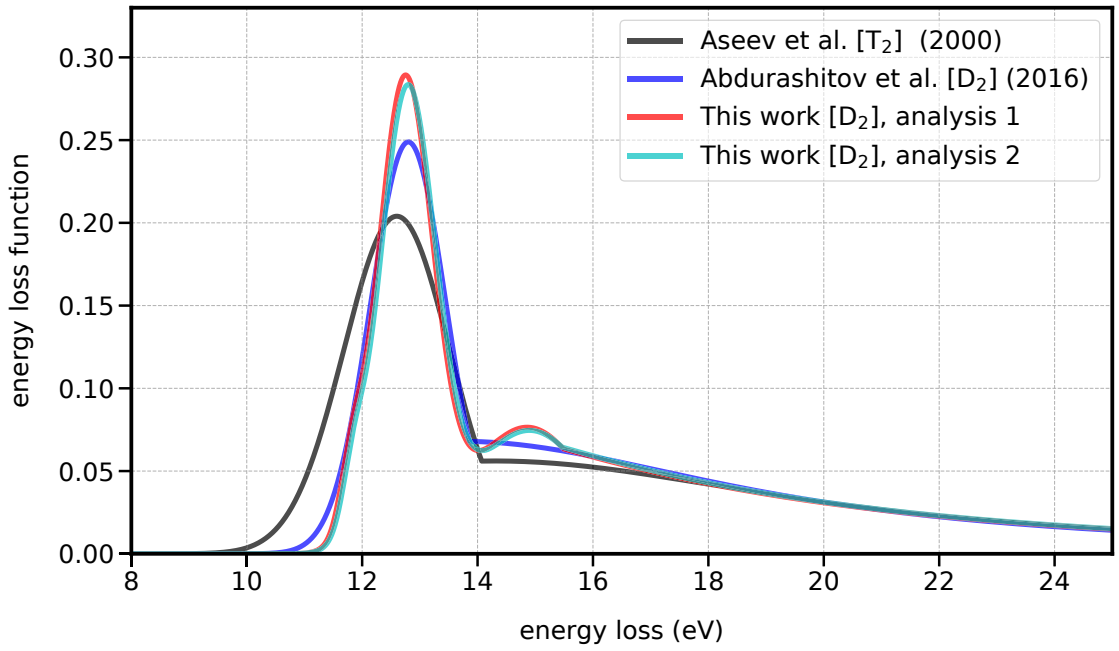

Figure 4.12: Energy loss models by Aseev [T_2], Abdurashitov [D_2] and from this work [D_2]. Analysis 1 refers to the C program, and analysis 2 to the python program, see section 4.2.5. Those two curves are in good agreement. The position of the first peak also agrees with the Abdurashitov model. The peak position in the Aseev model is shifted to the left, but this might be because the position is not a free fit parameter in their analysis. The ionization tails are in good agreement in all models from about 18 eV onward.
In analysis 1 the data sets are slightly shifted. The mean shift of the three data sets is used to create this plot. This is only a minor effect of order 10 meV.

4.2.8 Discussion and outlook

The energy loss measurements on deuterium gas in the STS3a measurement phase of KATRIN have successfully demonstrated that it is possible to measure the energy loss function with high precision with the e-gun described in chapter 3. It can further show that the measurement and analysis can be done with an integrating and with a differential, time of flight based method. Both measurements can be analyzed in a combined fit and show good agreement. The resulting new energy loss model has surpassed the expectations in terms of precision.

We can demonstrate that a time of flight based measurement at low column density is good at resolving the shape of the energy loss function in the region of single scattering. An integral measurement at high column density can fit the scattering probability $\mu = \rho \cdot d/cos\theta \cdot \sigma$ with a precision of better than 1 %.

Two programs have been developed to analyze the data. Since the results of both are in good agreement with each other only one will be further developed for the analysis of the measurements with tritium.

Several minor problems have been identified in this work and will be improved for the energy loss measurements with tritium. The voltage supply of the inner electrode system was already replaced and a precision voltmeter was added. The e-gun light intensity will be reduced in future measurement to reduce problems with the monitoring of the light intensity and also to reduce pile-up effects on the FPD. Additionally, some problems with the time synchronization occurred and have been fixed.

In this work the BED model by Liu et al. is used to describe the ionization tail and the comparison of the estimated mean energy loss is consistent with literature values. This indicates that this model can be used. However, this model is made for hydrogen and one might be able to improve it by using the differential oscillator strength of deuterium or tritium instead of the one of hydrogen.

Chapter 5

Q-value of tritium

5.1 Motivation to measure the Q-value

The KATRIN experiment aims to measure the neutrino mass m_ν from the shape of the tritium β decay spectrum near the endpoint. To do this with great accuracy, a detailed description of the spectrum with all shape distorting aspects is needed. These aspects are for example the energy loss model, the final state distribution, or experimental broadening effects such as potential fluctuations or drifts. In most cases, not only the parameter of interest m_ν^2, but also the fitted endpoint E_0 is affected. This makes the endpoint a great observable to check if there are any additional or underestimated experimental effects. The Q-value, which can be obtained from E_0, gives the opportunity to compare a fit parameter of the m_ν^2 fit with a quantity that can be measured independently by other experiments, such as Penning traps.

5.2 Q-value from other experiments

The Q-value is the amount of energy released in a decay. This value can easily be derived if one knows the mass difference of tritium (T) and helium-3 (^{3}He). This mass difference, or to be more precise the difference between T^+ and $^3He^+$, can be measured in Penning trap experiments. The leading measurement to this date [93] gives a value of

$$\Delta m(^3\mathrm{He}, \mathrm{T}) = m\,(\mathrm{T}) - m\,(^3\mathrm{He}) = 18592.01 \pm 0.07\,\mathrm{eV}. \tag{5.1}$$

The connection from $\Delta m(^3$He,T) to $Q(T_2)$ can be made via the atomic and molecular binding energies, which are known to meV precision or better from literature. Figure 5.1 shows a scheme of the binding energies involved. For the KATRIN experiment the value

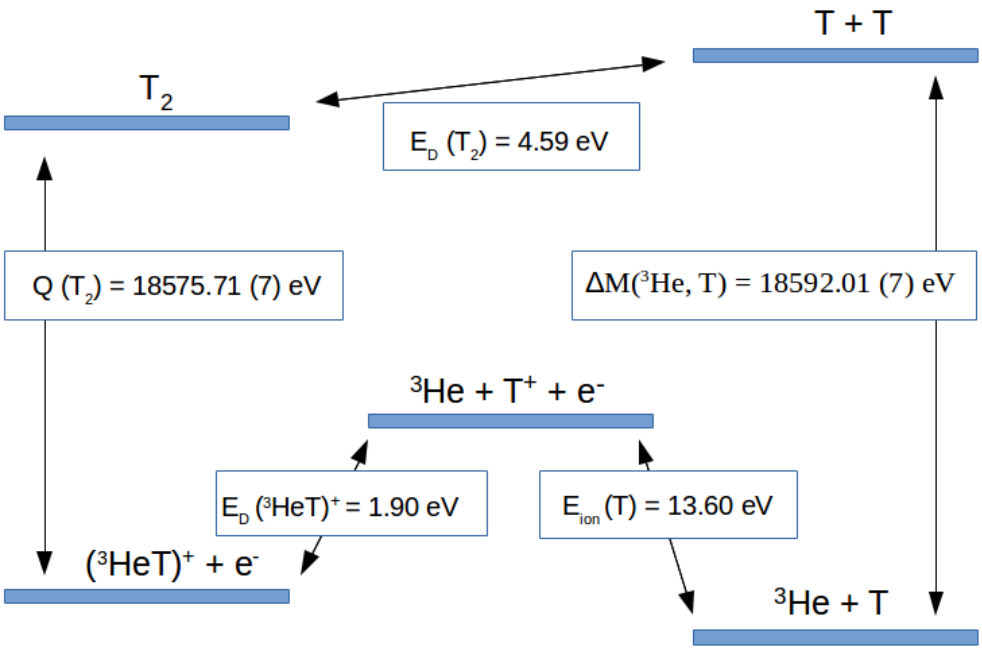

Figure 5.1: Connection of $\Delta m(^3\mathrm{He,T})$, which has been measured in Penning trap experiments, and $Q(\mathrm{T}_2)$, which can be determined at the KATRIN experiment. Subtracting the recoil of the daughter molecule from $Q(\mathrm{T}_2)$ gives the endpoint E_0.

$Q(\mathrm{T}_2)$ is needed.

5.3 Endpoint and recoil

The endpoint is one of the four fit parameters in KATRIN and describes the maximum kinetic energy the β-electron can have assuming $m_\nu = 0$ and no excitation of the daughter molecule. Due to energy and momentum conservation, a fraction of the kinetic energy is taken by the daughter molecule $(^3\mathrm{HeT})^+$. This energy, often referred to as recoil energy, can be calculated by

$$E_{\mathrm{rec,TX}} = \frac{E_0^2 + 2E_0 m_e}{2m_{(^3\mathrm{HeX}^+)}} \tag{5.2}$$

where X can be any of the hydrogen isotopologues H, D and T. Depending on the initial molecule, one gets

$$E_{\mathrm{rec,max}}(^3\mathrm{HeT}^+) = 1.720\,\mathrm{eV} \tag{5.3}$$

$$E_{\mathrm{rec,max}}(^3\mathrm{HeD}^+) = 2.064\,\mathrm{eV} \tag{5.4}$$

$$E_{\mathrm{rec,max}}(^3\mathrm{HeH}^+) = 2.580\,\mathrm{eV} \tag{5.5}$$

as a recoil, assuming $E_0 = 18574\,\mathrm{eV}$.
Here the recoil energy is calculated using the center of mass motion of the molecule and neglecting molecular excitation effects. However, one can argue that the amount of energy transferred to the molecule is on average always the same for any of these molecules. This means, that the energy difference between the recoil of a T-atom and the recoil of a T-X molecule is equal to the average rovibrational excitation energy of the respective molecule [99]. In the KATRIN experiment the molecular composition is a mixture of T_2, DT and HT. To be able to fit a single endpoint, the final state distributions of DT and HT are shifted by the difference of the recoil with respect to T_2. This correction is displayed in table 5.1. Due to this correction, the Q-value in KATRIN is given by

$$Q = E_0 + 1.720\,\mathrm{eV}\ (+\Delta\Phi) \tag{5.6}$$

independent of the isotopologue composition. In addition to that also differences of the work functions ($\Delta\Phi$) need to be taken into account. This will be explained in detail in the following sections.

FSD	Shift (eV)
T_2	0
DT	0.3427
HT	0.8585

Table 5.1: Shift of FSDs used in KATRIN to account for the different recoil energies of the different molecules.

5.4 Determination of $Q(T_2)$ in KATRIN

The determination of the $Q(T_2)$ value with KATRIN requires a fit of the tritium spectrum and knowledge about the potentials in the source and the analyzing plane. At first, an overview of all important potentials is given. Then the following subsections describe in detail the investigations on the potentials in the source and the analyzing plane, which have been performed in this thesis. First, the Fowler method is presented and the required optical setup is characterized. With this knowledge, the work function of the e-gun can be determined and finally, the work function of the inner electrode (IE) system can be estimated. In the second part, the Fowler method is used to investigate the work function of the rear wall and it is discussed how this influences the starting potential of the electrons in the source.

5.4.1 Overview over the potentials in KATRIN

Figure 5.2 shows in a schematic way the different contributions to the potential difference between the source and the analyzing plane (AP) of KATRIN. The effective potential in the WGTS is assumed to be given by the work function of the rear wall, a bias voltage of the rear wall relative to the WGTS ground potential, and possibly an additional plasma potential. The potential in the analyzing plane is given by the applied high voltage on the inner electrode, the work function of the inner electrode system, and a voltage depression resulting from the geometry of the setup.
The voltage depression can be simulated with the KASSIOPEIA toolkit [46] and the uncertainty on this value is on the order of 10 mV, which is negligible compared to other uncertainties.
The electric potential of the main spectrometer inner electrode system is measured with respect to the beam tube with the K-35 precision high voltage divider. A calibration based on the position of two Kr lines has been performed by O. Rest [107]. The uncertainty value from this publication translates to $\sigma U = 93\,\mathrm{mV}$ at the endpoint energy of KATRIN. For simplicity a rounded value of 100 mV is assumed for the combined uncertainty of the electric potential in the center of the analyzing plane including the voltage depression.

5.4.2 Fowler method

The idea of the Fowler method is to measure the electron rate at different wavelengths and to fit the Fowler function (formula 9 in [39]) to the data. The Fowler function contains the work function as a parameter that, in a simplified picture, shifts the function along the

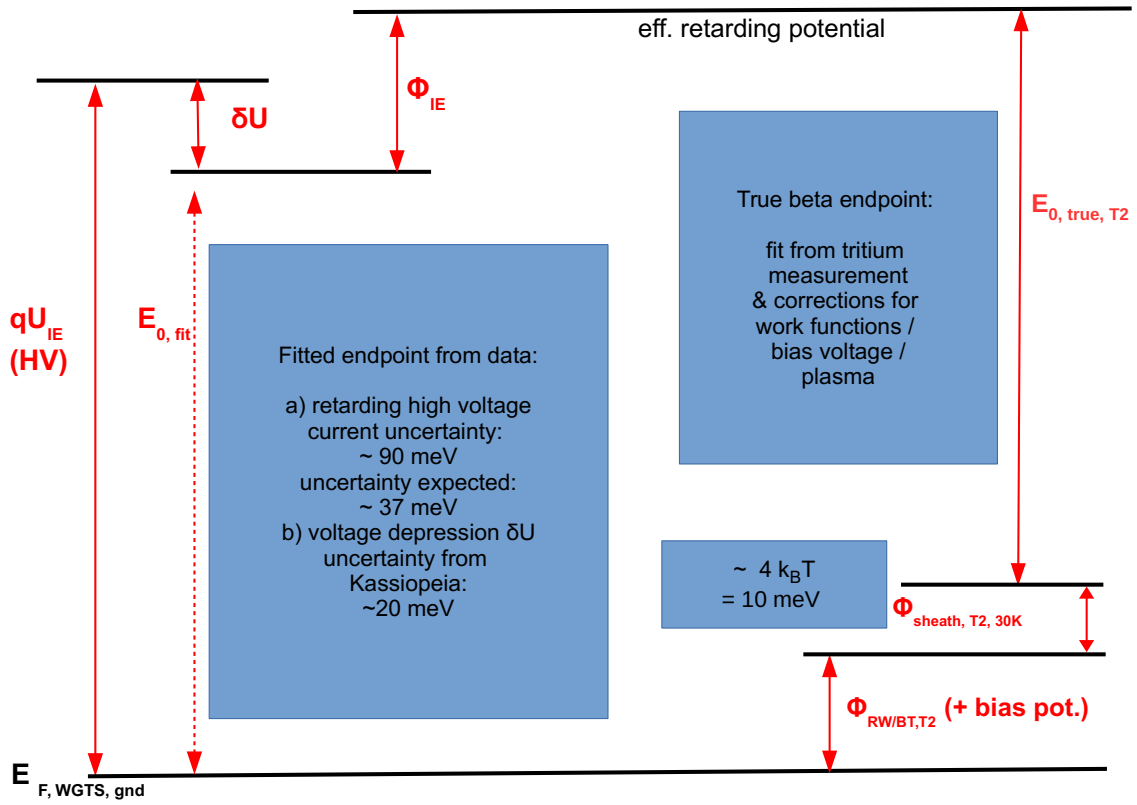

Figure 5.2: Schematic of the potentials in KATRIN. The WGTS is defined as the reference ground. The true endpoint $E_{0,\,\mathrm{true}}$ is the difference between the effective retarding potential in the analyzing plane and the effective WGTS potential. The fitted endpoint $E_{0,\,\mathrm{fit}}$ (shown here as used in KNM 1) can be translated to the true endpoint if the work functions and potentials are known.

x-axis (wavelength). The Fowler function is defined in the following way:

$$I = A \cdot T^2 \cdot f(\mu) \tag{5.7}$$

$$f(\mu) = [e^{\mu} - \frac{e^{2\mu}}{2^2} + \frac{e^{3\mu}}{3^2} - ...] \quad \text{for } \mu \leq 0$$

$$f(\mu) = [\frac{\pi^2}{6} + \frac{\mu^2}{2} - (e^{-\mu} - \frac{e^{-2\mu}}{2^2} + \frac{e^{-3\mu}}{3^2} - ...)] \quad \text{for } \mu > 0$$

$$\mu = \frac{\hbar\omega - \Phi}{k_B T}$$

Here T is the temperature in Kelvin, $\hbar\omega$ the energy of the photon and Φ the work function. In this theory the electron distribution is assumed to be a Fermi sphere, as is typically the case for alkali metals. The broadening at the surface of the Fermi sphere is described by the Fermi distribution:

$$W(E) = \frac{1}{exp\left(\frac{E-\kappa}{k_B T}\right) + 1} \tag{5.8}$$

At $T = 0\,\mathrm{K}$ the chemical potential κ equals the Fermi energy E_F. Since the temperature of the e-gun of about $T = 300\,\mathrm{K}$ is small compared to the Fermi temperature of gold of $T_F \approx 59000\,\mathrm{K}$, the interpretation $\kappa = E_F$ is reasonable.
In this description, the temperature is the only parameter that describes a broadening. If an additional broadening appears, for example, because of inhomogeneities or dirt on the surface, this would show up in the fit as an increased temperature.
The idea leading to the Fowler function is that electrons from the valence band, which have an energy according to the Fermi-Dirac distribution, can be released as photoelectrons, if they gain enough energy from the absorption of a photon to get them above the vacuum level. The remaining surplus energy is converted to kinetic energy of the emitted electron. With increasing energy of the photon, more electrons from the metal are available which leads to an increase of the photocurrent. The integral over the Fermi distribution in the energy range from the vacuum level to the available energy of the photon $E_{\text{available}} = -\hbar\omega$ gives the number of available electrons. Figure 5.3 displays this for an exemplary set

of parameters. A comparison of this description of the Fermi edge with measurements of the Fermi edge of gold, i.e. figure 7 in [135], shows a good qualitative agreement. Fowler's approach is to assume, that only those electrons with a sufficient kinetic energy perpendicular to the Fermi surface $E_{e,\perp}$ can be emitted. This one-dimensional approach leads to an integral which can not be solved analytically. For this reason simplifications and approximations are made (see e.g. equation 1-4 in [42]). This finally leads to equation 5.7. It has to be noted, that the approximation is only valid near $\mu \approx 0$.

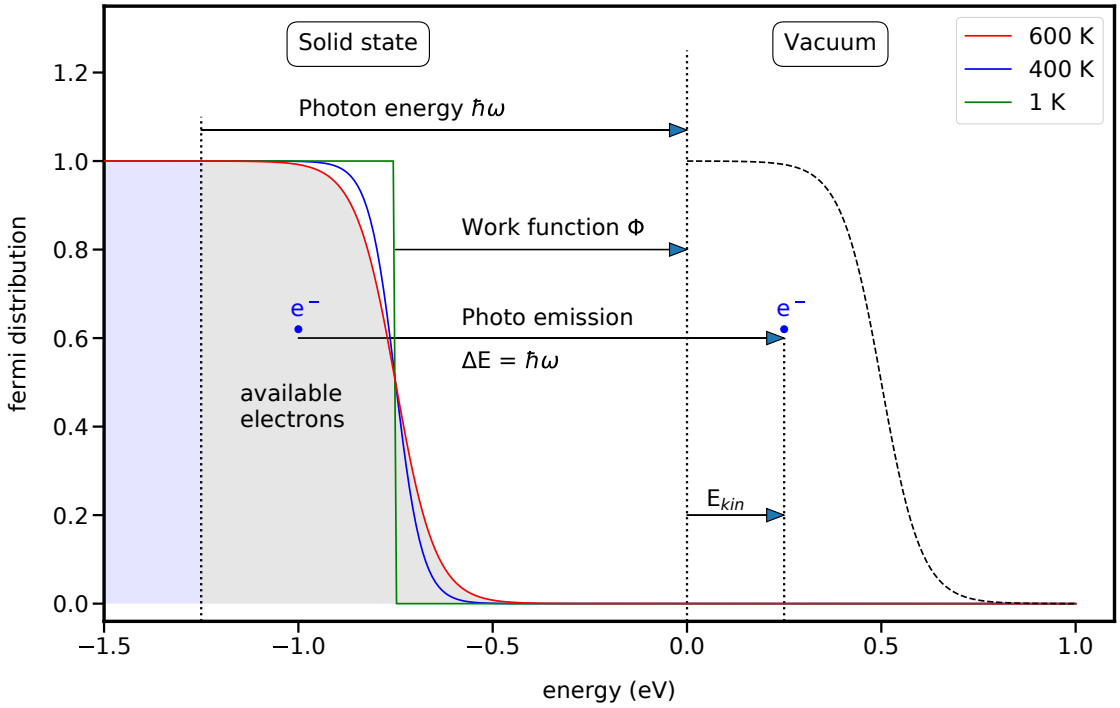

Figure 5.3: Illustration of the Fermi distribution and the photoemission for an exemplary set of parameters: $E_F = -0.75\,\mathrm{eV}$, $E_\gamma = 1.25\,\mathrm{eV}$, $T = 600\,\mathrm{K}$. The left side shows the electron distribution in the valance band. The green, blue and red curve show the Fermi distribution for three different temperatures. The grey area shows the electrons available for photoemission, assuming $T = 600\,\mathrm{K}$. The electrons in the blue area are not available for photons of this energy, but would be in case of a larger photon energy. The photon transfers all its energy to the electron. The remaining surplus energy above the vacuum level is available as kinetic energy of the electron. This is illustrated by the exemplary indicated electron.

5.4.3 Numerical artifacts in fitting the Fowler function

The Fowler function in the form of equation 5.7 is a Taylor series on both sides of the work function. Since only a finite number of elements of the series can be used in a calculation, the function is not continuous at the work function. The involved functions of shape $e^{k\mu}$ and $e^{-k\mu}$ go to either very large or very small values for large k and large distances from the work function. This can cause numerical problems. However, an expansion to larger k gives a better description of the function close to the work function. If the work function is close to a measurement point, problems in the minimization may appear. Figure 5.4 shows the Fowler function close to the work function for the expansion up to $k = 3$, $k = 5$ and $k = 9$. In this work $k_{max} = 9$ is used in a range of $|\mu| < 0.2$, $k_{max} = 7$ for $|\mu| < 1$, and $k_{max} = 5$ elsewhere, with μ as defined in equation 5.7. The fit results with $k_{max} = 9$ close to the work function and $k_{max} = 7$ close to the work function are almost identical. For this reason it is not needed to go beyond $k = 9$ in this work. In former works performed at KATRIN, i.e. [12], [11], $k_{max} = 3$ was used.

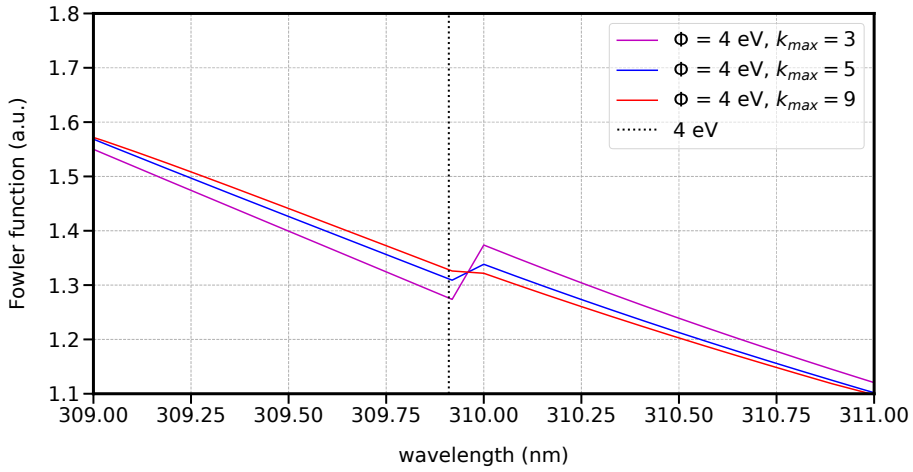

Figure 5.4: Fowler function plotted near the work function (dashed line) for $k_{max} = 3$, $k_{max} = 5$ and $k_{max} = 9$. A larger k reduces the nonphysical step in the Fowler description near the work function.

5.4.4 Corrections to the measured data

To get the work function from the Fowler method correct it is important to know the relative change of the light intensity with respect to the wavelength.
In this work measurements have been performed to characterize the wavelength dependence of the optical system of the rear section e-gun. This optical system was also used for the Fowler measurements of the rear wall (RW).

Wavelength dependence of the beam splitter:
The splitter redirects the light which comes from the light source onto two targets. The majority of the light (about 90 %) is transmitted to the high-intensity end, which is normally connected to the e-gun. The other end is connected to a UV-diode to monitor the light output. According to the manufacturer, the split ratio should be 9 : 1. However, a ratio between 17 : 1 and 12 : 1 has been measured. The wavelength-dependent ratio between the high-intensity and the low-intensity end can be seen in figure 5.5. For this measurement, the diode was mounted to one end of the splitter and then to the other end to avoid having two different diodes with possibly different characteristics.
When the measurements of the RW were performed the splitter was not in place, which means that there was no live data recorded during the measurement. Therefore it is assumed that a measurement, performed at the low-end of the splitter at a different time, can be used to estimate the light power at the RW during the actual measurement at the RW. The power measured at the low-end plus the power at the high end, which can be easily calculated with the splitter ratio, gives the total power of the light. The absolute power is not important since only relative changes with respect to the wavelength are of interest for the analysis of the work function measurement.

Wavelength dependence of the diode:
The current measured at the photodiode is used to get information about the amount of light received at different wavelengths. The efficiency of the diode changes with the wavelength, which has to be taken into account. In the Elwetritsche setup, as the test stand is called, where a lot of measurements with the LDLS have been performed, a diode from Thorlabs has been used. We use the information on the wavelength dependence of the diode, which is provided by the manufacturer [133], to correct the measured signal. Since there is only a picture showing the response over the wavelength, the graph is extracted from the picture on the website and shown in figure 5.6. For the e-gun measurements in STS3a a diode from Hamamatsu [58] was used. The characteristics are similar and can be seen in the appendix in figure A.6.

Light power on the diode:
The light power on the photodiode was measured during the Fowler measurement with

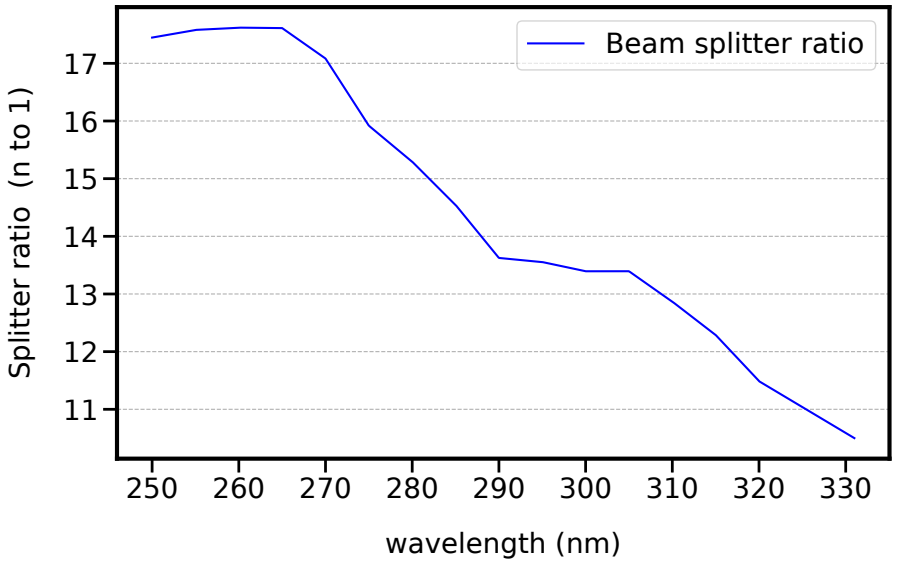

Figure 5.5: Ratio of light power at the long end of the splitter (usually connected to the e-gun) relative to the short end (connected to the UV-diode). According to the manufacturer, the ratio is about 9:1. The measured values are ranging from 17:1 to 11:1 with a strong wavelength dependence. A linear interpolation is used between the data points. The measurement was performed with the LDLS light source. The width of the monochromator was set to 3 nm.

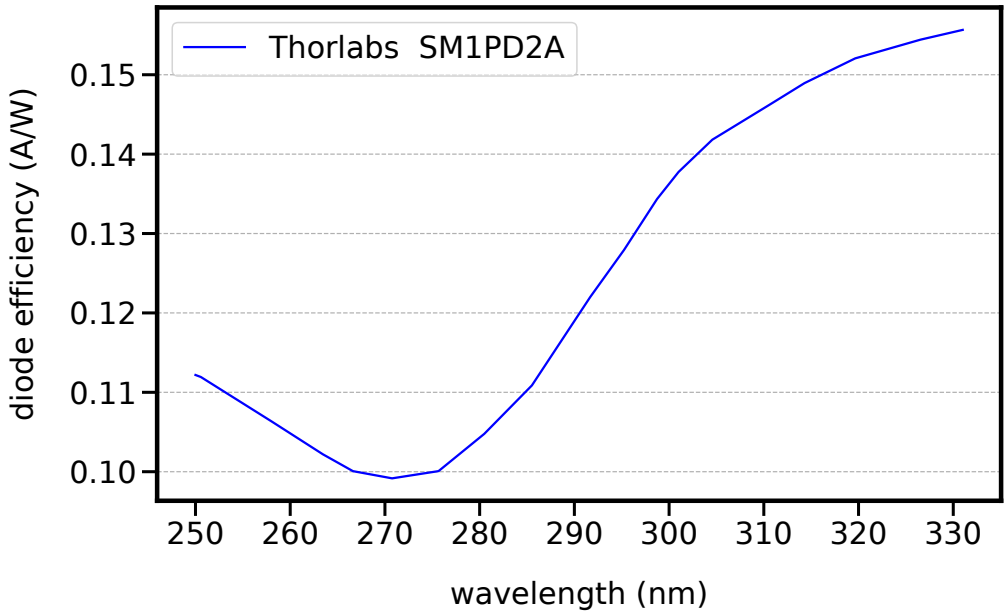

Figure 5.6: Response of the diode Thorlabs SM1PD2A. This information is extracted from a picture on the company website [133].

the e-gun at KATRIN and also previously at the Elwetritsche test setup. The wavelength dependence is assumed to be valid for the measurements at the rear wall as well, even though no live monitoring was possible during the Fowler measurements at the rear wall. To measure the current from the diode an amplifier 'Femto DLPCA-200' [52] was used, which converts the current signal of the diode to a voltage signal, which can easily be read out. An exemplary measurement is shown in figure 5.7.

Light spectrum in the setup with LDLS:

The combination of the measured power on the diode with the information about the splitter ratio and the diode efficiency gives a realistic idea of the spectrum which is used in the Fowler measurement. Figure 5.8 shows the corrected spectrum. The light intensity is calculated as:

$$\text{light intensity} = \text{read value} \cdot \frac{\text{splitter ratio}}{\text{diode efficiency}} \tag{5.9}$$

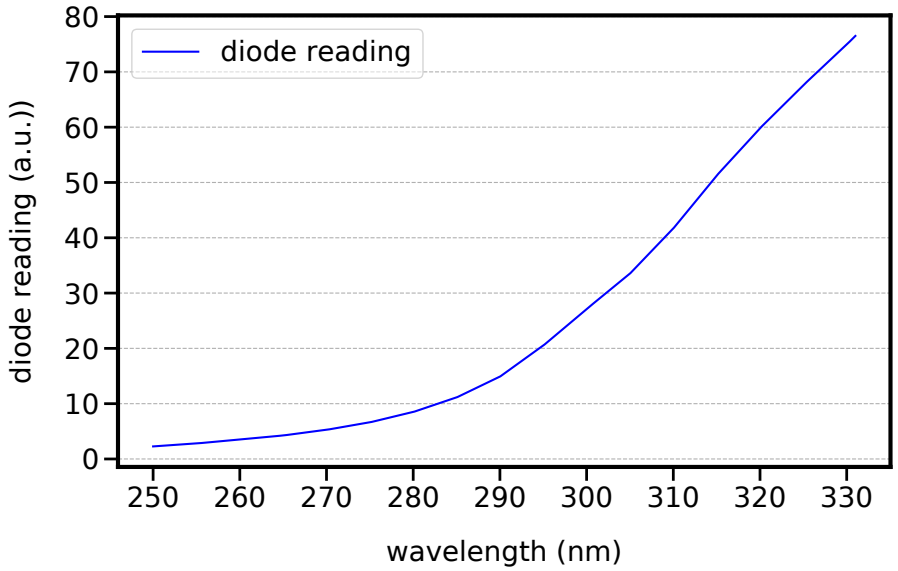

Figure 5.7: The read-values of the diode [133] without any corrections applied. The diode was mounted to the low-intensity ($\approx$ 10 %) end of the splitter. The signal from the diode was amplified with the DLPCA-200 [52]. The light source is the LDLS with the monochromator set to a slit width of 3 nm.

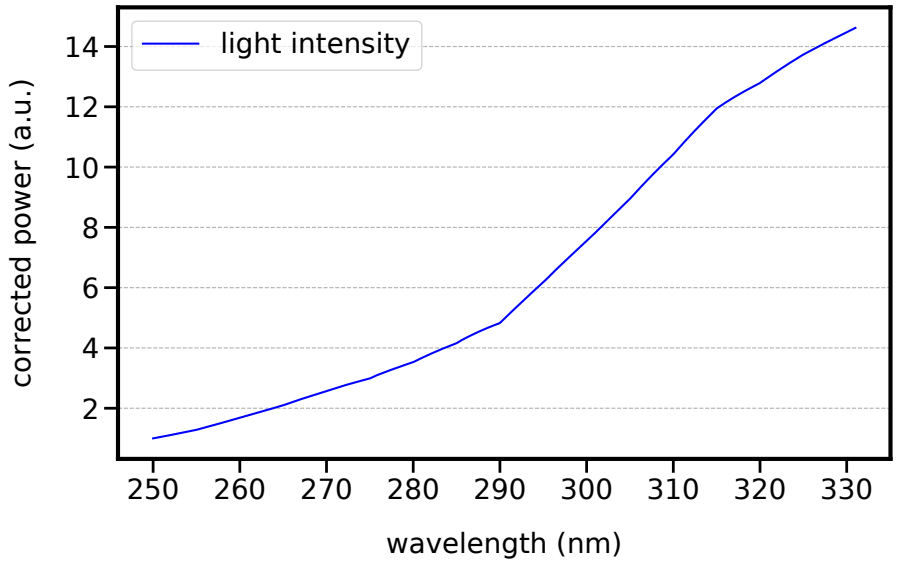

Figure 5.8: This plot shows the estimated relative light intensity (power) of the LDLS with the optical setup as it is used in KATRIN.

5.4.5 Fowler model including corrections

Using the Fowler model (eq. 5.7) and the estimation of the light output (figure 5.8) one can plot the model to see the expected spectrum for different work functions or different effective temperatures. As mentioned in chapter 5.4.2 the temperature parameter describes a broadening of the electron distribution and can absorb other broadening effects. Figure 5.9 shows the model spectrum for $\Phi = 4.0, 4.2, 4.4\,\text{eV}$. It can be seen, that the expected rate at and above the work function is low, but not zero.

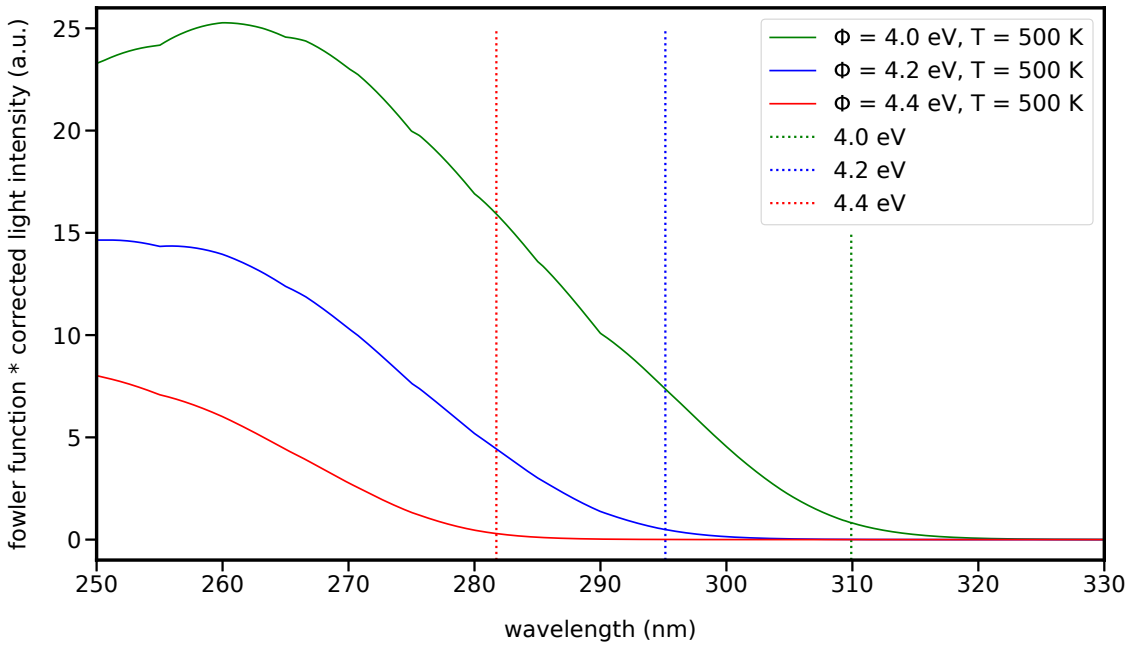

Figure 5.9: This plot shows the model spectrum for $\Phi = 4.0, 4.2, 4.4\,\text{eV}$ including the light intensity spectrum of the optical setup in KATRIN with the LDLS. The dashed lines indicate the work function. A lower work function shifts the curve to the right and also increases the amplitude. The y-axis is proportional to the predicted electron rate.

Measurements with the e-gun at the Elwetritsche setup before the first KATRIN measurement phase showed a work function of the e-gun of about $\Phi = 4.0\,\text{eV}$ and a maximum rate at $\lambda = 260$ - $265\,\text{nm}$. This indicates, that the model can qualitatively describe the spectrum and has some predictive power. In the KATRIN measurements the work function of the e-gun has increased to about $\Phi = 4.44\,\text{eV}$ and the maximum rate has shifted to $\lambda = 250\,\text{nm}$.
Some characterization measurements, for example, the splitter ratio, have not been per-

formed for wavelength below $\lambda < 250\,\mathrm{nm}$, because this region is of no interest for e-gun operation and the shift of the work function from 4.0 to 4.4 eV was not expected at the time these measurements have been performed.
The maximum rate of the e-gun at the KATRIN experiment with the LDLS is lower compared to the test measurements by at least a factor of 30. According to this model, this drop of the rate can not be explained with the change in work function alone. From the STS3a campaign to the KNM1 campaign the rate of the e-gun has reduced by another factor of 1.3, without a significant change of the work function, which would be visible in a change of the optimal wavelength (maximum of the e-gun rate with the LDLS). This gives a hint that some kind of degrading, possibly of the gold coating on the photocathode, is going on.
As mentioned in chapter 5.4.2 the temperature parameter T describes a broadening of the electron distribution near the work function. This leads to an increase of the rate near and above the work function. In the limit of $T \to 0$ the electron density, and for this reason also the rate, would go to zero. In case of a finite temperature states above the work function get more and more populated. This leads to an increase of the rate at and above the work function. Figure 5.10 shows the model curve for $T = 1$, 400 and 600 K. One can see that the region at smaller wavelengths and higher rates is barely affected by the temperature, whereas the region at higher wavelength, around and above the work function, shows a strong increase of the rate with temperature.

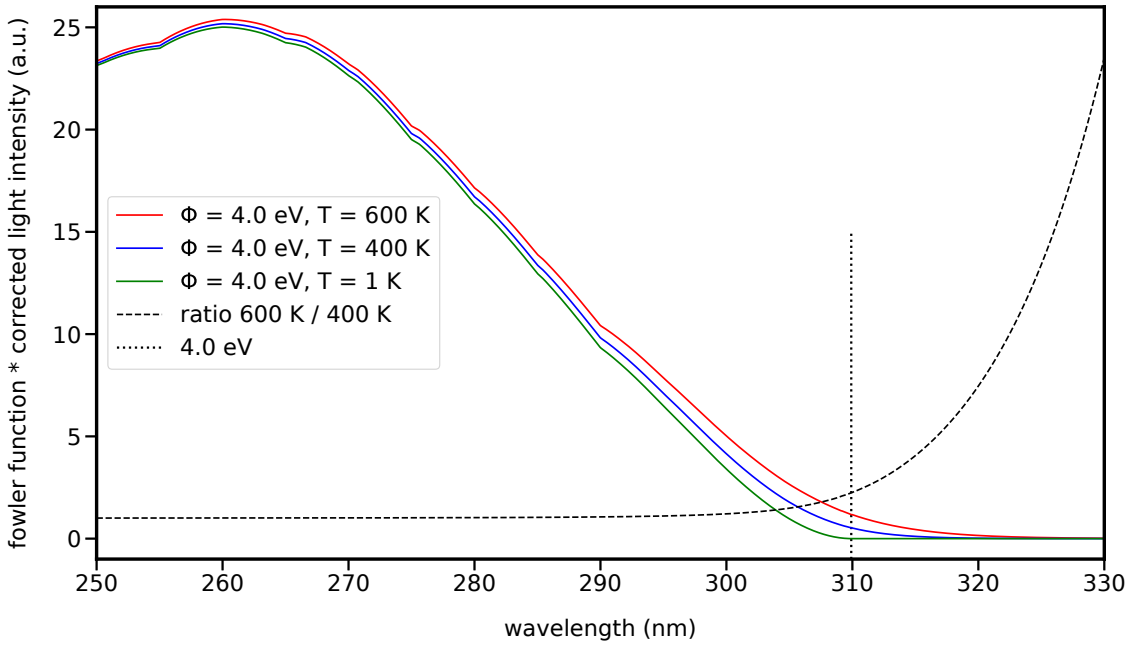

Figure 5.10: Model spectrum for $T = 1$, 400 and 600 K. The dashed vertical line indicates the work function. The dashed curve shows the ratio of the curve at $T = 600$ K and the curve at $T = 400$ K. The ratio increases strongly with wavelength at and above the work function.

5.4.6 Work function of the e-gun

To determine the work function of the main spectrometer with the e-gun, first the work function of the e-gun needs to be measured. This can be done with the Fowler method, which is described in detail in the previous section. For this measurement the LDLS light source is used above and below the expected work function. The retardation voltage of the spectrometer is more positive than the back plate of the e-gun to ensure that no electrons are blocked. The angle of the e-gun is set to $\theta = 0°$, but using a different angle should not affect the measurement. The measured rate is plotted versus the wavelength and fitted with the Fowler model. The light intensity was recorded during the measurement with the diode from Hamamatsu. The efficiency of the diode is extracted from a picture at the manufacturer's website and shown in figure A.6. In the fit, the set value for the wavelength is used for the x-parameter. The light intensity was measured in real-time during the measurement. For this reason it is convenient to use the e-gun rate divided by the light intensity as the y-parameter. In this case, the light intensity curve of figure 5.7 is not used in the model. The y error bars are Poisson error bars of the e-gun counts with a small additive smoothing of 0.5. This reduces the impact of data points with a very low rate at large wavelengths. Data points above the work function (at larger wavelengths) seem to be described less well by the Fowler model, probably because the broadening of the electron distribution in this region is not only caused by a temperature effect, as assumed in the model, but also by defects and impurities. Figure 5.11 shows a measurement of the e-gun work function, which was performed using the FBM detector. Since all electrons are counted an energy filtering with the spectrometer is not needed if there is no tritium in the source. The fit with the Fowler function, including the corrections for the diode efficiency and the splitter ratio, shows that the model function and the data do not agree perfectly and some structure in the residuals is visible. As a consequence, the result of the fit depends on the fit range and a large uncertainty on the work function of $\sigma_\Phi = 60\,\mathrm{mV}$ should be assumed for a conservative approach. The reasons for the discrepancies between the model and the data are most likely dominated by missing input of the optical model. In this work, the light intensity is measured in front of the e-gun and effects caused by the lenses and the light-guiding fibers inside the vacuum are neglected. Further, one should remember that the Fowler function (eq. 5.7) is only valid close to the work function. The results of the work function measurements of the e-gun in STS3a vary between 4.40 eV and 4.46 eV. Based on these results a value of $\Phi_{\mathrm{egun}} = 4.43\,\mathrm{eV}$ and a more optimistic uncertainty of $\sigma_\Phi = 30\,\mathrm{meV}$ is assumed. This uncertainty should at least be correct for the comparison of two Fowler measurements.

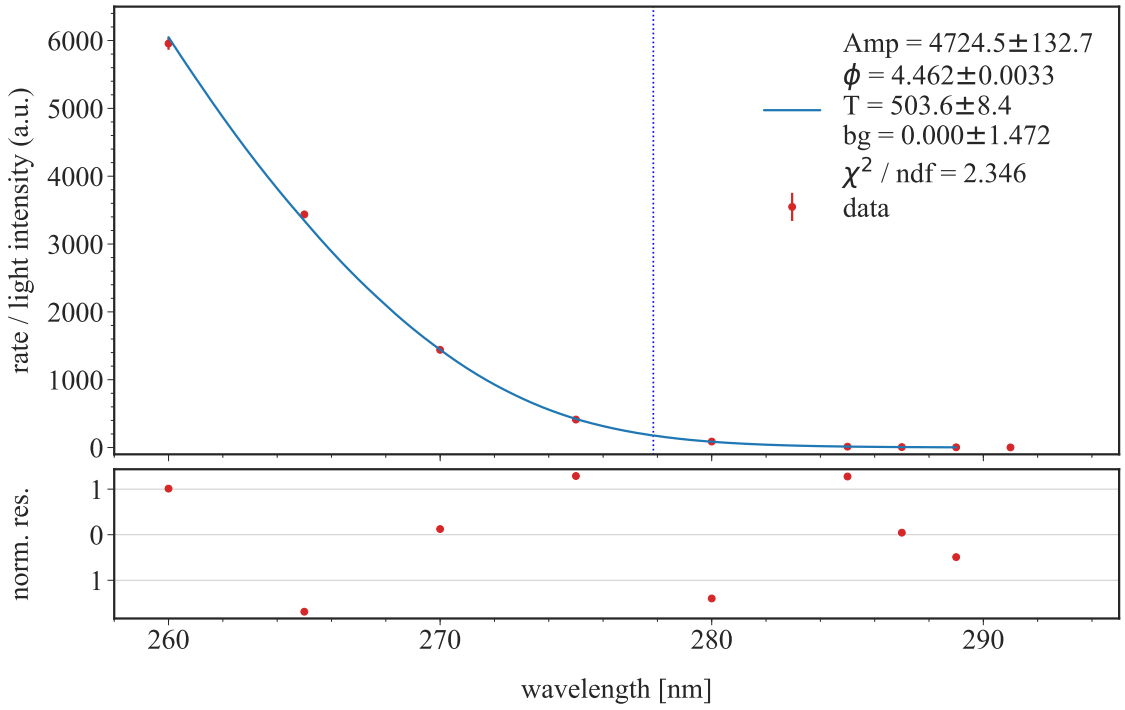

Figure 5.11: Fowler scan of the e-gun performed with the FBM detector. The measurement was performed during the STS3a measurement campaign. The measurement time distribution is such that the data points at large wavelengths and low rates have good statistics. The blue dashed line indicates the position of the fitted work function Φ. *Amp* is the amplitude, T the temperature, and *bg* the background. The fit value of the work function depends on the model of the optical setup and on the fit range. The error of the fit underestimates the uncertainty of the work function. The results from different measurements performed in STS3a vary from 4.40 to 4.46 eV.

Change of the e-gun work function compared to tests: The measurements with the e-gun in KATRIN have shown distinct differences compared to the test measurements before the e-gun was mounted to the KATRIN setup. The first difference is the rate, which was at least a factor of 30 higher during testing than at KATRIN. Secondly, the optimal wavelength for maximum rate has changed from $\lambda = 260\text{-}265\,\text{nm}$ to $\lambda = 250\,\text{nm}$, and finally the work function has changed from $\Phi = 4.0\,\text{eV}$ to $\Phi = 4.43(3)\,\text{eV}$. The second and third observations are directly connected and in good agreement with the model shown in figure 5.9. The strong drop of the rate, however, is not predicted by the model and might be due to hardware changes on the fiber holding structure of the e-gun flange which have been performed shortly before mounting the e-gun to the KATRIN beamline without additional testing. The change of the work function of about $0.4\,\text{eV}$ is most likely caused by the better vacuum conditions in the KATRIN setup, where the vacuum system was pumped for several weeks before the measurements started, whereas the vacuum system during the test measurements was opened frequently and the piping from the e-gun to the TMP had much larger resistance. The pressure during the test measurements can be estimated to be in the $10^{-6}\,\text{mbar}$ range. In KATRIN the pressure at the e-gun is in the $10^{-8}\,\text{mbar}$ range. The exact value is hard to estimate because the pressure gauge is located at a small side arm of the vacuum system at safe distance to the e-gun and most likely at worse vacuum conditions. Nevertheless, this pressure gauge shows a pressure of $p = 2 \cdot 10^{-7}\,\text{mbar}$ (STS3a) and improved into the $10^{-8}\,\text{mbar}$ range in later measurement campaigns.

5.4.7 Determination of the spectrometer work function

The work function of the main spectrometer is crucial for the determination of the tritium Q-value with KATRIN. The work function, together with the applied high voltage and magnetic fields, determines the retarding potential for the signal electrons.
The work function of the main spectrometer can be determined with the e-gun if the energy of the e-gun electrons is known. The energy of the electrons relative to the spectrometer is given only by the offset voltage of the e-gun back plate, the voltage configuration of the inner electrode system and the work function difference between the e-gun and the main spectrometer. To some extent also the high voltage of the vessel has an effect because of the voltage depression. However, since the HV cage of the e-gun and the MS-vessel are on the same potential, it is not required to know the absolute voltage with sub volt precision to determine the work function of the spectrometer. The work function of the e-gun can be determined with the Fowler method as described in the previous section. The back plate offset voltage is measured with a voltmeter with few mV precision. This is also the case for the inner electrode system. To know the effective voltage in the center of the analyzing plane a detailed simulation of the electric fields in the spectrometer is required.
In the standard configuration of the main spectrometer, namely $U_{\mathrm{V}} = -18375\,\mathrm{V}$, $U_{\mathrm{IE}} = -200\,\mathrm{V}$ and $U_{\mathrm{SC}} = +40\,\mathrm{V}$ the voltage depression in the center of the analyzing plane is $\delta U(r = 0) = +1.93\,\mathrm{V}$. Here the subscript V indicates the vessel, IE the inner electrode system (relative to the vessel) and SC the so-called steep cone electrodes (SC offset is relative to IE). This means that the transmission condition in this configuration for e-gun electrons flying along the beam axis is

$$E_{\mathrm{e}} \geq q \cdot U_{\mathrm{V}} + q \cdot U_{\mathrm{IE}} + q \cdot \delta U(r = 0) + \Phi_{\mathrm{MS}}. \tag{5.10}$$

The starting energy they get from the e-gun is

$$E_{\mathrm{e}} = q \cdot U_{\mathrm{V}} + q \cdot U_{\mathrm{BP}} + \Phi_{\mathrm{egun}} + E_{\gamma,\,\mathrm{surplus}}. \tag{5.11}$$

Here U_{BP} is the offset voltage of the back plate and $E_{\gamma,\,\mathrm{surplus}}$ is the kinetic energy of the electrons emitted from the back plate due to the photoelectric effect. This energy ranges from zero to $E_\gamma - \Phi_{\mathrm{egun}}$ (at $T \approx 0$) as is illustrated in figure 5.3. Using the fit result shown in figure 5.11 and using the wavelength of the UV-laser of $\lambda = 266\,\mathrm{nm}$ one can estimate from the Fowler model (eq. 5.7) that about 6 % of the electrons are emitted from the region above the work function. If the same measurement is done with the LDLS at $\lambda = 250\,\mathrm{nm}$ only about 1.2 % of the electrons are emitted from energy states above the work function. In order to find the work function of the spectrometer Φ_{MS} a transmission

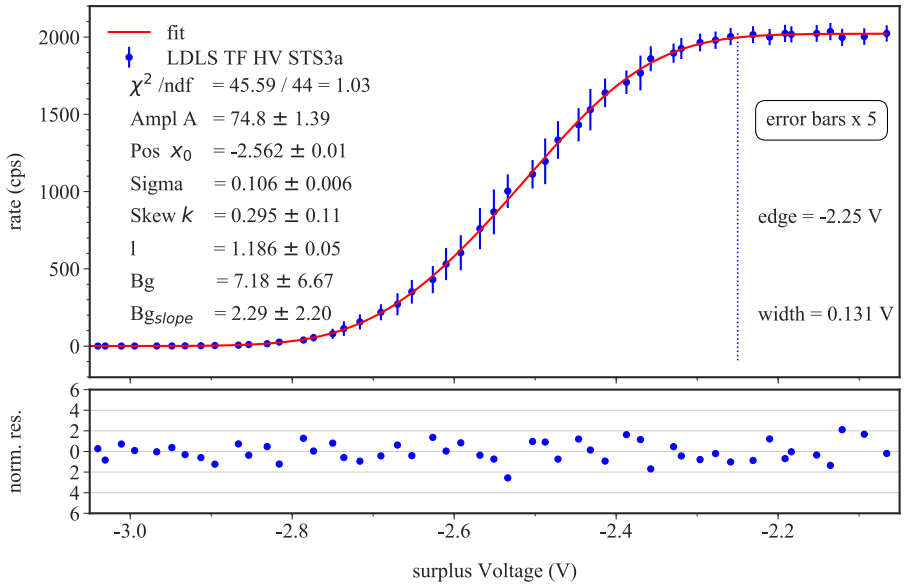

Figure 5.12: Measurement of the transmission function of the e-gun in STS3a using the LDLS light source. The surplus voltage is $U_{\mathrm{IE}} - U_{\mathrm{BP}}$. The 'edge' at 98.8 % transmission is indicated with a blue dashed line at $-2.25\,\mathrm{V}$. The edge position consists of the voltage depression in the analyzing plane of 1.93 V and the difference of the work function of the e-gun and the main spectrometer. The work function of the e-gun is $2.25\,\mathrm{V} - 1.93\,\mathrm{V} = 0.32\,\mathrm{V}$ larger than the work function of the MS.

function is measured and the position is determined where all electrons but 6 % (1.2 % for the LDLS) are transmitted. This position of the transmission function is labeled as 'edge' and indicated with a dashed vertical line in figure 5.12. This method assumes, that the width of the transmission function is entirely caused by the photoelectric effect, which is of course not completely true. In addition to that, the exact surplus energy was not known in STS3a because there was no voltmeter installed at the IE. For this reason an uncertainty on the absolute value of the work function of $\Delta\Phi_{\mathrm{MS}} = 100\,\mathrm{mV}$ has to be assumed. The relative error between two measurements performed under the same conditions is only about 10-20 mV. From the edge position in figure 5.12 and the work function of the e-gun from the previous section we can now calculate the work function of the MS in STS3a:

$$\Phi_{\mathrm{MS}} = \Phi_{\mathrm{egun}} + \text{edge position} \cdot q - \delta U \cdot q \tag{5.12}$$

$$\Phi_{\mathrm{MS}} = (4.43 \pm 0.03)\,\mathrm{eV} - (2.25 \pm 0.1)\,\mathrm{eV} + 1.93\,\mathrm{eV} = (4.11 \pm 0.1)\,\mathrm{eV} \tag{5.13}$$

In this measurement, the voltage of the main spectrometer vessel cancels out because both the IE and the e-gun back plate are based on it. The surplus voltage in figure 5.12 is the difference between the back plate offset and the inner electrode offset

$$\text{surplus voltage} = U_{\text{IE}} - U_{\text{BP}}. \tag{5.14}$$

The main uncertainties are the work function of the e-gun, the voltage of the IE (because the precision voltmeter was installed only after STS3a) and the definition of the 'edge'.

5.4.8 Stability of the work functions

To measure the work function of the spectrometer the work function of the e-gun and the position of the transmission edge have to be determined as described in the previous sections. During the first measurement campaign of **K**ATRIN to find the **n**eutrino **m**ass, the so-called KNM1 phase, the work function of the e-gun was not measured again due to the prioritization of other measurements. However, the e-gun system remained evacuated and untouched between the measurement phases. For this reason it may be assumed, that the work function of the e-gun has not changed significantly. A measurement of the e-gun work function in KNM2, which is discussed later in this section, supports this assumption. In KNM1 the transmission function of the e-gun was measured several times with the UV-laser. When using the UV-laser, the edge is taken at 94 % of the height because 6 % of the electrons are emitted from a region above the work function according to the Fowler model. Figure 5.13 shows a dedicated measurement of the transmission function. In KNM1 many Eloss measurements at different column densities have been performed. These measurements can also be used to find the position of the transmission edge. The effect of inelastic scattering should be negligible as no change of the shape or the width of the transmission edge was observed at higher column densities. The fitted edge positions are listed in table 5.2. The corresponding plots are shown in the appendix in figure A.7 - A.10.
The edge positions found in KNM1 are in good agreement with the edge position found in STS3a. The deviation is within the assumed uncertainty of $\sigma = 100\,\text{mV}$. These measurements show that the work function difference between the main spectrometer and the e-gun has not changed significantly. Since the system was evacuated and untouched between STS3a and KNM1 it is reasonable to assume that both work functions are stable within the assumed uncertainty of the method. The values in table 5.2 further show that a change of the column density does not affect the edge position. This means, that the work function of the e-gun has not changed by more than 100 meV during the Eloss and tritium commissioning phase, because the work function of the MS can not be affected by this.
Since the work function of the e-gun was not measured in KNM1 a conservative approach

is taken and a work function of the main spectrometer in KNM1 of

$$\boxed{\Phi_{\mathrm{MS,\,KNM1}} = 4.1\,\mathrm{eV} \pm 0.2\,\mathrm{eV}} \tag{5.15}$$

is assumed for the Q-value analysis.

Possible change of e-gun work function in KNM2 based on rate change:
The work function of the e-gun was not measured at the end of KNM2 after the neutrino mass measurement. A limit on the change of the work function can be obtained by comparing the rate of the e-gun with the LDLS at 250 nm. In KNM1 the achieved rate was $R = 1500\,\mathrm{cps}$. After the neutrino mass measurements in KNM2 a rate of $R = 1200\,\mathrm{cps}$ was achieved. Assuming that this reduction in rate is not due to degradation but due to an increase of the work function a conservative limit of a possible work function change of the e-gun of

$$\Phi_{\mathrm{egun,\,KNM2}} - \Phi_{\mathrm{egun,\,KNM1}} = 60\,\mathrm{meV} \tag{5.16}$$

can be set based on the Fowler model presented in chapter 5.4.5.

Change of e-gun work function based on Fowler measurements:
The only measurement used in this work that gives direct access to the absolute value of the e-gun work function is the Fowler method. Measurements with the Fowler method have been performed at the beginning of the STS3a campaign in September 2018 and a year later at the beginning of the KNM2 campaign in September 2019. The measurements from STS3a give a work function of

$$\Phi_{\mathrm{egun,\,STS3a}} = 4.43(3)\,\mathrm{eV} \tag{5.17}$$

as stated in section 5.4.6. The measurements at the beginning of the KNM2 campaign have been performed with the FBM in an updated version with a new 'Tristan' detector [136] [27]. These measurements, fitted with the Fowler function and the corrections for the splitter ratio and the diode efficiency give a value of

$$\Phi_{\mathrm{egun,\,KNM2}} = 4.466(20)\,\mathrm{eV}. \tag{5.18}$$

Some example plots are displayed in Appendix A.7. The difference of $\Delta\Phi = 36\,\mathrm{meV}$ is almost within the estimated errors. Since the errors are dominated by the systematic effects of the measurement and also depend slightly on the fit range, it is not clear whether the work function of the e-gun has changed or an external effect, for example a wavelength depending degrading effect of the setup, causes the change. This result is a strong indication that the work function of the e-gun is stable over long time periods.

Possible change of MS work function during KNM2:

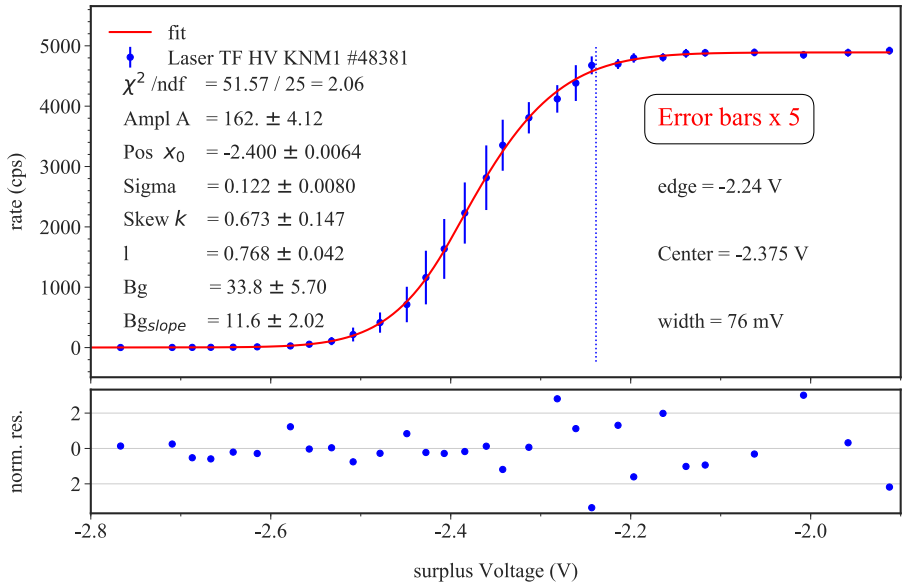

Figure 5.13: Measurement of the transmission function of the e-gun in KNM1 using the UV-laser light source. The surplus voltage is $U_{\mathrm{IE}} - U_{\mathrm{BP}}$. The 'edge' at 94 % transmission is indicated with a blue dashed line at $-2.24\,\mathrm{V}$. The edge position consists of the voltage depression in the analyzing plane of 1.93 V and the difference of the work function of the e-gun and the main spectrometer.

Based on the assumption that the work function of the e-gun did not change by more than 60 meV and comparing the last value in table 5.2, which was taken after the neutrino mass measurements, with the second to last, which was taken before the neutrino mass measurements, one can set a conservative limit on the change of the main spectrometer work function of

$$\Delta\Phi_{\mathrm{MS,\,KNM2}} < 0.1\,\mathrm{eV} \tag{5.19}$$

during the time of the KNM2 neutrino mass measurements. The results of the individual measurements are shown in table 5.2 and figure 5.14.

Date(dd.mm.yy)	Campaign	Measurement	CD (%)	Edge (V)	Φ_{MS} (eV)
26.09.18	STS3a	TF w. LDLS	0	-2.25	4.11
01.03.19	KNM 1	TF w. laser	0	-2.24	4.12
02.03.19	KNM 1	Eloss	0	-2.22	4.14
08.03.19	KNM 1	Eloss	15	-2.21	4.15
11.03.19	KNM 1	Eloss	50	-2.21	4.15
29.03.19	KNM 1	Eloss	25	-2.19	4.17
15.09.19	KNM 2	Eloss	0	-2.05	4.31
24.09.19	KNM 2	Eloss	100	-2.11	4.25
29.11.19	KNM 2	Eloss 100 K	~ 30	-2.13	4.23

Table 5.2: Fitted edge positions in STS3a and in Eloss measurements with tritium in KNM1 and KNM2. The Eloss measurements are performed with the UV-laser. The changes in the edge position for different measurements during KNM1 is small compared to the systematic uncertainties of about 100 mV. This is a hint the work function does not change with time or column density. However, there are changes to KNM2. This might be because the MS was baked between KNM1 and KNM2. The MS work function Φ_{MS} is calculated assuming a constant work function of the e-gun. The absolute value of the work function has an uncertainty of 0.2 eV. However, relative changes during a measurement phase have a smaller uncertainty of only 20 mV. The drop of the work function from the 0% CD Eloss measurement in KNM2 to the 100% CD measurement can be regarded as significant. The CD given in this table is the set value.

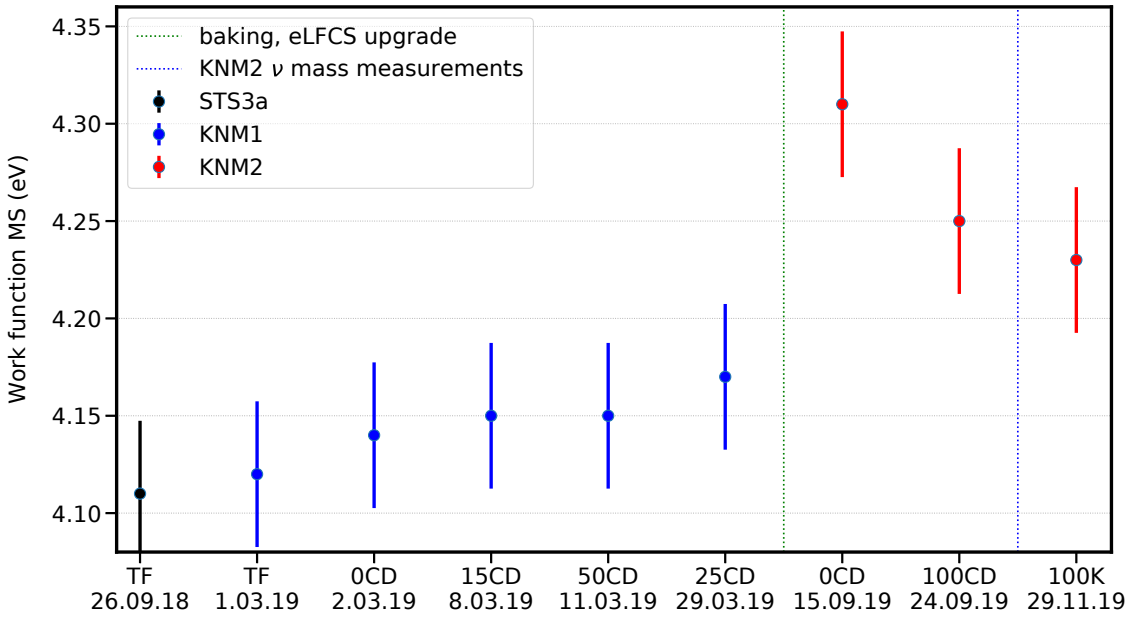

Figure 5.14: Evolution of the MS work function assuming a constant e-gun work function of $\Phi_{\text{egun}} = 4.43\,\text{eV}$. The black data point is from a TF measurement in STS3a with the LDLS, all other data points are measured with the laser. The green dashed line indicates the period between KNM1 and KNM2 where a lot of changes happened, i.e. the MS was baked, the alignment of the detector changed, the air coil system was upgraded, the IE voltage supply and readout was changed, etc. This can lead to systematic effects which are neglected in this analysis. The blue dashed line indicates the KNM2 m_ν measurements. The data point to the right of it is taken in the WGTS high temperature mode. The plotted error bars of 41 meV assume an uncertainty of the e-gun work function of 30 meV, of the transmission edge position of 20 meV and on the voltage depression of 20 meV.

5.5 Work function of the rear wall

The rear wall (RW) is a gold plated stainless steel disk upstream of the WGTS. The magnetic field configuration in KATRIN is such that the magnetic flux is covered by the focal plane detector on one end and by the RW on the other end. Further, the magnetic field between the source tube and the RW is limited to the magnetic field of the WGTS so that every electron or ion starting in the WGTS can reach the RW, without magnetic reflection, independent of their starting angle. It is assumed that the plasma in the WGTS is conductive and connected to the RW. For this reason, the RW determines the potential in the WGTS, at least if the RW bias voltage is within a certain range. So-called 'PRO (**p**lasma **r**ear wall **o**ptimization in) KATRIN' measurements investigate this in detail and show that a change of the electric potential of the RW changes the potential in the source, see e.g. [45]. The RW bias voltage in KNM1 was set to $U_{\mathrm{RW}} = -150\,\mathrm{mV}$. According to the PRO KATRIN measurements, this results in a strong coupling in the inner half of the flux tube and less coupling in the outer half. For more details in this see [41] [45].

5.5.1 Work function investigations in STS3a

At the beginning of the STS3a measurement campaign, the work function of the RW was measured with the Fowler method. The FPD is used as a detector and the analysis is done for each detector pixel to get spatial resolution. Due to the low statistics of the measurement only the central pixels can be evaluated. In addition to the work function also the transmission function was measured. The position of the transmission function is not used to find the absolute value of the work function, but to get some information on the radial structure and the shift over time.

After deuterium has been in the source to do the Eloss measurements with the e-gun, the work function measurements of the RW have been repeated. This time there was residual gas, including tritium, at the rear wall, which disturbed the measurements. In the case of the work function measurement, tritium acts as a constant background, which makes it harder to perform the fit. For the transmission function measurement, the low energy electrons of the tritium create an additional signal, which broadens and, most likely, slightly shifts the transmission function.

Figure 5.15 shows the result of the work function measurements before and after the deuterium gas (which contains traces of tritium) has been injected into the source. One can see, that the work function was lowered by the gas by roughly $\Delta\Phi_{\mathrm{RW}} = 100\,\mathrm{meV}$. However, because of the background caused by residual gas, the analysis of this data is less reliable.

To do a robust analysis of the transmission function measurement, an error function was

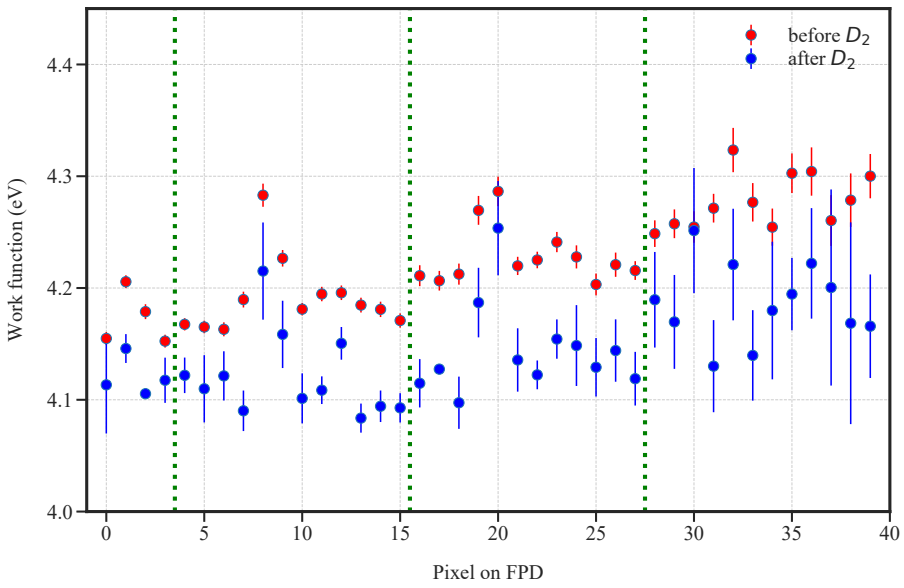

Figure 5.15: Work function fitted for each pixel with the Fowler function. The measurement was performed before (red) and after (blue) a gas mixture of 99 % deuterium and 1 % tritium was in the WGTS. For the measurement the source was pumped down again, but some residual gas remained at the rear wall. The green dashed lines indicate the rings of the FPD. The light signal is strongest in the center (pixels 0-3) and gets weaker to the outside, which explains the increasing size of the error bars. The data points in the individual fits use statistical error bars and the error bars shown in the plot are the errors from the Fowler fit with minuit.

fitted to the data. The used fit function is defined as

$$\frac{1}{2}A(1 - ERF[(x - \mu)/(\sqrt{2}\sigma)]) + Bg \tag{5.20}$$

where A is the amplitude, μ the position, and σ the width of the functions. Bg is a constant to describe the background and ERF is the error function defined as

$$ERF(x) = \frac{2}{\sqrt{\pi}} \int_0^x e^{-y^2} dy \tag{5.21}$$

Equation 5.20 is not the optimal description of a transmission function, but it is simple and robust. The result of the fit to the individual pixels can be seen in figure 5.16, which shows the fitted position for each pixel. As stated above the fit of the data after gas was inside the source may be systematically shifted because of the tritium present in the source. However, this measurement confirms the trend that the work function is lowered by the gas, which can also be seen in the measurement of the work function with the Fowler method.

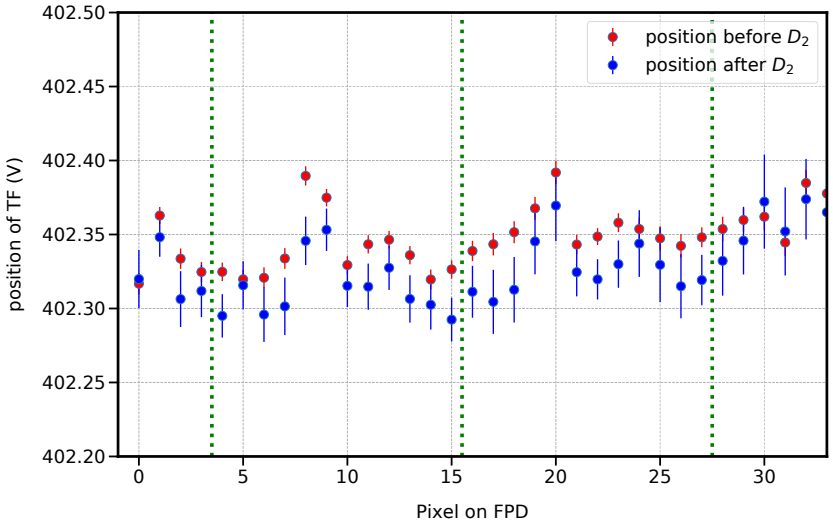

Figure 5.16: Position of the fitted transmission function (eq. 5.20) for each pixel. The measurement was performed before (red) and after (blue) a gas mixture of 99 % deuterium and 1 % tritium was in the WGTS. For the measurement, the source was pumped down again, but some residual gas remained at the surface of the rear wall. A higher position of the TF indicates a higher work function. The fit of the data after gas was inside might be systematically shifted because of the additional signal caused by the residual tritium.

5.5.2 Work function investigations before KNM1:

At the beginning of KNM1, before tritium was inserted for the first time, the work function of the RW has been measured with the Fowler method. Compared to STS3a the optical system was modified and provided more light intensity at the same wavelength. With this upgrade it is possible to fit the work function of more pixels even though the light was mainly focused on only three pixels in the first ring. An exemplary measurement is shown in figure 5.17. The result of the measurement for all available pixels is shown in figure 5.18.

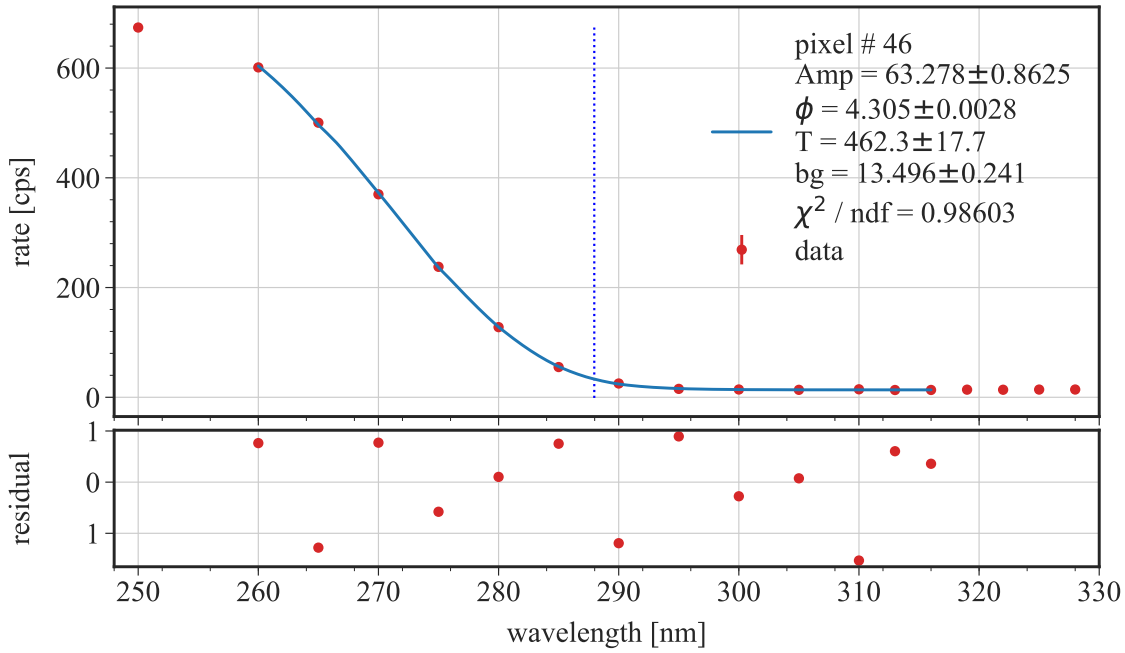

Figure 5.17: Fowler measurement of the rear wall. This plot shows the data taken on pixel 46 of the FPD. The fit is performed using the model described in chapter 5.4.5. The blue dashed line indicates the best fit value of the work function. The set value of the monochromator is used as the x-value.

One can see a ring wise structure and also a trend towards higher work functions for outer radii. The best fit values are plotted again in figure 5.19 where the pattern is more easily understandable. The fitted amplitude is shown in the appendix in figure A.11. It gives a good impression of the light intensity distribution.
After the injection of T_2 it is unfortunately no longer possible to measure the work function of the rear wall with this hardware setup, because the T_2 sitting on or in the RW cannot be removed efficiently enough. The remaining T_2 causes a large background rate which makes

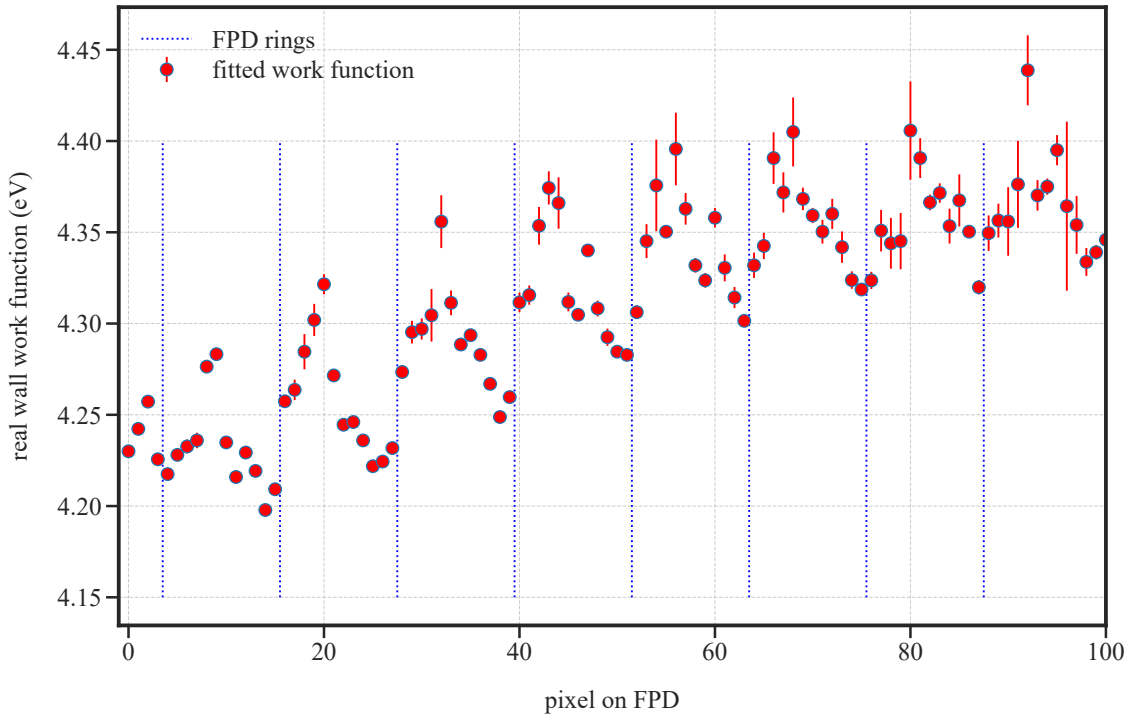

Figure 5.18: Result of the Fowler measurement performed before tritium was injected in KNM1. The plot shows the fit result of the work function parameter for each pixel. The error bars are the error given by minuit. The dashed lines indicate the ring structure of the FPD that is shown in a more visually accessible way in figure 5.19. The mean value of the plotted data points is $\Phi_{mean} = 4.29\,\mathrm{eV}$ with a standard deviation of $0.05\,\mathrm{eV}$.

it impossible to measure with the FPD at only $U_{\mathrm{MS}} = 500\,\mathrm{V}$ retarding voltage at the MS. For the future, it might be possible to perform the Fowler measurement with a readout of the current at the RW instead of counting electrons at the FPD. This would require an upgrade of the hardware and better understanding of the interaction between the RW and the charged particles in the source, which is both outside the scope of this thesis. The average work function over the measured pixels is $\Phi_{\mathrm{RW}} = 4.29\,\mathrm{eV}$ with a standard deviation of about $54\,\mathrm{meV}$. Note that due to the strong focus of the light to the center region of the rear wall, the outer one-third of the pixels is excluded from this analysis. In the KATRIN KNM1 analysis the outer rings are also excluded and only 117 of the 148 pixels are used. In addition to that, the analysis contains some systematic effects. The fitted result does, for example, depend a bit (shift of Φ_{mean} by $10\,\mathrm{meV}$) on the fitting range of the Fowler function, and on assumptions on the exact wavelength dependence of the light

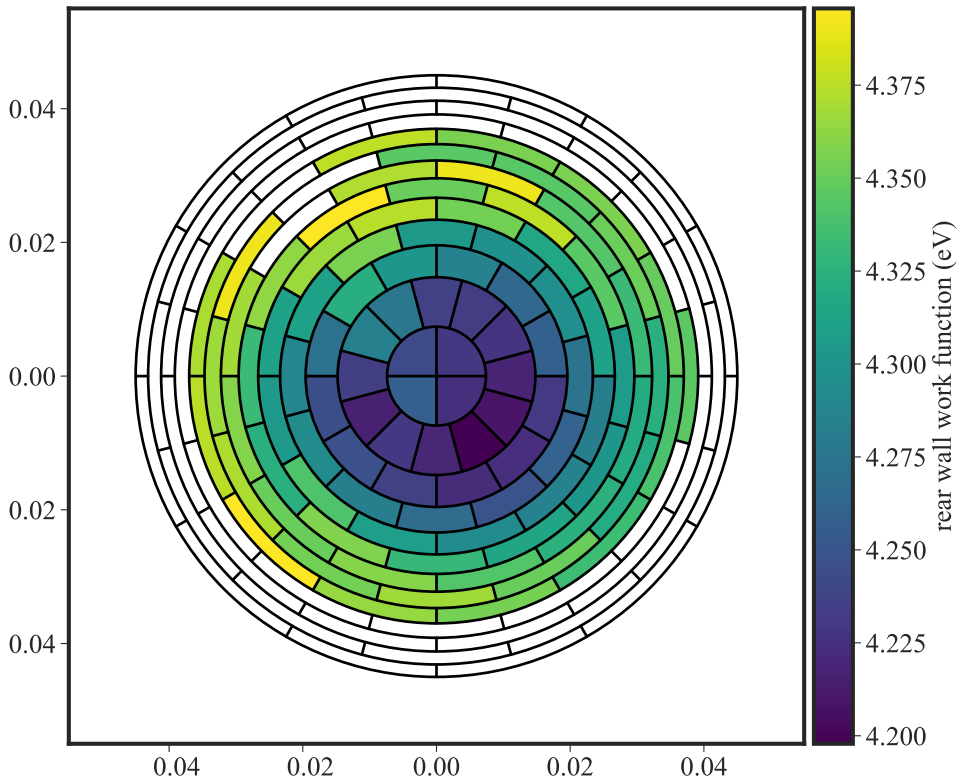

Figure 5.19: Result of the Fowler measurement performed before tritium was injected in KNM1. The plot shows the best fit value of the work function parameter for each pixel. The outer pixels (white) have not been fitted because the signal from the photoeffect is too weak in those pixels and the fit does not work reliably.
The x- and y-axis show the detector size in m.
Remark1: The alignment of the setup is such that the hole at the center of the RW is mapped mostly on the top left bullseye pixel and partly on the top right and bottom left.
Remark2: The potential depression in the analyzing plane of the MS does not affect this result since all electrons have sufficient surplus energy to overcome the electric filtering.

intensity. For example the wavelength dependence of the entrance window to the WGTS is not included in the model. However, the pattern visible in figure 5.19 is robust and still appears even if the fit parameters like the fitting range or the allowed temperature range are changed. Also the spread of the work function from the inner to the outer pixels of about 150 meV is large compared to the systematic effects. The radial dependence is also qualitatively consistent with a Kelvin probe measurement by F. Friedel, which is displayed in figure A.12. In the Fowler measurement, a radial pattern is visible, but it seems to be shifted a bit to the lower right in figure 5.19. Since the e-gun beam, which goes through the center of the RW, hits the detector in the central pixels, this shift can not be explained by a misalignment between the detector and the rear wall and is most likely a real feature.

5.5.3 Summary of RW work function investigations

The work function of the RW in the KATRIN beamline can be measured with the Fowler method if the source is empty and the background from tritium is at maximum a few cps per FPD pixel at an MS retardation voltage of maximum $|U_{\mathrm{MS,\,max}}| = 500\,\mathrm{V}$. Under these source conditions the RW has a mean work function of about 4.3 eV and shows a radial increase of about 0.1 eV from the center to the outside. The center of this radial structure is slightly shifted to the lower right (bottom west) as seen from behind the FPD, putting the minimum in the first ring. A radial dependence with a lower work function in the center was also observed by a measurement with a Kelvin probe before the RW was mounted to the KATRIN beamline. Measurements before and after the Eloss measurements with D_2 gas in STS3a indicate that deuterium on the surface of the RW lowers the work function by about 100 meV. Since the measurement can only be done after the gas is pumped out of the source again, the effect might be even stronger in nominal KATRIN conditions for a neutrino mass run. An additional uncertainty of the work function value of 50 meV should be assumed because of the uncertainties and the incompleteness of the optical model which is required as an input for the Fowler method. This value is larger compared to the work function uncertainty of the e-gun because the light intensity was not recorded during the measurement.

5.6 Starting potential in the WGTS

The starting potential of β-electrons in the WGTS is a key ingredient for the determination of the tritium Q-value. Plasma simulations of the WGTS and RW setup, for example by L. Kuckert [84], suggest that the plasma couples to the RW if the bias voltage of the RW

is chosen such that the bias voltage compensates the work function difference between the RW and the WGTS beam tube. In this case, the RW work function and the bias voltage would be equivalent to the starting potential of the electrons of the source. Measurements with the PRO-KATRIN method, where the RW bias voltage is changed and the resulting change of the rate of tritium signal electrons is compared to a change of the MS-retarding voltage, indicate that the RW bias voltage in KNM1 was chosen such that the RW couples to plasma in the source and influences the starting potential of the electrons in the inner half area of the tube. It is assumed here, that the potential in the inner half of the WGTS is equivalent to the RW work function plus the additional bias voltage. Deep scans into the spectrum to evaluate the endpoint show that there is no radial dependence of the endpoint within the uncertainties. This indicates, that the starting potential over the whole radius is the same. For more details on this see [41]. Studies of the plasma coupling with an additional RW illumination and potential changes of the RW work function with the RW illumination can be found in [45]. In KNM1 this RW illumination was not used during the neutrino mass science runs.
The simulations and measurements mentioned above allow us to estimate the starting potential in the WGTS from the measured RW work function of 4.3 eV, the observed reduction of the work function by 100 meV due to the additional tritium gas load, and by the applied bias voltage of −150 mV, which acts equivalent to an increase of the work function. Because of the uncertainty how the work function behaves with tritium in the source and whether this line of arguments for the starting potential really holds, we assume a conservative uncertainty of 400 meV. This leads to a starting potential of the electrons in the WGTS of

$$\Phi_{\mathrm{e,\,WGTS}} = \Phi_{\mathrm{RW}} - 0.1\,\mathrm{eV} + 0.15\,\mathrm{eV} \pm 0.4\,\mathrm{eV} \tag{5.22}$$

$$\Phi_{\mathrm{e,\,WGTS}} = 4.35\,\mathrm{eV} \pm 0.4\,\mathrm{eV}. \tag{5.23}$$

5.7 Q-value of tritium in the first tritium campaign

The first tritium (FT) campaign of KATRIN was a commissioning run for the tritium system and the neutrino mass scanning. This campaign took place in spring 2018, before the rear section (RS) was ready for operation. As a direct consequence, there was no rear wall (RW) and no e-gun available to do any work function measurements. The stainless steel gate valve upstream of the WGTS was closed and acted as the RW in the sense that the magnetic flux is completely guided to this surface. Since there is no work function

measurement of this valve it is assumed to have the same work function as the inner electrode system because both are made from stainless steel. This assumption does of course have a large uncertainty because it is known that the vacuum conditions have a strong effect on the work function and can easily change it by $\Delta\Phi = 0.5\,\mathrm{eV}$ or more. The used gas mixture was 99 % D_2 and 1 % T_2. With this small amount of tritium, it is unlikely to have a significant plasma potential. Since no additional information is available eq. 5.6 can be used with a conservative approach to the potential difference of $\Delta\Phi = 0 \pm 1\,\mathrm{eV}$:

$$Q = E_0 + 1.72\,\mathrm{eV} \pm 1\,\mathrm{eV}. \tag{5.24}$$

The reported endpoint from this first tritium measurement is [2]:

$$E_{0,FT} = 18574.39 \pm 0.25\,\mathrm{eV}, \tag{5.25}$$

which leads to a Q-value of

$$\boxed{Q_{\mathrm{FT}}(\mathrm{T_2}) = 18576.1 \pm 1\,\mathrm{eV}.} \tag{5.26}$$

5.8 Q-value of tritium in the first science run of KATRIN

In the first science run (KNM1) the full beamline of KATRIN was operational and the investigations on the potentials presented previously in this chapter can be used to determine the Q-value of tritium β-decay in KATRIN.
The fitted endpoint E_0 from the first science run is presented in [33]:

$$E_{0,\mathrm{KNM1}}(\mathrm{T_2}) = 18573.7\,\mathrm{eV} \pm 0.1\,\mathrm{eV}. \tag{5.27}$$

This includes the uncertainty of the absolute value of the applied retardation voltage of about 93 mV [107]. As mentioned earlier in this chapter the recoil E_{rec} is given by

$$E_{rec} = 1.72\,\mathrm{eV}. \tag{5.28}$$

The work function of the main spectrometer is

$$\Phi_{\mathrm{MS}} = 4.1\,\mathrm{eV} \pm 0.2\,\mathrm{eV} \tag{5.29}$$

and the starting potential of the electrons in the WGTS is

$$\Phi_{\mathrm{WGTS}} = 4.35\,\mathrm{eV} \pm 0.4\,\mathrm{eV}. \tag{5.30}$$

The Q-value of tritium $Q(T_2)$ in KATRIN is given by

$$Q(T_2) = E_0(T_2) + E_{rec} - \Phi_{\mathrm{WGTS}} + \Phi_{\mathrm{MS}}, \tag{5.31}$$

which adds up to

$$\boxed{Q_{\mathrm{KNM1}}(\mathrm{T_2}) = 18575.2\,\mathrm{eV} \pm 0.5\,\mathrm{eV}.} \tag{5.32}$$

This result can now be compared to results from Penning trap measurements. Figure 5.20 shows the results of several measurements with Penning traps and the value of the KATRIN experiment obtained with the work function investigations performed in this work. The values for the mass difference $\Delta M(^3\mathrm{He,T})$ are taken from [93] and the energy difference of

$$\Delta M(^3\mathrm{He,T}) - Q(\mathrm{T_2}) = 16.29\,\mathrm{eV} \tag{5.33}$$

is subtracted. The detailed energy scheme from which this value was extracted, is displayed in figure 5.1. The obtained Q-value of KATRIN and the results of the Penning trap measurements agree within the uncertainties. This indicates that the absolute energy scale of KATRIN is well understood. The uncertainty of the Q-value determination of KATRIN is dominated by the uncertainty of the source potential. To improve the result, further investigations of the source potential are needed.

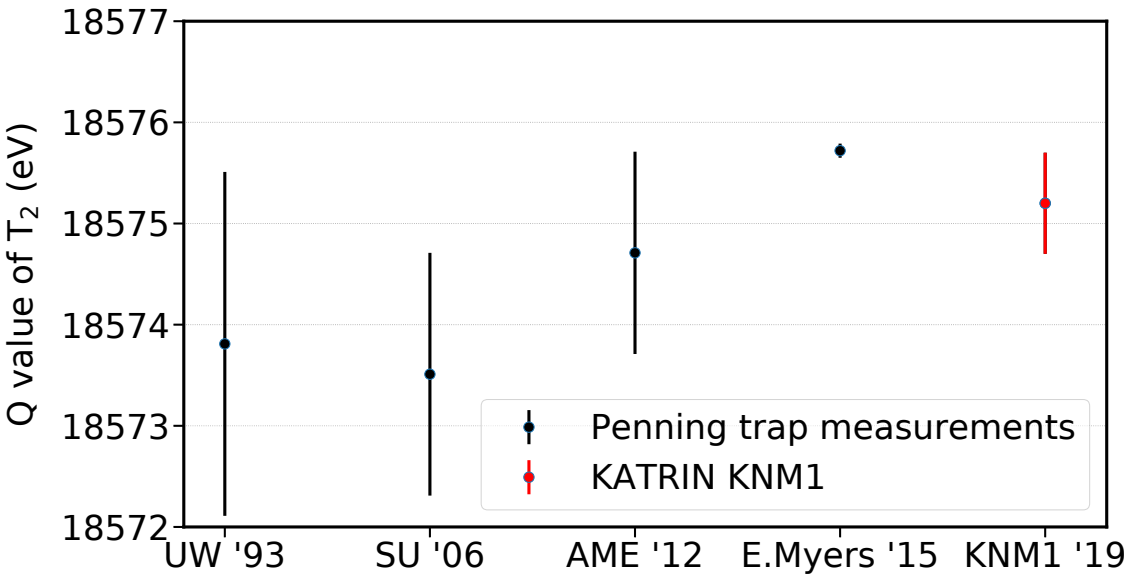

Figure 5.20: Comparison of the tritium Q-value obtained by Penning trap measurements (black) and the result obtained in the first neutrino mass run of KATRIN (red). The results agree within the uncertainties. The values for the Penning trap measurements are taken from [140], [94], [143] and [93].

Chapter 6

Possible plasma instabilities in KATRIN

6.1 General introduction to plasma instabilities

To understand electromagnetic waves and possibly resulting instabilities in a plasma one needs to understand the response tensor of the plasma. This is most simple for cold and unmagnetized plasma. An easy derivation can be made starting from the fluid equations. This derivation can be found in most textbooks on plasma physics.
We start with the differential form of the Maxwell equations

$$\nabla \times \vec{B} = \mu_0 j + \frac{1}{c^2}\frac{\partial \vec{E}}{\partial t} \quad ; \quad \nabla \times \vec{E} = -\frac{\partial \vec{B}}{\partial t} \tag{6.1}$$

and perform a harmonic analysis

$$i\,\vec{k} \times \vec{B} = \mu_0 \vec{j} + \frac{-i\omega}{c^2} E \quad ; \quad i\,\vec{k} \times \vec{E} = i\omega \vec{B} \tag{6.2}$$

We eliminate B and get

$$\vec{k} \times (\vec{k} \times \vec{E}) + \frac{\omega^2}{c^2}\vec{E} + i\omega\mu_0 \vec{j} = 0 \tag{6.3}$$

We try to get a relation between $\vec{j}$ and $\vec{E}$. With the help of Ohm's law $\vec{j} = \underline{\underline{\sigma}}\vec{E}$ we get

$$\vec{k}(\vec{k} \cdot \vec{E}) - \vec{k}^2 \vec{E} + \frac{\omega^2}{c^2}\vec{E} + i\omega\mu_0\sigma\vec{E} = 0 \tag{6.4}$$

for a homogeneous medium. For a dielectric we can write Ampere's law as

$$\frac{1}{\mu_0}\nabla \times \vec{B} = \vec{j}_{ext} + \frac{\partial \vec{D}}{\partial t} = \frac{\partial}{\partial t} \quad | \text{ if } j_{ext} = 0 \tag{6.5}$$

with the dielectric tensor ϵ being

$$\underline{\underline{\epsilon}} = 1 + \frac{1}{-i\omega\epsilon_0}\underline{\underline{\sigma}} = 1 + \frac{i\mu_0 c^2}{\omega}\underline{\underline{\sigma}}. \tag{6.6}$$

With this tensor we find

$$\vec{k}(\vec{k}\cdot\vec{E}) - k^2\vec{E} + \frac{\omega^2}{c^2}\epsilon(\vec{k},\omega)\vec{E} = 0 \tag{6.7}$$

This can be written as

$$\underline{\underline{D}}\cdot\vec{E} = 0 \tag{6.8}$$

with

$$\underline{\underline{D}} = \vec{k}\vec{k} - k^2\mathbb{1} + \frac{\omega^2}{c^2}\underline{\underline{\epsilon}} \tag{6.9}$$

To get a non-trivial solution of $\underline{\underline{D}}\cdot\vec{E} = 0$ we need

$$\det|D| = 0 \tag{6.10}$$

This gets us equations which relate k and ω, which tells us the wavelength and frequencies we can expect.
If ω is a complex number it can be written as

$$\omega = \omega_r + i\gamma \tag{6.11}$$

where γ describes the damping or growth of the wave over time.

6.2 General Introduction

The WGTS tube is a 10 m long metal tube with 9 cm diameter and a temperature of $T = 30\,\mathrm{K}$. The tritium gas, which is constantly injected in the center of the KATRIN WGTS and flows to either end of the tube, forms a cold, partially ionized and strongly magnetized plasma. The number of neutral particles is many orders of magnitude larger than that of the charged particles. For this reason the movement of these neutral particles can be taken from gas dynamic simulations, which do not take the plasma into account. The motion of the ions is strongly effected by the neutral gas as they will thermalize quickly and move from the center towards either end of the source. The motion of ions and electrons is in addition to that also strongly effected by the magnetic field parallel to the WGTSs long axis. In the KATRIN experiment it is generally assumed, that all beta electrons from the tritium decay are born in the same electric starting potential. However, it has to be assumed, that a plasma could lead to a spatial profile of the electric potential or to variations in time. This has to be investigated in order to properly understand the measured beta spectrum in the KATRIN experiment.

In the following the growth rate of three possible plasma instabilities is investigated based on analytic formula. In this investigation the properties displayed in Table 1 are assumed. These numbers correspond to the average electron and ion density in the WGTS tube. The particle density, temperature and magnetic field are assumed to be homogeneous.

Name	Comment	Value
Magnetic Field	$0.7 \cdot$ 3.6 T	25200 G
Neutral Density		10^{14} cm^{-3}
Electron Density		10^{6} cm^{-3}
Ion Density		10^{6} cm^{-3}
Temperature		30 K

Table 6.1: Plasma conditions in KATRIN.

6.3 Electron spectrum

The electron energy spectrum is provided by F. Glueck et al. [95] in dN/dlogE shape. We are interested in the velocity, so we transform it to a dN/dv spectrum (see section A.8). We approximate the dN/dv spectrum by two Gaussians.

A Gaussian can be defined as

$$G(x) = A \cdot e^{\frac{-(x-x_0)^2}{(2\sigma^2)}} . \tag{6.12}$$

In this case the integral is given by

$$\int_{-\infty}^{x} G(x')dx' = \frac{1}{2}B \cdot \left(1 + erf\left(\frac{x - x_0}{\sqrt{2} \cdot \sigma}\right)\right) \tag{6.13}$$

with $B = \sqrt{2\pi} \cdot A \cdot \sigma$.

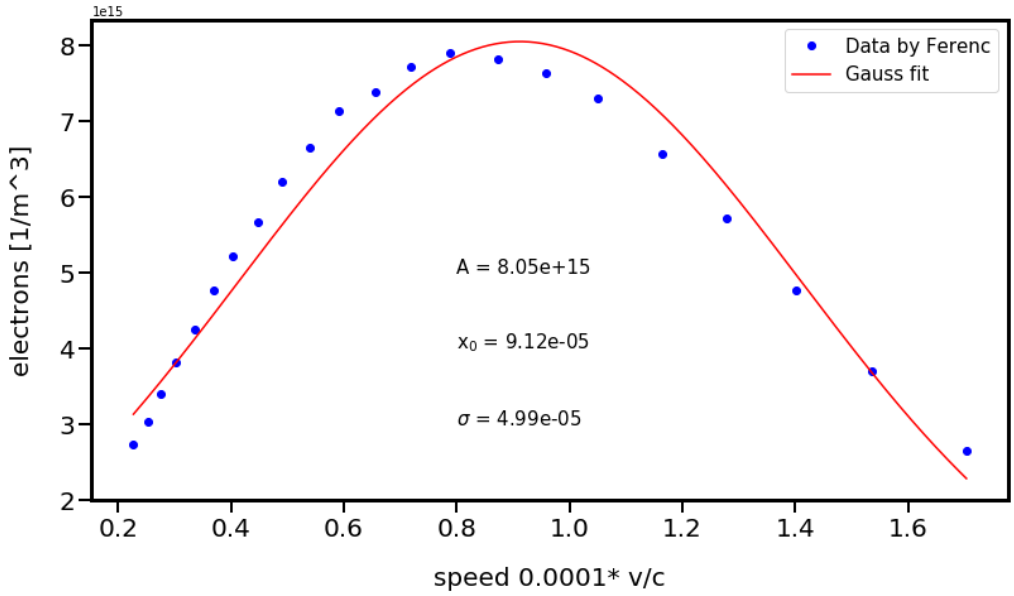

Figure 6.1: Gauss fit to the velocity distribution of the background ("core") electrons e_c in the KATRIN WGTS. The Gauss is clearly only a rough approximation of the spectrum, but it is sufficient to get first estimations on the plasma properties.

We interpret the position as the drift velocity $v_{0i} = x_{0i}$ and get the thermal speed from width of the Gaussian $v_i = \sigma_i$. The integral over the functions gives the number density of electrons N_e. We normalize the spectrum such that the amount of slow electrons N_c is

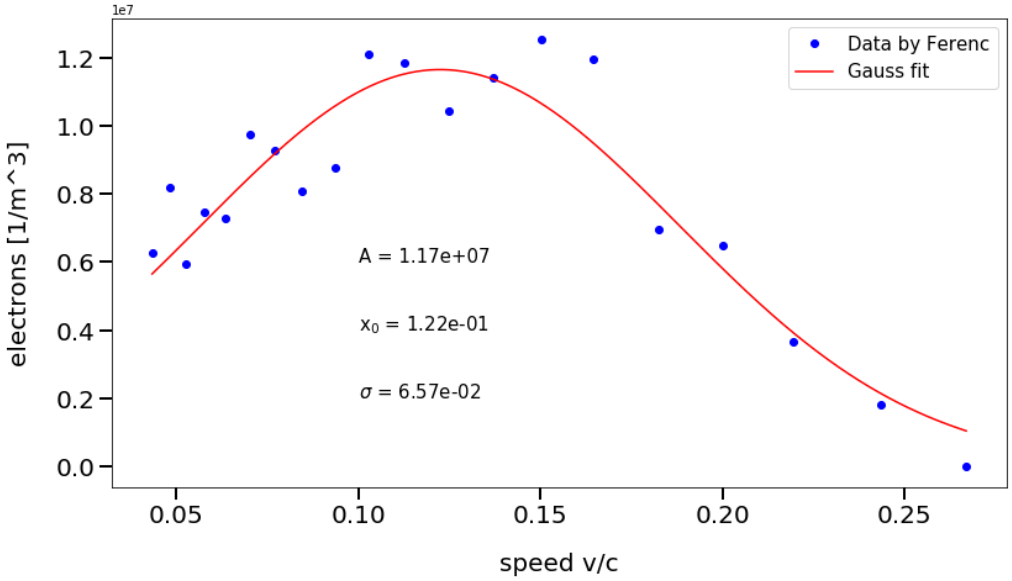

Figure 6.2: Fit to the fast ("beam") electrons e_b.

approximately the total number density of electrons N_e, thus $N_e \approx N_c = 10^{12}$ m^{-3}.

The electron density is given by the integral of the fit curve. For the background electrons we get, as mentioned above, $N_c = 10^{12}\ m^{-3}$ by construction. This is our estimated number of electrons in the source. For the fast electrons we get $N_b = 1.8 \cdot 10^6\ m^{-3}$ (with $v = 0$ as lower bound of the integral). The drift speed of the slow electrons is overestimated by this analysis, because the effective drift speed of the electrons is about the same as the drift speed of the ions because of charge conservation. The drift speed of the ions is about the same as the flow speed of the tritium gas. This means that the drift speed of the slow electrons x_{0c} is of order 10 m/s. For the fast electron population this argument does not apply, and we can take the fit result $x_{0b} = 0.122\,c$, where c is the speed of light. The numbers are again summarized in table 6.2.

Population	observable	value
core	avg. number density	$N_c = 10^{12}\,\mathrm{m}^{-3}$
	drift speed	$v_{0c} = 10\,\mathrm{m/s}$
	thermal speed	$v_c = \sigma_c = 15\,000\,\mathrm{m/s}$
beam	avg. number density	$N_b = 10^{6}\,\mathrm{m}^{-3}$
	drift speed	$v_{0b} = x_{0b} = 0.122\,c = 3.66 \cdot 10^{7}\,\mathrm{m/s}$
	thermal speed	$v_b = \sigma_b = 1.97 \cdot 10^{7}\,\mathrm{m/s}$

Table 6.2: Electron populations in the WGTS assumed for the plasma estimations in this chapter.

6.4 Current driven instability in partially ionised media

The current driven instability in partially ionised media is investigated based on a paper by Reville et al. [109]. The growth rate of the instability is given in formula 6 of the paper. In our case both the background and the jet component consist of electrons. For simplicity reasons we use the number of electrons $N_e = 10^{12}$ m^{-3} instead of n_i and $\omega_{ce} = 4.4 \cdot 10^{11} s^{-1}$ instead of ω_{ci}. The speed of sound in tritium at $T = 30$ K is assumed to be $v_s = 234$ m/s. With the Alfven velocity $v_A = 3.17 \cdot \ 10^{10}$ m/s we obtain

$$Im(\omega) = \frac{1}{2} \frac{v_s}{v_A} \frac{N_b}{N_e} \omega_{ce} = 3.24 \text{ mHz} \tag{6.14}$$

The resulting growth rate is many orders of magnitude slower than the plasma frequency and the time of a particle spent in the WGTS. Because of this, such a mode cannot form in KATRIN.

6.5 Plasma instability in the Whistler mode caused by a gyrating electron stream

A whistler mode is a transverse electromagnetic wave with a frequency above the ion gyro frequency. The investigation of the Whistler instability is based on a paper by Bell and Buneman [13]. Formula 12 of the paper describes the growth rate of the instability at the optimal angle of 60° of the wave vector with respect to the magnetic field. We assume k to be the inverse of the electron gyro radius and the speed to be the drift speed of the fast electrons, so $v_z = v_{0b} = 0.122\ c$. We read that $u = -v_z$ and use $v_\perp = v_z \cdot sin(\psi)$. In the notation of the paper $\omega_H = \omega_{ce}$ is the gyro frequency of the electrons and $\omega_1 = \omega_H - ku$. From the number densities we get $\omega_m^2 = e^2 N_b / m_e \epsilon_0$ and $\omega_0^2 = e^2 N_c / m_e \epsilon_0$. For comfort reasons we list all the values again:

- $v_z = v_{0b} = 0.122\ c$
- $v_\perp = v_z \cdot sin(\psi) \quad | \psi = 60°$
- $\omega_{ce} = \frac{qB}{m_e}$
- $k = \frac{1}{l_{gyro}} = \frac{\omega_{ce}}{v\perp} = \frac{\omega_{ce}}{v_z sin(60°)}$
- $\omega_m^2 = e^2 N_b / m_e \epsilon_0$
- $\omega_1 = \omega_H - ku = \omega_H + kv_z = \omega_{ce} + kv_z$

The formula finally gives:

$$(\delta sin(\psi))_{max} = 0.69 \cdot \left(\frac{k^2 < v_\perp^2 > \omega_m^2}{2\omega_1 + \omega_0^2 \omega_H / (\omega_H - \omega_1)^2} \right)^{1/3} \approx 84 \text{ MHz} \tag{6.15}$$

If our assumptions are correct, this mode could exist in KATRIN. This needs to be checked with numerical simulations.

6.6 Two stream instability

Two components of electrons with different velocity distributions can cause instabilities in a plasma. We evaluate the possibility of having such an instability in the KATRIN WGTS based on a paper by Gary [48]. The paper assumes an unmagnetized plasma, which is not true in KATRIN. However, it still gives an idea whether an instability could exist or not. In Table 1 of Garys paper a list of possible instabilities is given. In the conditions present at KATRIN only the Langmuir beam instability may appear because the condition $n_b/n_e < (v_b/v_{0b})^3$ is fulfilled. Here n_b is the number of high energy beta electrons and n_e is the total number of electrons, which is many orders of magnitude larger. $v_b = \sigma_b$ is the thermal speed of the beta electrons and $v_{0b} = x_{0b}$ is the drift velocity, which is about $0.5 \cdot v_b$. Langmuir modes are longitudinal waves of the electric field. The wave vector k of the Langmuir instability is given by

$$k_j = \sqrt{\frac{4\pi n_j e_j^2}{k_B T_j}} \tag{6.16}$$

where the index j indicates the electron species. Here n is the number density, e the charge and $k_B T$ the kinetic energy of the electron compound. In our case the thermal electrons may cause the instability. For this mode we get

$$k_c = 26.45 \text{ cm}^{-1} \leftrightarrow \lambda = 0.238 \text{ cm}. \tag{6.17}$$

Based on this estimation we see that this instability could exist in the KATRIN experiment. However, there is a strong magnetic field in KATRIN and there is no analytic calculation of Langmuir modes in magnetic field available. For this reason the result needs to be validated with a numerical simulation.

Appendix A

Appendix

A.1 Eloss results

Table A.1 shows the parameters from the Eloss fit with the C++ program to the ToF, the 50 % CD and the 100 % CD integral data on deuterium. This corresponds to the plots in figure 4.8 and figure 4.9. The χ^2 of the fit is $\chi^2/\text{ndf} = 2741.79/2534 = 1.082$.
Table A.2 shows the parameters from the Eloss fit with the Python program to the ToF, the 15 % CD and the 50 % CD integral data on deuterium. This corresponds to the plots in figure 4.10 and figure 4.11. The χ^2 of the fit is $\chi^2/\,\text{ndf} = 1769/1568 = 1.1285$.

Table A.1: Result of the combined Eloss fit of ToF, 50 % CD integral and 100 % CD integral Data using the C++ program. The shifts of the individual data sets have been determined before. The 'tail factor' is multiplied to μ except for the unscattered electrons which determine the height of the transmission edge. The tail factor is the fraction of the Eloss function in our measurement range of 0-55 eV.
Note that this function is not properly normalized, and that the shifts of the data sets need to be taken into account for the positions μ_1, μ_2, μ_3.

Parameter	value	uncertainty	fixed	comment
A_1	+4.72240230E-01	+1.61390709E-02	no	
μ_1	+1.17907532E+01	+1.13579124E-02	no	
σ_1	+1.89280622E-01	+7.18303991E-03	no	Eloss
A_2	+3.86780654E+00	+8.32526223E-03	no	model
μ_2	+1.27160216E+01	+2.77267305E-03	no	parameters
σ_2	+4.78400864E-01	+1.14315334E-03	no	
A_3	+1.05551575E+00	+1.80941182E-03	no	
μ_3	+1.48384762E+01	+3.65576460E-03	no	
σ_3	+1.02484089E+00	+4.30676373E-03	no	
tail factor	+9.44053789E-01	+1.89941664E-04	no	
μ_{50}	+6.56685468E-01	+1.93915397E-04	no	μ is the
shift $_{50}$	+1.54024692E-02	0	yes	scattering
μ_{100}	+1.64602250E+00	+1.31750563E-04	no	probability
shift $_{100}$	+2.68477702E-02	0	yes	in each
μ_{ToF}	+1.06871325E-01	+1.54678094E-03	no	data set
shift $_{ToF}$	+2.30976975E-02	0	yes	
Amp $_{ToF}$	+9.73272648E-01	+1.32589191E-02	no	
Area	+9.95428961E-01	+1.08523197E-03	no	
c	+1.12871210	0	yes	parameters
d	6.40273295	0	yes	of
e	-7.80442058	0	yes	BED model
f	+2.16461570	0	yes	
E_{ion}	+1.54600000E+01	0	yes	lit. val.

Table A.2: Result of the combined Eloss fit of ToF, 6 % CD integral and 50 % CD integral Data using the Python program. The red. χ^2 of the fit is $\chi^2/\,\mathrm{ndf} = 1769/1568 = 1.1285$.

Parameter	value	uncertainty	fixed	comment
A_1	0.0314653	0.00182775	no	
μ_1	11.8496	0.0171574	no	
σ_1	0.186672	0.0131646	no	Eloss
A_2	0.273726	0.00125314	no	model
μ_2	12.7809	0.0040227	no	parameters
σ_2	0.483822	0.0028528	no	
A_3	0.0745642	0.000350984	no	
μ_3	14.9006	0.0101218	no	
σ_3	1.04957	0.00638181	no	
μ_{15}	0.0866429	9.7415e-05	no	μ is the
μ_{50}	0.657479	0.000225468	no	scattering
μ_{ToF}	0.101277	0.000238972	no	probability
Amp $_{15}$	1.08308	0.000896573	no	in each
Amp $_{50}$	0.969175	0.000490712	no	data set
Bg	-1.45079e-05	2.1732e-06	no	
c	+1.1262	0	yes	c-f from
d	6.3982	0	yes	BED paper
e	-7.8055	0	yes	
f	+2.1440	0	yes	
E_{ion}	+1.54600000E+01	0	yes	lit. val.

A.2 Transmission functions

Figures A.1 to A.5 show fits to transmission functions at different plate angles. For details of the measurement see KATRIN Elog knm1/222. The e-gun was operated with the LDLS light source and with a voltage difference between the plates of 4250 V. The magnetic field settings of the KATRIN beamline are the ones used in KNM1. The magnetic field in the center of the analyzing plane is about $B = 6.3\,\mathrm{G}$. The e-gun beam hit the detector in the bulls eye (pixel 2). The parameters of the fit as well as the position of the stepper motor for the plate angle are given in the plots.

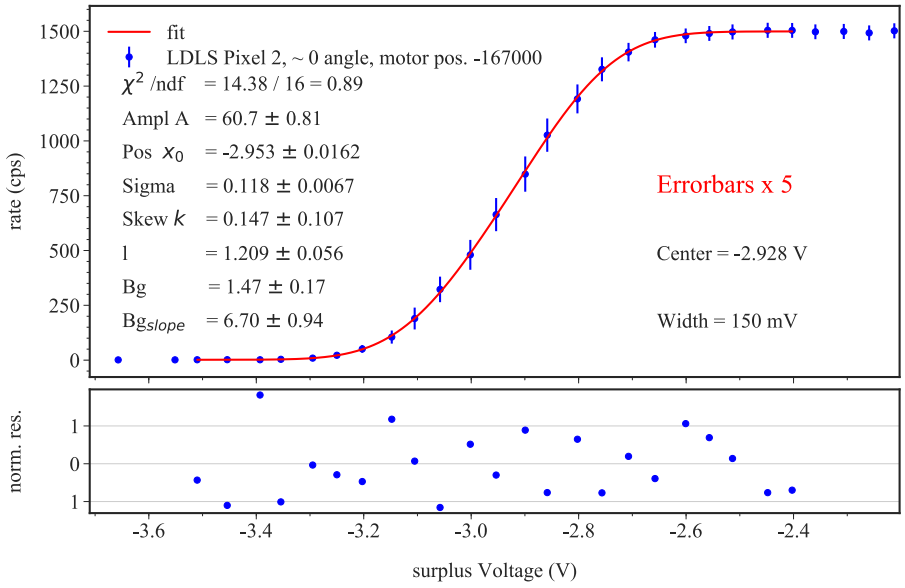

Figure A.1: Transmission function at zero angle

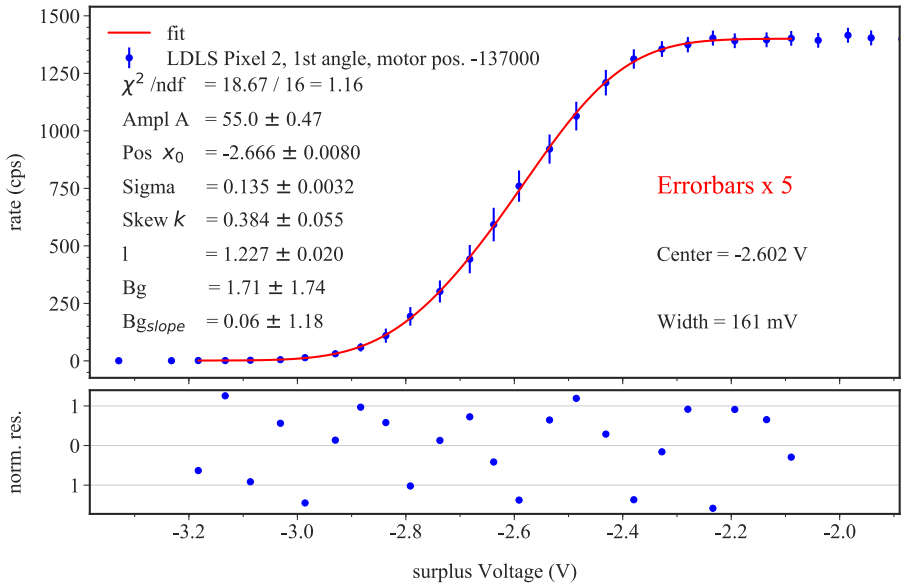

Figure A.2: second measured angle

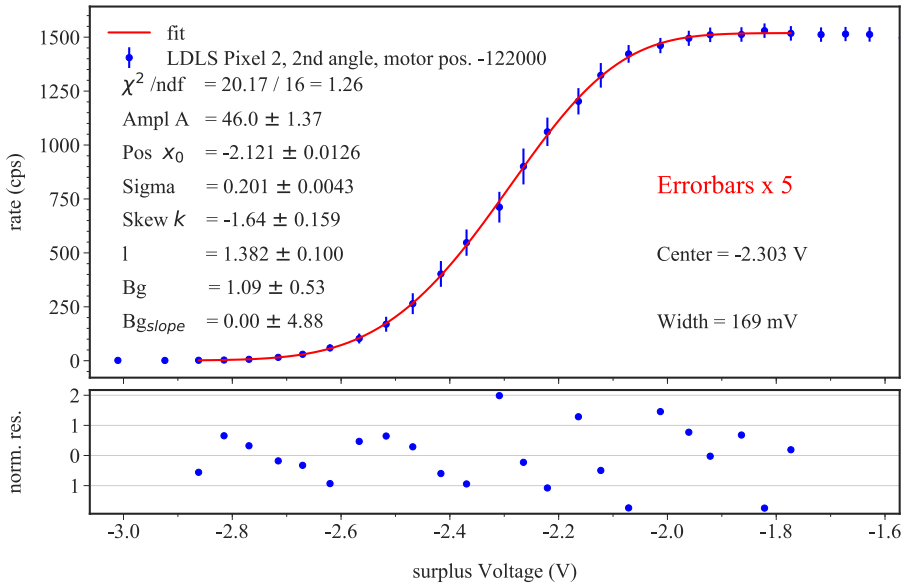

Figure A.3: third measured angle

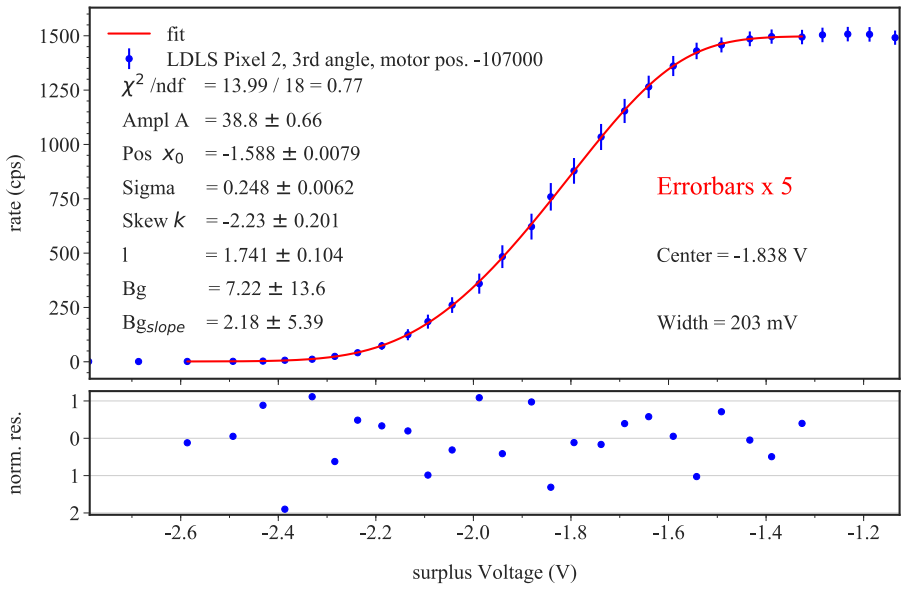

Figure A.4: fourth measured angle

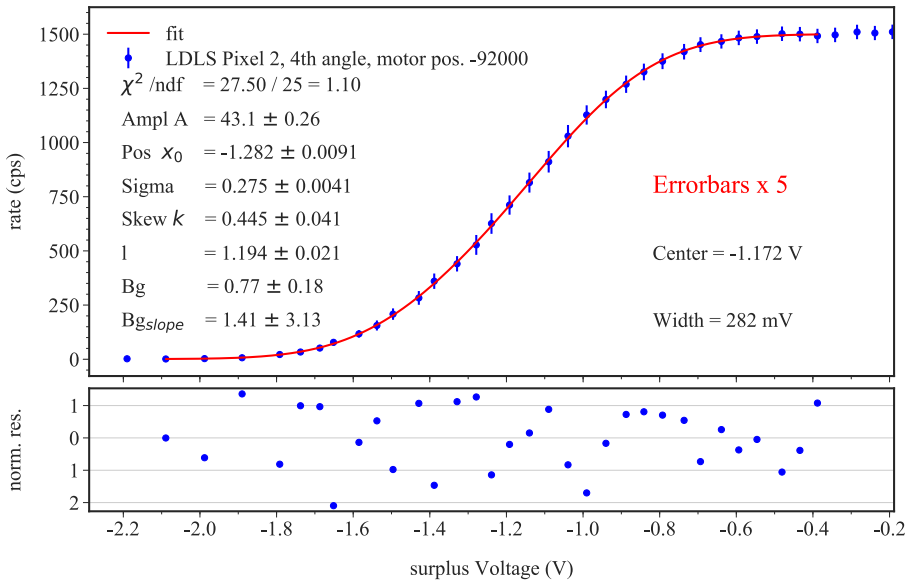

Figure A.5: highest measured angle

A.3 E-gun diode efficiency

For the e-gun measurements in KATRIN (STS3a, KNM1, KNM2) a photo diode from Hamamatsu of type S2592-03 (in a temperature controlled housing) was used. The wavelength dependend efficiency is extracted from the Data sheet [58] and is displayed in figure A.6.

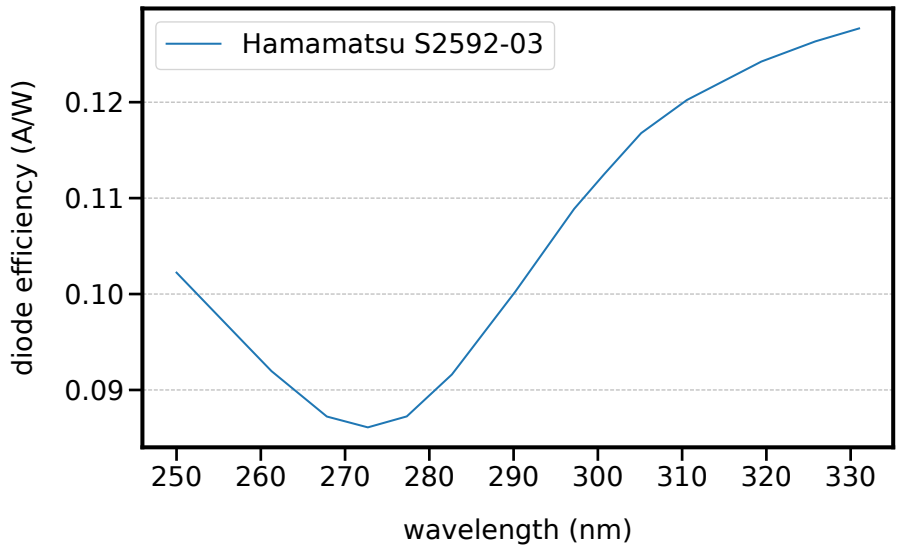

Figure A.6: Diode efficiency of S2592-03. Data extracted from [58]. This diode is used for e-gun measurements in STS3a and KNM1.

A.4 Appendix: Edge positions

Fit of the transmission edge of the Eloss measurements of KNM1. The measurements are performed with the UV-laser. The Eloss data is provided by L. Schimpf. The transmission edge is at 94 % of the hight of the transmission function.

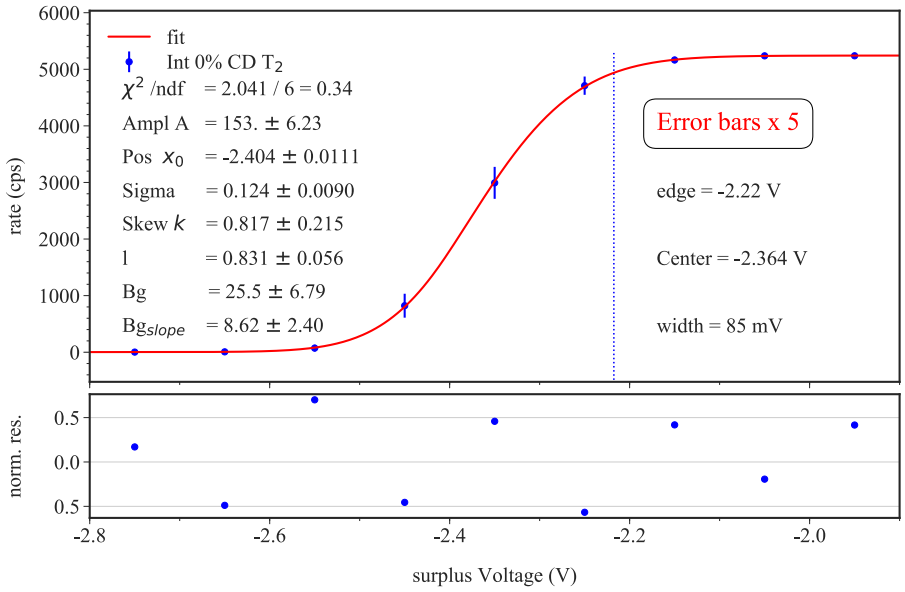

Figure A.7: Transmission edge of the KNM1 Eloss measurement with 0 % CD.

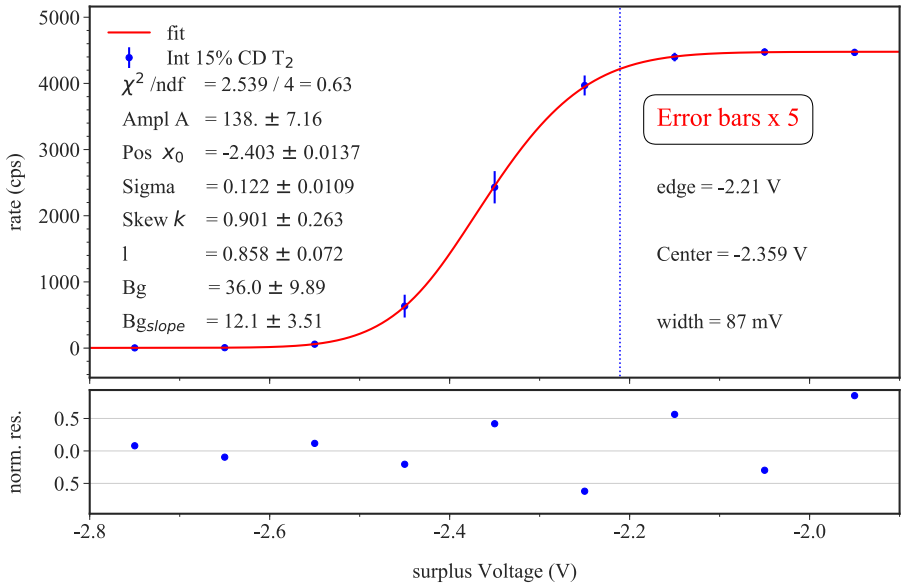

Figure A.8: Transmission edge of the KNM1 Eloss measurement with 15 % CD.

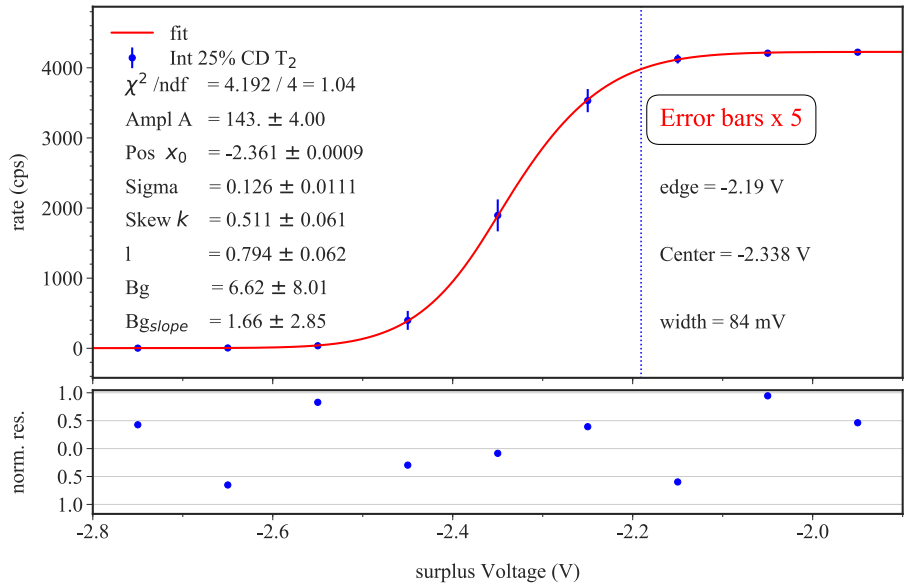

Figure A.9: Transmission edge of the KNM1 Eloss measurement with 25 % CD.

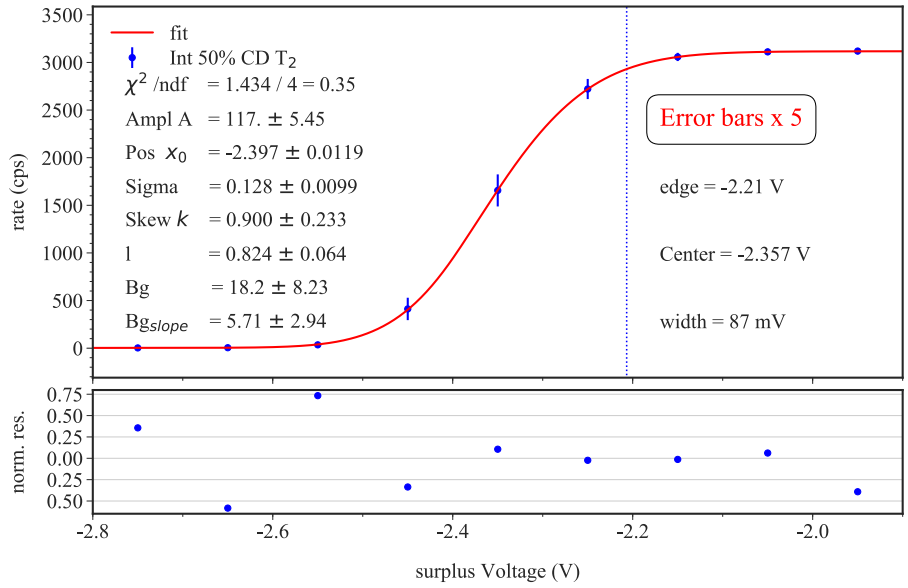

Figure A.10: Transmission edge of the KNM1 Eloss measurement with 50 % CD.

A.5 Light intensity distribution on rear wall

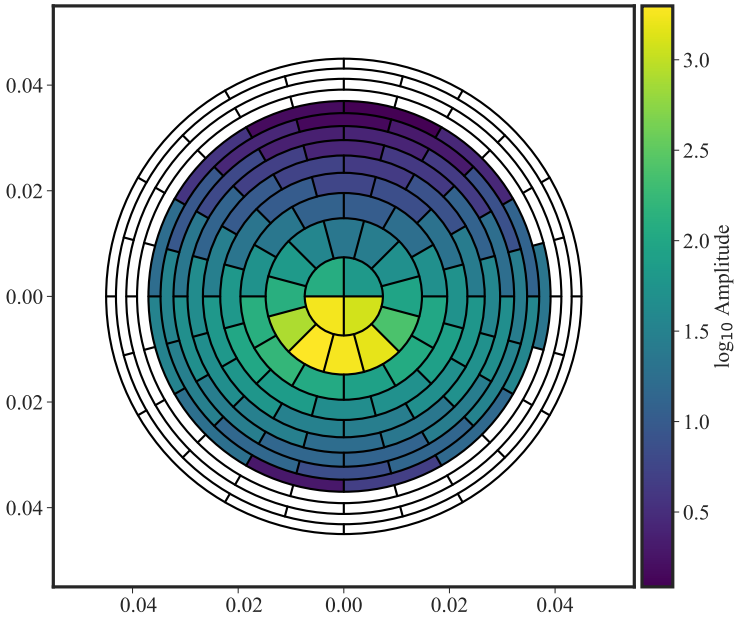

Figure A.11: Fitted amplitude of the Fowler measurement of the RW at the beginning of KNM1. This value gives a good impression of the light intensity distribution. Notice the log_{10} scale.

A.6 Contact potential difference with Kelvin probe on rear wall

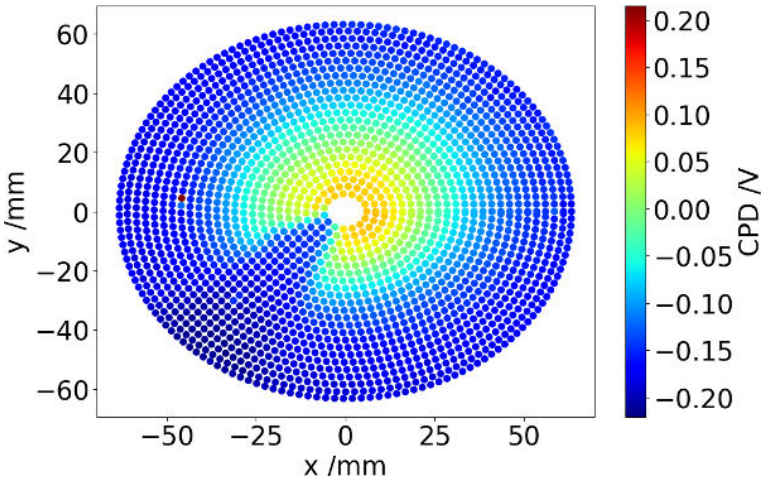

Figure A.12: Contact potential difference (CPD) measurement of the KATRIN rear wall measured with a Kelvin probe before the RW was mounted to the KATRIN experiment. A low CPD (blue) corresponds to a large work function.
Measurement and picture by F. Friedel, KIT. The orientation does not correspond to the one shown in the Fowler measurements.

A.7 KNM2 e-gun work function measurement

Example plots of e-gun Fowler measurements in the beginning of KNM2.

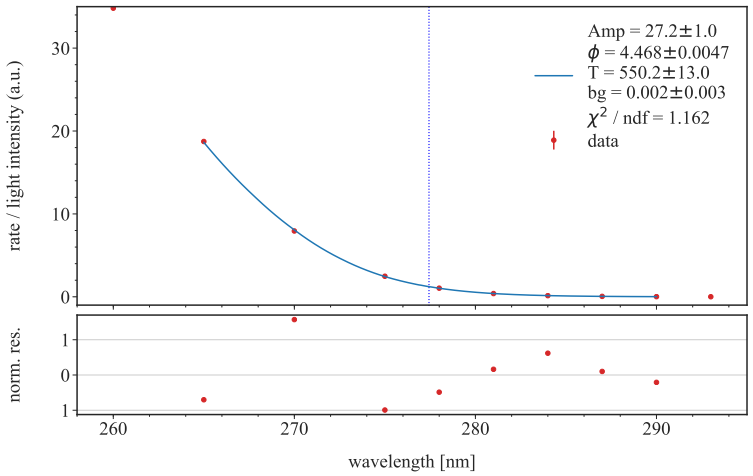

Figure A.13: Fowler measurement of the e-gun with the FBM-Tristan detector at the beginning of KNM2.

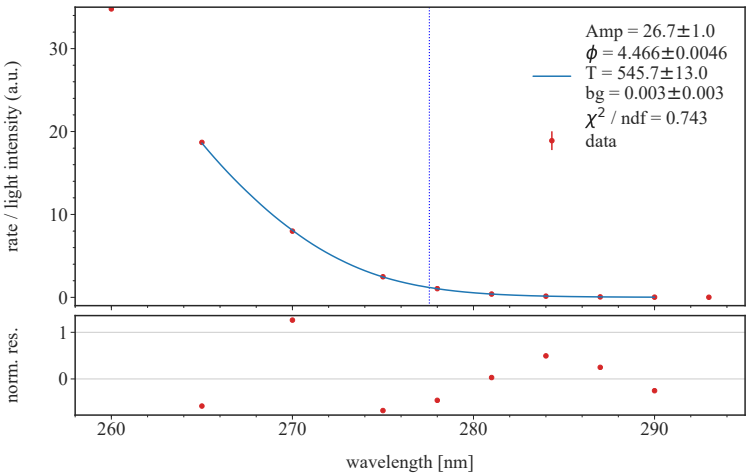

Figure A.14: Fowler measurement of the e-gun with the FBM-Tristan detector at the beginning of KNM2.

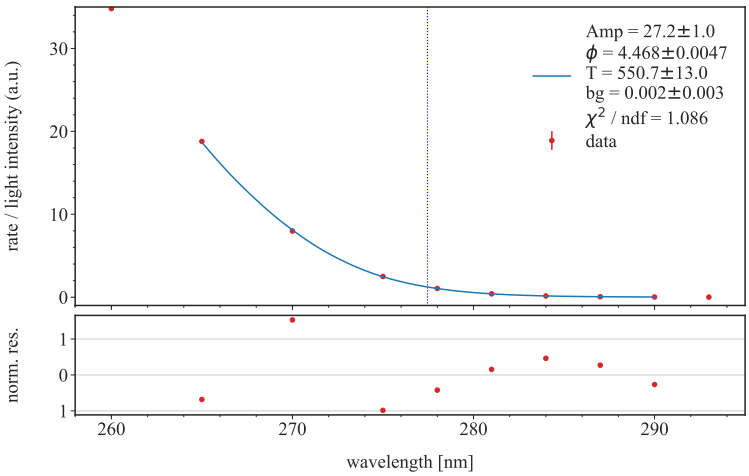

Figure A.15: Fowler measurement of the e-gun with the FBM-Tristan detector at the beginning of KNM2.

A.8 Plasma

Calculation how to get from a $\frac{dN}{dlogE}$ to a $\frac{dN}{dv}$ spectrum:

$$\frac{dN}{d\,logE} = \frac{dE}{d\,logE}\frac{dN}{dE} \tag{A.1}$$

$$= (\frac{d\,logE}{dE})^{-1}\frac{dN}{dE} \tag{A.2}$$

$$= (\frac{1}{E})^{-1}\frac{dN}{dE} \tag{A.3}$$

$$= E\frac{dN}{dE} \tag{A.4}$$

$$= E\frac{dv}{dE}\frac{dN}{dv} \tag{A.5}$$

$$= \frac{1}{2}mv^2(\frac{dE}{dv})^{-1}\frac{dN}{dv} \tag{A.6}$$

$$= \frac{1}{2}mv^2\frac{1}{mv}\frac{dN}{dv} \tag{A.7}$$

$$= \frac{1}{2}v\frac{dN}{dv} \tag{A.8}$$

$$\frac{dN}{dv} = \frac{2}{v}\frac{dN}{d\,logE} \tag{A.9}$$

$$= 2\sqrt{\frac{m}{2E}}\frac{dN}{d\,logE} \tag{A.10}$$

$$= \sqrt{\frac{2m}{E}}\frac{dN}{d\,logE} \tag{A.11}$$

Bibliography

[1] D. N. Abdurashitov, A. I. Belesev, V. G. Chernov, E. V. Geraskin, A. A. Golubev, G. A. Koroteev, N. A. Likhovid, A. A. Nozik, V. S. Pantuev, V. I. Parfenov, and et al. Electron scattering on hydrogen and deuterium molecules at 14–25 kev by the "troitsk nu-mass" experiment. *Physics of Particles and Nuclei Letters*, 14(6):892–899, Nov 2017.

[2] Max Aker, Konrad Altenmüller, Marius Arenz, Woo-Jeong Baek, John Barrett, Armen Beglarian, Jan Behrens, Anatoly Berlev, Uwe Besserer, Klaus Blaum, and et al. First operation of the katrin experiment with tritium. *The European Physical Journal C*, 80(3), Mar 2020.

[3] Ali Ashtari Esfahani et al. Determining the neutrino mass with cyclotron radiation emission spectroscopy—project 8. *Journal of Physics G: Nuclear and Particle Physics*, 44(5):054004, mar 2017.

[4] J.F. Amsbaugh, J. Barrett, and A. Beglarian et al. Focal-plane detector system for the katrin experiment. *Nuclear Instruments and Methods in Physics Research Section A: Accelerators, Spectrometers, Detectors and Associated Equipment*, 778:40 – 60, 2015.

[5] V. Aseev, A.I. Belesev, A. Berlev, E. Geraskin, O. Kazachenko, Yu.E. Kuznetsov, V. Lobashev, Roman Ostroumov, Nikita Titov, Sergey Zadorozhny, Yu.I. Zakharov, J. Bonn, B. Bornschein, L. Bornschein, E. Otten, M. Przyrembel, Ch Weinheimer, and A. Saenz. Energy loss of 18 kev electrons in gaseous t and quench condensed d films. *The European Physical Journal D*, 10:39–52, 03 2000.

[6] V. N. Aseev, A. I. Belesev, A. I. Berlev, E. V. Geraskin, A. A. Golubev, N. A. Likhovid, V. M. Lobashev, A. A. Nozik, V. S. Pantuev, V. I. Parfenov, and et al. Upper limit on the electron antineutrino mass from the troitsk experiment. *Physical Review D*, 84(11), Dec 2011.

[7] Martin Babutzka. *Design and development for the Rearsection of the KATRIN experiment*. PhD thesis, Karlsruher Institut für Technologie, 2014.

[8] S. Bauer, R. Berendes, F. Hochschulz, H.W. Ortjohann, S. Rosendahl, T. Thümmler, M. Schmidt, and C. Weinheimer. Next generation KATRIN high precision voltage divider for voltages up to 65kV. *Journal of Instrumentation*, 8(10):P10026, 2013.

[9] Stephan Bauer. *Energy calibration and stability monitoring of the KATRIN experiment*. PhD thesis, Westfälische Wilhelms-Universität Münster, 2014.

[10] G Beamson, H Q Porter, and D W Turner. The collimating and magnifying properties of a superconducting field photoelectron spectrometer. *Journal of Physics E: Scientific Instruments*, 14(2):256–256, feb 1981.

[11] J. Behrens, P. C.-O. Ranitzsch, M. Beck, A. Beglarian, M. Erhard, S. Groh, V. Hannen, M. Kraus, H.-W. Ortjohann, O. Rest, K. Schlösser, T. Thümmler, K. Valerius, K. Wierman, J. F. Wilkerson, D. Winzen, M. Zacher, and C. Weinheimer. A pulsed, mono-energetic and angular-selective UV photo-electron source for the commissioning of the KATRIN experiment. *The European Physical Journal C*, 77(6):410, 2017.

[12] Jan D. Behrens. *Design and commissioning of a mono-energetic photoelectron source and active background reduction by magnetic pulse at the KATRIN spectrometers*. PhD thesis, Westfälische Wilhelms-Universität Münster, 2016.

[13] T. F. Bell and O. Buneman. Plasma instability in the whistler mode caused by a gyrating electron stream. *Phys. Rev.*, 133:A1300–A1302, Mar 1964.

[14] Fabian Block. *Statistical Data Analysis Tools and Magnetic Field Systematics for Neutrino Mass Analysis with KATRIN*. PhD thesis, Karlsruher Institut für Technologie, preliminary.

[15] J Bonn, L Bornschein, B Degen, E.W Otten, and Ch Weinheimer. A high resolution electrostatic time-of-flight spectrometer with adiabatic magnetic collimation. *Nuclear Instruments and Methods in Physics Research Section A: Accelerators, Spectrometers, Detectors and Associated Equipment*, 421(1):256 – 265, 1999.

[16] Salvador Centelles Chuliá, Rahul Srivastava, and José W.F. Valle. Seesaw roadmap to neutrino mass and dark matter. *Physics Letters B*, 781:122–128, Jun 2018.

[17] Planck Collaboration. Planck 2018 results. vi. cosmological parameters. `https://arxiv.org/abs/1807.06209`, 2018.

[18] E. Cosulich, F. Fontanelli, G. Gallinaro, F. Gatti, and S. Vitale. The Beta decay of Re-187 studied with a cryogenic microcalorimeter: Status report. *Nucl. Phys.*, A592:59–68, 1995.

[19] G. Danby, J-M. Gaillard, K. Goulianos, L. M. Lederman, N. Mistry, M. Schwartz, and J. Steinberger. Observation of high-energy neutrino reactions and the existence of two kinds of neutrinos. *Phys. Rev. Lett.*, 9:36–44, Jul 1962.

[20] P.F. de Salas, D.V. Forero, C.A. Ternes, M. Tórtola, and J.W.F. Valle. Status of neutrino oscillations 2018: 3 hint for normal mass ordering and improved cp sensitivity. *Physics Letters B*, 782:633 – 640, 2018.

[21] W. Demtröder. *Experimental Physik 4: Kern- Teilchen- und Astrophysik*. Springer-Verlag, Berlin, 2005. 2. Auflage, ISBN 3-540-21451-8.

[22] Michelle J. Dolinski, Alan W.P. Poon, and Werner Rodejohann. Neutrinoless double-beta decay: Status and prospects. *Annual Review of Nuclear and Particle Science*, 69(1):219–251, Oct 2019.

[23] Stephan Dyba. *Background reduction by the inner wire electrode and set-up of the condensed krypton source at the neutrino mass experiment KATRIN*. PhD thesis, Westfälische Wilhelms Universität Münster, 2018.

[24] A. Einstein. Über einen die erzeugung und verwandlung des lichtes betreffenden heuristischen gesichtspunkt. *Annalen der Physik*, 322(6):132–148, 1905.

[25] S. Eliseev, K. Blaum, M. Block, S. Chenmarev, H. Dorrer, Ch. E. Düllmann, C. Enss, P. E. Filianin, L. Gastaldo, M. Goncharov, U. Köster, F. Lautenschläger, Yu. N. Novikov, A. Rischka, R. X. Schüssler, L. Schweikhard, and A. Türler. Direct measurement of the mass difference of ^{163}Ho and ^{163}Dy solves the q-value puzzle for the neutrino mass determination. *Phys. Rev. Lett.*, 115:062501, Aug 2015.

[26] S. Eliseev, K. Blaum, M. Block, S. Chenmarev, H. Dorrer, Ch. E. Düllmann, C. Enss, P. E. Filianin, L. Gastaldo, M. Goncharov, U. Köster, F. Lautenschläger, Yu. N. Novikov, A. Rischka, R. X. Schüssler, L. Schweikhard, and A. Türler. Direct measurement of the mass difference of ^{163}Ho and ^{163}Dy solves the q-value puzzle for the neutrino mass determination. *Phys. Rev. Lett.*, 115:062501, Aug 2015.

[27] Enrico Ellinger. *Development and investigation of the Forward Beam Monitor for the KATRIN experiment*. PhD thesis, Bergische Universität Wuppertal, 2019.

[28] Energetiq. Eq-99xfc-ldls. `https://www.energetiq.com/fiber-coupled-laser-driven-light-source-long-life-compact`, 2019.

[29] M. Erhard, J. Behrens, S. Bauer, A. Beglarian, R. Berendes, G. Drexlin, F. Glück, R. Gumbsheimer, J. Hergenhan, B. Leiber, S. Mertens, A. Osipowicz, P. Plischke, J. Reich, T. Thümmler, N. Wandkowsky, C. Weinheimer, and S. Wüstling. Technical design and commissioning of the KATRIN large-volume air coil system. *Journal of Instrumentation*, 13(02):P02003, 2018.

[30] Moritz G. Erhard. *Influence of the magnetic field on the transmission characteristics and neutrino mass systematic of the KATRIN experiment.* PhD thesis, Karlsruher Institut für Technologie, 2016.

[31] Ivan Esteban, M. C. Gonzalez-Garcia, Alvaro Hernandez-Cabezudo, Michele Maltoni, and Thomas Schwetz. Global analysis of three-flavour neutrino oscillations: synergies and tensions in the determination of 23, cp, and the mass ordering. *Journal of high energy physics*, 2019(1):106, 2019. 51.03.06; LK 01.

[32] A. Marsteller et al. Neutral tritium gas reduction in the katrin differential pumping sections. to be published.

[33] Aker et al. Improved upper limit on the neutrino mass from a direct kinematic method by katrin. *Physical Review Letters*, 123(22), Nov 2019.

[34] M. Aker et al. Suppression of penning discharges between the katrin spectrometers, 2019.

[35] M. Klein F. Glueck. Neutralisation of the ring electrode potentials. KATRIN internal report, 2019.

[36] E. Fermi. Versuch einer theorie der β-strahlen. i. *Zeitschrift für Physik*, 88(3):161–177, Mar 1934.

[37] E. Ferri, D. Bagliani, M. Biasotti, G. Ceruti, D. Corsini, M. Faverzani, F. Gatti, A. Giachero, C. Gotti, C. Kilbourne, A. Kling, M. Maino, P. Manfrinetti, A. Nucciotti, G. Pessina, G. Pizzigoni, M. Ribeiro Gomes, and M. Sisti. The status of the mare experiment with 187re and 163ho isotopes. *Physics Procedia*, 61:227 – 231, 2015. 13th International Conference on Topics in Astroparticle and Underground Physics, TAUP 2013.

[38] Sebastian Fischer. *Commissioning of the KATRIN Raman system and durability studies of optical coatings in glove box and tritium atmospheres.* PhD thesis, Karlsruher Institut für Technologie (KIT), 2014.

[39] R. H. Fowler. The analysis of photoelectric sensitivity curves for clean metals at various temperatures. *Phys. Rev.*, 38:45–56, Jul 1931.

[40] F. Friedel, C. Röttele, L. Schimpf, J. Wolf, G. Drexlin, M. Hackenjos, A. Jansen, M. Steidl, and K. Valerius. Time-dependent simulation of the flow reduction of d2 and t2 in the katrin experiment. *Vacuum*, 159:161 – 172, 2019.

[41] Fabian Friedel. *Investigations of plasma related systematic effects for the first KATRIN neutrino mass measurement* . PhD thesis, Karlsruher Institut für Technologie, preliminary.

[42] R. Friedl. Enhancing the accuracy of the fowler method for monitoring non-constant work functions. *Review of Scientific Instruments*, 87(4):043901, 2016.

[43] F M Fränkle, F Glück, K Valerius, K Bokeloh, A Beglarian, J Bonn, L Bornschein, G Drexlin, F Habermehl, M L Leber, A Osipowicz, E W Otten, M Steidl, T Thümmler, C Weinheimer, J F Wilkerson, J Wolf, and S V Zadorozhny. Penning discharge in the KATRIN pre-spectrometer. *Journal of Instrumentation*, 9(07):P07028–P07028, jul 2014.

[44] Y. Fukuda et al. Evidence for oscillation of atmospheric neutrinos. *Phys. Rev. Lett.*, 81:1562–1567, 1998.

[45] Alexander Fulst. *Investigations of Systematics at the KATRIN experiment.* PhD thesis, Westfälische Wilhelms Universität Münster, 2020.

[46] Daniel Furse, Stefan Groh, Nikolaus Trost, Martin Babutzka, et al. Kassiopeia: a modern, extensible C++ particle tracking package. *New Journal of Physics*, 19(5):053012, 2017.

[47] A. Gando, Y. Gando, T. Hachiya, A. Hayashi, S. Hayashida, H. Ikeda, K. Inoue, K. Ishidoshiro, Y. Karino, M. Koga, and et al. Search for majorana neutrinos near the inverted mass hierarchy region with kamland-zen. *Physical Review Letters*, 117(8), Aug 2016.

[48] S. Peter Gary. Electrostatic instabilities in plasmas with two electron components. *Journal of Geophysical research*, 90(A9):8213–8221, 1985.

[49] L. Gastaldo, K. Blaum, K. Chrysalidis, T. Day Goodacre, A. Domula, et al. The electron capture in ^{163}Ho experiment – ECHo. *The European Physical Journal Special Topics*, 226(8):1623–1694, Jun 2017.

[50] F. Glück. internal talk. *KATRIN Wiki*, 2019.

[51] Ferenc Glueck. Internal communication.

[52] FEMTO Messtechnik GmbH. Datasheet dlpca-200. `https://www.femto.de/images/pdf-dokumente/de-dlpca-200.pdf`, 2019.

[53] S. Goerhardt, J. Bonn, L. Bornschein, G. Drexlin, F. M. Fraenkle, R. Gumbsheimer, S. Mertens, F. R. Mueller, T. Thuemmler, N. Wandkowsky, C. Weinheimer, and J. Wolf. Impact of a cryogenic baffle system on the suppression of radon-induced background in the katrin pre-spectrometer, 2018.

[54] Juan Gómez-Cadenas, J. Martin-Albo, Mauro Mezzetto, F. Monrabal, and M. Sorel. The search for neutrinoless double beta decay. *Rivista del Nuovo Cimento*, 35, 09 2011.

[55] S. Görhardt, J. Bonn, L. Bornschein, G. Drexlin, F.M. Fränkle, R. Gumbsheimer, S. Mertens, F.R. Müller, T. Thümmler, N. Wandkowsky, C. Weinheimer, and J. Wolf. Impact of a cryogenic baffle system on the suppression of radon-induced background in the KATRIN pre-spectrometer. *Journal of Instrumentation*, 13(10):T10004–T10004, oct 2018.

[56] Moritz Hackenjos. *KATRIN First Light - Commissioning and Modelling of the Beamline*. PhD thesis, Karlsruhe Institute of Technology, 2019.

[57] Otto Hahn and Lise Meitner. Das β-strahlenspektrum von radium und seine deutung. *Zeitschrift für Physik*, 26(1):161–168, Dec 1924.

[58] Hamamatsu. S2592 - si photodiode. `https://www.hamamatsu.com/resources/pdf/ssd/s2592-03_etc_kspd1003e.pdf`, 2020.

[59] V. Hannen, I. Heese, C. Weinheimer, A. Sejersen Riis, and K. Valerius. Deconvolution of the energy loss function of the KATRIN experiment. *Astroparticle Physics*, 89:30 – 38, 2017.

[60] Fabian Harms. *Characterization and Minimization of Background Processes in the KATRIN Main Spectrometer*. PhD thesis, Karlsruher Institut für Technologie (KIT), 2015.

[61] Norman Haussmann. *Simulation and measurement of the Forward Beam Monitor detector signal for the KATRIN experiment*. PhD thesis, Bergische Universität Wuppertal, 2019.

[62] Oliver T Hofmann Hermann Edlbauer, Egbert Zojer. Postadsorption work function tuning via hydrogen pressure control. *The journal of physical chemistry. C*, 2015.

[63] H. Hertz. Ueber einen einfluss des ultravioletten lichtes auf die electrische entladung. *Annalen der Physik*, 267(8):983–1000, 1887.

[64] Markus Hötzel. *Simulation and analysis of source-related effects for KATRIN*. PhD thesis, Karlsruher Institut für Technologie (KIT), 2012.

[65] K Huber. *Molecular Spectra and Molecular Structure*. Springer US, Berlin, 1979. ISBN: 978-1-4757-0963-6.

[66] K. Hugenberg. An angular resolved pulsed uv led photoelectron source for katrin. *Progress in Particle and Nuclear Physics*, 64(2):288 – 290, 2010. Neutrinos in Cosmology, in Astro, Particle and Nuclear Physics.

[67] iminuit team. iminuit – a python interface to minuit. `https://github.com/scikit-hep/iminuit`. Accessed: 2018-03-05.

[68] MITIO INOKUTI. Inelastic collisions of fast charged particles with atoms and molecules—the bethe theory revisited. *Rev. Mod. Phys.*, 43:297–347, Jul 1971.

[69] F. James and M. Roos. Minuit – A System for Function Minimization and Analysis of the Parameter Errors and Correlations. *Computer Physics Communications*, 10:343–367, December 1975.

[70] Alexander Jansen. *The Cryogenic Pumping Section of the KATRIN Experiment - Design Studies and Experiments for the Commissioning*. PhD thesis, Karlsruher Institut für Technologie (KIT), 2015.

[71] P. B. Johnson and R. W. Christy. Optical constants of the noble metals. *Phys. Rev. B*, 6:4370–4379, Dec 1972.

[72] P. B. Johnson and R. W. Christy. Optical constants of transition metals: Ti, v, cr, mn, fe, co, ni, and pd. *Phys. Rev. B*, 9:5056–5070, Jun 1974.

[73] H. Kanter. Slow-electron mean free paths in aluminum, silver, and gold. *Phys. Rev. B*, 1:522–536, Jan 1970.

[74] KATRIN collaboration. KATRIN design report. FZKA scientific report 7090, 2005.

[75] Katrin collaboration. working title: Katrin hardware paper. *tba*, preliminary.

[76] Yong-Ki Kim and M. Eugene Rudd. Binary-encounter-dipole model for electron-impact ionization. *Phys. Rev. A*, 50:3954–3967, Nov 1994.

[77] H.V Klapdor-Kleingrothaus, I.V Krivosheina, A Dietz, and O Chkvorets. Search for neutrinoless double beta decay with enriched 76ge in gran sasso 1990–2003. *Physics Letters B*, 586(3-4):198–212, Apr 2004.

[78] Manuel Klein. *Tritium ions in KATRIN: blocking, removal and detection.* PhD thesis, Karlsruher Institut für Technologie (KIT), 2019. 51.03.01; LK 01.

[79] K. Kodama, N. Ushida, C. Andreopoulos, and N. Saoulidou et al. Observation of tau neutrino interactions. *Physics Letters B*, 504(3):218 – 224, 2001.

[80] W. Kolos and L. Wolniewicz. Accurate computation of vibronic energies and of some expectation values for H_2, D_2, and T_2. *The Journal of Chemical Physics*, 41(12):3674–3678, 1964.

[81] H. A. Kramers. Xciii. on the theory of x-ray absorption and of the continuous x-ray spectrum. *The London, Edinburgh, and Dublin Philosophical Magazine and Journal of Science*, 46(275):836–871, 1923.

[82] Ch Kraus, B. Bornschein, L. Bornschein, J. Bonn, B. Flatt, A. Kovalik, B. Ostrick, E. W. Otten, J. P. Schall, Th. Thümmler, Ch. Weinheimer, and et al. Final results from phase ii of the mainz neutrino mass searchin tritium β decay. *The European Physical Journal C*, 40(4):447–468, Apr 2005.

[83] L. Kuckert, F. Heizmann, G. Drexlin, F. Glück, M. Hötzel, M. Kleesiek, F. Sharipov, and K. Valerius. Modelling of gas dynamical properties of the KATRIN tritium source and implications for the neutrino mass measurement. *Vacuum*, 158:195–205, 2018.

[84] Laura Kuckert. *The Windowless Gaseous Tritium Source of the KATRIN Experiment – Characterisation of Gas Dynamical and Plasma Properties.* PhD thesis, Karlsruher Institut für Technologie (KIT), 2016.

[85] Leybold. Data sheet turbovac mag w 600. `https://www.leyboldproducts.de/media/pdf/a6/16/28/TD_410600V0506_DE595e9bf97018d.pdf`, 2019.

[86] J. W. Liu. Total cross sections for high-energy electron scattering by h_2 ($^1\Sigma_g^+$), n_2 ($^1\Sigma_g^+$), and o_2 ($^3\Sigma_g^-$). *Phys. Rev. A*, 35:591–597, Jan 1987.

[87] V.M. Lobashev and P.E. Spivak. A method for measuring the electron antineutrino rest mass. *Nuclear Instruments and Methods in Physics Research Section A: Accelerators, Spectrometers, Detectors and Associated Equipment*, 240(2):305 – 310, 1985.

[88] M. Arenz et al., KATRIN collaboration. Calibration of high voltages at the ppm level by the difference of ^{83m}Kr conversion electron lines at the katrin experiment. *The European Physical Journal C*, 78(5):368, May 2018.

[89] M. Tanabashi, K. Hagiwara, K. Hikasa et al. Review of particle physics. *Phys. Rev. D*, 98:030001, Aug 2018.

[90] Moritz Machatschek. *Preliminary title: 'Evaluation and systematic analysis of the ^{83m}Kr mode and the KNM1-krypton measurements of the KATRIN experiment'*. PhD thesis, Karlsruhe Institut für Technologie, 2020.

[91] Lise Meitner. Über die rolle der γ-strahlen beim atomzerfall. *Zeitschrift für Physik*, 26(1):169–177, Dec 1924.

[92] Peter Minkowski. μ to eγ at a rate of one out of 109 muon decays? *Physics Letters B*, 67(4):421 – 428, 1977.

[93] E. G. Myers, A. Wagner, H. Kracke, and B. A. Wesson. Atomic masses of tritium and helium-3. *Phys. Rev. Lett.*, 114:013003, Jan 2015.

[94] Sz Nagy, T Fritioff, M Björkhage, I Bergström, and R Schuch. On the q -value of the tritium -decay. *Europhysics Letters (EPL)*, 74(3):404–410, may 2006.

[95] Anatoly F. Nastoyashchii, Nikita A. Titov, Igor N. Morozov, Ference Glück, and Ernst W. Otten. Effects of plasma phenomena on neutrino mass measurements process using a gaseous tritium beta-source. *Fusion Science and Technology*, 48(1):743–746, 2005.

[96] NIST. Estar program to calculate the stopping power. detailed reference list see https://physics.nist.gov/physrefdata/star/text/ref.html, link to the program:. `https://physics.nist.gov/PhysRefData/Star/Text/ESTAR.html`, 2020.

[97] Nobel. The Nobel Prize in Physics 2015. `https://www.nobelprize.org/prizes/physics/2015/press-release/`, 2019.

[98] A. O'HAGAN and TOM LEONARD. Bayes estimation subject to uncertainty about parameter constraints. *Biometrika*, 63(1):201–203, 04 1976.

[99] E W Otten and C Weinheimer. Neutrino mass limit from tritium β decay. *Reports on Progress in Physics*, 71(8):086201, Jul 2008.

[100] W. Pauli. Fünf arbeiten zum ausschliesungsprinzip und zum neutrino. *Wissenschaftliche Buchgesellschaft (1977) - ISBN 10: 3534067339*.

[101] Pfeiffer. Data sheet hipace 300 pmp 04 234. `https://www.pfeiffer-vacuum.com/de/produkte/vakuumerzeugung/turbopumpen/hybridgelagert/hipace-300/5382/hipace-300-mit-tc-110-profibus-dn-100-cf-f`, 2019.

[102] A. Picard, H. Backe, H. Barth, J. Bonn, B. Degen, Th. Edling, R. Haid, A. Hermanni, P. Leiderer, Th. Loeken, A. Molz, R.B. Moore, A. Osipowicz, E.W. Otten, M. Przyrembel, M. Schrader, M. Steininger, and Ch. Weinheimer. A solenoid retarding spectrometer with high resolution and transmission for kev electrons. *Nuclear Instruments and Methods in Physics Research Section B: Beam Interactions with Materials and Atoms*, 63(3):345 – 358, 1992.

[103] M Prall, P Renschler, F Glück, A Beglarian, H Bichsel, L Bornschein, Z Chaoui, G Drexlin, F Fränkle, S Görhardt, S Mertens, M Steidl, Th Thümmler, S Wüstling, C Weinheimer, and S Zadorozhny. The KATRIN pre-spectrometer at reduced filter energy. *New Journal of Physics*, 14(7):073054, jul 2012.

[104] Florian Priester. *Tritiumtechnologie für die fensterlose Quelle WGTS von KATRIN*. PhD thesis, Karlsruher Institut für Technologie (KIT), 2013.

[105] Florian Priester. personal communication, 2017.

[106] F. Reines and C. L. Cowan. Detection of the free neutrino. *Phys. Rev.*, 92:830–831, Nov 1953.

[107] O Rest, D Winzen, S Bauer, R Berendes, J Meisner, T Thümmler, S Wüstling, and C Weinheimer. A novel ppm-precise absolute calibration method for precision high-voltage dividers. *Metrologia*, 56(4):045007, jul 2019.

[108] Oliver Rest. *Precision high voltage at the KATRINexperiment and new methods for anabsolute calibration at ppm-level forhigh-voltage dividers*. PhD thesis, Westfälische Wilhelms Universität Münster, 2019.

[109] Reville, B., Kirk, J. G., Duffy, P., and O'Sullivan, S. A cosmic ray current-driven instability in partially ionised media. *A&A*, 475(2):435–439, 2007.

[110] Adam G. Riess, Stefano Casertano, Wenlong Yuan, Lucas M. Macri, and Dan Scolnic. Large magellanic cloud cepheid standards provide a 1% foundation for the determination of the hubble constant and stronger evidence for physics beyond λcdm. `http://dx.doi.org/10.3847/1538-4357/ab1422`, May 2019.

[111] C. Rodenbeck. Measuring Energy Loss with Time of Flight, Talk at KATRIN CM35 P3, 2018.

[112] Caroline Rodenbeck. *Investigation of inelastic scattering of beta electrons in KATRIN's gaseous tritium source using time of flight methods to determine the neutrino mass.* PhD thesis, Westfälische Wilhelms Universität Münster, preliminary.

[113] M Röllig. Studien zu einem röentgendetektorsystem zur bestimmung der aktivität in der katrin tritiumquelle. *Diploma Thesis*, 2011.

[114] V. A. Rubakov. Cosmology, 2015.

[115] M. E. Rudd. Differential and total cross sections for ionization of helium and hydrogen by electrons. *Phys. Rev. A*, 44:1644–1652, Aug 1991.

[116] M. E. Rudd, K. W. Hollman, J. K. Lewis, D. L. Johnson, R. R. Porter, and E. L. Fagerquist. Doubly differential electron-production cross sections for 200–1500-ev e^-+h_2 collisions. *Phys. Rev. A*, 47:1866–1873, Mar 1993.

[117] M. Röllig, F. Priester, M. Babutzka, J. Bonn, B. Bornschein, G. Drexlin, S. Ebenhöch, Ernst W. Otten, M. Steidl, and M. Sturm. Activity monitoring of a gaseous tritium source by beta induced x-ray spectrometry. *Fusion Engineering and Design*, 88(6):1263 – 1266, 2013. Proceedings of the 27th Symposium On Fusion Technology (SOFT-27); Liège, Belgium, September 24-28, 2012.

[118] Carsten Röttele. *Tritium suppression factor of the KATRIN transport section.* PhD thesis, Karlsruher Institut für Technologie (KIT), 2019. 51.03.01; LK 01.

[119] W.M.H. Sachtler, G.J.H. Dorgelo, and A.A. Holscher. The work function of gold. *Surface Science*, 5(2):221 – 229, 1966.

[120] Alejandro Saenz, Svante Jonsell, and Piotr Froelich. Improved molecular final-state distribution of het^+ for the β-decay process of T_2. *Phys. Rev. Lett.*, 84:242–245, Jan 2000.

[121] Lutz Schimpf. *Characterisation of energy loss processes of 18.6 keV electrons in the gaseous tritium source of KATRIN*. PhD thesis, Karlsruher Institut für Technologie, preliminary.

[122] Magnus Schlösser. *Accurate calibration of the Raman system for the Karlsruhe Neutrino Experiment*. PhD thesis, Karlsruher Institut für Technologie (KIT), 2013.

[123] M. Schlösser, S. Fischer, M. Sturm, B. Bornschein, R. J. Lewis, and H. H. Telle. Design implications for laser raman measurement systems for tritium sample-analysis, accountancy or process-control applications. *Fusion Science and Technology*, 60(3):976–981, 2011.

[124] Magnus Schlösser, Simone Rupp, Hendrik Seitz, Sebastian Fischer, Beate Bornschein, Tim M. James, and Helmut H. Telle. Accurate calibration of the laser raman system for the karlsruhe tritium neutrino experiment. *Journal of Molecular Structure*, 1044:61 – 66, 2013. MOLECULAR SPECTROSCOPY AND MOLECULAR STRUCTURE 2012.

[125] Kerstin Schönung. *Development of a Rear Wall fot the KATRIN Rear Section and investigation of tritium compatibility of Rear Section components*. PhD thesis, Karlsruhe Institute of Technology, 2016.

[126] Johannes S. Schwarz. *The Detector System of the KATRIN Experiment - Implementation and First Measurements with the Spectrometer*. PhD thesis, Karlsruher Institut für Technologie (KIT), 2014.

[127] C. S. Shern. Changes in work function of hydrogen and oxygen adsorption on pt(110) surface measured by mirror electron microscope-leed. *Chinese journal of physics*, 1992.

[128] M Sisti, C Arnaboldi, C Brofferio, G Ceruti, O Cremonesi, E Fiorini, A Giuliani, B Margesin, L Martensson, A Nucciotti, M Pavan, G Pessina, S Pirro, E Previtali, L Soma, and M Zen. New limits from the milano neutrino mass experiment with thermal microcalorimeters. *Nuclear Instruments and Methods in Physics Research Section A: Accelerators, Spectrometers, Detectors and Associated Equipment*, 520(1):125 – 131, 2004. Proceedings of the 10th International Workshop on Low Temperature Detectors.

[129] SNO Collaboration, Q. R. Ahmad, R. C. Allen, T. C. Andersen, and J. D. Anglin et al. Measurement of the rate of ν_e + d $\rightarrow$ p + p + e interactions produced by

^{8}B solar neutrinos at the sudbury neutrino observatory. *Physical Review Letters*, 87(7):71301–1–71301–4, 8 2001.

[130] Daniel R. Stull. Vapor pressure of pure substances. organic and inorganic compounds. *Industrial & Engineering Chemistry*, 39(4):517–540, 1947.

[131] Michael Sturm. *Aufbau und Test des Inner-Loop-Systems der Tritiumquelle von KATRIN*. PhD thesis, Karlsruher Institut für Technologie (KIT), 2010.

[132] The L3 Collaboration The OPAL Collaboration The SLD Collaboration The LEP Electroweak Working Group The SLD Electroweak The ALEPH Collaboration, The DELPHI Collaboration and Heavy Flavour Groups. Precision electroweak measurements on the z resonance. *Physics Reports*, 427(5):257 – 454, 2006.

[133] Thorlabs. Sm1pd2a - mounted uv enhanced silicon photodiode. `https://www.thorlabs.com/thorproduct.cfm?partnumber=SM1PD2A`, 2019.

[134] Nikolaus Rainer-Maria Trost. *Modeling and measurement of Rydberg-State mediated Background at the KATRIN Main Spectrometer*. PhD thesis, Karlsruher Institut für Technologie (KIT), 2019. 51.03.01; LK 01.

[135] Huang-Ming Tsai, Huang-Wen Fu, Chang-Yang Kuo, Liang-Jen Huang, Chang-Sheng Lee, Chih-Yu Hua, Kai-Yang Kao, Hong-Ji Lin, Hok-Sum Fung, Shih-Chun Chung, Chun-Fu Chang, Ashish Chainani, Liu Hao Tjeng, and Chien-Te Chen. A submicron soft x-ray active grating monochromator beamline for ultra-high resolution angle-resolved photoemission spectroscopy. *AIP Conference Proceedings*, 2054(1):060047, 2019.

[136] Korbinian Urban. Application of a TRISTAN Silicon Drift Detector as Forward Beam Monitor in KATRIN. *Diploma Thesis*, 2019.

[137] K Valerius, M Beck, H Arlinghaus, J Bonn, V M Hannen, H Hein, B Ostrick, S Streubel, Ch Weinheimer, and M Zbořil. A UV LED-based fast-pulsed photoelectron source for time-of-flight studies. *New Journal of Physics*, 11(6):063018, jun 2009.

[138] K Valerius, H Hein, H Baumeister, M Beck, K Bokeloh, J Bonn, F Glück, H W Ortjohann, B Ostrick, M Zbořil, and Ch Weinheimer. Prototype of an angular-selective photoelectron calibration source for the KATRIN experiment. *Journal of Instrumentation*, 6(01):P01002–P01002, jan 2011.

[139] Kathrin Valerius. *Spectrometer-related background processes and their suppression in the KATRIN experiment*. PhD thesis, Westfälische Wilhelms-Universität Münster, 2009.

[140] R. S Van Dyck, D. L. Farnham, and P. B. Schwinberg. Tritium–helium-3 mass difference using the penning trap mass spectroscopy. *Phys. Rev. Lett.*, 70:2888–2891, May 1993.

[141] D. Venos, J. Kaspar, M. Zboril, O. Dragoun, J. Bonn, A. Kovalik, O. Lebeda, M. Rysavy, K. Schlosser, A. Spalek, and Ch. Weinheimer. Long term stability of the energy of conversion electrons emitted from solid 83rb/83mkr source, 2009.

[142] D. Vénos, J. Sentkerestiová, O. Dragoun, M. Slezák, M. Ryššavý, and A. Špalek. Properties of ^{83m}Kr conversion electrons and their use in the KATRIN experiment. *Journal of Instrumentation*, 13(02):T02012, 2018.

[143] M. Wang, G. Audi, A.H. Wapstra, F.G. Kondev, M. MacCormick, X. Xu, and B. Pfeiffer. The ame2012 atomic mass evaluation. *Chinese Physics C*, 36(12):1603–2014, dec 2012.

[144] C. Weinheimer. Direct determination of the energy loss spectrum by applying a single time-of-flight cut, Internal KATRIN document. `https://ikp-katrin-wiki.ikp.kit.edu/katrin/images/b/bf/18-08-08_Tof_eloss_v2.pdf`, 2018.

[145] Michael Zacher. *High-field electrodes design and an angular-selective photoelectron source for the KATRIN spectrometers*. PhD thesis, Westfälische Wilhelms-Universität Münster, 2015.

[146] Miroslav Zbořil. *Solid electron sources for the energy scale monitoring in the KATRIN experiment*. PhD thesis, Westfälische Wilhelms-Universität Münster, 2011.

[147] Kai Zuber. Neutrino Physics, Institute of physics publishing Bristol and Philadelphia, ISBN10:0-7503-0750-1, 2004.

Danksagung (note of thanks)

Meine Doktorarbeit wäre niemals ohne die großzügige Hilfe vieler Kollegen an der WWU Münster und dem KIT zustande gekommen. Daher möchte ich mich ganz herzlich bei allen Helfern bedanken!

I would like to thank all my colleagues at WWU Münster and KIT for their great support!

I would like to thank especially

- Christian Weinheimer and Volker Hannen for the great supervision of my thesis and all the support they have offered to turn the e-gun from a delayed project with many problems into a true success story with great physics output.
- The GRK2149 for the great support this research training group offers to its students.
- Kathrin Valerius for her great organizational work around and during the measurement campaigns. And of course also for the joyful runs and bike rides.
- Philipp C.O. Ranitzsch for all his help with the e-gun and a great time.
- Hans Werner and all other engineers and the technical staff for their great support.
- Armen for his great support with the e-gun control.
- Beate, Lutz, the Loops team and all other people in TLK who have always been a helping hand during my time at KIT.
- Alexander Fulst and Jan Behrens for the great coding support.
- Lutz and Caroline for their great work at the e-gun and the e-loss model.
- Sanshiro for his great work on the pile-up correction and for the nice climbing trips.

- Alexey, Kevin, Mariia, Daniel, Oliver, Stephan, Nico and all other group members at WWU for a really nice time in the institude.
- Klaus Mehret. Was wäre das Leben der Studenten am KIT nur ohne dich?
- Ferenc for a nice time at KIT and fruitful discussions about the KATRIN experiment and especially the ionization model.
- Klaus Schlösser for his help at the rear section.
- Sascha Wüstling for his expertise, advise and help with the electronic setup at the e-gun and the rear wall.
- and many, many more ... :-)